Titre: Title:	Dispersion Engineered Real-Time Analog Signal Processing Components and Systems
Auteur: Author:	Shulabh Gupta
Date:	2012
Type:	Mémoire ou thèse / Dissertation or Thesis
Référence: Citation:	Gupta, S. (2012). Dispersion Engineered Real-Time Analog Signal Processing Components and Systems [Thèse de doctorat, École Polytechnique de Montréal]. PolyPublie. https://publications.polymtl.ca/795/

UNIVERSITÉ DE MONTRÉAL

DISPERSION ENGINEERED REAL-TIME ANALOG SIGNAL PROCESSING COMPONENTS AND SYSTEMS

SHULABH GUPTA
DÉPARTEMENT DE GÉNIE ELECTRIQUE
ÉCOLE POLYTECHNIQUE DE MONTRÉAL

THÈSE PRÉSENTÉE EN VUE DE L'OBTENTION
DU DIPLÔME DE PHILOSOPHIÆ DOCTOR (PH.D.)
(GÉNIE ELECTRIQUE)
MARS 2012

UNIVERSITÉ DE MONTRÉAL

ÉCOLE POLYTECHNIQUE DE MONTRÉAL

Cette thèse intitulée :

DISPERSION ENGINEERED REAL-TIME ANALOG SIGNAL PROCESSING COMPONENTS AND SYSTEMS

présentée par : GUPTA Shulabh.
en vue de l'obtention du diplôme de : Philosophiæ Doctor (PH.D.)
a été dûment acceptée par le jury constitué de :

M. WU Ke, Ph.D., président.
M. CALOZ Christophe, Ph.D., membre et directeur de recherche.
M. PLANT David, Ph.D., membre.
M. MANSOUR Raafat, Ph.D., membre.

To my Friends.

Acknowledgments

The biggest thanks goes to my advisor, Prof. Christophe Caloz, for his wonderful mentorship, constant encouragement, constructive criticism and education beyond just science. This thesis is a result of working in an ideal research environment that he has built over the years under his influential leadership. Thanks to him and his sense of humour, it has been a smooth and an enjoyable ride with a steep learning curve, where I could go one step closer to my true potential.

I would also like to thank Dr. Richard V. Snyder and Dr. Robert J. Wenzel with whom I had very educative interactions during my research. Thanks to Prof. Makoto Ando and Prof. Jiro Hirokawa for supporting me during my memorable stay in Japan. Further thanks to Prof. Alejandro Á. Melcón, Prof. Jose Azaña, Prof. Yasushi Horii and Prof. Pierre Lemaître-Auger for engaging in various scientific discussions and work with me along with their timely guidance in my research work.

I would also like to acknowledge the members of my thesis jury, Prof. David V. Plant from McGill University, Prof. Rafaat Mansour from University of Waterloo and Prof. Ke Wu from École Polytechnique, for having accepted to examine this work and for their valuable comments.

Many components and systems which I designed would not have been realized without the assistance of all technical staffs at the Poly-Grames Research Centre. I want to thank Mr. Jules Gauthier, Mr. Steve Dubé and Mr. Traian Antonescu who have helped in realizing many of the first devices. I am grateful to Mr. Jean-Sébastien Décarie for troubleshooting of all computer problems and to Mrs. Louise Clément, Mrs. Nathalie Lévesque, and Mrs. Ginette Desparois for all of the administrative matters.

I owe a lot to my team. Thanks to Louis, Dimitrios, Simon and Luiz for spending countless hours educating me about science, brainstorming about new research ideas, engaging me in incredible discussions about whatever scientific and social issues we generally discuss during those late beer hours after work. Thanks to Hoang, Sam, Ning, Toshiro, Armin, Babak and Attieh for their unlimited guidance in my research and their patience in dealing with me during my unsolicited and untimely visits to their office spaces. Special thanks to Sebastian with whom I had a productive

time during his one year stay in Montréal. Thanks to Miro, Yuanfeng, Kim, Takashi, Sugano-San, Takumi, Claude and my other Japanese colleagues as well. Equal thanks to other people in Polygrames, such as Leandro, Simone, Marta, Sulav, Tristan, Fan Fan and Liang whom I bothered a lot during these past few years with random evening jabbers and shared good happy times.

Special thanks to my friend, Durga Prasad Pandey, for those long hour discussions about research and life in general. It helped me realize and introspect those subtle aspects of my personality and goals where I could learn a bit more about myself. Thanks to my other three friends; Jitendra Mohan Jha, Vikrant S. Yagnick and Priyank Nandan, who kept my spirits high with their sharp wits and contagious energies throughout my graduate student life.

Finally, a big thanks to my other friends, specially Martin, Vuk, Leah, Herb, Gargi, Fang Xin, Francisco, Thien and many more friends around the world who contributed one way or the other in me becoming a better human being. This thesis is rightly dedicated to my Friends who greatly helped me in living a rather balanced lifestyle and appreciate those little important things in life!

Résumé

Avec la demande croissante pour une plus grande efficacité d'utilisation du spectre de fréquences et l'émergence de systèmes à bande ultra large (UWB) qui en découle, l'analyse d'environnements RF en temps réel est devenue d'une importance capitale. Traditionnellement, ceci est fait en utilisant des techniques d'analyse des signaux en temps réel basées soit sur une approche digitale, soit sur une approche analogique. Les appareils digitaux sont plus attrayants aux basses fréquences à cause de leur grande flexibilité, de leur taille compacte, de leur faible coût et de leur grande fiabilité. Par contre, aux plus hautes fréquences, notamment aux fréquences micro-ondes, les appareils digitaux ont des problèmes fondamentaux tels des performances faibles, un coût élevé des convertisseurs A/D et D/A et une consommation de puissance excessive. À ces fréquences, des appareils et systèmes analogiques sont requis pour des applications d'analyse des signaux en temps réel. à cause de leur mode d'opération fondamentalement analogique, ces systèmes sont appelés analyseurs analogiques de signaux, et l'opération qu'ils effectuent est appelée analyse analogique de signaux (ASP). Cette thèse présente les plus récentes avancées au niveau des ASP. Le concept de ASP est introduit au chapitre 1. La contribution de cette thèse au domaine des ASP est également présentée au chapitre 1.

Le coeur d'un analyseur analogique de signaux en temps reel est une structure de délai dispersive (DDS). Dans une structure dispersive, la vélocité de groupe v_g est une fonction de la fréquence, ce qui cause une dépendance en fréquence du délai de groupe. Par conséquent, un signal à large bande qui se propage le long d'une telle structure est sujet à un espacement dans le temps puisque ses différentes composantes spectrales voyagent avec différentes vitesses de groupes, et sont donc réarrangées dans le temps. En exploitant ce réarrangement temporel, les différentes composantes spectrales d'un signal à large bande peuvent être directement transposées dans le domaine temporel et peuvent alors être analysées en temps réel pour diverses applications. Ce concept, qui constitue le fondement des techniques ASP, est décrit au chapitre 2.

En se basant sur ces principes de dispersion, le présent travail contribue au développement de nouveaux systèmes et composantes ASP ainsi qu'au développement de nouvelles DDS. Deux types de DDS sont utilisés dans le présent travail : a) Lignes

de transmission (TL) composites main-gauche/main-droite (CRLH), et b) structures dispersive passe-tout. En particulier, les réseaux de délai dispersif passe-tout sont étudiés en plus grand détail en se basant sur des réseaux passe-tout avec sections en C dans différentes configurations et en se basant aussi sur de nouvelles procédures de synthèses et des analyses électromagnétiques pour générer des DDS avec des délais de groupe arbitraires.

Le premier type de DDS passe-tout est une cascade de sections en C avec différentes longueurs et différentes caractéristiques de couplage utilisée pour générer un délai de groupe prédéterminé et résultant en un DDS ayant des longueurs non commensurables. Pour cette structure, une procédure itérative basées sur des solutions explicites et utilisée pour générer des réponses en phase quasi-arbitraires est présentée. La synthèse consiste à faire correspondre les pôles de transmission de la cascade de sections en C avec les pôles de transmission de la fonction de transfert spécifiée, où ces derniers pôles sont calculés en utilisant une méthode de génération de polynômes basée sur des solutions explicites. Les pôles de transmission réels et complexes de la fonction de transfert spécifiée sont réalisés en utilisant des sections en C de différentes longueurs et ayant des coefficients de couplage différents. La procédure de synthèse proposée est validée par des analyses électromagnétiques complètes d'un prototype multi-couche. Ce DDS, ainsi que la méthode de synthèse correspondante, est décrite au chapitre 3.

Le deuxième DDS passe-tout est une extension de la structure avec cascade de sections en C où on permet aux sections en C voisines de se couplées entre-elles en utilisant le couplage électrique et magnétique. Ce réseau est obtenu en interconnectant les ports alternés des lignes adjacentes d'un réseau de lignes de transmission couplées ayant **2N** ports, et il est modélisé en utilisant la théorie des lignes de transmission avec plusieurs conducteurs caractérisées par la matrice de capacité **C** et la matrice d'inductance **L**.

En permettant aux différentes sections en C du réseau d'avoir différentes longueurs, une procédure généralisée pour l'ingénierie du délai de groupe est proposée, où des réponses en délai de groupe quasi-arbitraires sont générées en combinant la réponse en délai de groupe de sections en C de différentes longueurs. Une approche de conception informatisée et basée sur des algorithmes génétiques est appliquée pour la synthèse et consiste à déterminer les paramètres structurels des différents groupes de sections en C. En utilisant cette approche, des réseaux avec des longueurs non-

commensurables sont conçus en fonction du délai de groupe à l'aide de la technologie des lignes micro-ruban avec couplages aux bords, et des réponses de délai de groupe gaussiennes, linéaires et quadratiques sont validées par des expériences. Ce DDS est décrit en détail au chapitre 4.

Finalement, ces DDS sont exploitées dans les deux régimes suivants pour des applications d'ASP.

Applications avec ondes guides

Parmi les premières classes d'applications à ondes guidées, les concepts suivants sont présentés et démontrés à l'aide de prototypes au chapitre 5 :

1. Lignes de délai ajustable pour des déphaseurs en temps réel et des sources de délai à temps vrai. 2. Discriminateurs de fréquence pour des détecteurs de fréquence et des appareils faisant des transformées de Fourier en temps réel. 3. Codage par modulation de la position de pulse pour des systèmes d'identification radiofréquences (RFID). 4. Compensation de la dispersion pour des antennes log-périodiques.

Applications avec ondes rayonnées

Parmi les applications à ondes rayonnées, deux systèmes sont démontrés au chapitre 6, basés sur des structures CRLH à ondes de fuite :

1. Transmetteur/récepteur en mode duplex basé sur la division en fréquence. 2. Analyseur de spectre en temps réel (RTSA).

Finalement, le chapter 7 présente la conclusion de la thèse et indique des travaux futurs potentiels dans le domaine des ASP.

Abstract

With the ever increasing demand on higher spectral efficiencies and the related emergence of ultra-wideband (UWB) systems, monitoring RF environments in real-time has become of paramount interest. This is traditionally done using real-time signal processing techniques based on either digital or analog approaches. Digital devices are most attractive at low frequencies due to their high flexibility, compact size, low cost, and strong reliability. However, at higher frequencies, such as millimeter-wave frequencies, digital devices suffer of fundamental issues, such as poor performance, high cost for A/D and D/A converters, and excessive power consumption. At such frequencies, analog devices and systems are required for real-time signal processing applications. Owing to their fundamentally analog mode of operation, these systems are referred to as Analog Signal Processors, and the operation as Analog Signal Processing (ASP). This dissertation presents the most recent advances in these ASP concepts which are introduced in Chapter 1 along with the contribution of this thesis in this domain.

The core of an analog real-time signal processor is a dispersive delay structure (DDS). In a dispersive structure, the group velocity v_g is a function of frequency, which results in a frequency-dependent group delay. Consequently, a wide-band signal traveling along such a structure experiences time spreading, since its different spectral components travel with different group velocities and are therefore temporally rearranged. By exploiting this temporal rearrangement, the various spectral components of a wideband signal can be directly mapped onto time domain and can then be processed in real-time for various applications. This concept is described in Chapter 2 which forms the background of ASP techniques.

Based on these dispersion principles, this work contributes to the development of novel ASP systems and devices along with the developments of novel DDSs. Two types of DDSs are used in this work: a) Composite Right/Left-Handed (CRLH) transmission lines (TL), and b) all-pass dispersive structures. In particular, the all-pass dispersive delay networks are investigated in greater details based on C-section all-pass networks in various configurations along with novel synthesis procedures and electromagnetic analysis to synthesize arbitrary group delay responses of the DDSs.

The first type of all-pass DDS is a cascade of all-pass C-section with different lengths and coupling characteristics to synthesize a prescribed group delay response, resulting in a non-commensurate DDS. For this structure, a closed-form iterative procedure for synthesizing quasi-arbitrary phase responses is presented. The synthesis consists in mapping the transmission poles of the cascaded C-section structure onto the transmission poles of the specified transfer function, where the latter poles are computed using a closed-form polynomial generation method. The real and complex transmission poles of the specified transfer function are realized using C-sections of different lengths and different couplings coefficients. The proposed synthesis is validated by full-wave analysis in a multilayer prototype. This DDS and its corresponding synthesis method is described in details in Chapter 3.

The second all-pass DDS is an extension of the cascaded C-Section structure by allowing neighbouring C-sections to couple to each other via electric and magnetic couplings. This network is obtained by interconnecting the alternate ports of adjacent lines of a **2N**-port coupled transmission line network with transmission line sections, and it is modeled using multiconductor transmission line theory with per-unit-length capacitance matrix **C** and inductance matrix **L**. By allowing the different C-sections of the network to exhibit different lengths, a generalized group delay engineering procedure is proposed, where quasi-arbitrary group delay responses are achieved by combining the group delay responses of C-sections with different lengths. A computer design approach based on genetic algorithms is applied for synthesis, which consists in determining the structural parameters of the different C-section groups. Using this approach, non-commensurate networks are group delay engineered in edge-coupled stripline technology, and gaussian, linear and quadratic group delay responses are realized. The theoretical results are validated by experiment. This DDS is described in details in Chapter 4.

Finally, these DDSs are exploited in following two regimes for various ASP applications.

Guided-wave Applications

In the first class of guided-wave applications, the following concepts are presented and are demonstrated using experimental prototypes in Chapter 5.

1. Tunable delay lines for real-time phase shifters and true-time delayers.
2. Frequency discriminator for spectrum sensors and real-time Fourier transform-

ers.

3. Pulse position modulation coding for radio-frequency identification (RFID) systems.
4. Dispersion compensation in log-periodic antennas.

Radiated-wave Applications

In the second class of radiated-wave applications, two systems are experimentally demonstrated based on CRLH leaky-wave structures in Chapter 6:

1. Frequency division duplexing transceiver.
2. Real-time spectrum analyzer (RTSA).

Chapter 7 finally provides the conclusions of the thesis and outlines some of the future works in the field of analog signal processing.

Contents

List of Tables

List of Figures

Liste des annexes au besoin.

List of Appendices

List of Abbreviations and Notations

Abbreviations

ASP:	Analog Signal Processing
DDS:	Dispersive Delay Structure
CRLH:	Composite Right/Left-Handed
LH:	Left-Handed
LWA:	Leaky-wave Antenna
MoM:	Method of Moments
PPM:	Pulse Position Modulation
TL:	Transmission Line
RH:	Right-Handed
UWB:	Ultra Wideband
RFID:	Radio-Frequency Identification
RTSA:	Real-Time Spectrum Analyzer
FREG:	Frequency Resolved Electrical Gating
RTFT:	Real-Time Fourier Transformer

Symbols Used

c:	speed of light in vacuum $3 \cdot 10^8$m/s
ε_0:	permittivity of free space
μ_0:	permeability of free space
k_0:	free space wave number
λ:	wavelength
β:	propagation constant
Z_B:	Bloch impedance

Chapter 1

Introduction

1.1 Motivation

Today's ever increasing demand for faster, more reliable and more ubiquitous wireless access poses unprecedented challenges to radio and communication engineers. Monitoring the radio frequency (RF) environment in real time for higher temporal, spectral or temporal efficiency has become highly desirable to meet these new challenges. Real-time (RT) monitoring has been traditionally accomplished using RT analog signal processing (ASP) techniques in some specific application areas. For example, pulse compression is used in radars for detection and ranging [7], while real-time Fourier transformation is used in surveillance systems for the detection of illegal eavesdropping and in military systems for electronic spying [8]. However, ASP has been quite under-exploited in communication to date.

Currently, the manipulation of signals (modulation / coding, demodulation / decoding) in wireless communication systems is dominated by digital signal processing (DSP). Digital devices are attractive due to their advantages of flexibility, compact size and reliability, but they also suffer of fundamental drawbacks, such as poor performance at high frequencies, high (sometimes prohibitive) cost of AD/DA converters, low speed and high power consumption. In contrast, ASP devices are inherently frequency scalable up to millimeter-wave frequencies (e.g. 60 GHz band), they are faster since they operate in real time and do not require any data buffering, they tend to be less expensive due to higher simplicity, and they consume less power because they include no logic circuits. Therefore, they have a potential to provide alternative solutions to the wireless industry in near future, leading to a new paradigm in signal processing - *microwave analog signal processing*.

1.1.1 Microwave Analog Signal Processing Paradigm

Microwave ASP devices involves detecting, manipulating, modulating, coding, characterizing and processing RF signals through analog means without requiring signal samplers and digital processors. The signals thus have to be manipulated completely in the time-domain by means of wave propagation through microwave structures which are engineered in terms of their dispersion characteristics thereby controlling the wave propagation through them. This represents a new paradigm shift, with novel technique and systems in signal processing, for processing RF signals without using conventional digital processing techniques.

In a dispersive structure, which is a core of an ASP system, the group velocity v_g is a function of frequency, which results in a frequency-dependent group delay. These structure will now be referred to as dispersive delay structures (DDSs). Consequently, a wide-band signal traveling along such a structure experiences time spreading, since its different spectral components travel with different group velocities and are therefore temporally rearranged. By exploiting this temporal rearrangement, the various spectral components of a wideband signal can be directly mapped onto time domain and can then be processed in *real-time* for various applications. The dispersive structure therefore acts as a phase-filter and since it simply rearranges different spectral energies in time domain, its an *energy-efficient* process. This entire process is fundamentally *analog* in nature, and is inherently capable of handling ultrashort or *broadband* signals with *fast processing speeds*. Depending on the kind of ASP applications, the dispersive networks need to be dispersion engineered (group delay engineered) to achieve the desired group delay versus frequency response.

1.1.2 Dispersive Delay Structures

Different ASP technologies, essentially characterized by the nature of the DDS they employ, have been used, including surface acoustic wave (SAW) [9], magnetostatic wave (MSW) [10], multi-section coupler [11], chirped transmission line [12], and composite right/left-handed (CRLH) metamaterial [4] technologies. SAW devices, due to their slow-wave characteristic, provide large delays ($\approx$ 1s); hence, a large time-bandwidth (here time means group delay difference, or swing, between the smallest and largest frequencies of the bandwidth) product, while also having a compact size. However, they are restricted to narrowband ($\approx$2 GHz) and low-frequency

($<$ 2 GHz) applications due to limitations in the current photolythographical processes. MSW devices can be employed for high-frequency and wideband operation, while also achieving a high time-bandwidth product. However, in addition to being lossy, they require a permanent magnet, which is bulky and renders planar fabrication difficult. Conversely to the transmission-type SAW and MSW structures, reflection-type structures, such as multi-section coupler based structures and chirped microstrip lines, are also possible. The multisection coupler structures are composed of several series connected coupled-line couplers operating at contiguous frequencies. Thus, high-frequency ($\approx$10 GHz) and wideband ($>$ 3 GHz) operation can be achieved. However, the bandwidth is dependent on the size of the structure, i.e., more couplers are required for larger bandwidth, which also leads to a long and extremely lossy structure. In order to decrease loss, high-temperature superconductors (HTSs), along with cryogenics, must be utilized, resulting in a complex fabrication procedure. On the other hand, chirped transmission line structures are a simple and planar structures, which utilize Bragg reflections based on impedance mismatch. However, similar to the coupled-line structures, their bandwidth is dependent on size, and they are highly lossy due to their operation in the stopband. Moreover, they require a circulator to separate the incident and reflected signals.

Considering these constraints and state-of-the-art DDS technologies, new development in the microwave DDSs are proposed in this thesis which solves some of the issues highlighted above.

1.2 Thesis Contributions

In the proposed domain of microwave ASP, this thesis concerns with two major directions: First, is in development of new DDSs with enhanced dispersion capabilities and second, is the conceptualization and demonstration of new ASP applications.

1.2.1 DDS and Group Delay Synthesis Techniques

Designing a microwave DDS structure for efficient and versatile ASP essentially consists in designing the phase of an all-pass type filter structure. Despite the huge body of literature available on conventional filters, e.g. [13], which are mostly (except for equalizers) designed in terms of amplitude phase responses, relatively little

phase engineering synthesis methods and technological implementations have been reported for phase specified all-pass structures, especially when it comes to linear but non-constant group delay responses, as required for ASP. This thesis has deployed systematic efforts to fill up this gap. In particular, the following contributions are made in this thesis towards this direction.

1. Conceptualization and demonstration of non-commensurate C-section all-pass microwave DDSs with engineered group delay responses in a wide frequency band [14][6].
2. A systematic effort to synthesize quasi-arbitrary dispersion responses in these structures using closed form iterative techniques or efficient optimization procedures along with rigorous electromagnetic analysis [14][6].
3. Novel techniques to enhance the dispersion of the DDSs using both material dispersion and engineered metamaterial structures [15][16].

1.2.2 ASP Applications

As mentioned before, the RT monitoring has been traditionally accomplished only in some specific application areas such as pulse compression and Fourier transformations. These applications have been substantially expanded as a part of this ASP research effort and some of these applications are presented in details in this thesis.

1. Tunable delay lines and phase shifters [17][5].
2. True-time delayers [18].
3. Radio-frequency identification (RFID) systems [19].
4. Pulse-position modulators [20].
5. Talbot repetition rate multipliers [21].
6. Talbot temporal-spatial pulse power combiners [22][23].
7. Real-time Fourier transformers [24].
8. Real-time inverse Fourier transformers [25].
9. Dispersion compensators in log-periodic antennas [26].
10. Frequency division diplexing transceivers [27].
11. Real-time spectrum analyzers [28][29].

12. Frequency resolved electrical gating analyzers [30].

In particular, the following original applications among the above list, are contributed in this thesis:

1. **Tunable delay lines and phase shifters:** This system, which incorporates a DDS, two mixers, and a low-pass filter, achieves a tunable group delay for impulse and continuous-wave signals, controlled by a local oscillator. This group delay tunability follows from the dispersion property of the CRLH transmission line and is achieved without suffering from the drawbacks of conventional delay lines in terms of matching, frequency of operation, and planar circuit implementation.
2. **Radio-frequency identification (RFID) systems:** The concept of pulse-position modulation coding based on group delay engineered microwave C-section dispersive delay structures (DDSs) is experimentally demonstrated as a novel chipless RFID system. The tags consist of various DDSs whose group delay responses can be engineered to provide different PPM codes. A 3-bit system is presented with an RFID reader and various different DDS based tags. The proposed concept offers system simplicity, frequency scalability and M-ary coding capability for large ID coding diversity.
3. **Dispersion compensators in log-periodic antennas:** A general technique to compensate for pulse distortion induced in log-periodic antennas, due to their frequency dispersive response, is presented and demonstrated by full-wave simulations for the case of log-periodic dipole array (LPDA). A C-section based all-pass dispersive delay structure (DDS) exhibiting a dispersion profile opposite to that of an LPDA is used as a pre-distorter before the antenna. A faithful reconstruction of the pulse is demonstrated using time-domain simulations.
4. **Frequency division diplexing transceivers:** A frequency division full-diplexing transceiver system is proposed based on the beam-scanning property of the composite right/left-handed (CRLH) leaky-wave antenna (LWA). A full-diplexing operation of simultaneous transmission and receiving is experimentally demonstrated. Compared to the conventional systems, the proposed system operates with a single passive CRLH antenna resulting in lesser hardware requirements and provides high signal isolation due to the directive nature of the leaky-wave antenna and the band-pass filter employed in the system.

5. **Real-time spectrum analyzers:** A novel analog real-time spectrum analyzer (RTSA) for the analysis of complex non-stationary signals (such as radar, security and instrumentation, and EMI/EMC signals) is presented, demonstrated, and characterized. This RTSA exploits the space-frequency mapping (spectral-spatial decomposition) property of the composite right/left handed (CRLH) leaky-wave antenna (LWA) to generate the real-time spectrograms of arbitrary testing signals. Compared to digital RTSAs, it exhibits the advantages of instantaneous acquisition, low computational cost, frequency scalability, and broadband or ultra wideband (UWB) operation. The systems is tested for a large diversity of non-stationary signals and generates in all cases spectrograms in excellent agreement with theoretical predictions. The fundamental tradeoff between time and frequency resolutions inherent to all RTSA systems is also discussed.
6. **Frequency resolved electrical gating analyzers:** An analog frequency resolved electrical gating (FREG) system based on a composite right/left-handed (CRLH) leaky-wave antennas for UWB signal characterization is proposed. This system is based on spatial-spectral decomposition property of the leaky-wave antenna and on the self-gating principle to suppress the time-frequency resolution dependence on the antenna physical length in the spectrograms. The system is demonstrated numerically using an efficient time-domain Green's function technique and spectrograms are shown for various time domain test signals.

Chapter 2

Dispersion Engineering for Analog Signal Processing

This chapter introduces the crux of this thesis by explaining Analog Signal Processing concept in context of dispersion and conventional digital signal processing techniques. Starting from fundamental dispersion concept, a dispersion parameter based classification of analog signal processing is presented with an emphasis on dispersion and group delay engineering.

2.1 Dispersion Concept

Lets consider a two port linear time invariant structure whose transfer function $H(\omega)$ is given by

$$H(\omega) = |H(\omega)| \exp[-j\gamma(\omega)z] = |H(\omega)| \exp[-\alpha(\omega)z] \exp[-j\beta(\omega)z] \tag{2.1}$$

where z is the signal propagation length from the input of the system to its output, $\gamma(\omega) = \beta(\omega) - j\alpha(\omega)$, $\beta(\omega)$ and $\alpha(\omega)$ being the propagation and attenuation constants respectively, assuming a homogenous medium. Let us further consider a lossless case ($\alpha = 0$) and the device with unity transmittance ($|H(\omega) = 1|$). In such a case, Eq. 2.1 becomes $H(\omega) = \exp[-j\beta(\omega)z]$. Now, considering an arbitrary input signal $v(z = 0, t)$, the signal out of the device is given by $\tilde{v}(z, \omega) = \tilde{v}(0, \omega) \exp[-j\beta(\omega)z]$, where $\tilde{v}(z, \omega)$ is the Fourier transform of the time signal $v(z, t)$. This can be written in a differential equation form which reads

$$\frac{d\tilde{v}(z, \omega)}{dz} = -j\beta(\omega)\tilde{v}(z, \omega), \tag{2.2}$$

Now, the dispersion relation $\beta(\omega)$ of a medium can be expanded in Taylor series about a center (or carrier) frequency ω_c as follows:

$$\beta(\omega) = \beta_0 + \beta_1(\omega - \omega_c) + \frac{1}{2}\beta_2(\omega - \omega_c)^2 + ...\text{where} \quad \beta_n(\omega) = \left.\frac{d^n\beta(\omega)}{d\omega^n}\right|_{\omega=\omega_c}$$

The Taylor series coefficients β_0, β_1 and β_2 represent the phase velocity (PV) parameter, the group velocity (GV) parameter, and the group velocity dispersion (GVD) parameter, respectively. β_1^{-1} is the propagation velocity, while β_2 is a measure of the dispersion strength. Using, Eq. 2.3 in Eq. 2.2 retaining the third term (second-order dispersive terms β_2), the signal propagation can be simplified for the signal envelope $[A(t)]$ propagation in a retarded frame $T = t - \beta_1 z$, resulting in (derived in the Appendix for a case of CRLH transmission line metamaterials),

$$j\frac{dA}{dz} - \frac{|\beta_2|}{2}\frac{d^2A}{dT^2} = 0. \tag{2.3}$$

This equation is a special case which models the propagation of an envelope of the pulse along a dispersive structure exhibiting second order dispersion (or a linear non-constant group delay versus frequency which is a foundation for several important signal processing applications to be later introduced in the thesis), for any arbitrary input.

Consequently, in any dispersive medium, the group velocity v_g is a function of frequency, which results in a frequency-dependent group delay. A wide-band signal subsequently suffers from distortion in such a medium because its different spectral components travel with different group velocities. This is generally perceived as an undesirable effect and is avoided. However, if dispersion (phase) is designed in a well-controlled manner, useful components can be designed. The dispersion results in three major effects on a broadband signal: 1) pulse broadening, 2) peak amplitude reduction and 2) frequency chirp across the temporal profile of the signal, as shown in Fig. 2.1, and this fact will be used in the next section for establishing the analog signal processing concept.

2.2 Analog Signal Processing

In a dispersive structure, the group velocity v_g is a function of frequency, which results in a frequency-dependent group delay. Consequently, a wide-band signal trav-

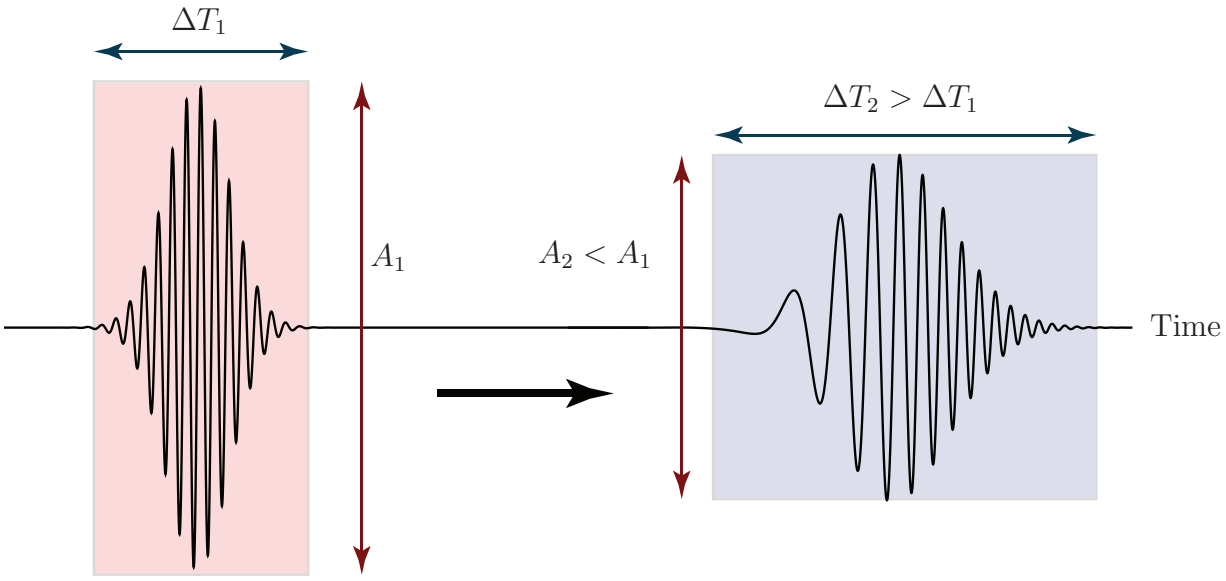

Figure 2.1 Typical pulse propagation scenario in a dispersive structure resulting in pulse broadening, amplitude decrease and a frequency chirp.

eling along such a structure experiences time spreading, since its different spectral components travel with different group velocities and are therefore temporally rearranged. By exploiting this temporal rearrangement, the various spectral components of a wideband signal can be directly mapped onto time domain and can then be processed in *real-time* for various applications. The dispersive structure therefore acts as a phase-filter and since it simply rearranges different spectral energies in time domain, its an *energy-efficient* process. This entire process is fundamentally *analog* in nature, and is inherently capable of handling ultrashort or *broadband* signals with *fast processing speeds*. Thus the core of an analog real-time signal processor is a dispersive structure.

On the other hand, conventional digital signal processing relying on digital computations works with the digitized version of the signal concerned, and usually exhibits additional buffer times requiring extra hardware resources such as data memories and speedy computational processors. Digital devices are most attractive at low frequencies due to their high flexibility, compact size, low cost, and strong reliability. This is due to that fact that the field of digital signal processing has been matured and advanced enough specially at lower end of the spectrum, thanks to decades of research

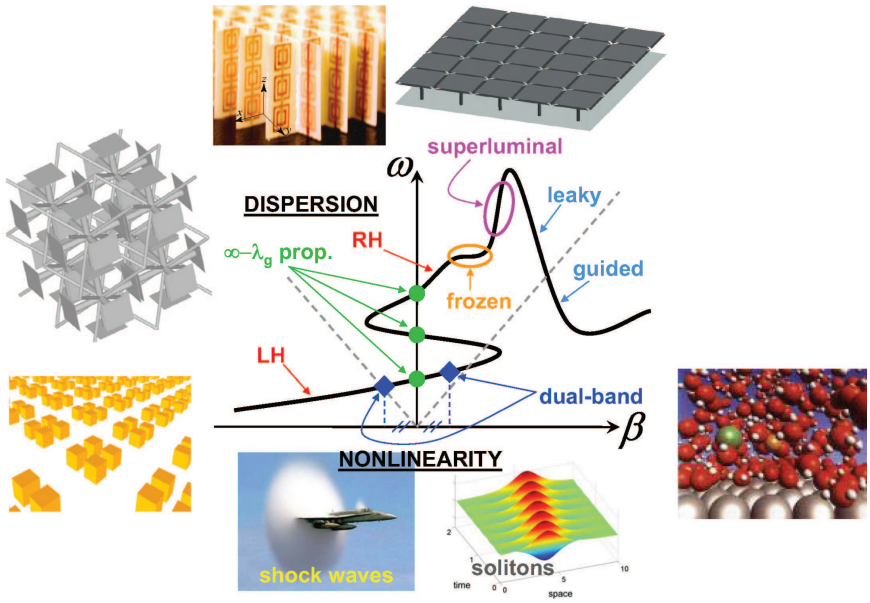

Figure 2.2 Illustration of the dispersion engineering concept.

and well-developed technologies as opposed to analog signal processing. However, at higher frequencies, such as millimeter-wave frequencies, digital devices suffer of fundamental issues, such as poor performance, high cost for A/D and D/A converters, and excessive power consumption. At such frequencies, analog devices and systems are required for real-time signal processing applications. This thesis emphasizes a renewed interest in corresponding analog signal processing concepts due to some of its fundamental benefits as mentioned above, which may prove extremely useful specially at higher frequencies where digital techniques are difficult to implement or are simply not possible so far.

To illustrate the strength of analog signal processing concept, lets consider a classical Fourier transform operation over a nanosecond time signal. Digital processing will consist of Fast Fourier Transform (FFT) operation requiring 1) a fast enough data sampler for signal digitization that can handle large bandwidth signals (few GHz bandwidth), 2) Memory buffer to store digitized signals and 3) a fast enough processor to digitally compute the FFT. These requirements become more and more stringent as the original signal is lies in high frequency range spectrum which directly impacts the cost and performance of the system, assuming such components are available, which may not be the case at millimeter wave and Terahertz frequencies. On the

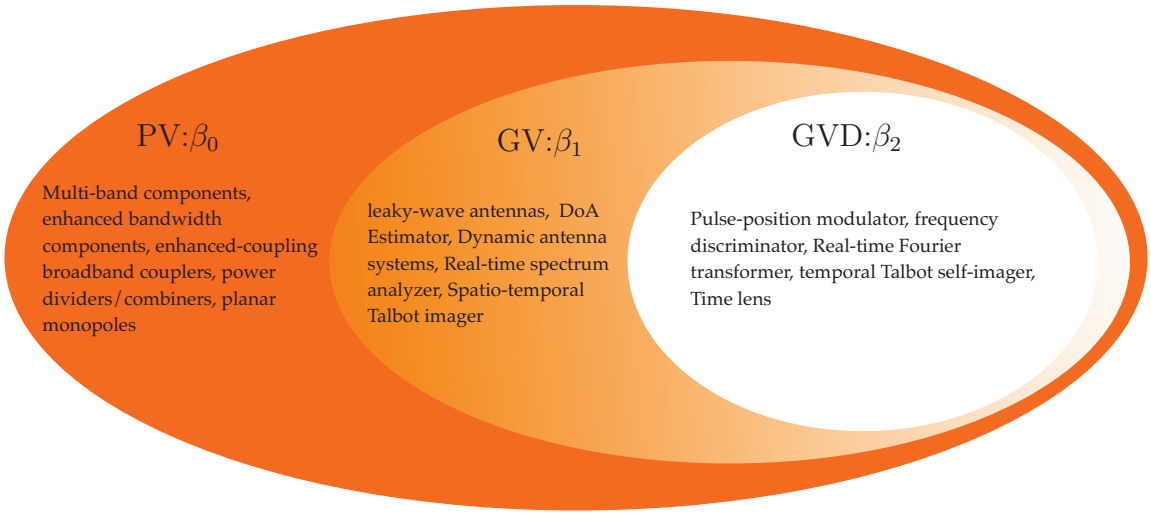

Figure 2.3 Analog signal processing application classifications based on dispersion parameters.

other hand, analog signal processing will require fundamentally a dispersive structure through which the testing nanosecond signal will simply pass resulting in a frequency chirping (separation of frequencies in time). In simple terms, if the dispersion is strong enough, after a certain propagation time, the various spectral components of the signal (along with their respective strengths) will completely isolate from other terms resulting in a one-to-one mapping between time and frequency. In strict terms, it can be shown that under certain conditions, the propagating signal inside the dispersive evolves into a signal shape proportional to the mathematical Fourier transform of the signal [31]. A dispersive structure thus acts as a Fourier transformer without needing any computational and memory resources as opposed to the conventional digital technique. Therefore, analog signal processing requires basically a dispersive structure, capable of doing complex signal processing operations, which is expected to lead to a cheap and simplified system as compared to what is conventionally need in a digital processing scheme.

2.3 Dispersion Engineering

A dispersive structure is basically characterized by its phase response. The phase versus frequency characteristics defines $\beta(\omega)$ for a uniform structure which in turns determines the phase velocity parameter β_0, group velocity parameter β_1 and group velocity dispersion parameter β_2, for example. The amplitude response of such a structure is desired to be unity in the operating frequency band.

Various analog signal processing applications require different dispersions, and thus different phase responses. Where systems such as Fourier transformers requires a non-zero β_2 with $\beta_n = 0$ for $n > 2$ (linear group delay response), applications such a dispersion compensators and frequency transceivers may requires higher order dispersion terms and thus complex dispersion response. Therefore, an attempt will be made in this work to systematize a generalized synthesis procedure for engineering arbitrary (but causal) phase and group delay responses. This is termed as *Dispersion Engineering*. Fig. 2.2 illustrates the concept of dispersion engineering, where phase manipulation provides various interesting effects and functionalities - for both guided-wave and radiative-wave applications.

A closely related term to dispersion engineering is *Group Delay Engineering*. Where dispersion $\beta(\omega)$ is possible to define in uniform periodic structures where effective medium theory is valid (unit cell size $p << \lambda_g$), it is not be possible to define it for every 2-port network, where the concept of a guided wavelength doesn't hold anymore. In such cases, Eq. 2.3 is replaced by the corresponding taylor expansion of the phase response, which reads,

$$\Phi(\omega) = \Phi_0 + \Phi_1(\omega - \omega_c) + \frac{1}{2}\Phi_2(\omega - \omega_c)^2 + ...\text{where} \quad \Phi_n(\omega) = \left.\frac{d^n\Phi(\omega)}{d\omega^n}\right|_{\omega=\omega_c}$$

where Φ_0, Φ_1 and Φ_2 are now the phase delay parameter, group delay parameter and group delay dispersion parameter, respectively. In particular, Φ_2 is the slope of the corresponding group delay verse frequency response evaluated at the carrier frequency ω_c.

Fig. 2.3 shows a list of various analog signal processing applications classified into three dispersion parameter categories and the following chapters will discuss some of these applications in detail.

Chapter 3

All-Pass Dispersive Delay Structures - Uncoupled C-Sections

This chapter is the first of three chapters which present the guided-wave components and systems developed in the thesis. In all of the guiding applications discussed in the present and the next chapters, the applied electromagnetic energy is confined inside the components and systems and generally does not leak out to the surrounding space. This chapter in particular focusses on two dispersive delay structures – metamaterial transmission line structures and coupled-line all-pass networks – which will be used for guided-wave analog signal processing applications described in the next chapter.

3.1 Microwave Dispersive Delay Structures (DDSs)

The core of an analog real-time signal processor is a dispersive delay structure (DDS). In a dispersive structure, the group velocity v_g is a function of frequency, which results in a frequency-dependent group delay. Consequently, a wide-band signal traveling along such a structure experiences time spreading, since its different spectral components travel with different group velocities and are therefore temporally rearranged [32]. By exploiting this temporal rearrangement, the various spectral components of a wideband signal can be directly mapped onto time domain and can then be processed in real-time for various applications.

At microwaves, dispersion can be achieved using different technologies. Surface acoustic wave devices [11], thanks to their slow-wave characteristic, provide large delays ($\approx 1\mu s$), and hence a large time-bandwidth product, while exhibiting a compact size. However, they are restricted to narrow-band (2 GHz) and low-frequency applications ($<$ 2 GHz) due to limitations of photolithography. Magnetostatic-wave devices [10] offer high-frequency and wide-band operation along with large time-bandwidth

product. However, in addition to being lossy, they require a bulky and non-planar permanent magnet. Reflection-type structures, such as multi-section coupler based structures and microstrip lines, have also been reported [33]. These structures are composed of series-connected coupled-line couplers operating at contiguous frequencies, and may achieve high frequency ($\approx$ 10 GHz) and wide-band ($\approx$ 3 GHz) operation. However, their bandwidth is proportional to the size of the structure, which leads to long and extremely lossy structures for high bandwidth. In order to decrease loss, high-temperature superconductors (HTS), requiring cryogenics, must be utilized, which results in complex and expensive devices [34]. On the other hand, the chirped microstrip line [35, 36] is a simple and planar structure, which utilizes Bragg reflections based on impedance mismatch. However, due to multiple internal reflections as a result of Bragg phenomenon at the impedance steps, the group delay and the magnitude response always fundamentally exhibit undesired ripples resulting in uneven responses. At the same time, the Bragg structure require a broadband circulator in turn requiring a magnet which can be challenging to realize specially at higher frequencies. None of these technologies provide ideal solutions for analog signal processing and more research is required in this direction. This chapter describes two technologies which provide attractive solutions with distinct benefits compared to the existing ones.

3.2 Transmission-Line Metamaterials

Electromagnetic (EM) metamaterials (MTMs) are a class of effectively homogenous structures exhibiting unusual properties not readily available in natural materials. EM MTMs are therefore artificial, engineered structures, generally composed of periodically arranged sub-wavelength inductive and capacitive elements in 1D, 2D, or 3D configuration. The size of a unit cell (UC) containing these elements is much smaller than the operating wavelength (λ_g), i.e. $p \ll \lambda_g$, and therefore EM MTMs operate in the long-wavelength regime.

The first microwave MTM was demonstrated by Smith *et al.* in 2000 [37] using thin-wires and split-ring resonators to synthesize a medium with simultaneously effective negative permittivity ε and negative permeability μ. Because of the inherent resonant nature of the proposed structure, this first MTM had a narrow bandwidth. In addition, the structure was volumetric, bulky and lossy. Therefore, it is not suitable

for microwave applications where most of the components and systems have planar implementations.

In 2002, the first planar transmission line (TL) MTMs operating at microwave frequencies were introduced by Caloz and Itoh [38], Iyer and Eleftheriades [39], and Oliner [40]. In contrast to the previous generation MTMs, planar TL MTMs, which are constituted of printed or discrete inductors and capacitors, are *not* resonant. As a result, planar TL MTMs exhibit broad bandwidth, low loss and the capability to be easily integrated with other microwave components and systems. The most general and practical TL MTMs are the composite right/left-handed (CRLH) TL MTMs. The next section summarizes useful formulas and key properties of CRLH TL MTMs used in this work.

3.2.1 Composite Right/Left-handed Transmission Line Structures

The CRLH artificial TL is composed of right-handed elements (L_R, C_R) and left-handed elements (L_L, C_L) and is characterized by the following dispersion relation [4]

$$\begin{aligned} &\beta(\omega) = \frac{1}{p}\cos^{-1}\left(1-\frac{\chi}{2}\right), \\ &\text{with} \quad \chi = \left(\frac{\omega}{\omega_R}\right)^2 + \left(\frac{\omega_L}{\omega}\right)^2 - \kappa\omega_L^2, \end{aligned} \tag{3.1}$$

where $\kappa = L_L C_R + L_R C_L$, $\omega_R = 1/\sqrt{L_R C_R}$, $\omega_L = 1/\sqrt{L_L C_L}$, and p is the unit cell size or period, and by the Bloch impedance

$$Z_B = Z_L \sqrt{\frac{(\omega/\omega_{se})^2 - 1}{(\omega/\omega_{sh})^2 - 1} - \frac{\omega_L}{2\omega}\left[\left(\frac{\omega}{\omega_{se}}\right)^2 - 1\right]^2}. \tag{3.2}$$

where $\omega_{se} = 1/\sqrt{L_R C_L}$ and $\omega_{sh} = 1/\sqrt{L_L C_R}$. The corresponding dispersion relation, Bloch impedance and group delay ($\tau_g = -\partial\phi/\partial\omega$, where ϕ is the phase shift across the structure) curves are shown in Figs. 3.1(a), (b), and (c), respectively. As seen in Eq. (3.1), the CRLH TL offers an unprecedented level of dispersion (phase) control via the CRLH parameters L_R, C_R, L_L and C_L. The manipulation of the CRLH dispersion relation has already led to wealth of novel narrow-band devices, such as

multi-band system (dual-, tri-, and quad-band), bandwidth enhancers, to name a few.

The most important property of a dispersive structure is its frequency-dependent group delay. In the case of a balanced CRLH transmission line ($L_R C_L = L_L C_R$), the group velocity of a modulated signal propagating along the structure is obtained by taking the inverse derivative of the propagation constant with respect to frequency, as given in Eq. (3.1), evaluated at the carrier frequency. The corresponding group delay for the modulated signal is

$$\tau_g(\omega_c) = \frac{N}{\sin(\beta p)} \left(\frac{\omega_c}{\omega_R^2} + \frac{\omega_L^2}{\omega_c^3} \right) \tag{3.3}$$

where N represents the number of unit cells of the line. Thanks to its dispersive properties and subsequent design flexibility, the CRLH transmission line provides low-loss, compact and planar dispersion-engineered solutions, avoiding frequency limitations, complex fabrication, cryogenics, circulators or amplifiers. Moreoever, the CRLH TL's operational frequency and bandwidth dependent only on a single unit cell's right/left-handed capacitor and inductor values [4]. Thus, a compact CRLH TL can be designed to operate at high frequencies while also exhibiting wide bandwidth, as shown by the relatively constant Bloch impedance in Fig.3.1(b).

3.2.2 Limitations

As mentioned in the previous section, the CRLH transmission lines provides an attractive solution due to its low-loss, compact and planar properties, which have already lead to several analog signal processing applications. These applications include tunable delay lines [5], compressive receiver and frequency discriminator [41], true-time delayers [18], Pulse position modulators [20] and real-time spectrum analyzer [29] to name a few. Some of these applications will be described in next two chapters. On the other hand, CRLH transmission line dispersive structures have a major drawback: these structures exhibit a *fixed group delay profile* i.e. hyperbolic delay response. For several applications such as Real-Time Fourier Transformers [35] and temporal Talbot phenomenon [42], a linear group delay response is required, which is not conveniently achieved using a CRLH structure. This is due to the fact that the CRLH structure is fundamentally a ladder-type network, whose amplitude and group delay response is related by a Hilbert transform [43] so that any effort to modify the group delay response may make the magnitude response worse. An

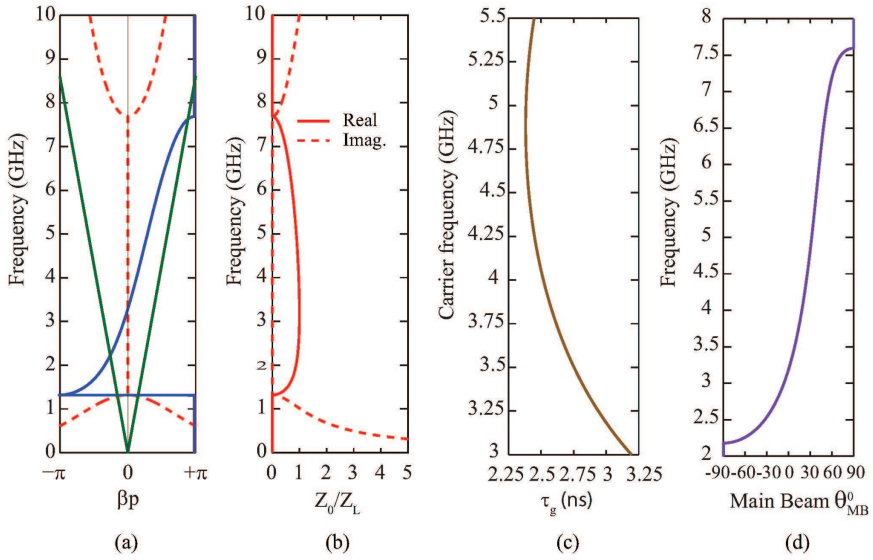

Figure 3.1 CRLH transmission line characteristics. a) Typical dispersion curve $\beta(\omega)$. b) Bloch impedance Z_B normalized to $Z_L = 50$ ohms. c) Group delay. d) Beam-scanning law.

alternative structure for analog signal processing is described next in order to tackle this issue.

3.3 Microwave All-pass Networks

An ideal dispersive structure should provide a flat magnitude response with a smooth and a continuous group delay profile within the operation frequency range. Achieving such characteristics requires an independent control over the magnitude and group delay of the structure, which is only possible with non-minimum phase filters exhibiting an all-pass response [43]. These structures typically operate in transmission mode, where smooth group delay responses can be achieved and arbitrary operational frequencies with arbitrary operational bandwidth are attainable, including in planar MMIC compatible technologies. They possess many degrees of freedom for group delay engineering. For example, an exact synthesis of cascaded *commensurate* transmission line (same length for all the lines) C-section all-pass network was reported in [44] to realize prescribed phase characteristics. However, the synthesis presented in [44] is limited to a maximum of three C-sections and is demonstrated

only for narrowband phase shifting applications. Many related works on the design of phase shifters based on coupled transmission lines have been later reported such as for instance [45][46][47]. Similarly, an all-pass filter design method for equalizing acoustic signals is presented in [48] and another one using lumped lattice circuit model in [49].

3.4 Group Delay Engineering using Microwave C-Sections

Whereas well-known synthesis procedures exist for magnitude filters, whether direct-coupled [13, 50] or cross-coupled [51][52], no general closed-form synthesis procedure has ever been reported to realize arbitrary phase responses, to the best of our knowledge. The only existing techniques towards this purpose are in the form of closed-form iterative procedures, and are restricted to low-frequency phase filters, realized as lumped-element all-pass filters based on lattice networks [53]. On the other hand, high-frequency phase filters, realized in the form of distributed all-pass networks, are usually synthesized via optimization procedures [54, 55, 6], with the exception of a few works where closed-form iterative procedures have been developed for specific mathematical forms of the phase functions [56, 57]. Recently, a closed form phase synthesis procedure has been proposed for the *reflection-type* one-port all-pass filter to synthesize arbitrary group delay response [58]. However as opposed to transmission-type networks, reflection-type filters require external components such as a circulator or a quadrature hybrid, due to their reflective-type nature.

In this part of the chapter, we propose a closed-form iterative procedure for synthesizing arbitrary physically realizable phase responses using *transmission-type* non-commensurate microwave C-section all-pass networks [14]. Such structures were first proposed in [54]. The non-commensurate configuration reported in [6] are similar to them except that they include cross-couplings between the adjacent C-sections, with the benefit of richer dispersive responses but at the cost of increased design complexity.

3.4.1 Group Delay Synthesis

3.4.1.1 C-Section All-Pass Structure

A microwave C-section is an end-connected coupled transmission-line structure with an all-pass frequency response as shown in Fig. 3.2(a) [13, 57]. Its transfer function may be obtained by prescribing $b_4 = a_3$ and $b_3 = a_4$ in the 4×4 scattering matrix of a coupled-line pair (as derived in the Appendix B), and reads and may be written as [57]

$$S_{21}(\theta) = \left[\frac{j\rho\cot\theta + 1}{j\rho\cot\theta - 1}\right], \tag{3.4}$$

with

$$\theta = \frac{\omega}{c}\sqrt{\varepsilon_{\text{eff}}\mu_{\text{eff}}}\ell, \tag{3.5a}$$

$$\rho = \left(\sqrt{\frac{1+k}{1-k}}\right). \tag{3.5b}$$

where ω is the angular frequency, c is the speed of light in vacuum, ε_{eff} is the effective permittivity, μ_{eff} is the effective permeability, ℓ is the physical length of the structure, and k is the voltage coupling coefficient.

The C-section's transmission magnitude is unity ($|S_{21}(\theta)| = 1$), and its group delay response is obtained from (3.4) as

$$\tau(\omega) = -\frac{d}{d\omega}\arg\{S_{21}(\omega)\} = \frac{2\rho}{1 + (\rho^2 - 1)\cos^2\theta}\frac{d\theta}{d\omega}. \tag{3.6}$$

Due to the distributed nature of the C-section's structure, $\tau(\omega)$ is periodic versus frequency. In fact, the $(\tau - \omega)$ area is constant and unity, as demonstrated in the Appendix C. Since, according to (3.5a), $d\theta/d\omega = \sqrt{\epsilon_{\text{eff}}\mu_{\text{eff}}}\ell/c$ is a constant, the maxima of $\tau(\omega)$ simply correspond to the zeros of the cosine function in (3.6), i.e.

$$\theta_p = (2p+1)\frac{\pi}{2}, \tag{3.7}$$

where p is an integer. In terms of the length, these maxima correspond to odd multiples of the quarter wavelength, i.e. $\ell_p = (2p+1)\lambda/4$.

For later convenience, we wish now to eliminate the parameter θ, and hence the physical parameters ϵ_{eff}, μ_{eff} and ℓ, from the function τ in (3.6). For this purpose, we

first find the relation between ℓ and the maxima frequencies ω, by equating (3.5a) and (3.7), which yields $\ell = (2p+1)\pi\ c/(2\omega_p\sqrt{\varepsilon_{\text{eff}}\mu_{\text{eff}}})$. Upon substitution of this expression into (3.5a), one finds for the first maximum, corresponding to $p = 0$,

$$\theta = \frac{\pi\omega}{2\omega_0}, \tag{3.8}$$

from which (3.6) can be rewritten as

$$\tau(\omega) = \frac{2\rho}{1 + (\rho^2 - 1)\cos^2[(\pi\omega)/(2\omega_0)]}\frac{\pi}{2\omega_0}, \tag{3.9}$$

where ω_0 is the frequency of the first maximum. This function is plotted in Fig. 3.2(b) for two different lengths. The periodicity is apparent in the curves, where each group delay peak corresponds to a specific order p for each length.

The group delay swing, $\Delta\tau(\omega)$, of a C-section may be conveniently obtained from (3.6) with (3.5a) a

$$\Delta\tau(\omega) = (\tau_{\max} - \tau_{\min}) = 2\left(\rho - \frac{1}{\rho}\right)\sqrt{\varepsilon_{\text{eff}}\mu_{\text{eff}}}\ell. \tag{3.10}$$

Thus, the group delay swing can be controlled by varying ρ, through k according to (3.5b), and ℓ. Alternatively, for a given $\Delta\tau$, the requirement on k can be relaxed by increasing ℓ. However increasing ℓ shifts ω_0 downwards and therefore higher order group delay peaks ($p > 0$), instead of the fundamental one ($p = 0$), have to be used in order to keep the frequency of maximum group delay unchanged, as illustrated in Fig. 3.2(b). This fact will be exploited in Sec. 3.4.2.2 to allow the practical realization of dispersive delay structures.

3.4.1.2 Group Delay Synthesis Objective and Approach

A quasi-arbitrary group delay response can be realized by cascading N C-sections with different k's, and hence different ρ's, and with different lengths, $\gamma\ell$'s, where γ is a length scaling factor for each of the C-sections, as illustrated in Fig. 3.2(c). Accounting for the re-scaled lengths, (3.4) may be generalized to

$$S_{21}(\theta) = \left[\frac{j\rho\cot(\gamma\theta) + 1}{j\rho\cot(\gamma\theta) - 1}\right], \tag{3.11}$$

with its group delay

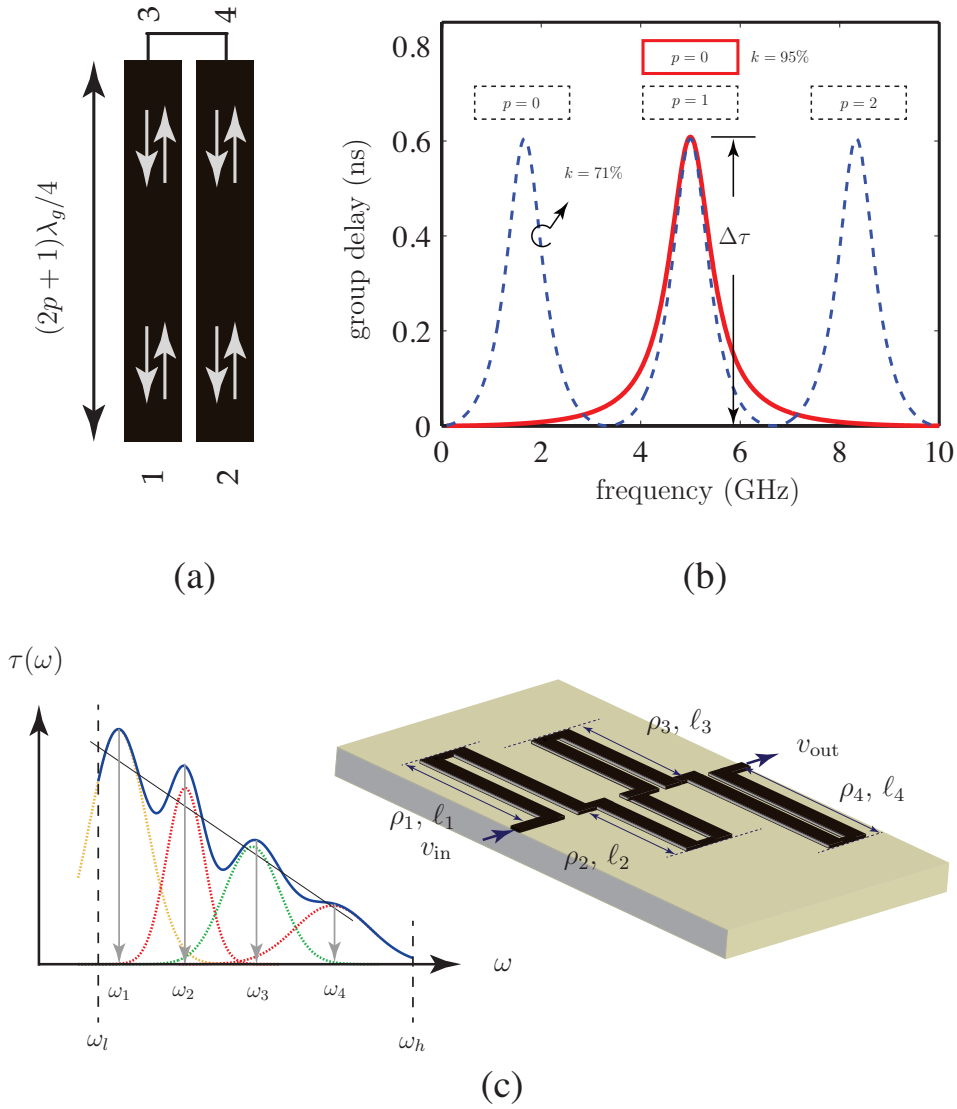

Figure 3.2 C-sections for dispersion synthesis. a) Single C-section layout. (b) Corresponding typical group delay response, computed by (3.9), for two different lengths ℓ, corresponding to the first-maximum frequencies $f_0 = 5$ GHz (solid curve) and $f_0 = 5/3$ GHz (dashed curve), and two different coupling coefficients, $k = 0.95$ (solid curve) and $k = 0.71$ (dashed curve), yielding the same group delay swing $\Delta\tau = 0.6$ ns, according to (3.10). c) Principle of group delay synthesis by superposition of group delays with maxima at different frequencies realized by a ascaded C-section structure.

$$\tau(\omega) = \frac{2\gamma\rho}{1 + (\rho^2 - 1)\cos^2(\gamma\theta)} \frac{d\theta}{d\omega}. \tag{3.12}$$

Similar to that of (3.7), the locations of the group delay maxima can be derived as

$$\theta_p = (2p + 1)\frac{\pi}{2\gamma}. \tag{3.13}$$

The transfer function of the overall structure is then simply obtained by multiplying the transfer functions of the adjacent C-sections, which yields, assuming no coupling between the C-sections,

$$S_{21}^{\text{struct}}(\theta) = S_{21,N}(\theta) = \prod_{i=1}^{N} \left[\frac{j\rho_i \cot(\gamma_i\theta) + 1}{j\rho_i \cot(\gamma_i\theta) - 1} \right]. \tag{3.14}$$

The synthesis objective is to determine the ρ_i's and γ_i's of the different C-sections to realize a specified transfer function

$$S_{21}^{\text{spec}}(\theta) = \exp(j\phi^{\text{spec}}) \tag{3.15}$$

within a bandwidth $[\theta(\omega_l), \theta(\omega_h)]$. This may be achieved by mapping the transmission poles of $S_{21}^{\text{struct}}(\theta)$ in (3.14) onto the transmission poles of $S_{21}^{\text{spec}}(\theta)$ in (3.15) [1]. Therefore, a mathematical representation of (3.15) is required. Since this is a real function, it can be expressed as the ratio of two polynomials, whose poles can be easily identified [59]. The required polynomials will be generated by an iterative numerical procedure operating in the complex Laplace plane or s-plane. Since the poles of (3.15) are expressed in the s-plane, the poles of the (3.14) will also have to be expressed in the s-plane. This is the objective of the next subsection.

3.4.1.3 Transmission Poles of a C-section

In order to obtain the poles of the C-section in the s-plane, we first substitute the mathematical identity [59]

$$j\cot(\gamma\theta) = \frac{(j\cot\theta + 1)^\gamma + (j\cot\theta - 1)^\gamma}{(j\cot\theta + 1)^\gamma - (j\cot\theta - 1)^\gamma} \tag{3.16}$$

1. In this work, the *transmission poles* refer to the zeros of the denominator of the S_{21} transfer function (3.4). They do *not* correspond to singularities of S_{21}, since in an all-pass transfer function the zeros of the numerator cancel out the zeros of the denominator.

with the variable change

$$j\cot\theta = -s, \tag{3.17}$$

into (3.11), which yields

$$S_{21}(s) = \frac{(\rho+1)(s-1)^\gamma + (\rho-1)(s+1)^\gamma}{(\rho-1)(s-1)^\gamma + (\rho+1)(s+1)^\gamma}. \tag{3.18}$$

The mapping $\theta \leftrightarrow s$ of (3.17) is represented in left part of Fig. 3.3, where $\theta = \pi/2$ is mapped onto the origin of the $s-$plane, and $\theta = 0$ and π are mapped onto $-\infty$ and $+\infty$ on the imaginary axis, respectively. Next, using the bilinear transformation [59] and then (3.17),

$$z = \frac{s+1}{s-1} = \frac{-j\cot\theta + 1}{-j\cot\theta - 1} = e^{2j\theta}, \tag{3.19}$$

the transfer function (3.18) may be expressed in the $z-$plane as

$$S_{21}(z) = \frac{(\rho+1) + (\rho-1)z^\gamma}{(\rho-1) + (\rho+1)z^\gamma}, \tag{3.20}$$

which is most convenient to visualize the poles, as will be seen shortly. The mapping from the $s \leftrightarrow z$ of (3.19) is represented in right part of Fig. 3.3, where $s = 0$ ($\theta = \pi/2$) is mapped onto $z = -1$, and $s = -j\infty$ ($\theta = 0$) and $s = +j\infty$ ($\theta = \pi$) are mapped onto $z = 0$ and $z = 1$, respectively. More generally, the bilinear transformation maps the imaginary axis of the $s-$plane onto the unit circle in the $z-$plane, and all the transmission poles, which are in the left half of the $s-$plane ($\mathrm{Re}\{s\} < 0$) subsequently map into the unit circle of the $z-$plane, as shown in Fig. 3.3 [59].

The transmission poles in the z-plane are then obtained by nullifying the denominator of (3.20) as

$$z_p = \left(\frac{\rho-1}{\rho+1}\right)^{1/\gamma} \exp\left[j(2p+1)\frac{\pi}{\gamma}\right], \tag{3.21}$$

where p is the same integer as in (3.7). This can be seen by noting that θ_p of (3.13) maps to angle $2\theta_p$ in the $z-$plane, following the transformation $z = e^{2j\theta}$ [(3.19)], which is the same as $\arg\{z_p\}$ in (3.21). This means that the location of the poles of the transfer function in the $z-$plane correspond to the maxima of the group delay function (in all the planes).

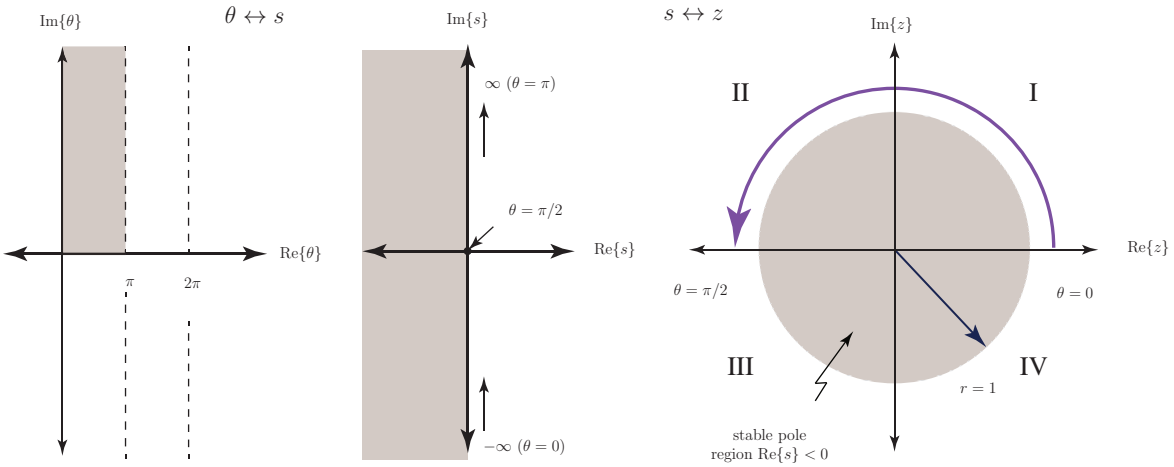

Figure 3.3 Mappings between the θ, s and z planes. The arrow in the $z-$plane indicates the direction of increasing frequency.

This expression provides the location of the complex poles of a C-section in the $z-$plane as a function of the coupling parameter ρ and of the length parameter γ. It is apparent from (3.21) that the magnitude of the poles depends on both ρ and γ, while the phase depends only on γ. Fig. 3.4 shows typical distributions of the poles in the $z-$plane for different ranges of γ for $0 < \arg\{z\} < 2\pi$. It can be seen that as the length parameter γ increases, new poles, corresponding to higher-order group delay peaks of the C-section, gradually appear in a given frequency range.

3.4.1.4 Bandwidth Constraints

To understand the problematic of bandwidth constraints in the proposed cascaded C-section structure, first consider the case of a single C-section. As shown in (3.9) and illustrated in Fig. 1(b), the group delay response of a C-section is a periodic function of frequency. This response is further represented in Fig. 3.5 with additional parameters for the sake of the following discussion. Figure 3.5 represents scenario where the p^{th} peak is selected within the specified bandwidth $[\omega_l, \omega_h]$. This peak is associated with a zeroth order peak at ω_0 such that the frequency at the maximum of the the p^{th} peak is $\omega_x = (2p+1)\omega_0$, according to (3.7). The frequency separation between adjacent peaks is $(2p+1)\omega_0 - (2p-1)\omega_0 = 2\omega_0$, which depends on the length of the C-section $\ell = \pi c/(2\omega_0\sqrt{\varepsilon_{\text{eff}}\mu_{\text{eff}}})$. In order to avoid group delay distortion from the $(p-1)^{\text{th}}$ and

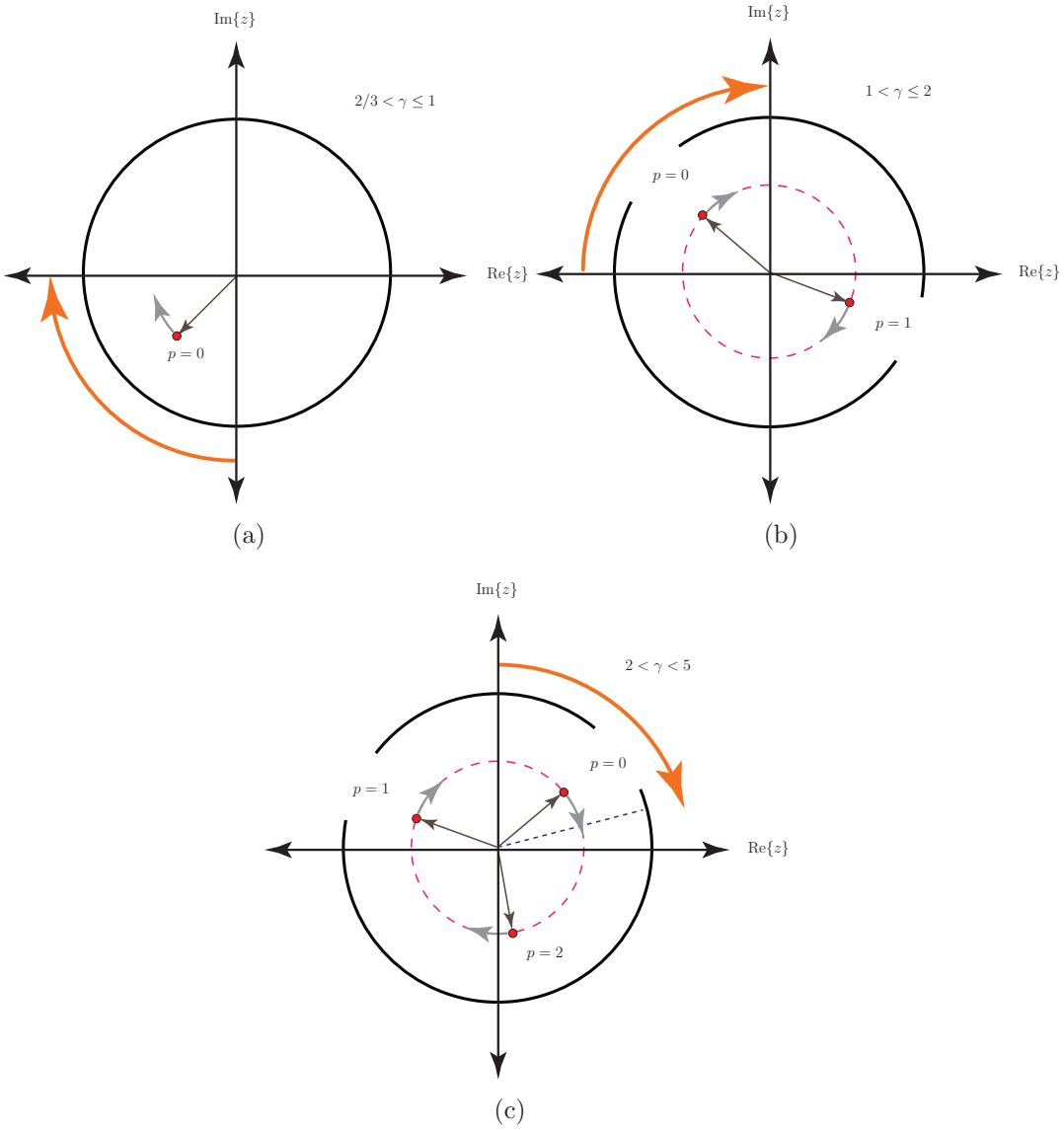

Figure 3.4 Distribution of the transmission poles of a C-section in the $z-$plane for $0 < \arg\{z\} < 2\pi$, computed by (3.21) for a) $2/3 < \gamma \leq 1$, b) $1 < \gamma \leq 2$, and c) $2 < \gamma < 5$. The direction of the arrows indicates to the motion of the poles as the length parameter γ is increased while the spans of the arrows indicate the sector of the pole $p = 0$.

$(p+1)^{\text{th}}$ peaks in the bandwidth of interest, we must avoid their penetration into $[\omega_l, \omega_h]$, i.e.

$$\omega_h < (\omega_x + \omega_0) = 2\left(\frac{p+1}{2p+1}\right)\omega_x, \tag{3.22}$$

$$\omega_l > (\omega_x - \omega_0) = 2\left(\frac{p}{2p+1}\right)\omega_x. \tag{3.23}$$

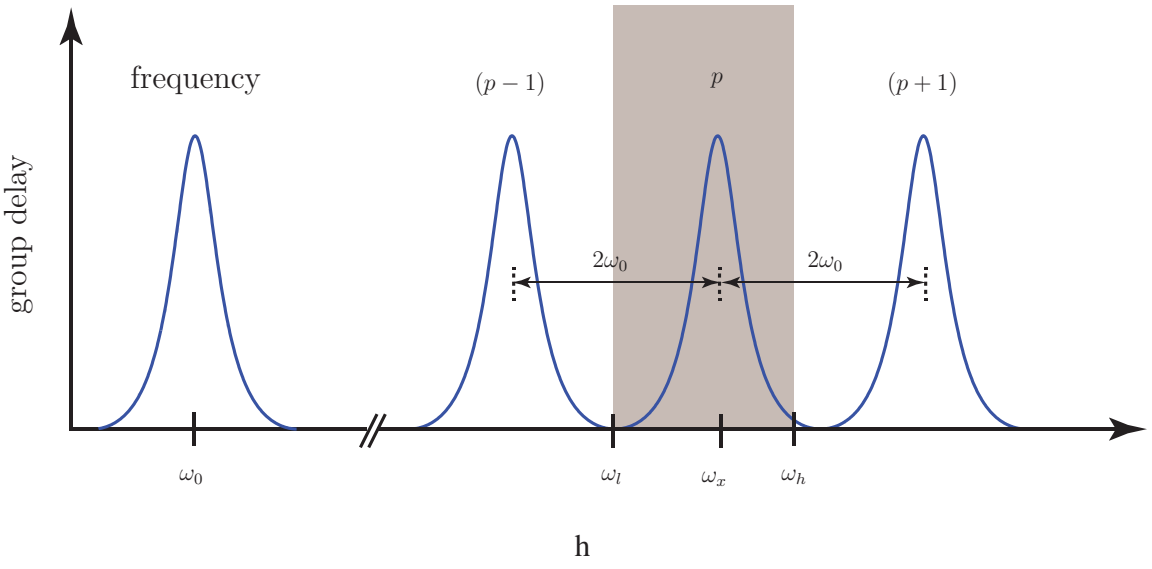

Figure 3.5 Location of transmission poles of $S_{21}^{\text{spec}}(z)$ for the case of a) $\omega_h < 2\omega_l$, and b) $\omega_h \geq 2\omega_l$.

The practical situation of a cascaded C-section structure, including several C-sections of different length, is more complex, since its group delay is a superposition of N periodic functions, as represented in Fig. 3.6. This situation is also more restrictive in terms of bandwidth because the delay peaks of the other C-sections penetrate into $[\omega_l, \omega_h]$ at frequencies closer to the center frequency. Quantitatively, the corresponding bandwidth restriction is

$$\omega_h < \min_i \left\{ 2 \left(\frac{p_i + 1}{2p_i + 1} \right) \omega_{x,i} \right\}, \tag{3.24}$$

$$\omega_l > \max_i \left\{ 2 \left(\frac{p_i}{2p_i + 1} \right) \omega_{x,i} \right\}. \tag{3.25}$$

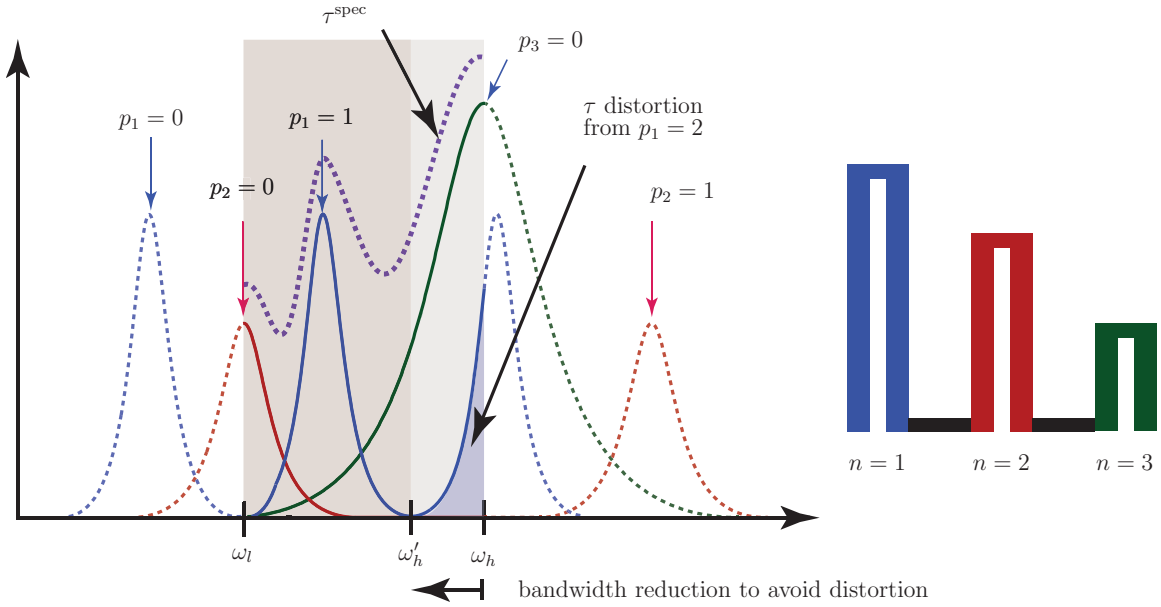

Figure 3.6 Illustration of the problematic of group delay distortion occurring in the case of cascaded C-sections, when the higher-order group delay peaks of some C-sections penetrate into the specified bandwidth.

In the particular case where only the $p = 0$ peak is used for all the C-sections ($p_i = 0, \forall i$), (3.25) and (3.24) reduce to $\omega_l > 0$ and $\omega_h < \min_i \{2\omega_{x,i}\}$. Since $\min_i \{2\omega_{x,i}\} = 2\omega_l$, we obtain the following explicit bandwidth restriction: $\omega_h < 2\omega_l$, corresponding to an octave bandwidth.

Another perspective for bandwidth restrictions, of interest for later examples, is to establish the maximal range of the length parameter ensuring no distortion. This may be best found by monitoring the bandwidth limits, ω_l and ω_h in the $z-$plane. Consider again the case $p_i = 0, \forall i$, until the end of this subsection. Let us choose $\theta_h = \theta(\omega_h) = \pi/2$ so that the upper edge of the specified bandwidth lies on the

negative real axis of the $z-$plane (see mapping in Fig. 2), or $z_h = z(\omega_h) = e^{j\pi}$. This choice implies, via (5) and (12), that

$$\theta(\omega) = \frac{\pi\omega}{2\omega_h} \tag{3.26}$$

respectively. Since $z = e^{2j\theta}$ from (14), the lower edge of the bandwidth in the $z-$plane is found from this relation as $z_l = e^{2j\theta_l} = e^{j\pi\omega_l/\omega_h}$. The $z-$plane locations of ω_h and ω_l for two different bandwidths are represented in Fig. 3.7.

For the case of a specified bandwidth of less than an octave, $\omega_l/\omega_h > 1/2$, $\arg\{z_l\} > \pi/2$, as shown in Fig. 3.7(a). Therefore, the transmission poles of $S_{21}^{\text{spec}}(z)$ lie only inside the second and the third quadrants, because the poles occur in complex conjugate pairs, as will be established in the next section. Consequently, the poles can be realized using C-sections with $2/3 < \gamma < 2$, as shown in Fig. 3.4(a) and (b). Since the higher-order poles do not penetrate into the second and third quadrants, as may be verified from (16) and is illustrated in Fig. 3(b), no group delay distortion is incurred.

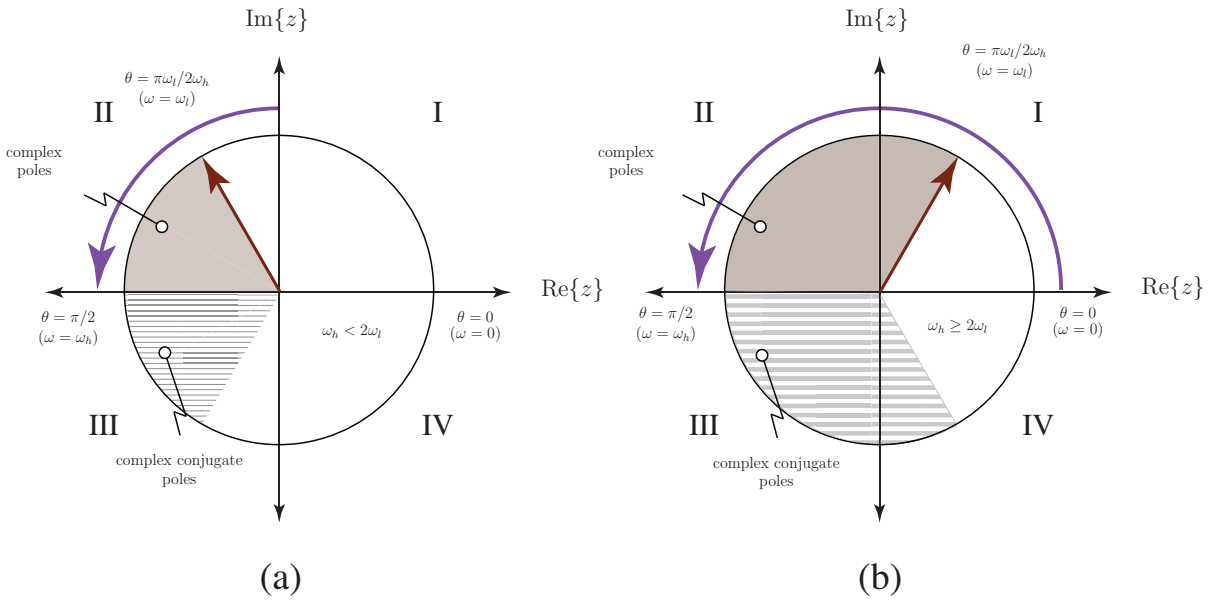

Figure 3.7 Location of transmission poles of $S_{21}^{\text{spec}}(z)$ for the case of a) $\omega_h < 2\omega_l$, and b) $\omega_h \geq 2\omega_l$.

On the other hand, if the bandwidth exceeds one octave, $\omega_l/\omega_h \leq 1/2$, $\arg\{z_l\} \leq \pi/2$, as shown in Fig. 3.7(b). Consequently, some of the transmission poles of $S_{21}^{\text{spec}}(z)$ may lie inside the first quadrant. This requires C-sections with $\gamma > 2$, as shown Fig. 3.4(c), a range for which the pole corresponding to $p = 1$ penetrates first into the third and next into the second quadrant as γ increases, as also apparent in Fig. 3.4(c). These additional poles thus lead to the distortions in the realized group delay. In summary, if the specified phase is restricted to an octave bandwidth, the proposed synthesis is guaranteed to work, while otherwise group delay distortions may occur.

In a similar way, the higher order group delay peaks ($p > 0$) can be used to realize the transmission poles of S_{21}^{spec} as long as the bandwidth conditions of (3.24) and (3.25) are satisfied. As shown in Fig. 3.2(a), selecting higher-order group delay peaks relaxes the constraints on the required coupling coefficients of the C-sections, which may be useful in practical implementations, as will be shown in a later example.

3.4.1.5 Synthesis Procedure

Based on the properties of the transmission poles of a C-section, a synthesis procedure can be devised to realize a specified group delay, or phase response. The overall synthesis procedure is summarized in Fig. 3.8, and is detailed next.

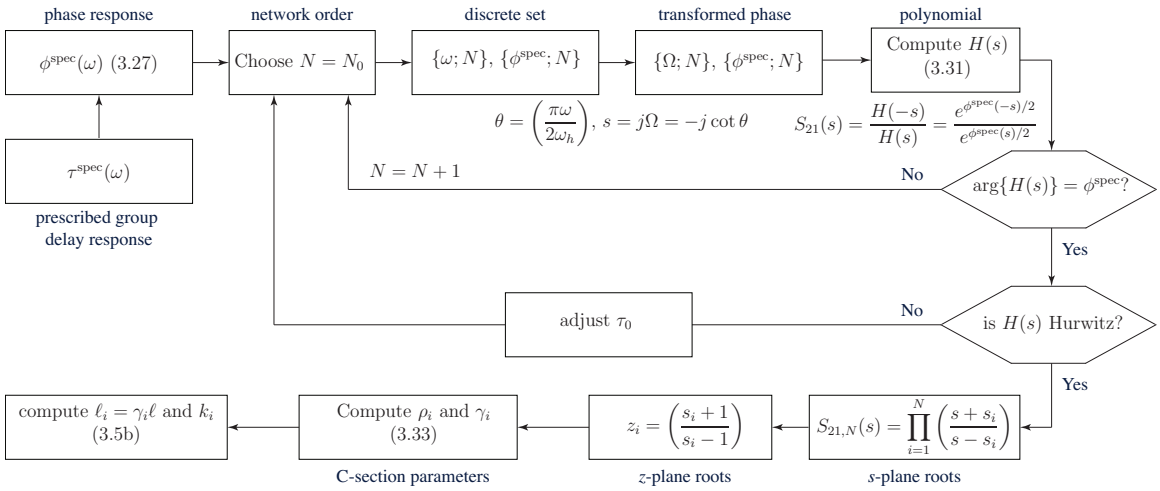

Figure 3.8 Proposed group delay synthesis procedure.

Let us consider a specified group delay $\tau^{\text{spec}}(\omega)$ within the bandwidth $\omega \in [\omega_l, \omega_h]$,

where $\omega_h \leq 2\omega_l$. The corresponding transfer function, which is to be synthesized, is $S_{21}^{\text{spec}}(\omega) = \exp[j\phi^{\text{spec}}(\omega)]$. The group delay $\tau^{\text{spec}}(\omega)$ can be decomposed into a constant delay τ_0 and a dispersive part $\tau(\omega)$, i.e. $\tau^{\text{spec}}(\omega) = \tau_0 + \tau(\omega)$. In practice, $\tau(\omega)$ is the part of interest, whereas τ_0 can take an arbitrary value. The corresponding phase $\phi^{\text{spec}}(\omega)$ is computed from $\tau^{\text{spec}}(\omega)$ using

$$\phi^{\text{spec}}(\omega) = -\int_{-\infty}^{\omega} \tau^{\text{spec}}(\omega) d\omega. \tag{3.27}$$

Now the task is to find an N^{th} order polynomial $H_N(\omega)$ such that $\arg\{H_N(\omega)\} \approx \phi^{\text{spec}}(\omega)/2$, so that the prescribed transfer function

$$S_{21}^{\text{spec}}(\omega) = \frac{H_N(-\omega)}{H_N(\omega)}, \tag{3.28}$$

from which the corresponding transmission poles of $S_{21}^{\text{spec}}(\omega)$ can be obtained. Moreover, to ensure a stable, and hence realizable, transfer function, $H_N(\omega)$ must be a Hurwitz polynomial [13]. Although there is no straightforward way to obtain this polynomial in the $\omega-$domain, a simple iterative technique exists to obtain it in the transformed low-frequency $s-$plane [53, 60].

First, we chose an initial (reasonably small) number N of C-sections, and construct the discretized frequency and phase vectors

$$\{\omega; N\} = \{\omega_0, \omega_1, \ldots, \omega_i, \ldots, \omega_{N-1}\}, \tag{3.29a}$$

$$\{\phi^{\text{spec}}; N\} = \{\phi_0, \phi_1, \ldots, \phi_i, \ldots, \phi_{N-1}\}, \tag{3.29b}$$

where $\omega_l \leq \omega_0 < \omega_1 < \ldots < \omega_{N-1} \leq \omega_h$, and $\phi_i = \phi^{\text{spec}}(\omega_i)$. Applying the transformation $s = j\Omega = -j\cot(\pi\omega/2\omega_h)$ of (3.17) with (3.26), a new vector $\{\Omega, N\}$ is obtained as

$$\{\Omega; N\} = \{\Omega_0, \Omega_1, \ldots, \Omega_i, \ldots, \Omega_{N-1}\}. \tag{3.30}$$

where the order of the frequencies has been reversed by the transformation of (3.17). For computational convenience, $\{\Omega; N\}$ and $\{\phi^{\text{spec}}; N\}$ are flipped, so that $\{\Omega; N\}$ is rearranged in the order of increasing frequencies, and $\{\phi^{\text{spec}}; N\}$ is offset so that the first element of $\{\phi^{\text{spec}}; N\}$ that corresponds to $\Omega = 0$ is zero. This condition allows to generate the N^{th} degree Hurwitz polynomial $H(s)$ corresponding to the

pair $\{\Omega; N\}$, $\{\phi^{\text{spec}}; N\}$ using the following closed-form iterative procedure [53, 60], derived in Appendix D:

$$\begin{cases} H_N(s) = \alpha_{N-1} H_{N-1}(s) + (s^2 + \Omega_{N-1}^2) H_{N-2}(s), \\ \text{with} \quad H_0(s) = 1, H_1(s) = s + \alpha_0 \end{cases} \tag{3.31}$$

and

$$\alpha_i = \cfrac{\Omega_{i+1}^2 - \Omega_i^2}{\alpha_{i-1} - \cfrac{\Omega_{i+1}^2 - \Omega_{i-1}^2}{\alpha_{i-2} - \cfrac{\Omega_{i+1}^2 - \Omega_{i-2}^2}{\ddots \\ \alpha_0 - (\Omega_{i+1}/\tan\psi_{i+1})}}},$$

where $\{\psi; N\} = -\{\phi^{\text{spec}}; N\}/2$ and $\alpha_0 = \Omega_1/\tan\psi_1$. The specified transfer function can then be constructed as

$$S_{21}^{\text{spec}}(s) = \frac{H_N(-s)}{H_N(s)}. \tag{3.32}$$

We next check if $\arg\{H_N(j\Omega)\} \approx \phi^{\text{spec}}(\Omega)/2$ for all the frequency points. If this is not the case, the order N is incremented to $N+1$ and a new polynomial $H_{N+1}(s)$ is generated using (3.31) until the specified phase is satisfactorily realized by the polynomial, as shown in Fig. 3.8. It is to be noted that this iterative procedure does not always ensure a Hurwitz polynomial. However, by varying the minimum group delay τ_0, a Hurwitz polynomial can *always* be obtained for a given phase response [60]. Once, the appropriate polynomial has been obtained, its poles are computed by fatorization and transferred to the $z-$plane using (3.19). Since the coefficients of $H_N(s)$, related to the α_i's and Ω_i's, are purely real, the corresponding roots are either purely real or occuring in complex conjugate pairs [59]. These roots can now be realized using microwave C-sections whose parameters are found reversing (3.21) as

$$\gamma_i = \frac{(2p_i + 1)\pi}{\arg\{z_i\}} \quad \text{and} \quad \rho_i = \left(\frac{1 - |z|^{\gamma_i}}{1 + |z|^{\gamma_i}}\right). \tag{3.33}$$

A practical layout can be straightforwardly obtained from (3.33), which provide the lengths ℓ_i and coupling coefficients k_i of the different C-sections as

$$\ell_i = \gamma_i \ell \quad \text{and} \quad k_i = \left(\frac{\rho_i^2 - 1}{\rho_i^2 + 1} \right). \tag{3.34}$$

3.4.2 Results

3.4.2.1 Group Delay Design Examples

Lets consider the following group delay specification: linear positively-sloped group delay with a delay swing $\Delta\tau = 1$ ns within the bandwidth of 4 to 8 GHz (octave bandwidth). For a linear group delay, the phase response is quadratic and is easily obtained using (3.27) as

$$\phi^{\text{spec}}(\omega) = -\frac{1}{2} \frac{\Delta\tau}{\omega_h - \omega_l} \omega^2 - \left(\frac{\Delta\tau \omega_h}{\omega_h - \omega_l} + \tau_0 \right) \omega. \tag{3.35}$$

Using the transformation of (3.17) and (3.26), we have $s = -j \cot(\omega/32)$. Following the iterative synthesis procedure of Fig. 3.8, it is found that $N = 24$ is sufficient to generate a polynomial $H(s)$ such that $\arg\{H_N(s)\} = \phi^{\text{spec}}(\omega)/2$ with the specified parameters. Next, the minimum group delay τ_0 is adjusted to make $H(s)$, a Hurwitz polynomials. $\tau_0 = 2.0$ ns is found to satisfy this criterion. Now, the roots of $H(s)$ are computed and transferred to the $z-$plane using (3.19), as shown in Fig. 3.9(a). The fact that all the poles are inside the unit circle in the $z-$plane verifies that the polynomial generated is indeed a Hurwitz polynomial. Finally, for each complex pole, the length parameter γ and the coupling parameter ρ of the corresponding C-section are computed using (3.33) with $p = 0$, from which the final transfer function of (3.14) is obtained. The synthesis parameters are shown in Tab. 3.1. Fig. 3.9(a) shows the corresponding group delay response, and as can be seen, the specified group delay response is correctly realized using the C-section transfer function.

Fig. 3.9(b) shows the realization of a constant group delay response (linear phase) of $\tau_0 = 1$ ns with $\Delta\tau = 0.0$ ns in (3.35), obtained by following a similar procedure. This design requires $N = 9$ C-sections. Its design parameters are shown in Tab. 3.2.

Fig. 3.9(c) shows the realization of a positive-slope group delay with $\Delta\tau = 1.0$ ns within $4 - 5$ GHz of bandwidth, using both the fundamental group delay peak and the higher order peak, corresponding to $p = 0$ and $p = 1$, respectively. For this design, $N = 4$ C-sections are found to be sufficient for both cases. The corresponding synthesis parameters are shown in Tab. 3.3 when $p = 1$ is used in (3.33).

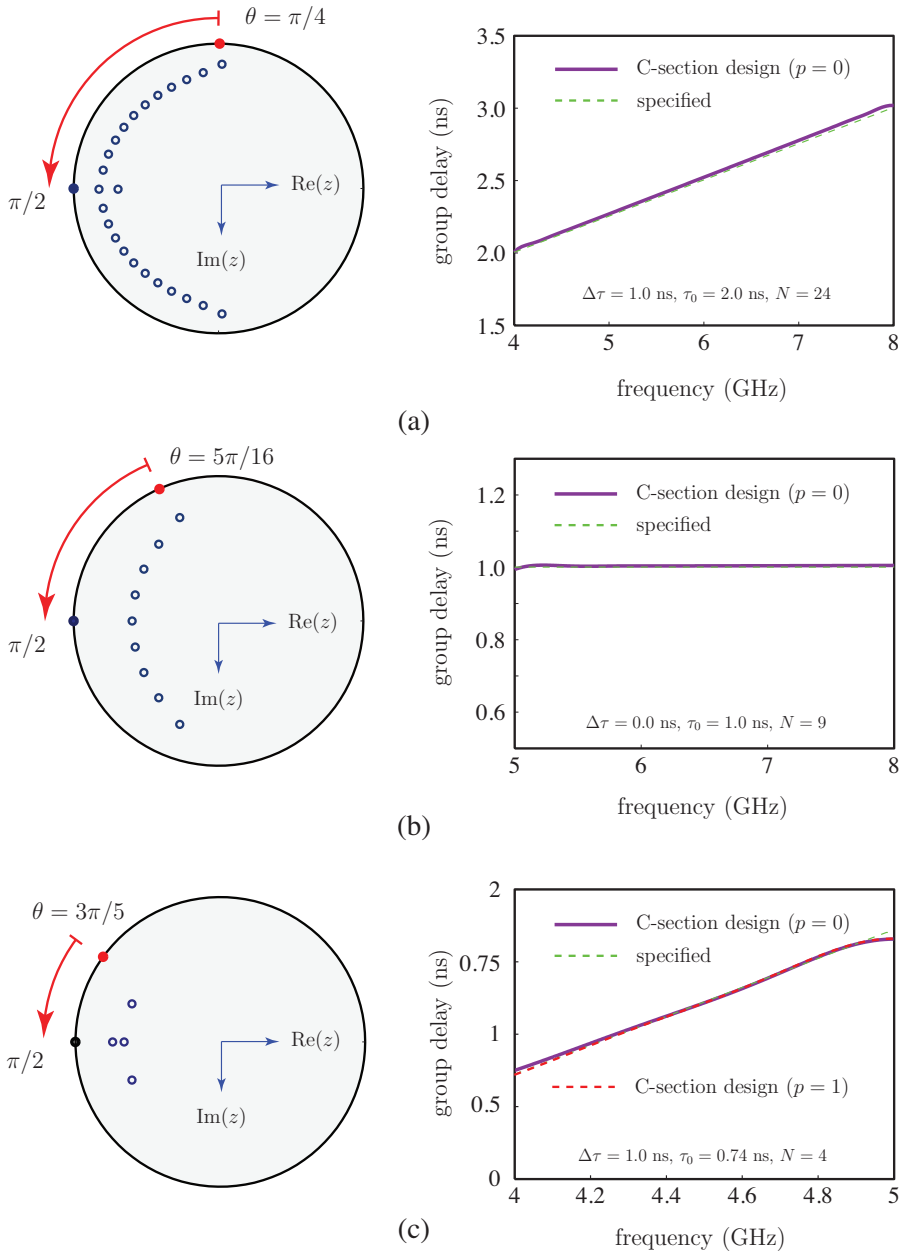

Figure 3.9 Group delay design examples. a) Positive-slope linear group delay using $p = 0$. b) Constant group delay using $p = 0$. c) Positive-slope linear group delay using $p = 1$.

Table 3.1 Synthesis parameters of the cascaded C-section structure corresponding to the design of Fig. 3.9(a)

C-section	$\gamma_n = \ell_n/\ell_0$	ρ_n	ω_n $(p = 0)$	k_n
$n = 1$	0.66	20.3	12.1 GHz	0.99
$n = 2$	2.02	6.7	3.9 GHz	0.95
$\vdots$	$\vdots$	$\vdots$	$\vdots$	$\vdots$
$n = 23$	1.05	9.2	7.6 GHz	0.97
$n = 24$	1.00	10.9	8.0 GHz	0.98

Table 3.2 Synthesis parameters of the cascaded C-section structure corresponding to the design of Fig. 3.9(b)

C-section	$\gamma_n = \ell_n/\ell_0$	ρ_n	ω_n $(p = 0)$	k_n
$n = 1$	0.72	21.4	11.06 GHz	0.98
$n = 2$	1.62	9.9	4.93 GHz	0.91
$\vdots$	$\vdots$	$\vdots$	$\vdots$	$\vdots$
$n = 8$	1.1	7.5	7.23 GHz	0.86
$n = 9$	1.0	6.82	8 GHz	0.88

Table 3.3 Synthesis parameters of the cascaded C-section structure corresponding to the design of Fig. 3.9(c)

C-section	$\gamma_n = \ell_n/\ell_0$	ρ_n	ω_n $(p = 0)$	k
$n = 1$	2.66	1.02	1.88 GHz	0.61
$n = 2$	3.45	1.65	1.45 GHz	0.46
$n = 3$	3.00	1.83	1.67 GHz	0.54
$n = 4$	3.23	2.34	1.67 GHz	0.70

3.4.2.2 High Coupling Coefficient Requirement

As seen in Sec. 3.4.2.1, the proposed procedure typically involves a few large coupling coefficients. Although such coupling coefficients are challenging to realize practically, they are nonetheless possible. Practical solutions involve:

1. implementation of broadside-coupled C-sections using low-temperature co-fired ceramics (LTCC) [61];

2. composite-right/left-handed (CRLH) transmission line coupled-line structures, which can provide quasi-0 dB couplings from their evanescent mode propagation characteristics [62], and as shown in [16] (to be explained in Chapter 7);
3. ferroelectric substrates with high dielectric constant (or ferromagnetic substrates with high permeability) for enhanced couplings [63].

One solution to avoid these high-cost or high-complexity approaches is to relax the high-coupling coefficient requirement by using higher-order group delay peaks ($p > 0$) for the C-section responses, as illustrated in Fig. 3.2(a) and explained in Sec. 3.4.1, assuming the associated higher bandwidth constraints can still be satisfied. This is the approach used next to demonstrate a practical C-section structure that can be realized using standard material and fabrication processes

Consider again the group delay design of Fig. 3.9(c). The coupling coefficients of the C-section with $p = 0$ in (3.33) are shown by the dashed curve in Fig. 3.10, where $\max[k] = 95\%$. If, instead, $p = 1$ is chosen, the coupling coefficients are considerably reduced, as shown by the solid curve in Fig. 3.10, where $\max[k] = 71\%$ only, which is easily realizable using broadside coupled C-sections in conventional substrates.

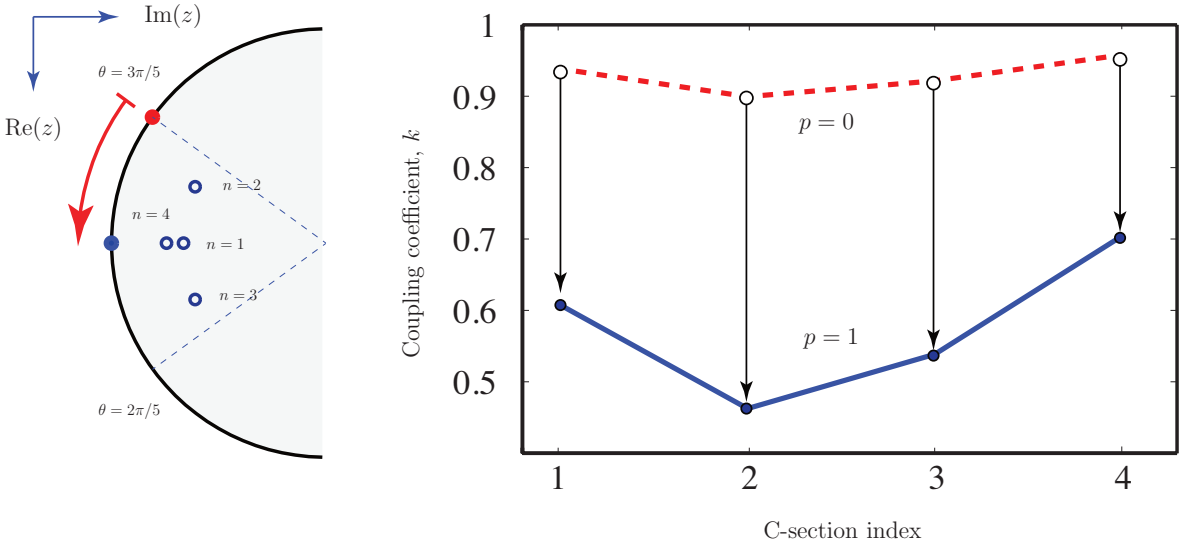

Figure 3.10 Reduction of C-section coupling coefficients using higher order group delay peaks of the C-section response. The distribution of the complex poles in the $z-$plane are also shown.

3.4.2.3 Full-Wave Demonstration

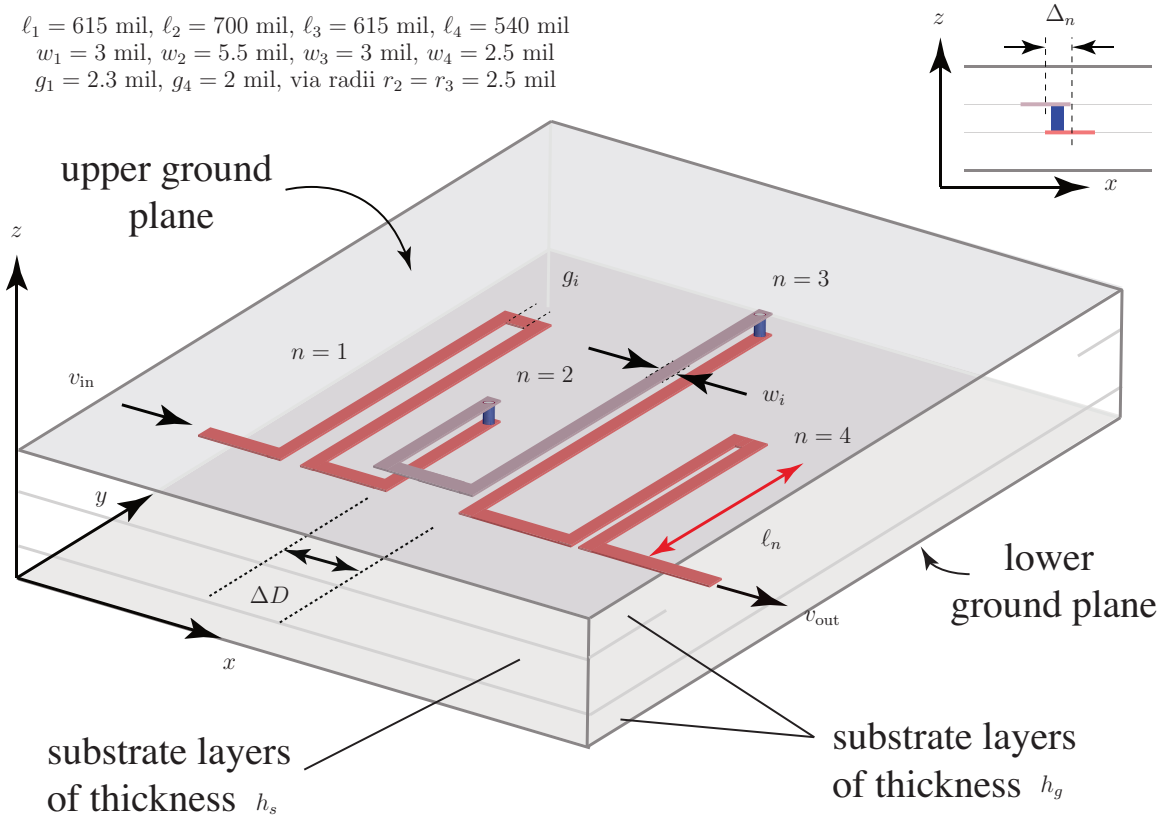

Figure 3.11 Proposed multilayer architecture of a typical all-pass dispersive delay structure prototype.

Fig. 3.11 shows a typical broadside coupled architecture of cascaded C-sections to realize a specified group delay response. It consists of 3 dielectric layers, sandwiched between two ground planes. By controlling the thickness h_s of the middle dielectric, and the strips offset Δ_n between the two broadside coupled transmission lines, the coupling coefficient k can be conveniently controlled [64]. In addition, the parameter ΔD is chosen large enough so that no significant coupling occurs between the adjacent C-sections. The substrate used in the full-wave prototype is Dupont 951 with permittivity $\epsilon_r = 7.8$ and $\tan\delta = 0.006$. The copper thickness is 8 μm. The top and bottom substrates have the height $h_g = 16.5$ mil and the middle substrate has the height $h_s = 1.65$ mil. For the C-section design of Tab 3.3, two C-sections can be

conveniently realized in edge-coupled configuration ($n = \{2, 3\}$) and the other two in broadside configuration ($n = \{1, 4\}$) as shown in Fig. 3.11 with the corresponding layout parameters. The prototype with all the structure dimensions can be fabricated within the current state-of-the-art PCB processes.

Fig. 3.12 shows the computed transmission and group delay response of the full-wave prototype. An acceptable matching is obtained over the design bandwidth with $S_{11} < -18$ dB. A maximum transmission loss of 5.45 dB is observed due to the dielectric and conductor losses. Besides, an amplitude imbalance in $\Delta S_{21} = (S_{21,h} - S_{21,l}) = 3.11$ dB is also seen. This imbalance can be easily corrected by using a resistive amplitude equalizing network [65]. Fig. 3.12(b) shows the realized group delay response compared to the ideal C-section response for the two cases of $p = 0$ and $p = 1$. An an excellent agreement is found. The maximum error of 0.05% is observed in the group delay which can be considered acceptable for practical purposes. This error could be reduced using full-wave fine tuning of the structure.

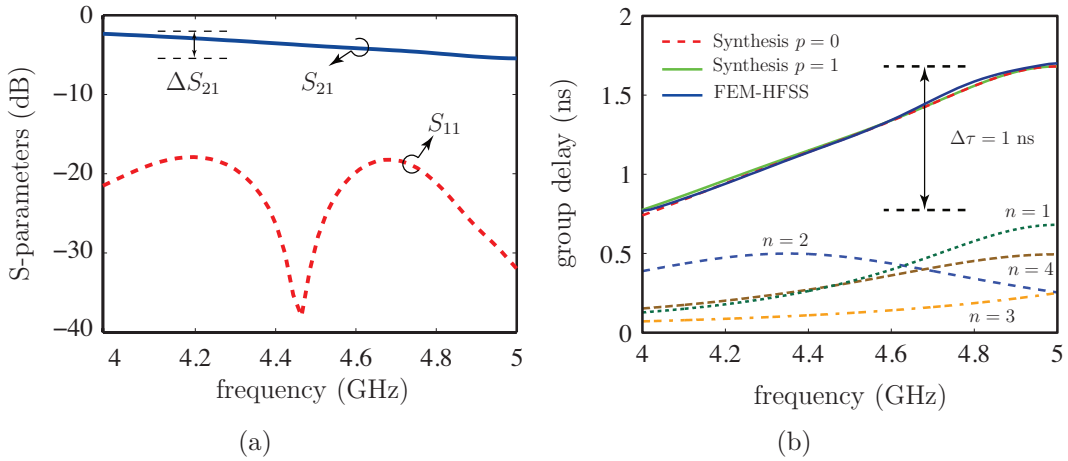

Figure 3.12 Full-wave FEM-HFSS results. a) S-parameters. b) Group delay response showing the ideal response of individual C-sections computed using (3.4) using the parameters given in Tab. 3.3.

3.5 Dispersion Enhancement of C-section based DDSs using Ferrimagnetic Substrates

As mentioned in the previous section, the high coupling coefficient in C-sections may be achieved using ferroelectric and ferromagnetic substrates. The possibility of using ferromagnetic materials is explored in this section. The proposed technique for $\Delta\tau$ enhancement in a transmission-line all-pass network is based an all-pass configuration in conjunction with ferrimagnetic materials, such as ferrites [66] or ferromagnetic nano-wires (FMNW) composites [1], as illustrated in Fig. 3.13, to achieve significant dispersion enhancement [15]. This technique exploits the coupling and dispersion boosting properties of the magnetic materials with large permeability $\mu(\omega)$ to achieve the desired dispersion in the resulting all-pass networks.

In a microwave C-section, the desired larger group delay swing $\Delta\tau$ can be achieved by increasing the coupling-coefficient k between the coupled lines, according to

$$\Delta\tau = (\tau_{\max} - \tau_{\min}) = \frac{4k}{\sqrt{1-k^2}}, \tag{3.36}$$

The coupling coefficient k is given by $k = \beta(k_m + k_e)/2$, where k_e and k_m are the electric and magnetic coupling coefficients, respectively [67]. For a given permittivity (i.e fixed k_e), considering that the magnetic coupling coefficient k_m relates the self-inductance $L_{\rm c}$ and $L_{\rm iso}$ of the lines in coupled and uncoupled configurations, the overall coupling coefficient $k \propto k_m = (L_{\rm iso} - L_{\rm c})/L_{\rm c} = L_m/L_{\rm c}$. This drop L_m in the inductance corresponds to the ratio of the mutual magnetic flux ϕ_m between the two coupled lines to the current I flowing along one of the conductors, i.e.

$$L_m = \frac{\phi_m}{I} = \frac{\int_\Omega \mu(\omega)\mathbf{H}\cdot\mathbf{d\Omega}}{\oint_\Gamma \mathbf{H}\cdot\mathbf{d\Gamma}}, \tag{3.37}$$

where the closed contour Ω and the surface Γ are defined in Fig. 3.14. Considering (3.36) and (3.37), we find that $\Delta\tau \propto k \propto \mu(\omega)$. Therefore, a ferrimagnetic material with a large μ, such as a ferrite relatively close to resonance, enhances the group delay swing of a transmission-line all-pass network by boosting the coupling coefficient k.

To demonstrate this principle, consider a 2-port microwave C-section in a stripline configuration, as illustrated in Fig. 3.15(a). The backward coupling C between the two corresponding coupled lines (computed from the 4-port network after removing

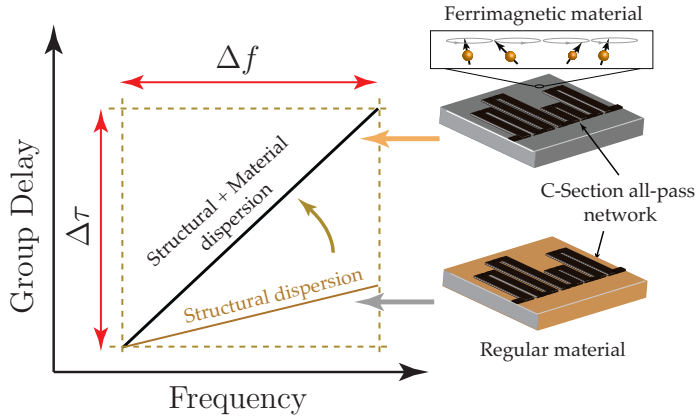

Figure 3.13 Group delay swing enhancement using a ferrimagnetic material substrate.

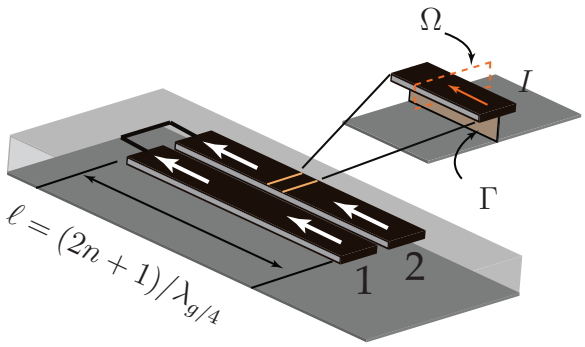

Figure 3.14 A microwave C-section all-pass network.

the short at the end of the C-section) is shown in Fig. 3.15(b) for the two cases of a regular substrate and a ferrite substrate. As expected, the C-section in the ferrite with $\mu > 1$ exhibits a larger coupling.

It is observed that the coupling C in the case of ferrite substrate is non-uniformly increased across the frequency range shown with the largest increase at the frequency where the length of the coupler $\ell = \lambda_g/4$ or $\theta = \pi/2$. This can be explained by comparing the electrical length $\theta(\omega)$ of the coupler in a ferrimagnetic medium with that in a regular medium, as shown in Fig. 3.15(c). Due to the dispersive nature of the ferrimagnetic material with a larger $(\theta - \omega)$ slope compared to that in a regular medium, the coupling C drops faster as the frequency gets farther from the maximum coupling condition of $\lambda_g/4$. Therefore, apart from providing a boosted coupling, ferrimagnetic materials provides an additional dispersion by yielding different couplings at different frequencies.

The group delay swing enhancement resulting from the combined structural and material dispersion boosting is shown in Fig. 3.15(d). Compared to a regular substrate, a 60% increase in the group delay swing is observed, thereby validating the proposed principle. This group delay swing can be further enhanced by operating near the ferrimagnetic resonance of the ferrite where μ is even larger (ferrimagnetic resonance being ≈ 5.5 GHz for the case considered).

Furthermore, the result of Fig. 3.15(d) is compared with (3.6) or (3.9) considering the effective $\mu(\omega)$ of the ferrite. As seen in Fig. 3.16(a), a small discrepancy between them is observed, which may be attributed to the non-reciprocal nature of the ferrite, evident from the field displacement effect shown in Fig. 3.16(b). Nonetheless, the closed form expression (3.6) provides an excellent initial estimate of the group delay response from an all-pass network on a ferrimagnetic material, which will thus be later used in the case of FMNW substrates.

3.5.1 Experimental Results

To experimentally verify the coupling and dispersion boosting properties of ferrimagnetic materials, a single microwave C-section and a commensurate all-pass network were fabricated on a ferrite substrate, as shown in Fig. 3.17(a). In order to avoid the difficulty of drilling via holes in the ferrite substrate for proper stripline ground plane connection, an alternative ferrite loaded microstrip configuration was adopted

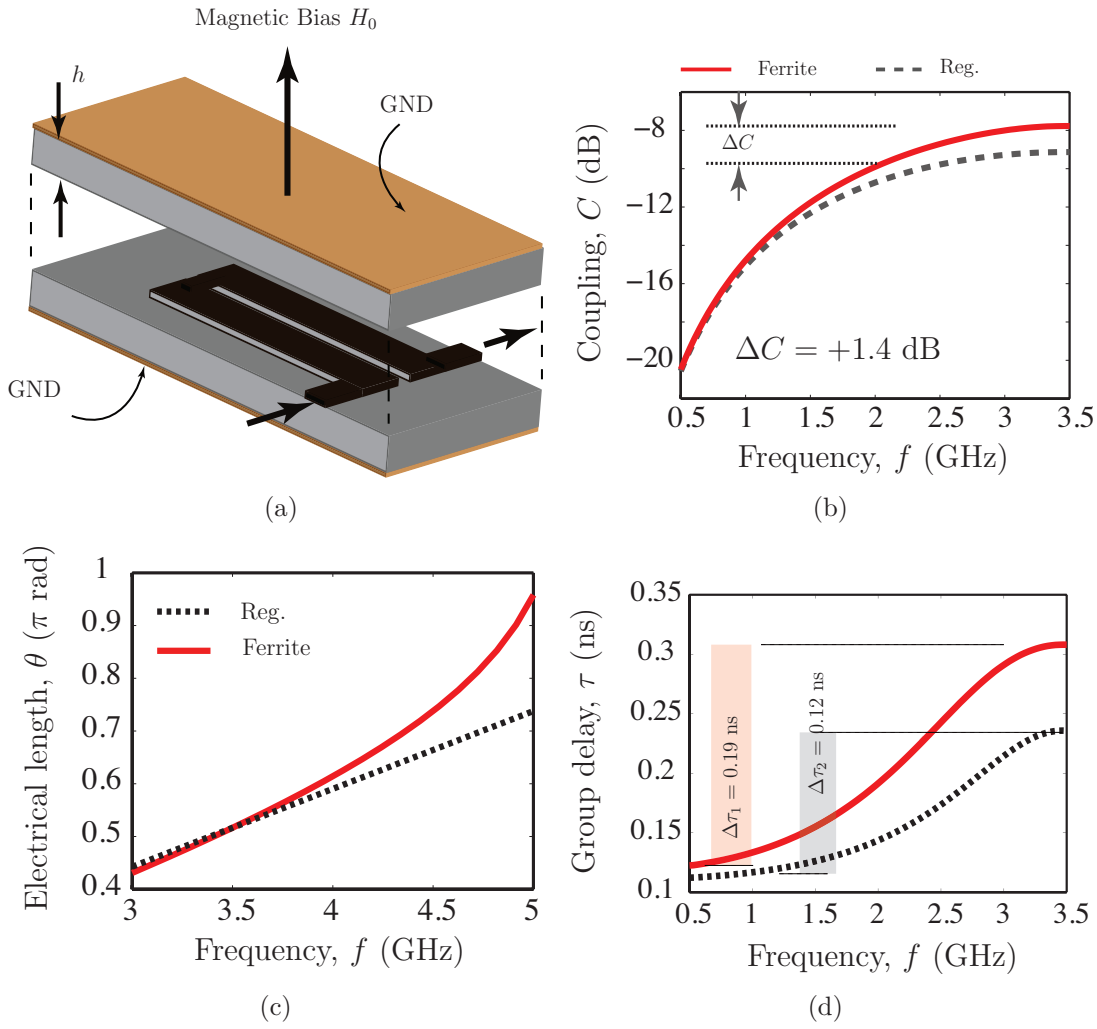

Figure 3.15 Comparison between the group delay response of a microwave stripline C-section in a regular substrate and in a ferrite substrate. a) Stripline structure considered. b) Coupling between the two lines. c) Electrical length variation versus frequency. b) Larger group delay swing ($\approx 60\%$ increase) due to increase in peak coupling value. All the lengths are designed so as to achieve maximum coupling and group delay at 3.5 GHz. Results are all computed using FEM-HFSS (considering magnetic losses only), where $S_{11} < -15$ dB (not shown) in all cases. The parameters of the ferrite used are: $\varepsilon_r = 14.59$, $M_s = 1577$ Gauss, $\Delta H = 6$ Oe measured at 9.4 GHz, height $h = 1$ mm and external magnetic bias field $H_0 = 15 \times 10^4$ A/m.

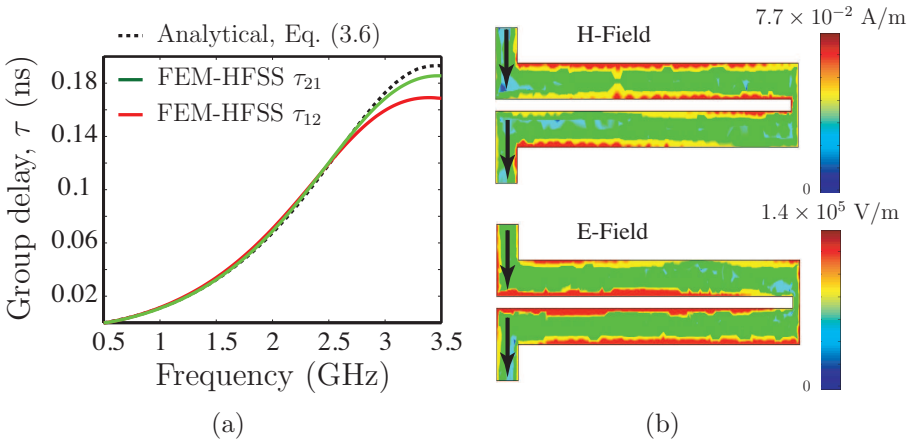

(a) (b)

Figure 3.16 Response of a single C-section all-pass structure [Fig. 3.15(a)]. (a) Comparison of the analytical group delays computed by (3.6) and by full-wave FEM-HFSS. b) E- and H-fields computed at the frequency having the largest group delay (3.5 GHz), showing the displacement effect due to the non-reciprocity of ferrite.

in the forthcoming proof-of-concept device. The structures consist of a ferrite substrate layer on top of a grounded ferrite slab with a signal traces, as illustrated in Fig. 3.17(a).

Fig. 3.17(b) shows the measured S-parameters and group delay responses for 1) a microwave C-section and 2) a commensurate network, obtained by varying the external magnetic bias using an electromagnet. The return loss is relatively poor, especially in case 1), which may be attributed to the inhomogeneity of the structure due to air gaps between the two layers and errors in the manual alignment of the two ferrite substrates. Nonetheless, a significant increase in group delay swing by $\approx 53\%$ and 70% compared to that in a regular substrate is clearly observed for the C-section and the commensurate all-pass network, respectively. Furthermore, by decreasing the magnetic bias thereby lowering the resonant frequency of the ferrite, the group delay swing [for case 2)] was further increased due to larger value of μ near the resonance, resulting in even larger group delay swing values. For example, a 225% increase in group delay swing compared to that in the regular substrate was achieved, as shown in Fig. 3.17(b). These results confirm the proposed principle of group delay enhancement despite the rudimentariness of the experimental ferrite prototypes used. A high-quality multi-layer fabrication process would naturally alleviate the issues of

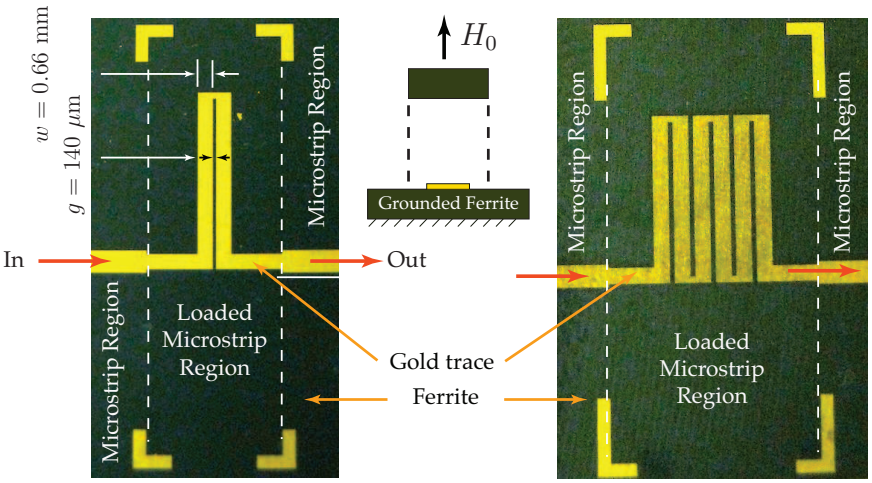

(a)

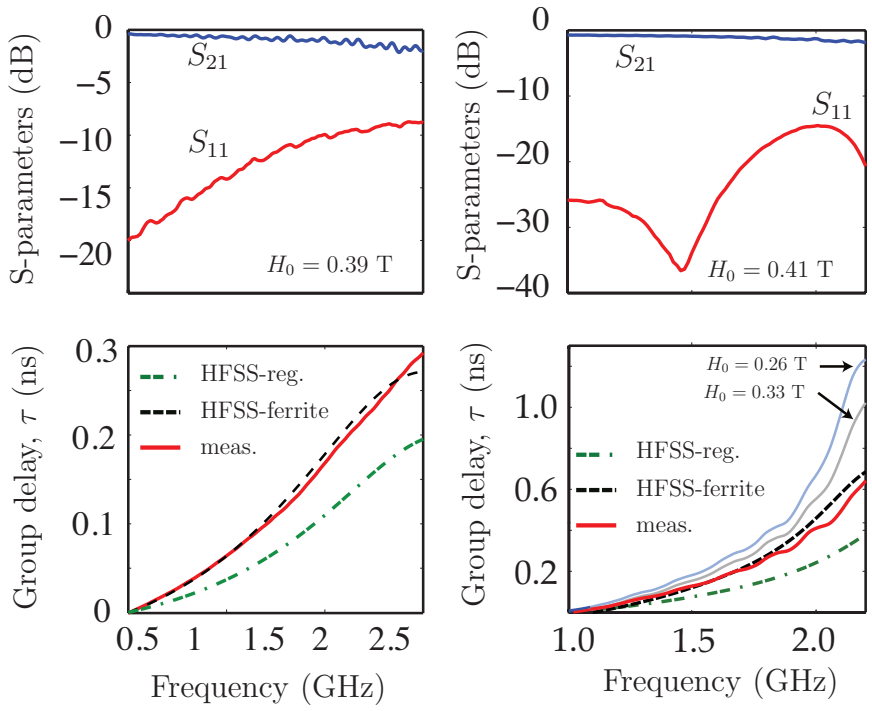

(b)

Figure 3.17 Prototypes and results for ferrimagnetic all-pass networks. a) Photographs of the prototypes for the case of a single C-section and a commensurate network. b) Corresponding measured S-parameters and group delay response. The ferrite parameters are the same as in Fig. 3.15 with varied external magnetic bias field. The measured responses are compared with FEM-HFSS simulations for the case when a regular substrate is used instead of ferrite.

air gaps and is expected to give improved transmission and group delay responses.

3.5.2 Benefits and features

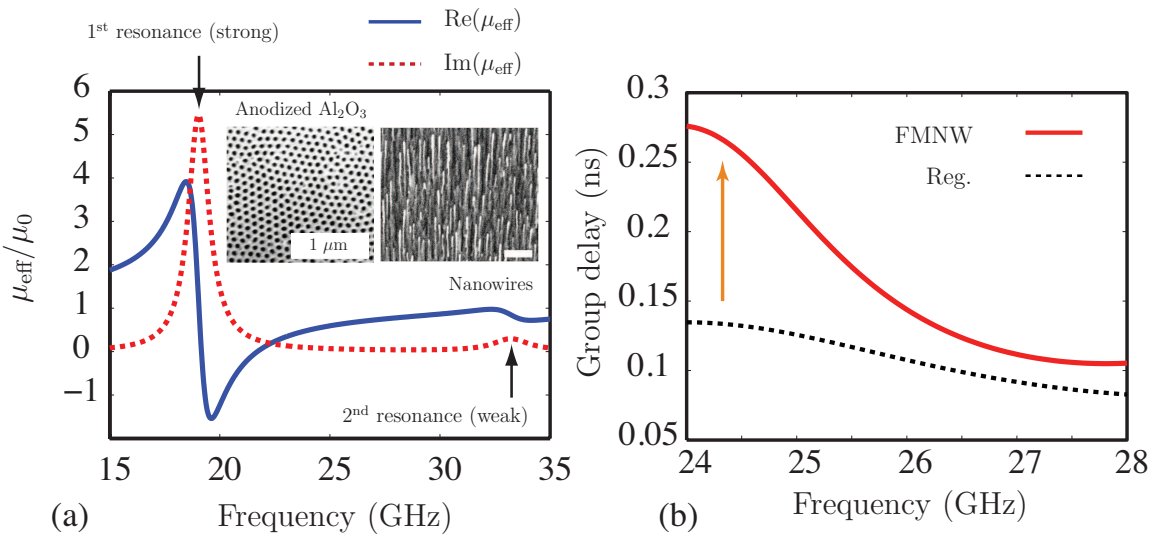

Figure 3.18 Illustrative example of a C-section all-pass network on a ferromagnetic nanowire (FMNW) substrate, avoiding the need for a magnet. a) Double-Lorentz response of a FMNW membrane (shown in inset) [1]. b) A typical group delay response of a single C-section computed by (3.6) with $\mu = \mu(\omega)$ of a). About 330% increase in group delay swing is observed compared to the case where an isotropic substrate property is used.

The proposed principle of combining the coupling and dispersion boosting properties of ferrimagentic material with transmission-line all-pass networks offers several benefits. Firstly, the resulting transmission-line all-pass network is compact in size, providing a larger dispersion per unit area compared to other passive techniques for dispersion enhancement (such as cascading or smaller line gaps). Secondly, the group delay swing of this network on a ferrimagnetic material can be tuned by an external magnetic bias H_0 and is thus suitable for various real-time signal processing applications. Thirdly, the dispersion profile of the ferrimagnetic material can be combined with the structural group delay response to achieve real-time group delay shaping. Fourthly, the proposed technique can be easily combined with alternative solutions

such as cascading, smaller line gaps or signal re-injection loop technique, to achieve even larger dispersion values. Finally, the requirement of an external magnetic bias in case of ferrites can be suppressed at high frequencies by using self-biased FMNW substrates [68]. These substrates consist of dense arrays of ferromagnetic nanowires grown inside an anodized alumina matrix and exhibit a double Lorentz dispersion characteristic with large μ values at high frequencies [1], as shown in Fig. 3.18(a). A typical group delay response of a microwave C-section on such a membrane is shown in Fig. 3.18(b), computed using (3.6) along with the double Lorentz characteristic resulting in a significant increase in the group delay swing.

3.6 Summary

In this chapter, two transmission-type dispersive delay structures has been described which are fundamentally working on two different principles. CRLH transmission line based delay structures are fundamentally ladder-type networks where the magnitude and the phase response are dependent on each other. On the other hand, all-pass structures provides an independent control over the phase and magnitude response. Both approaches provide attractive solutions of dispersive delay technologies due to their simplicity, frequency scalability and planar fabrication.

A closed-form procedure for synthesizing quasi-arbitrary phase responses has also been proposed using cascaded microwave C-sections of different lengths and different coupling coefficients. Using a closed-form polynomial generation method, both the real and complex transmission poles of the required transfer function have been derived and realized with different cascaded C-sections. Due to the distributed nature of the transmission lines, the proposed synthesis safely works for one octave bandwidth, when the first group delay peak of the C-section is used, but is not guaranteed beyond. C-section networks employing higher order group delay peaks have been found to reduce the required coupling coefficients of the C-sections to practically realizable values, at the cost of bandwidth reduction. Moreover, in contrast to the case of lumped-element all-pass networks, where both C-sections and D-sections are required [69], C-sections alone are found to be sufficient in distributed implementations. A multilayer architecture has been used to demonstrate the synthesis, which can easily be fabricated using standard PCB fabrication processes. This synthesis technique is expected to help efficient designs of microwave analog signal processors. Finally, to

increase the dispersion per unit area, the concept of combined material and structural dispersion has also been introduced using ferrimagnetic substrates.

Chapter 4

All-Pass Dispersive Delay Structures - Coupled C-sections

In chapter 3, the group delay synthesis using microwave C-sections was presented. In that case, the various C-sections were isolated from each other so that the transfer function of the overall structure could be written as a simple cascade of the individual C-sections. However, it is possible to enhance the dispersion of the structure for a given physical size, by allowing couplings between the various C-sections. These extra couplings between different C-sections can enhance the dispersion per unit size of the structure leading to increased dispersion engineering possibilities, at the cost of compromised matching. This will be the subject of this chapter.

The essence of this all-pass network approach was suggested by Hewitt back in 1967 [70]. However, the following distinctions exist between the proposed work [2] and the one of Hewitt: 1) Hewitt's structure was a volumetric folded tape meander line, which was non-planar and therefore incompatible with monolithic microwave integrated circuit (MMICs); it is also difficult to fabricate and suffers from high loss and from severe requirements on dimensional tolerances which tend to limit the upper frequency range of operation to about 5 GHz. In contrast, the proposed stripline (or microstrip) structure is much simpler, completely planar and fully compatible with MMICs, and may be realized easily in the millimeter-wave range.; 2) The structure of Hewitt used *commensurate* folded sections, and the different group delay - frequency states were achieved by the heavy and impractical insertion of dielectric slabs of different thicknesses between the folded sections; in contrast, the proposed structure achieves different delay - frequency states by simply modulating the lengths of the different sections; 3) Hewitt mentions only folded tape meander line and does not establish the equivalence between the folded line pairs and C-section all-pass equalizers; in contrast, this equivalence is demonstrated in the present paper, and it may be exploited for more efficient designs based on simple lumped element circuit models;

4) Hewitt uses approximate and empirical design formulas; in contrast, this paper presents an accurate numerical technique, based on the method of moments; 5) In addition, this work proposes a systematic and automated design procedure, using genetic algorithms, which allows the efficient design for complex group delay responses, as demonstrated in the paper.

4.1 Commensurate Coupled-Line Networks

The commensurate (or uniform) versions of the non-commensurate group delay networks, which will be described in Sec. 4.2, are shown in Fig. 4.1, where Fig. 4.1(a) represents the $2N$-port initial network while Fig. 4.1(b) represents the 2-port network obtained by short-circuiting the appropriate ports so as to build a meandered line structure to achieve a desired peak delay at the frequency where the couplers are a quarter-wavelength long.

4.1.1 Derivation of the Scattering Matrix of the $2N$-Port Network Using Multiconductor Transmission Line Analysis

Let us first consider the commensurate $2N$-port structure of Fig. 4.1(a), which may also be seen as a multiconductor transmission line network, and which includes N transmission lines of length ℓ. We call the input and output voltage vectors of the network $\mathbf{V}(0) = [V_1\ V_2\ V_3\ ...\ V_N]^t$ (at $x = 0$) and $\mathbf{V}(\ell) = [V_{N+1}\ V_{N+2}\ V_{N+3}\ ...\ V_{2N}]^t$ at $x = \ell$, respectively. The corresponding input and output current vectors are $\mathbf{I}(0) = [I_1\ I_2\ I_3\ ...\ I_N]^t$ and $\mathbf{I}(\ell) = [I_{N+1}\ I_{N+2}\ I_{N+3}\ ...\ I_{2N}]^t$ at $x = 0$ and $x = \ell$, respectively. Such a $2N$ port network can be characterized by a per-unit-length capacitance matrix $\mathbf{C}$ and an inductance matrix $\mathbf{L}$ [71]. The entries of $\mathbf{C}$ relate the total charge Q_i per unit of line length on the ith conductor to all the line voltages producing it by $\mathbf{Q} = \mathbf{CV}$ or

$$\begin{bmatrix} Q_1 \\ Q_2 \\ Q_3 \\ \dots \\ Q_N \end{bmatrix} = \begin{bmatrix} C_{11} & C_{12} & \dots & C_{1n} \\ C_{21} & C_{22} & \dots & C_{2N} \\ C_{31} & C_{32} & \dots & C_{3,2N} \\ \dots & \dots & \dots & \dots \\ C_{n1} & C_{n2} & \dots & C_{NN} \end{bmatrix} \begin{bmatrix} V_1 \\ V_2 \\ V_3 \\ \dots \\ V_N \end{bmatrix}. \tag{4.1}$$

The diagonal elements C_{ii} are the per-unit-length self-capacitances of the ith line, while the elements C_{ij} with $i \neq j$ are the per-unit-length capacitance between the i^{th} and the jth line. Similarly, the entries of $\mathbf{L}$ relate the total per-unit-length magnetic flux Ψ_i around ith line to all the line currents producing it by $\mathbf{\Psi} = \mathbf{LI}$.

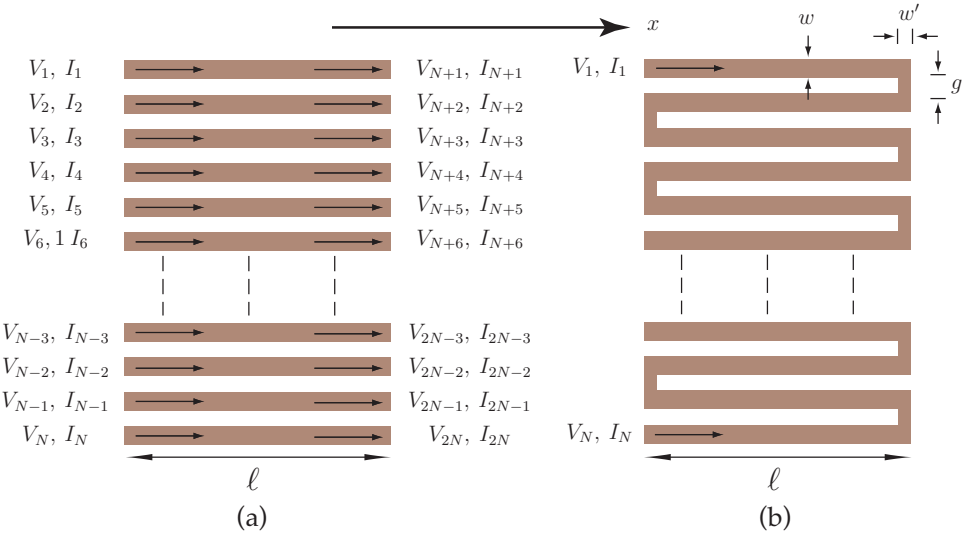

Figure 4.1 Commensurate (uniform-length) coupled-line network. a) $2N-$port structure. b) 2-port structure obtained by interconnecting all adjacent lines except at the 1^{st} and N^{th} ports.

The matrices $\mathbf{C}$ and $\mathbf{L}$ may be determined as static transverse field solutions for perfect line conductors, using in general an approximate numerical method. The corresponding Method of Moments (MoM) approach is outlined in the Appendix E. Furthermore, closed-form analytical expressions for stripline configurations, which will be used for group delay synthesis in Sec. 4.2, are also provided in this appendix.

Once the $\mathbf{C}$ and the $\mathbf{L}$ matrices have been determined for a given N-coupled-lines configuration, the generalized telegrapher's equations, which completely determine

the behavior of the structure, can be obtained assuming TEM wave propagation along the structure. These equations take the form [72]

$$\frac{\partial \mathbf{V}(x)}{\partial x} = -j\omega \mathbf{L}\mathbf{I}(x) \tag{4.2a}$$

$$\frac{\partial \mathbf{I}(x)}{\partial x} = -j\omega \mathbf{C}\mathbf{V}(x) \tag{4.2b}$$

$$\boldsymbol{\eta} = \frac{1}{\sqrt{\varepsilon_r \varepsilon_0 \mu_0}}\mathbf{C} \quad \text{and} \quad \boldsymbol{\xi} = \frac{1}{\sqrt{\varepsilon_r \varepsilon_0 \mu_0}}\mathbf{L} \tag{4.2c}$$

where $\mathbf{V}(x) = [V_1(x)\ V_2(x)\ ...\ V_n(x)]^t$, $\mathbf{I}(x) = [I_1(x)\ I_2(x)\ ...\ I_n(x)]^t$, ε_r is the relative permittivity of the stripline substrate and $\boldsymbol{\eta}$ and $\boldsymbol{\xi}$ are the characteristic admittance and impedance matrices, respectively, of the lines. Applying the boundary conditions $\mathbf{V}(x) = \mathbf{V}(0)$ at $x = 0$ and $\mathbf{V}(x) = \mathbf{V}(\ell)$ at $x = \ell$ in Eqs. (4.2) yields, assuming a lossless structure,

$$\mathbf{V}(\ell) = \mathbf{V}(0)\cos(\beta\ell) - j\boldsymbol{\xi}\mathbf{I}(0)\sin(\beta\ell) \tag{4.3a}$$

$$\mathbf{I}(\ell) = \mathbf{I}(0)\cos(\beta\ell) - j\boldsymbol{\eta}\mathbf{V}(0)\sin(\beta\ell) \tag{4.3b}$$

$$\gamma = \pm j\beta = \pm j\omega\sqrt{\varepsilon_{eff}\mu} \tag{4.3c}$$

Inverting the first two equations of (4.3) yields the following $ABCD$ matrix relation

$$\begin{bmatrix} \mathbf{V}(0) \\ \mathbf{I}(0) \end{bmatrix} = \begin{bmatrix} \mathbf{A} & \mathbf{B} \\ \mathbf{C} & \mathbf{D} \end{bmatrix} \begin{bmatrix} \mathbf{V}(\ell) \\ \mathbf{I}(\ell) \end{bmatrix}, \tag{4.4a}$$

$$\text{with} \quad \begin{bmatrix} \mathbf{A} & \mathbf{B} \\ \mathbf{C} & \mathbf{D} \end{bmatrix} = \begin{bmatrix} \cos(\beta\ell)\mathbf{U_N} & j\boldsymbol{\xi}\sin(\beta\ell) \\ j\boldsymbol{\eta}\sin(\beta\ell) & \cos(\beta\ell)\mathbf{U_N} \end{bmatrix} \tag{4.4b}$$

where $\mathbf{U_N}$ is the $N \times N$ identity matrix. The N transmission line network can then be analyzed as a $2N$-port network using (4.4), from which other network matrices can readily be derived using standard transformations. The corresponding scattering matrix, which will be used in the sections evaluating the group delay response of the

network, is

$$\mathbf{S}^{(2N)} = \begin{bmatrix} \mathbf{S_{11}} & \mathbf{S_{12}} \\ \mathbf{S_{21}} & \mathbf{S_{22}} \end{bmatrix}, \tag{4.5a}$$

$$= \begin{bmatrix} (\mathbf{A} + \mathbf{B}/Z_0 - \mathbf{C}Z_0 - \mathbf{D})\Delta^{-1} & 2(\mathbf{AD} - \mathbf{BC})\Delta^{-1} \\ 2\mathbf{U_N}\mathbf{\Delta^{-1}} & (-\mathbf{A} + \mathbf{B}/Z_0 - \mathbf{C}Z_0 - \mathbf{D})\Delta^{-1} \end{bmatrix} \tag{4.5b}$$

where $\Delta = (\mathbf{A} + \mathbf{B}/Z_0 + \mathbf{C}Z_0 + \mathbf{D})$, Δ^{-1} denotes the inverse of a matrix Δ and Z_0 is the reference impedance common to all the ports (assumed 50 Ω throughout this paper).

4.1.2 Transformation into a 2-Port All-Pass Network

As described in Chapter 3, a 4-port coupled-line pair consisting of 2 lines can be transformed into an all-pass network by connecting the ends of two lines, which converts it into a 2-port network. Similarly, the $2N$-port transmission line network of Fig. 4.1(a) can be converted into an all-pass 2-port network by interconnecting adjacent lines except at the 1^{st} and N^{th} ports, as shown in Fig. 4.1(b). This is achieved via (4.5), where the shorting sections are modeled by small transmission line sections of width w' and length g [66], following the procedure described in the Appendix F. Once the 2-port scattering matrix has been obtained, the group delay $\tau(\omega)$ is computed by

$$\tau(\omega) = -\frac{d\phi_{S_{21}^{(2)}}(\omega)}{d\omega} \tag{4.6}$$

where $\phi_{S_{21}^{(2)}}$ is the unwrapped transmission phase of the 2-port network with phase origin at $\omega = 0$.

4.2 Group Delay Design using Non-Commensurate Transmission Line Networks

This section extends the multiconductor transmission line analysis applied to equal-length (ℓ) transmission lines (or a commensurate or uniform network) in Sec. 4.1 to non-commensurate transmission lines (or a non-uniform network). Following the

principles described in Chapter 3, this allows to engineer desired group delay responses. The design is performed here using genetic algorithms and is verified experimentally for several responses.

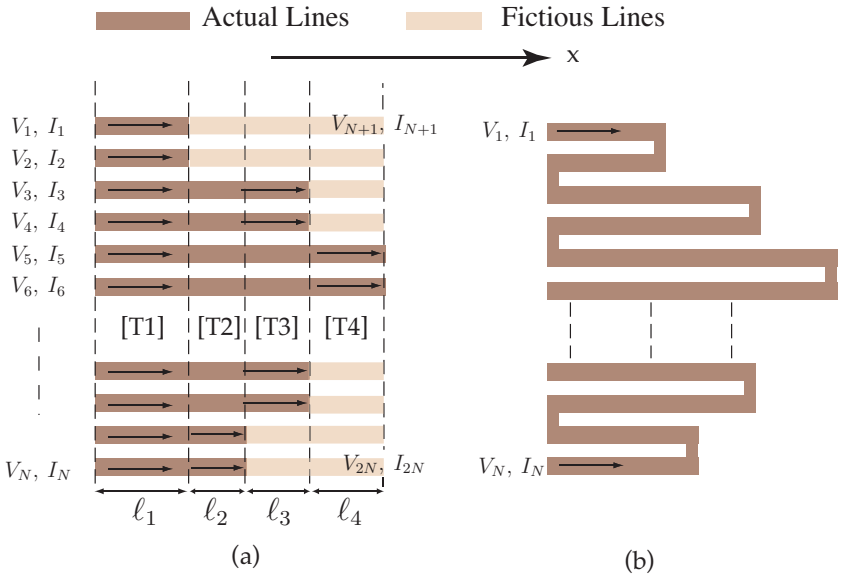

Figure 4.2 Non-commensurate coupled-line network. a) $2N-$port structure. b) 2-port structure obtained as in Fig. 4.1 from a).

4.2.1 Derivation of the 2-Port Scattering Matrix of the All-Pass Network

A generic non-commensurate transmission line network of N lines is shown in Fig. 4.2(a), where the $N/2$ line pairs may have different lengths. The new task is to obtain the scattering matrix of such a configuration, analogous to that obtained in (4.5) for the commensurate network. This structure of Fig. 4.2(a) can be considered as a longitudinal (x direction) cascade of commensurate networks of different lengths ℓ_i. The $2N$-port wave-transmission matrix $\mathbf{T}_i^{(2N)}$ of the i^{th} commensurate section may be obtained by standard transformation of the S-matrix of (4.5) [73]

$$\mathbf{T}_i^{(2N)} = \begin{bmatrix} \mathbf{T}_{11} & \mathbf{T}_{12} \\ \mathbf{T}_{21} & \mathbf{T}_{22} \end{bmatrix} = \begin{bmatrix} \mathbf{S}_{21} - \mathbf{S}_{22}\mathbf{S}_{12}^{-1}\mathbf{S}_{11} & \mathbf{S}_{22}\mathbf{S}_{12}^{-1} \\ -\mathbf{S}_{12}^{-1}\mathbf{S}_{11} & \mathbf{S}_{12}^{-1} \end{bmatrix}. \tag{4.7}$$

In general, the transfer matrices of the different commensurate sections, $\mathbf{T}_i^{(2N)}$, have dimensions which differ from $N \times N$. Therefore, the individual wave-transmission matrices cannot be simply cascaded due to incompatible dimensions. The matrices with dimensions less than $N \times N$ are therefore forced to become $N \times N$ matrices by the introduction of fictious transmission lines of zero length with perfect amplitude transmittance (i.e. $S_{21} = 1$ and $S_{11} = 0$) and no couplings between adjacent lines, as shown in Fig. 4.2(a).

The wave transmission matrix of the overall $2N$-port network $\mathbf{T}^{(2N)}$ is next obtained by cascading the individual transmission matrices $\mathbf{T}_i^{(2N)}$ as

$$\mathbf{T}^{(2N)} = [\mathbf{T}_K] \; ... \; [\mathbf{T}_i] \; ... \; [\mathbf{T}_3][\mathbf{T}_2][\mathbf{T}_1], \tag{4.8}$$

where K is the total number of commensurate subsections in the structure. The $2N$-port scattering matrix of the overall non-commensurate network is then obtained by the reverse transformation [73]

$$\mathbf{S}^{(2N)} = \begin{bmatrix} \mathbf{S}_{11} & \mathbf{S}_{12} \\ \mathbf{S}_{21} & \mathbf{S}_{22} \end{bmatrix} = \begin{bmatrix} \mathbf{T}_{22}^{-1}\mathbf{T}_{21} & \mathbf{T}_{22}^{-1} \\ \mathbf{T}_{11} - \mathbf{T}_{12}\mathbf{T}_{22}^{-1}\mathbf{T}_{21} & \mathbf{T}_{12}\mathbf{T}_{22}^{-1} \end{bmatrix}. \tag{4.9}$$

Finally, the $2N$-port configuration of Fig. 4.2(a) is transformed into the 2-port all-pass network of Fig. 4.2(b) by introducing the connections indicated in the figure. The final 2-port scattering matrix $\mathbf{S}^{(2)}$ is obtained from $2N$-port scattering parameters $\mathbf{S}^{(2N)}$ as

$$\Rightarrow \mathbf{S}^{(2)} = \begin{bmatrix} S_{11} & S_{12} \\ S_{21} & S_{22} \end{bmatrix} = \mathbf{S_1} + \mathbf{S_2}(\mathbf{S_5} - \mathbf{S_4})^{-1}\mathbf{S_3}. \tag{4.10}$$

which is derived in the Appendix F along with the matrices $\mathbf{S}_1$ to $\mathbf{S}_5$, which are not repeated here.

To confirm the validity of the proposed approach, the scattering matrix and the group delay response of both a commensurate and a non-commensurate coupled-

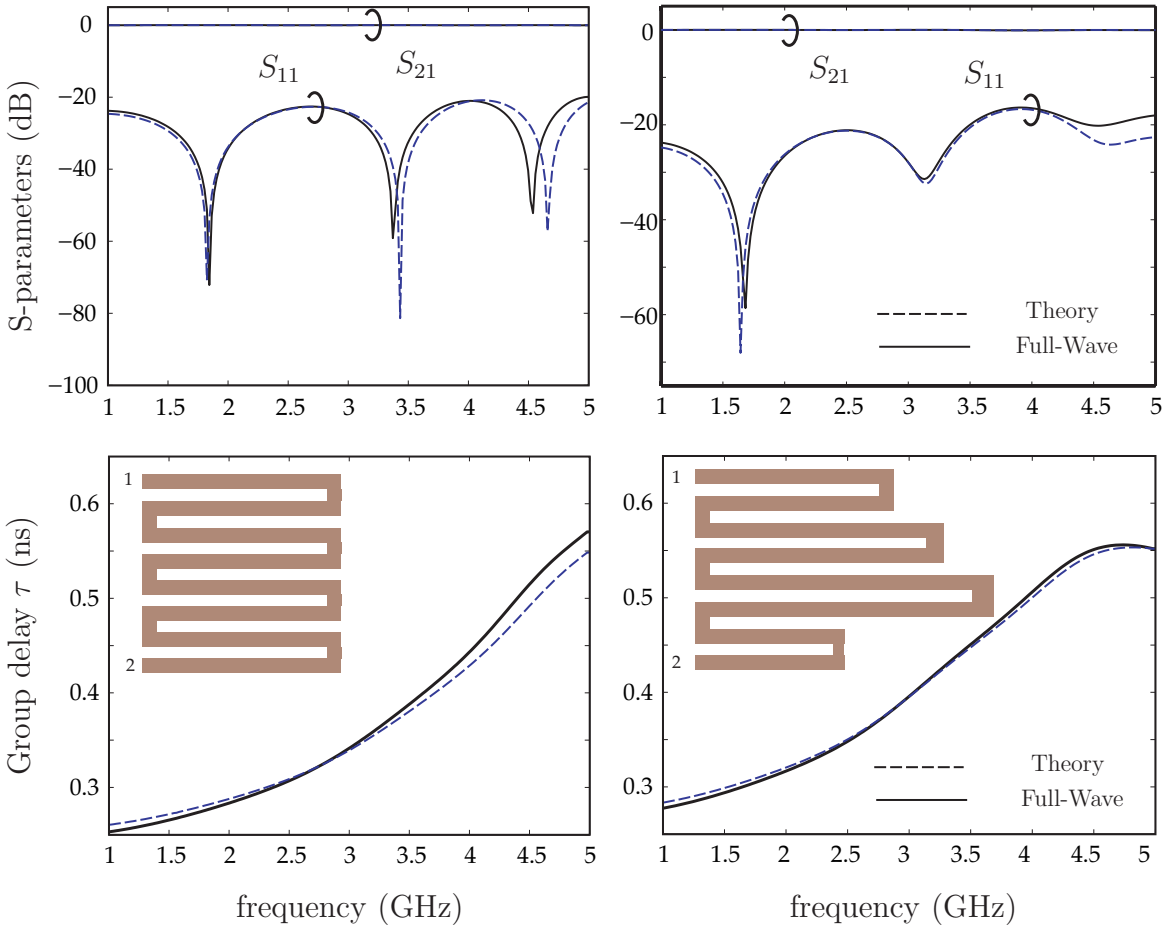

Figure 4.3 Comparison of the S-parameters and group delay obtained by theory using [(F.6) and (4.6)] and by full-wave simulation (Ansoft Designer) for stripline configurations. a) Commensurate coupled-line network. b) Non-commensurate coupled-line network using randomly chosen section lenghts. The structural parameters are: linewidth $w = 16$ mils, gap width $g = 16$ mils, $\varepsilon_r = 6.15$ and substrate thickness $h = 50$ mils.

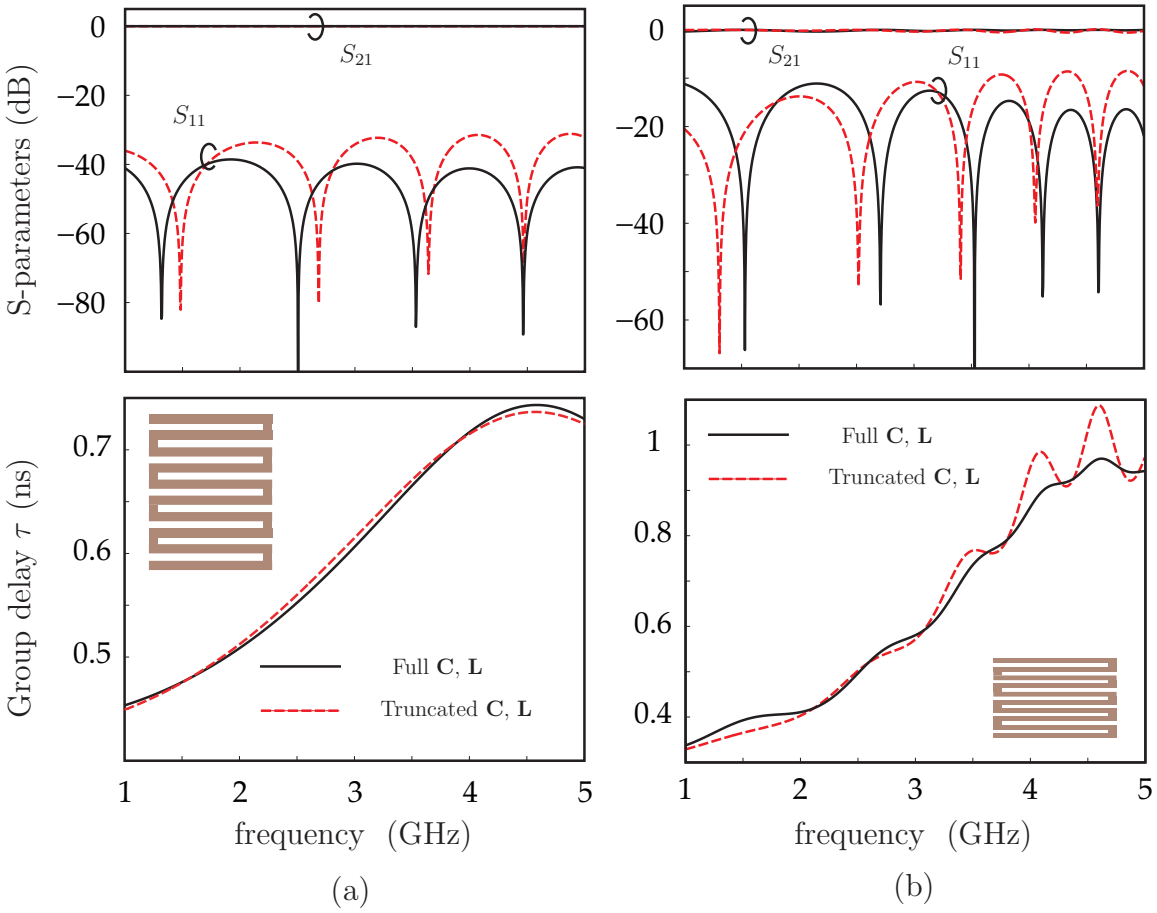

Figure 4.4 Effect of couplings between non-adjacent transmission lines on the S-parameter and group delay responses, shown here for the case of stripline commensurate all-pass networks. a) Weak coupling associated with large line and gap widths ($w = g = 16$ mils, $\varepsilon_r = 6.15$, $h = 50$ mils) b) Tighter coupling associated with smaller (half) line and gap widths ($w = g = 8$ mils, $\varepsilon_r = 6.15$, substrate thickness $h = 50$ mils and $w' = 9$ mils).

line all-pass networks, in stripline configurations, are compared with full-wave results in Fig. 4.3. Excellent agreement is found for the two cases, which validates the theoretical approach. The minor discrepancies observed in S_{11} at higher frequencies are may be attributed to inaccuracies of the theoretical results not taking into account corner discontinuities and subsequent small diffraction effects.

Since coupling is generally very low (typically less than 10-dB) in edge-coupled couplers [74], i.e. between adjacent transmission lines, it is expected that the capacitive and inductive coupling between the non-adjacent lines of the coupled-line networks of Figs. 4.1 and 4.2 should be negligible. In order to both confirm this expectation and quantify the minor effects of non-adjacent coupling, Fig. 4.4 compares the results obtained by using complete capacitance matrix $\mathbf{C}$ of (4.1) and complete corresponding inductance matrix $\mathbf{L}$ and by setting to zero all the coupling elements between the non-adjacent lines in this matrices. Fig. 4.4(a) confirms that the effects of coupling between non-adjacent lines are minor: the group delay response and S_{21} responses are almost undistinguishable between the two cases when the line and gap widths are relatively large, in the order of the dimensions used throughout this paper; these effects become naturally more apparent for smaller line and gap widths, as seen in Fig. 4.4(b). Nevertheless, the complete multiconductor approach used here proves useful to accurately model the low magnitude levels of S_{11} for optimal matching, as seen by comparing Figs. 4.3 (good accuracy even in S_{11}) and 4.4 (acceptable accuracy in S_{21} but poor accuracy in S_{11}). It should be noted that the situation may be different in the case of complex vertical structures using combinations of edge-coupled and broad-side coupled sections, where non-adjacent coupling effects may play a significant role. This problem will be investigated separately and reported elsewhere.

4.2.2 Genetic Algorithm Design

The commensurate coupled-line network of Fig. 4.1 exhibits a fixed group delay response of the type similar to that of a C-section, depending on the length ℓ and coupling factor k, as discussed in Chapter 2. However, flexibility in the group delay design can be introduced by allowing the different transmission line C-sections in the all-pass network, thereby making the network non-commensurate, to exhibit different lengths ℓ_i, as shown in Fig. 4.2 and illustrated in Fig. 4.3(b) for a random choice of

the lengths. In fact, by varying the lengths of the different C-sections, quasi-arbitrary group delay responses – such as linear non-constant, gaussian or quadratic responses – may be achieved with the non-commensurate all-pass network of Fig. 4.2(b).

To the authors' knowledge, no closed-form solutions are available for the design of group delay in a non-commensurate all-pass network. Therefore, a computer design approach is required to determine the structural parameters of the individual C-sections to realize a desired group delay response. Since the solution set is a priori unknown and may be potentially relatively complex, an efficient global optimization technique is required. *Genetic algorithms* (GAs) are a convenient approach to solve such global optimization problems, where the fitness landscape is complex, discontinuous, noisy, variant in time or exhibits several local optima [75]. They provide a quick scan of a vast solution set, particularly suitable for large-space problems where testing of all possible solutions in serial fashion would be too time consuming. However, a drawback of GAs is that they do not necessarily guarantee convergence to the optimal solution. Thus, the non-commensurate all-pass networks presented below are not necessarily optimal, although they essentially meet the design specifications.

A GA is now applied to the non-commensurate coupled-line network of Fig. 4.2 for group delay design. This is done with the Genetic Algorithm and Direct Search Toolbox from Matlab [76], with two sets of variables to be determined: $\{N_k\}$ and $\{\ell_k\}$, $(k = 1 \ldots M)$, where $\{N_k\}$ represents the set of number of C-sections corresponding to the lengths of the set $\{\ell_k\}$. In the following designs, the width w of the lines, the width w' of the end connecting transmission line sections, the gap g between them, the substrate thickness h and the substrate permittivity ε_r are assumed to be fixed, and w, w' and g are equal for all the lines. These parameters may also be varied, at little computational expense, but this was not found necessary. The parameter sets $\{N_k\}$ and $\{\ell_k\}$ are determined by minimizing the fitness function E, defined as

$$E = \sum_{n=1}^{n_f} |\tau(\omega_n) - \tau_d(\omega_n)|^2, \tag{4.11}$$

where $\tau(\omega)$ is iterative group delay computed by (4.6) and $\tau_d(\omega)$ is the target group delay function. Fig. 4.5 outlines the complete GA-based design procedure.

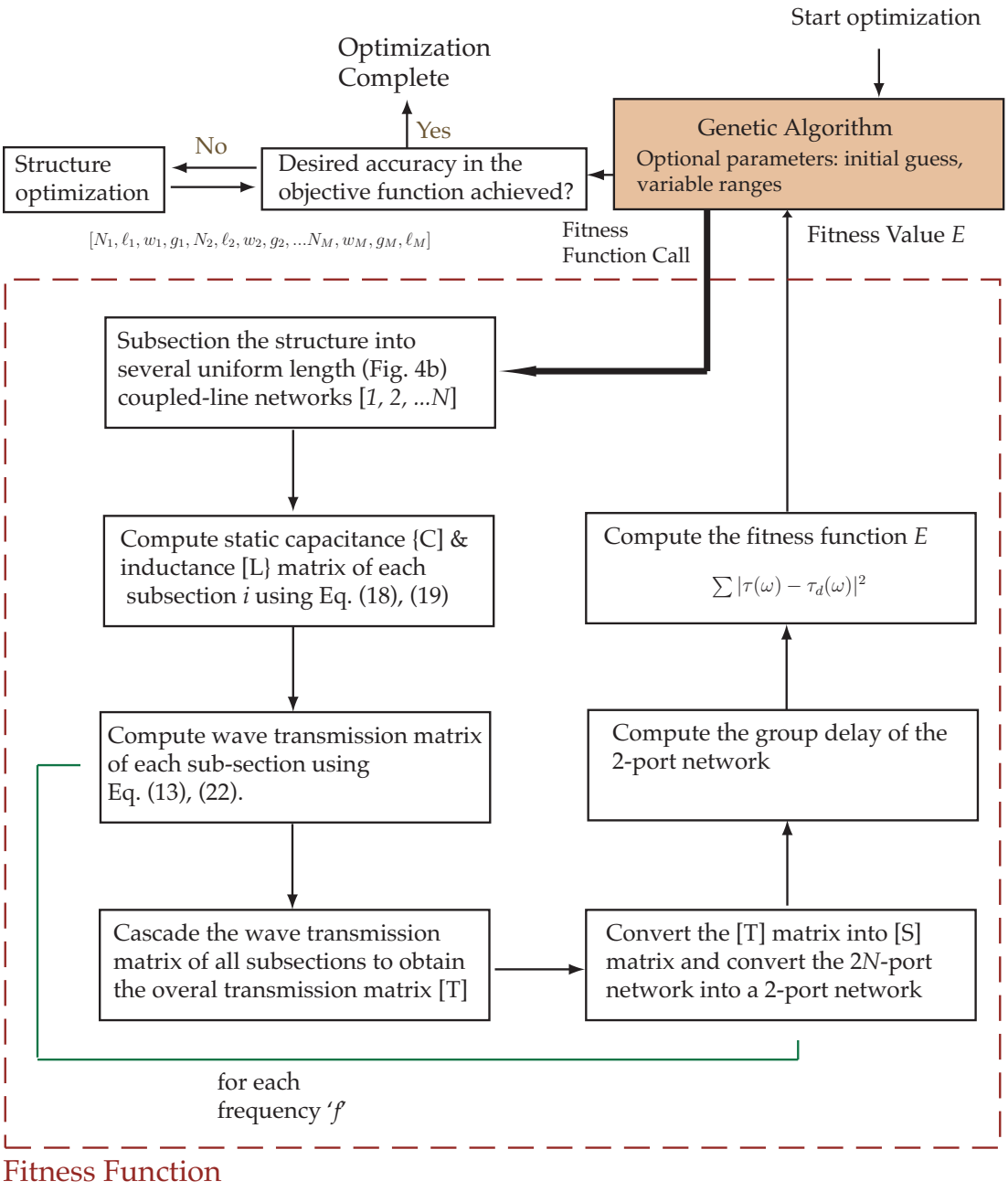

Figure 4.5 Genetic algorithm (GA) based design procedure.

4.2.3 Analytical and Experimental Results

The analytical results for the target group delay responses listed in Tab. 4.1 and with the parameters $w = 16$ mil, $w' = 9$ mil, $g = 16$ mil, $h = 50$ mil and $\varepsilon_r = 6.15$ are plotted in Fig. 4.6 for stripline configurations. The chosen line gap and line width corresponds to a coupling level of -16.8 dB. Fig. 4.6(b)-(e) show the structures obtained and while Fig. 4.6(a) shows the group delay response of a simple commensurate structure for reference. Excellent agreement is observed between the target group delay functions and the corresponding group delays of the non-commensurate all-pass network structures. Moreover, acceptable matching ($S_{11} < -20$ dB) is achieved in all the cases.

Table 4.1 Target Group Delay responses.

Group delay type	Group delay function and Parameters
Gaussian	$\tau_d(\omega) = \tau_1 + (\tau_2 - \tau_1)\exp^{-0.5\left(\frac{\omega-\omega_0}{\Delta\omega}\right)^2}$ $(\tau_2 - \tau_1) = 0.5$ ns, $\omega_0 = 2\pi(5)$ GHz, $\Delta\omega = 2\pi(1.55)$ GHz
Linear non-constant	$\tau_d(\omega) = \frac{\tau_2-\tau_1}{\omega_2-\omega_1}(\omega - \omega_1) + \tau_1$ $(\tau_2 - \tau_1) = 0.5$ ns and 1.0 ns
Quadratic	$\tau_d(\omega) = \frac{\tau_2-\tau 1}{\omega_2-\omega_1}(\omega - \omega_1) + \tau_1 + k(\omega - \omega_1)(\omega - \omega_2)$ $k = 0.25 \times 10^{-28}$ and $(\tau_2 - \tau_1) = 0.55$ ns

($\omega_1 = 2\pi(1)$ GHz, $\omega_2 = 2\pi(5)$ GHz and $\tau_1 = \min[\tau(\omega)]$ for all cases.)

The group delay profiles in Fig. 4.6 all exhibit a positive slope. In this case, the distributed nature of the non-commensurate lines benefits the compactness of the structure, whereas it may prohibit the realization of negative slope group delay profiles, as a consequence of the fact that C-sections exhibit maximal delay at all odd harmonics of ω_0, i.e. at $\ell = \ell_m = (2m + 1)\lambda_g/4$. This is illustrated in Fig. 4.7. Fig. 4.7(a) shows a positive slope scenario, with $\omega_2 = 3\omega_1$, where the third harmonic of the longer C-section strongly contributes to the delay at ω_2, thereby reducing the number of required shorter C-sections. Fig. 4.7(b) shows a negative slope scenario, also with $\omega_2 = 3\omega_1$, which cannot be realized with the proposed network, since the

larger C-section imposes the same delay at ω_2 as at ω_1, which adds to the delay provided there by the shorter C-section. Fig. 4.7(c) shows negative slope scenario, this time with $\omega_2 = 2\omega_1$, which can be realized by the proposed network if the third harmonic of the longer C-section falls above the frequency range of interest. However, this realization is inherently restricted to a smaller frequency range as compared to what can be achieved in the positive slope case of Fig. 4.7(a). The harmonic issue illustrated in Fig. 4.7(b) may be solved either by using a combinations of distributed transmission line C-sections for the shorter sections and lumped (chip) element equalizers for the longer sections, or by using the technique of mixer inversion [41].

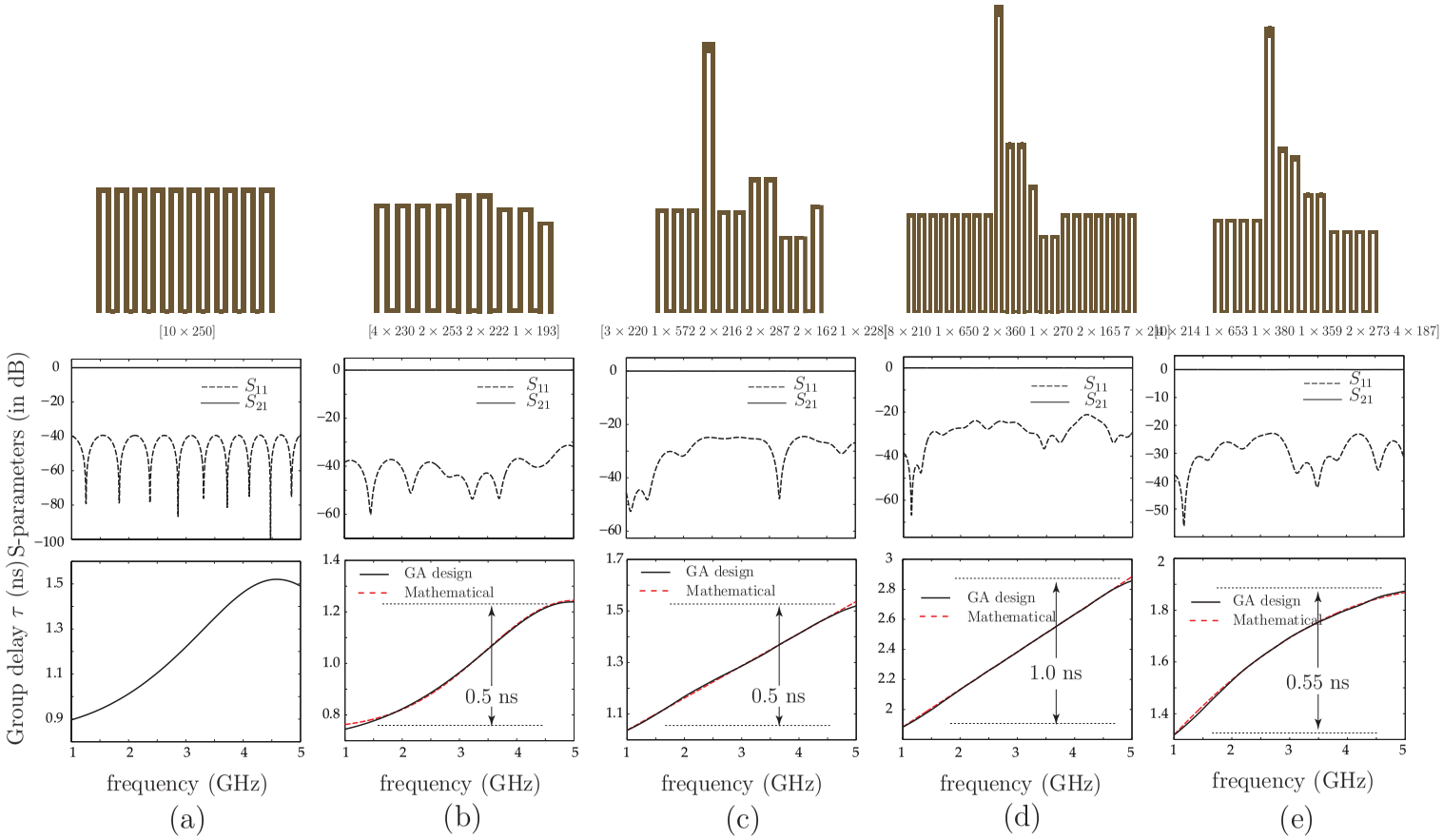

Figure 4.6 Various group delays responses corresponding to the target responses of Tab. 4.1 and obtained by genetic algorithm design (without any dielectric and conductor losses). a) Intrinsic response of the commensurate network. b) Gaussian group delay. c) Linear group delay with a slope of 0.125 ns/GHz. d) Linear group delay with a slope of 0.25 ns/GHz. e) Quadratic group delay.

It may be observed that the commensurate structure of Fig. 4.6(a) exhibits a fairly regular return loss pattern versus frequency across the whole operation bandwidth, somewhat like a transmission line except for slightly different distances between attenuation zeros due to dispersion. As the structure deviates from the commensurate configuration, and its group delay subsequently deviates from that of this configuration, as in Fig. 4.6(b-e), the return loss pattern loses its regularity in terms of frequency. The higher the degree of "commensurateness," the lower the degree of regularity is. This demonstrates the capability of non-commensurate all-pass network for group delay engineering and the appropriateness and accuracy of the proposed multiconductor transmission line analysis and GA design approach.

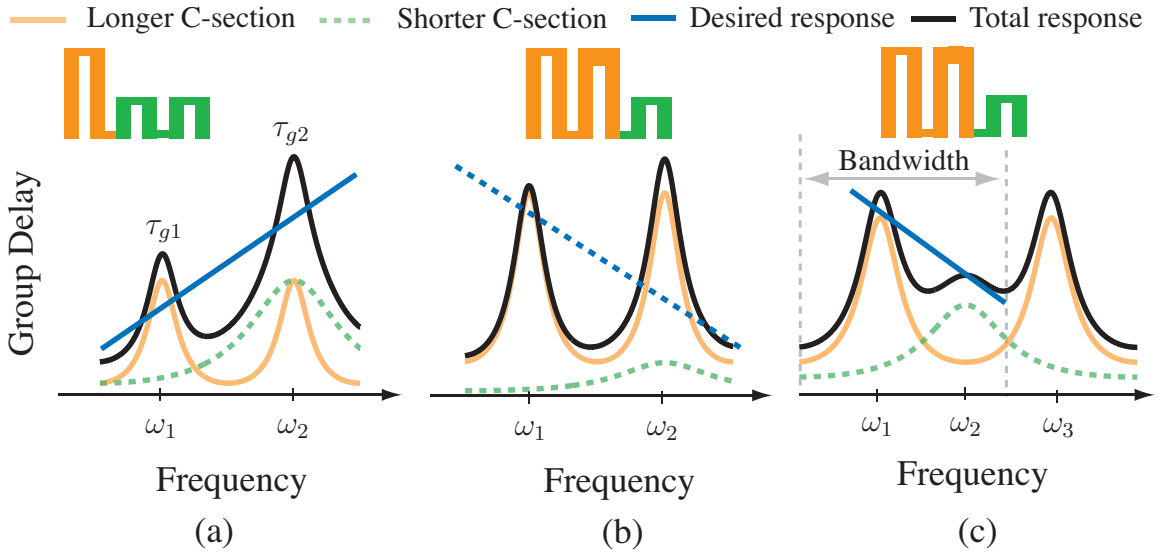

Figure 4.7 Illustration of the problematic of harmonics for the realizations of the negative-slope group delays with the specification: $\tau_g(\omega_1) = \tau_{g1}$ and $\tau_g(\omega_2) = \tau_{g2}$. a) Positive group delay scenario with $\omega_2 = 3\omega_1$. b) Negative group delay scenario with $\omega_2 = 3\omega_1$, which is unrealizable. c) Negative group delay scenario with $\omega_2 = 2\omega_1$, where $\omega_3 = 3\omega_1$ does not fall within the frequency range of interest.

Fig. 4.8 shows the measurement results for the fabricated non-commensurate all-pass network stripline prototypes corresponding to the structures of Figs. 4.6(b)-(e). The photogrpah of one of the prototypes, namely the one of Fig. 4.6(d) is shown in Fig. 4.9. The prototypes are shown in the insets of Fig. 4.8(a)-(d). The non-

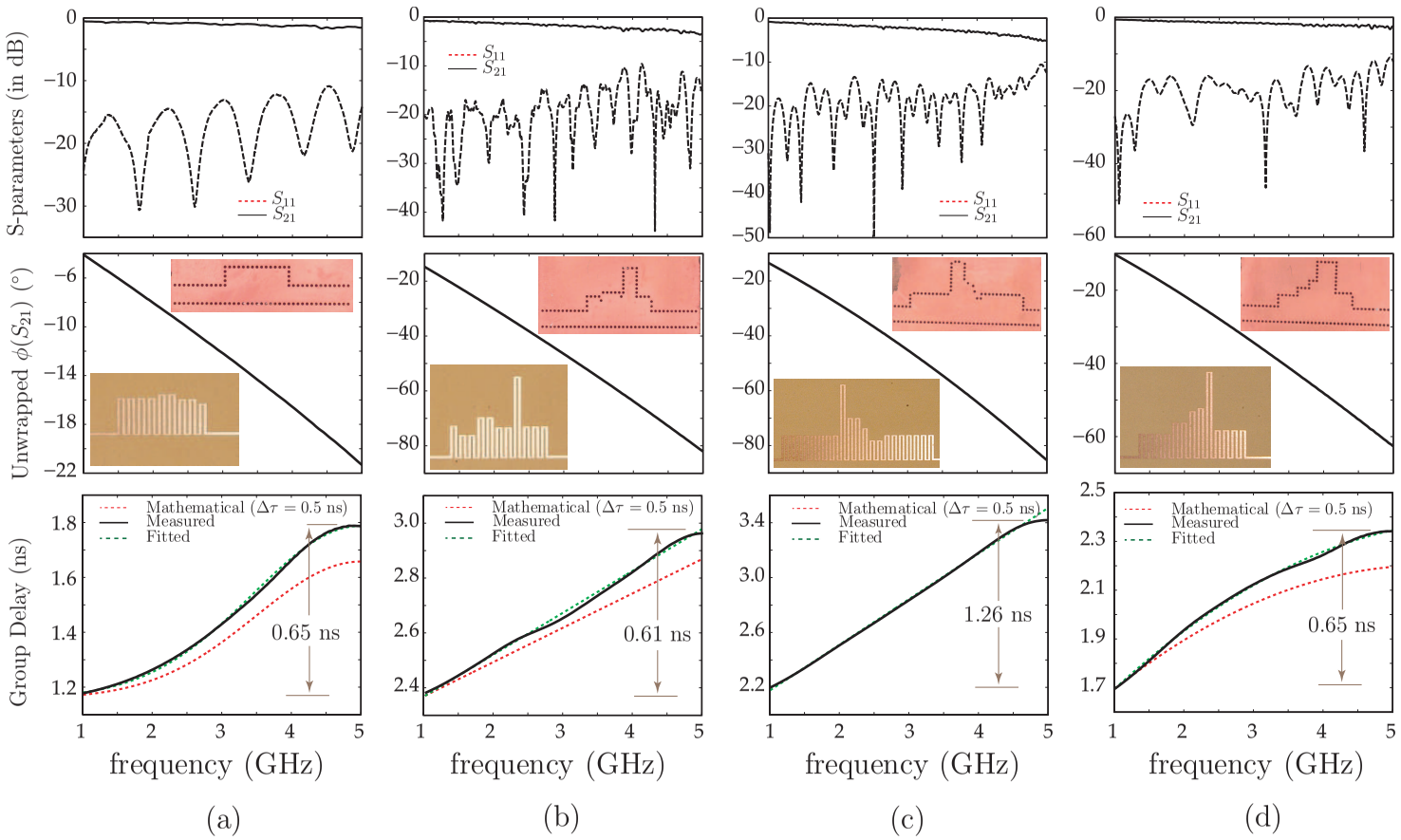

Figure 4.8 Experimental group delay responses of the prototypes. The group delay smoothing option of the vector network analyzer was used here to obtain a slope that can be clearly measured and compared with the ideal design. a) Gaussian group delay. b) Linear group delay with a slope of 0.15 ns/GHz. c) Linear group delay with a slope of 0.32 ns/GHz. d) Quadratic group delay.

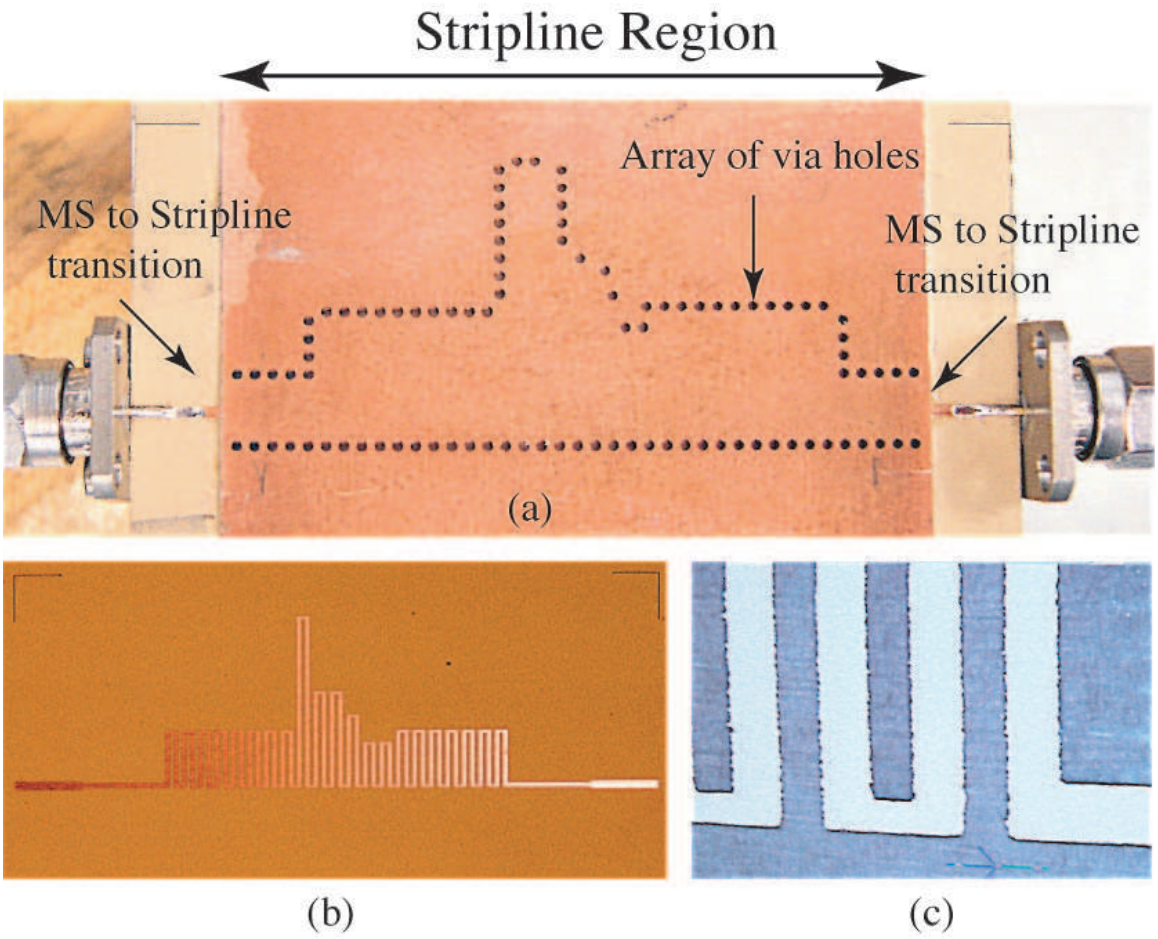

Figure 4.9 Photographs of fabricated Prototype. a) Overall view showing the array of via holes and microstrip-stripline transitions. b) Internal view of the printed C-section trace. c) Zoom of a small region of the C-section trace illustrating the etching inaccuracies of the strips.

commensurate strip structures are sandwiched between two dielectric layers (Rogers Duroid 3006, 25 mil of thickness) and closely spaced via holes are placed along the contours of these structures to provide proper connection between the two stripline ground planes and to avoid spurious radiation and resonances. The prototypes include a microstrip-to-stripline transition (not shown in the figure). The experimental results may be compared to the analytical results of Fig. 4.6. All the prototypes exhibit a perfectly smooth transmission phase response resulting in a smooth group delay profile. The various targeted group delay profiles (gaussian, linear and quadratic) are successfully achieved with reasonable insertion and return losses (RL < -10 dB and IL < 4 dB in all cases). However, discrepancies are observed between the experimental results and theoretical predictions. First, the experimental group delay swing exceeds the design group delay (following the specifications of Tab. I, based on MoM results without conductor and dielectric losses) by 20% to 30%. Second, the experimental insertion loss is higher by 1-2 dB than that predicted by full-wave simulations (not shown here), especially toward higher frequencies. In fact, the prototype is a complex multilayer structure. It includes a 5–22 μm thick (exact thickness unknown in the fabrication process used) lossy epoxy layer ($\tan\delta = 0.03$ and $\varepsilon_r = 3.5$) to hold the two substrates of the stripline structure together (not taken into account in above GA designs). Furthermore, the thickness of the metal strips (17 μm) is not negligible with respect to the epoxy layer (the metal thickness was set to zero in above GA designs), and may therefore have caused the formation of air gaps and slight substrate deformations. Thus, a significant level of uncertainty exists regarding the exact fabricated structure, and prevents its exact modeling.

In the mathematical and analytical (MoM) results of Figs. 4.6 and 4.8, several of the aforementioned detailed features of the fabricated prototype were not taken into account, namely the presence of the vias (with their exact locations), the adhesion epoxy layer, the strips copper thickness and the two microtrip-to-stripline transitions. To confirm that the observed discrepancies are due to these experimental parameters, one of the prototypes, which was arbitrarily chosen as the prototype of Fig. 4.8(c) [or 4.6(d)], was subjected to extensive full-wave analyses taking them all into account.

Fig. 4.10(a) shows the corresponding group delay response results. In these results, a significant increase in the group delay is observed over the bandwith of interest (1.2 ns) compared with the idealized theoretical model (1.0 ns). Various parametric simulations (not shown here) have revealed that the slight variation in the group delay

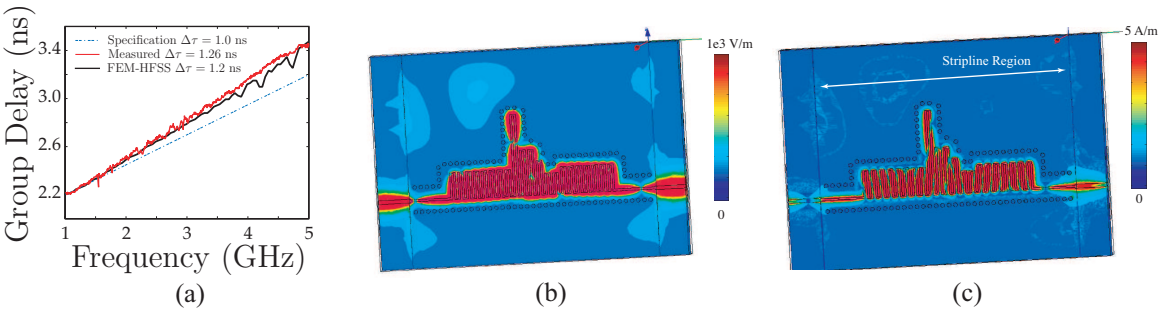

Figure 4.10 Full-wave (FEM-HFSS) and experimental results explaining the slight discrepancies observed in Fig. 4.8, specifically for the case Fig. 4.8(c), and clarifying the nature of loss in the structure. The simulation results take into account conductor and dielectric losses, the microstrip-to-stripline transitions, the 17 μm copper thickness, the 22 μm epoxy layer and the exact array of via holes of the prototype. (a) Group delay response. The measured result does not include any smoothing. b) Electric field distribution (magnitude) at 5 GHz. c) Magnetic field distribution (magnitude) at 5 GHz. The field distributions (both taken in the middle of the stripline structure) indicate that radiation losses are negligible.

swing was mostly due to the epoxy layer. This may be explained from the fact that the phase velocities of the even and odd modes of the coupled-line C-sections differ from each other due to the difference between the permittivities of the epoxy layer ($\varepsilon_r = 3.5$) and of the surrounding substrate ($\varepsilon_r = 6.15$), whereas these velocities are equal in the case of the homogeneous dielectric considered in the GA designs. Since the structure includes a large number of cascaded C-sections, these discrepancies add up along the structure and finally lead to a significant deviation of the group delay response compared to the original design. The large difference between measured and simulated data, shown in Fig. 9, was further investigated. The data of Fig. 4.10(a) compare measured data with a very detailed and time-consuming full wave simulation incorporating all of the details (epoxy, via location, etc.), on the network illustrated in Fig. 4.8(c). Given that the resulting difference between measured and full-wave-simulated results is only about 5% (1.26 ns measured versus 1.2 ns simulated) and considering that etching tolerance [as apparent in Fig. 4.9(c)] also contributes to deviations from the computed coupling values, especially for the low coupling levels considered here (−16.8 dB), it is asserted that the proposed theory is reasonably accurate and therefore is appropriate for the design of cascaded section networks

exhibiting a wide variety of group delay characteristics, i.e. group delay engineered networks. It is also evident that there is a room for improvement in implementation methods. Full-wave simulations further indicated (not shown here) that the presence of relatively lossy epoxy layer ($\tan\delta = 0.03$ as compared to $\tan\delta = 0.002$ of the surrounding substrate) also contributes to the extra insertion loss, which is essentially dissipative as they did not evidence any leakage between the vias or any other type of radiation, as shown by the electric and magnetic field distributions in Figs. 4.10(b) and (c). A high-quality, industrial-class fabrication process would naturally alleviate these issues.

As mentioned above, the group delay designs of Figs. 4.6 and 4.8 are not necessarily optimal. An ideal design would be the one achieving a maximum group delay swing $\times$ bandwidth product, $\Delta\tau\Delta f$, over the smallest footprint – which typically requires a small number N of C-sections and small strip widths w and gaps g – and with the lowest possible insertion and return losses. These requirements are clearly incompatible and trade-offs are subsequently necessary. In the designs of Figs. 4.6 and 4.8, all the strip widths and gap spacings were fixed to $w = g = 16$ mil in order to achieve a minimum insertion loss, which required for the specified group delay swings and bandwidths $N = 9$, 13, 21 and 13 C-sections for the designs of Fig. 4.8(a)-(d). According to extensive genetic algorithm tests with additional degrees of freedom (w and g in addition to N and the lengths ℓ_k of the C-sections), the number of C-sections can be dramatically reduced in all the cases. However, this is at the expense of higher insertion loss and poorer return loss. This issue may find good solutions in multilayer configurations with broadside-coupled (as opposed to edge-coupled) C-sections, where tight coupling is easily achieved and cross coupling between non-adjacent C-sections could become available.

4.3 Limitations

C-section all-pass networks provide a powerful way to realize arbitrary – within the limits of causality – group delay responses independent of the magnitude response. However, they suffer from size and loss limitations when achieving large dispersion, as typically required in practical applications. For example, the group delay swing (dispersion) required in radar systems is of the order of microseconds for MHz-bandwidth signals [7]. Similarly, instrumentation systems, such as real-time

Fourier transformers, demand a group delay swing in the order of tens of nanoseconds for few GHz-bandwidth signals [31].

Several approaches may be devised to achieve such amounts of dispersion with the transmission-line all-pass networks. The brute-force approach consists in cascading several all-pass networks until the required group delay swing is achieved. However, this leads to prohibitively large conductor and dielectric losses. Another approach is to decrease the spacing between the coupled lines, thereby increasing the coupling coefficient k, so as to increase total group delay swing $\Delta\tau$ following (3.36). In this case, either the maximum realizable coupling is limited by the lithography resolution in edge-coupled structures or the structure becomes complex to fabricate for the case of broadside coupled configuration. Alternatively, a signal re-injection loop configuration can be used where the output signal of the network is fed back multiple times to the input until the desired dispersion is achieved [77]. However, this configuration is complex, requiring active components, such as switches, and has difficulties to achieve a large number of signal turns due to noise accumulation, signal drift and loop resonances. Therefore, a pressing need exists for an efficient transmission-line all-pass configuration to mitigate the aforementioned issues.

4.4 Compact Multilayer Broadside-Coupled Configuration

As presented above, in [2], a simple, low-cost, wideband, flexible, and frequency-scalable, transmission-type non-commensurate coupled transmission line all-pass DDS was introduced and demonstrated to provide quasi-arbitrary group delay responses. However, due to its uniplanar edge-coupled configuration, this structure suffers of large size and limited group delay swing to frequency bandwidth ratios, which restricts the resolution of ASP devices. To overcome these two drawbacks, we present here a multilayer broadside-coupled implementation of this coupled transmission line based all-pass DDS.

4.4.1 Multilayer Broadside-Coupled DDS

Fig. 4.11(a) shows the stripline uniplanar edge-coupled DDS reported in [2]. Fundamentally, this structure consists of transversally cascaded C-section all-pass net-

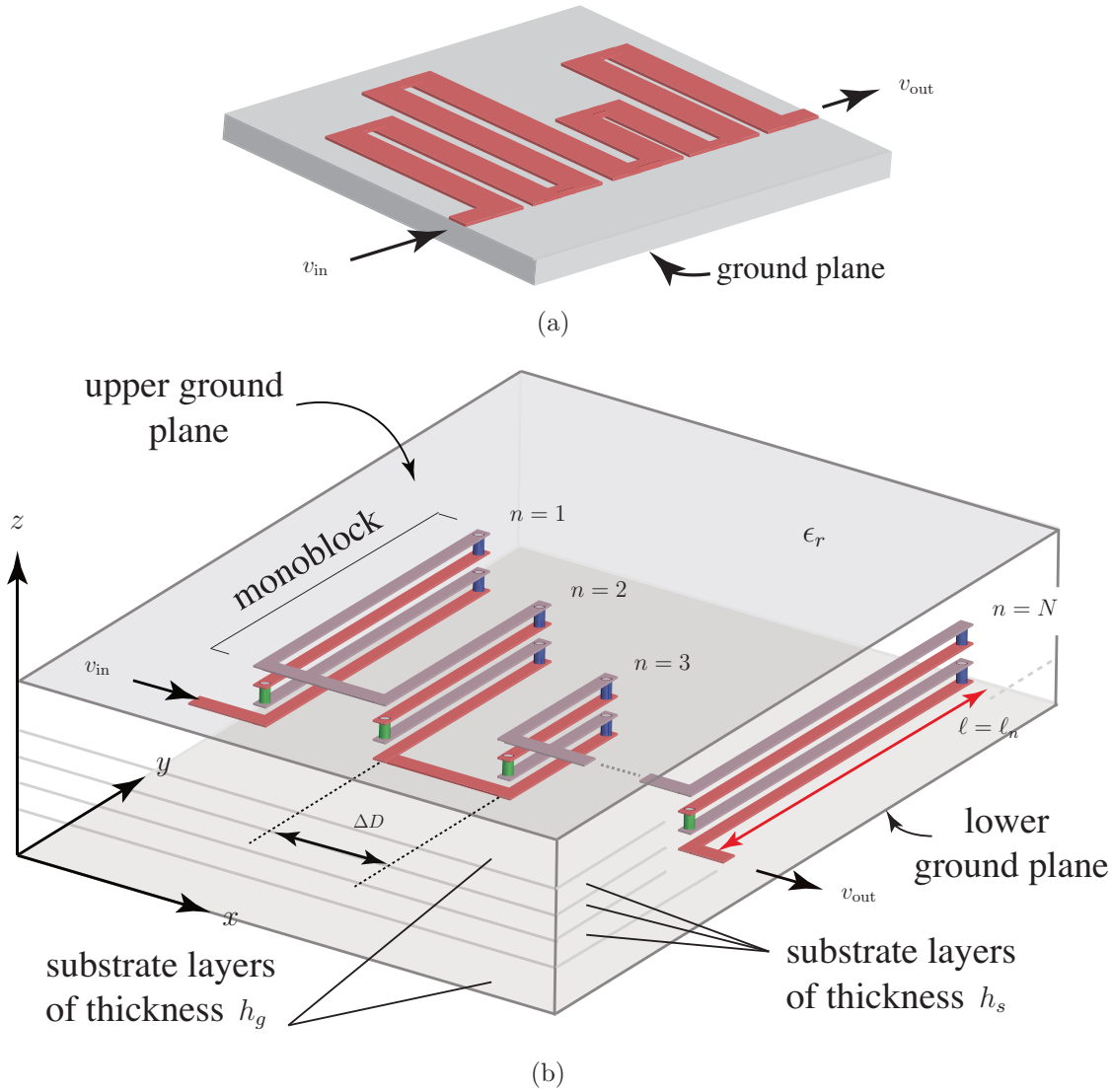

Figure 4.11 Coupled transmission line all-pass dispersive delay structures (DDS). a) Uniplanar edge-coupled DDS [2]. b) Proposed multilayer broadside-coupled DDS. In all the designs of the paper, there are total 5 substrate layers of identical permittivity $\epsilon_r = 5$ and each mono-block consists of 4 coupled strips of width w_i, where $i \in (1-4)$. The inter-block distance ΔD is fixed to 1.5 mm.

works (end-connected coupled transmission lines) of different lengths (non-commensurate structure), and can be designed to provide quasi-arbitrary group delay versus frequency responses [2]. The group delay swing, $\Delta\tau = (\tau_{\max} - \tau_{\min})$, in a single C-section depends on the voltage coefficient k between the two coupled-lines [2]. Specifically, $\Delta\tau \propto 2k/\sqrt{1-k^2}$. Consequently, due the weakness of the edge coupling mechanism (usually < 10 dB) the uniplanar design of Fig. 4.11(a) usually requires, large footprint structures with small ratio of group delay swing to frequency bandwidth, resulting in limited ASP resolution.

Fig. 4.11(b) shows the stripline multilayer broadside-coupled DDS proposed to increase the group delay swing to frequency bandwidth ratio in a compact footprint, as compared to its uniplanar counterpart. The proposed structure consists of N blocks of lengths, ℓ_n, $n = 1...N$, where each block includes several broadside-coupled end-connected strips to form the transversally cascaded C-section structures. Within each n^{th} block, all the strips are assumed here to be of the same length, ℓ_n. Furthermore, the N blocks are assumed to be sufficiently far apart so as to experience negligible coupling between each other. In contrast to the edge-coupled structure of Fig. 4.11(a), the proposed DDS features strong couplings between the different strips within each block, thereby increasing the group delay swing to frequency bandwidth ratio as required for enhanced ASP performances. In addition, the broadside implementation naturally leads to an efficient utilization of the vertical dimension [along the $z-$axis in Fig. 4.11(b)] resulting in compact miniaturized structures. In more sophisticated implementations, the blocks could be brought close to each other for adding inter-block coupling, which may further enhance the performances.

4.4.2 Multi-Block Non-Commensurate Implementation

In order to realize quasi-arbitrary responses within a given design bandwidth, a *non-commensurate* structure is required [2]. Such a structure is obtained by cascading several mono-blocks ($N > 1$) of different lengths resulting in quasi-arbitrary group delay responses (i.e. superposition of various group delay functions provided by mono-blocks with peak group delays τ_n centered at f_n).

Fig. 4.12 presents the full-wave and experimental performances of two multi-block non-commensurate multilayer broadside-coupled DDSs of Fig. 4.11(b) with a linear group delay response over a specified bandwidth, which is the group delay profile of

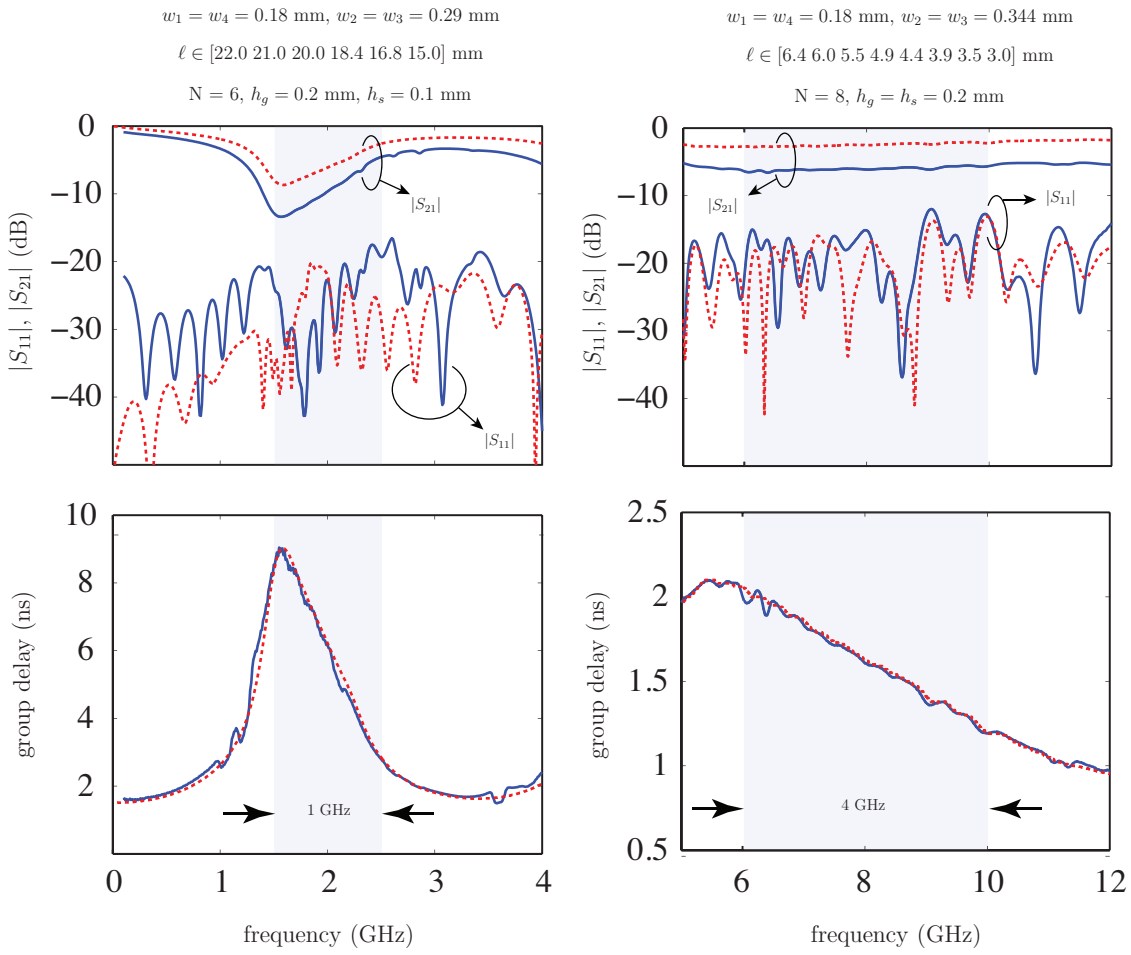

Figure 4.12 Simulated (dashed lines) and measured (solid lines) S-parameter amplitudes and group delays for two types of multilayer broadside-coupled DDSs with negative linear group delay slope. The strip widths in each DDS block are optimized using FEM-HFSS. (a) Narrowband DDS (b) Wideband DDS.

Table 4.2 Specification and Performance of Proposed Multilayer Broadside-Coupled Dispersive Delay Structures

	ϵ_r, $\tan\delta$	Δf	
Narrowband ML DDS, Fig. 4.12(a)	5.00, 0.001	1.6 - 2.6 GHz	6.58 ns/GHz
Wideband ML DDS, Fig. 4.12(b)	5.00, 0.001	6.0-10.0 GHz	0.215 ns/GHz
Wideband Uniplanar DDS, Fig. 4.13(b)	3.55, 0.002	6.0-10.0 GHz	0.225 ns/GHz

Unfolded ℓ	Size (w/o ports), mm^3	Insertion Loss
462.1 mm	$7.79 \times 22.3 \times 0.74$	-9.67 dB@ 2 GHz
165.7 mm	$6.74 \times 10.84 \times 1.04$	-6.15 dB@ 8 GHz
527.3 mm	$14.9 \times 34.6 \times 1.02$	-5.55 dB@ 8 GHz

the widest interest in practical applications [2][3][31]. Both structures are full-wave optimized designs to achieve the required transmission characteristics. The corresponding experimental prototypes, built in LTCC technology, are shown in Fig. 4.13. The prototypes were excited using a coplanar waveguide ports located on the top layer of the prototypes connecting the embedded signal layers using a 0.2 mm wide via.

The DDS of Figs. 4.12(a) is a relatively narrowband DDS, with a group delay swing to bandwidth ratio of 6.58 ns/GHz (i.e. 1.6-2.6 GHz). Such a ratio is typically appropriate for frequency discriminator and spectrum sniffer applications involving signals of few MHz of bandwidth [3]. The observed transmission magnitude imbalance is due to the frequency dependence of losses, which is here over-compensated by the negativeness of the group delay slope, where higher-frequencies, although suffering from higher loss, spend significantly less propagation time across the structure compared to lower frequencies. This effect can be compensated by using a magnitude-equalizing resistive network in series with the DDS [78].

The DDS of Figs. 4.12(b) is a relatively broadband DDS, with a group delay swing to bandwidth ratio of 1 ns/5 GHz = 0.2 ns/GHz (i.e. 6-11 GHz). Such a wideband response is most suited for real-time Fourier transforming applications for sub-nanosecond ultrashort pulsed signals [35][31]. It turns out that in this particular design, the negativeness of the group delay slope exactly compensates for the higher losses at higher frequencies, leading to a flat transmission response.

Tab. 4.2 summarizes the features and performances of the two multilayer DDSs

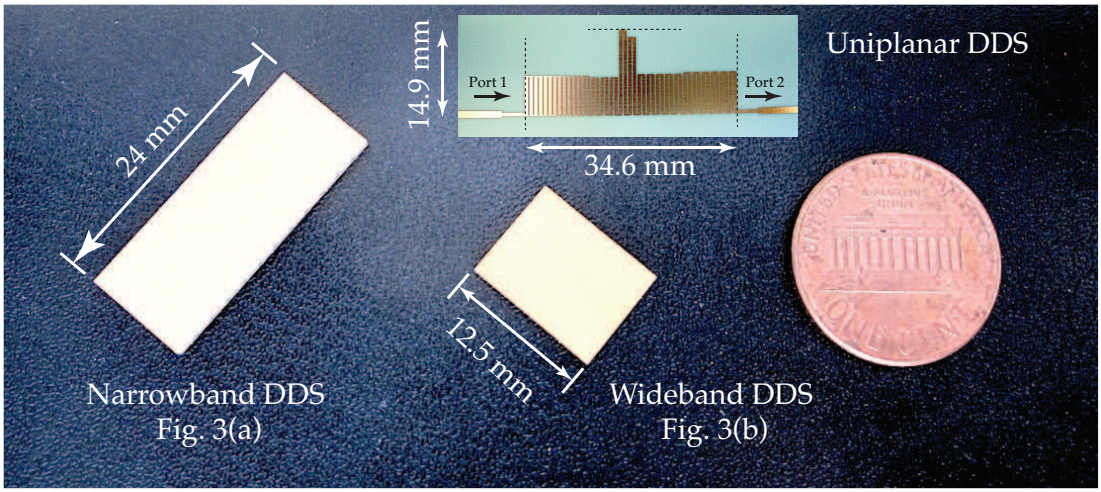

Figure 4.13 Narrowband and wideband DDS prototypes corresponding to Fig. 4.12(a) and 4.12(b). A wideband uni-planar DDS with similar specifications as compared to the wideband DDS of Fig. 4.12(b), for performance comparison is also shown in the inset. The substrate used in uniplanar DDS is Roger 4003C with $\epsilon_r = 3.55$.

of Fig. 4.12. In order to compare the performance of the proposed broadside coupled multilayer DDS, another uniplanar DDS was fabricated (top of Fig. 4.13) with bandwidth and group delay slope specifications similar to those of Fig. 4.12(b). The corresponding measured results are given in Tab. 4.2. It can be seen that for a similar group delay swing to frequency bandwidth ratio and comparable insertion losses, the proposed multilayer structure represents a footprint reduction of around 7. Thus, a successful miniaturization of the coupled-line DDS is achieved using the broadside-coupled multilayer architecture. Moreover, further miniaturization may be achieved by exploiting more intensively the free vertical dimension using LTCC technology.

4.5 Summary

A group delay engineered non-commensurate transmission line 2-port all-pass network for analog signal processing applications has been presented, along with an analytical modelling procedure and experimental demonstrations. Compared to the cascaded C-sections of Chapter 3, the proposed structure allows for inter-couplings between the various C-sections, leading to larger dispersion engineering possibilities. A

computer design approach based on genetic algorithms has been proposed to synthesize quasi-arbitrary group delay responses, i.e. to determine the structural parameters of the individual C-sections of the network. Edge-coupled stripline implementations have been demonstrated with gaussian, linear and quadratic group delay responses, and these results have been validated experimentally.

The proposed non-commensurate C-section networks are suitable for analog signal processing of broad bandwidth (a few GHz bandwidth) signals, where relatively low group delay values (up to a few tens of nanoseconds) are required. In narrow bandwidth applications, such as pulse compressive radar [7], delays in the order of microseconds are needed. In such cases, the proposed networks would become excessively large and would suffer of prohibitive losses. A possible solution to this issue, involving an active feedback loop system, will be presented in the next chapter.

Considering that genetic algorithms do not necessarily guarantee an optimum design, optimization efforts can be made in the future, by introducing additional goals, such as for instance minimizing the total length of the structure and the number of C-sections. This will reduce the insertion loss in addition to improving compactness. Moreover, more design flexibility will be introduced by using hybrid edge- and broadside-coupled lines structures, possibly in multi-layer configuration, where non-adjacent line couplings may significantly contribute to the phase response for optimal results. One of these broadside-coupled configuration has been shown using LTCC fabrication where a volume reduction by a factor 7 has been achieved.

Chapter 5

Guided-Wave Applications

This chapter continues the guided-wave applications, but in contrast, introduces impulse regime component and system. Under impulse regime, the component and system either generate or being driven by periodic pulse excitation source. The component (time differentiator) exploits the interesting time derivative characteristic (first and second order) of the coupled-line coupler and is used to generate periodic pulse signals. On the other hand, the system (PPM transmitter) exploits the dispersive property of the CRLH TL MTMs and is driven by a periodic Gaussian pulse signal. This is the first time the dispersive characteristic of a CRLH TL MTMs is introduced in the impulse regime and applied to design a complete transmitter.

5.1 Tunable Delay Lines ($\beta_1 \neq 0$ Application)

Delay lines are ubiquitously employed in various microwave devices and subsystems. Mainly used as time delayers or phase shifters, they find application in phased arrays, feed-forward amplifiers, delay-lock loops, phase noise measurement systems, and oscillators [79]. In terms of implementation, there are various ways to achieve time delays, where a simple transmission line is the simplest form of a delay line. For tunable delays however, several implementation approaches are employed, from using varactor diodes loaded on a transmission line, to surface acoustic wave (SAW) and magneto-static wave (MSW) devices.

Yet, all three approaches display an intrinsic disadvantage when operated in microwave circuits. A transmission line loaded with tunable varactors will exhibit a variation in its characteristic impedance, dependent on the varactor value [80]. In turn, this naturally leads to a mismatching effect between the line and its surrounding circuitry, leading to a deterioration in performance over a broad band. On the other hand, time delays in SAW [8][9][11] and MSW [10] devices are attained without altering their characteristics, hence removing the mismatch impediment. However,

SAW devices are limited in terms of operational frequency and bandwidth constrained to only several MHz, while MSW devices utilize a bulky magnet requiring accurate mechanical alignment, not conducive for planar microwave circuits.

We present the experimental verification and characterization of a tunable CRLH delay system previously introduced theoretically in [17], based on a dispersive transmission line, which overcomes the aforementioned drawbacks of conventional delay lines. The delay system, suitable for continuous wave (CW) and impulse wave, consists of a composite right/left-handed (CRLH) [4] transmission line (TL), two mixers, and a low-pass filter. The delay system is suitable for applications such as pulse-position modulation, phase discrimination, and signal compression.

5.1.1 System Principle

A CRLH TL is an artificial TL constructed of cascaded unit cells, composed of capacitors and inductors [4]. Operated in the balanced mode, the CRLH TL, shown in Fig. 5.3(a), can be considered as the combination of a RH and LH TLs, with a gapless transmission passband and broadband matching. The propagation constant of the balanced CRLH line is given as

$$\beta(\omega) = p\left(\frac{\omega}{\omega_R} - \frac{\omega_L}{\omega}\right), \tag{5.1}$$

where $\omega_R = 1/\sqrt{L_R C_R}$, $\omega_L = 1/\sqrt{L_L C_L}$, and p is the size of the unit cell. The transition frequency $\omega_0 = \sqrt{\omega_R \omega_L}$ occurs when $\beta = 0$ in (5.1).

The RH and LH contributions of the CRLH TL are manifested in the first and second term of (5.1), respectively, representing a simple delay in time (linear phase term) and distortion (hyperbolic phase term), respectively. Thus, considering a signal of restricted bandwidth $\Delta\omega$ centered at the frequency ω_c, with the condition $\Delta\omega \ll \omega_c$, the resulting group delay in a balanced CRLH TL is given as the derivative of (5.1) [4] at ω_c or

$$\tau_g(\omega_c) = N\left[\frac{1}{\omega_R} + \frac{\omega_L}{\omega_c^2}\right], \tag{5.2}$$

where N represents the number of unit cells in the CRLH TL. The center frequency ω_c represents the frequency of a carrier modulating the signal of bandwidth $\Delta\omega$. From (5.2), it can be seen that the group delay is dependent on this carrier frequency.

Thus, by varying ω_c, the delay of any input signal can be tuned accordingly, with the negative slope

$$\frac{\partial \tau_g}{\partial \omega} = -\frac{2N\omega_L}{\omega_c^3} < 0, \tag{5.3}$$

corresponding to the *anomalous dispersion* of the CRLH TL. Figure 5.3(a) shows the schematic of such a delay system. It should be noted that such a delay line system can be implemented using any 2-port dispersive delay structure. This section in particular employs a CRLH structure to demonstrate such a system, where instead other dispersive structure could have been used.

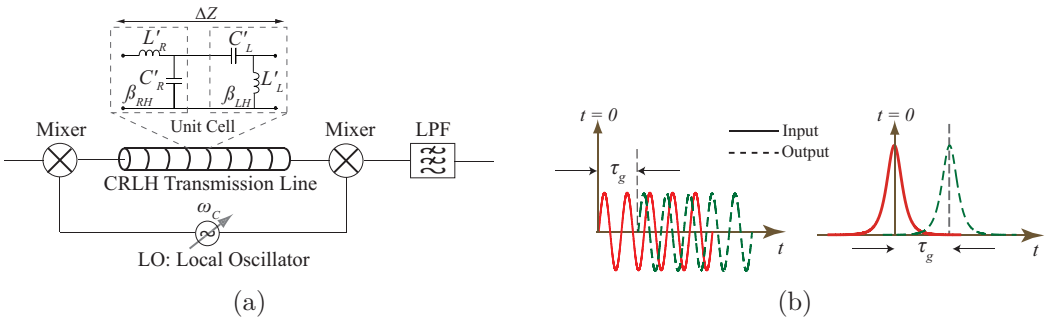

Figure 5.1 CRLH continuous wave and impulse wave tunable delay line system. (a) System schematic. (b) Continuous and impulse delayed signals.

5.1.2 Implementation of CRLH Delay System

As stated in the previous section, tunable delay is achieved by varying the carrier frequency. This leads to the delay system shown in Fig. 5.3(a), where a CRLH TL line along with two mixers and a low pass filter are used. In the first mixer, the input signal is modulated with a variable carrier frequency from a voltage-controlled oscillator. The resultant modulated signal is then passed through the CRLH TL, where it is delayed in time, demodulated in the second mixer, and finally passed though the low-pass filter to remove the modulation frequency. Two input signals (continuous and impulse wave) are shown in Fig. 5.1(b), along with their delayed outputs, where τ_g (delay in time) is controlled by ω_c.

Based on the design guidelines in [81], a 30-unit cells CRLH TL is implemented using metal-insulator-metal technology for capacitors and shorted stubs for induc-

tors. The MIM capacitors are printed on a 5 mils Rogers Duroid 5870 ($\epsilon_r = 2.33$) substrate, which is epoxied onto a Rogers Duroid 5870 20 mils substrate, for a total substrate height of 25 mils. The CRLH TL is shown in Fig. 5.2, along with the layout and dimensions of a unit cell. Figure 5.3 shows the full-wave simulated (Agilent's Momentum) and measured scattering parameters of the CRLH TL, with a transition frequency of 2.55 GHz. Triple-balanced commercial diode mixers (Mini-circuits MCA-50MH) were subsequently chosen with an IF range of $0.1 - 1.5$ GHz, able to handle narrow pulses, and LO and RF ranges of $1 - 5$ GHz, with acceptable isolation between all ports. The delay system prototype is shown in Fig. 5.2.

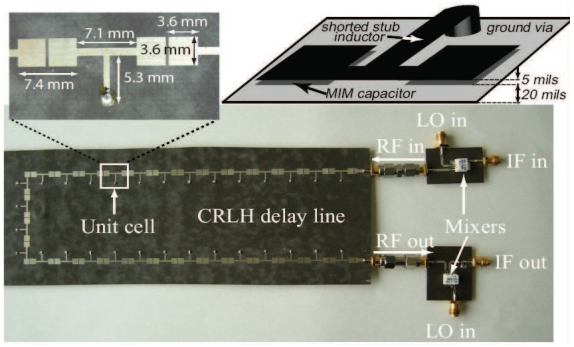

Figure 5.2 System prototype showing a 30-unit cell CRLH delay line system, along with the dimensions of a unit cell and its perspective view. The CRLH equivalent circuit model parameters of Fig. 1(a) are: $L_R = 4.2$ nH, $C_R = 2.1$ pF, $L_L = 2$ nH, $C_L = 1$ pF.

5.1.3 Results and Discussion

The proof-of-concept CRLH-based delay system was tested to experimentally characterize the achievable delays. Fig. 5.4(a) shows both the measured input and delayed output baseband impulse waveforms, along with their corresponding circuit simulation waveforms. Similarly, Fig. 5.4(b) shows the measured and simulated results for CW, with an IF of 100 MHz. Using Agilent's ADS, the simulation results were obtained by modelling the 30-unit cells CRLH transmission line by an equivalent LC circuit [4], shown in Fig. 5.3(a) with $L_R = 4.2$ nH, $C_R = 2.1$ pF, $L_L = 2$ nH, $C_L = 1$ pF, cascaded 30 times. As seen in Fig. 5.4(a), the delayed impulse with $f_c = 2$ GHz is more distorted than the delayed impulse with $f_c = 3.25$ GHz. This is due

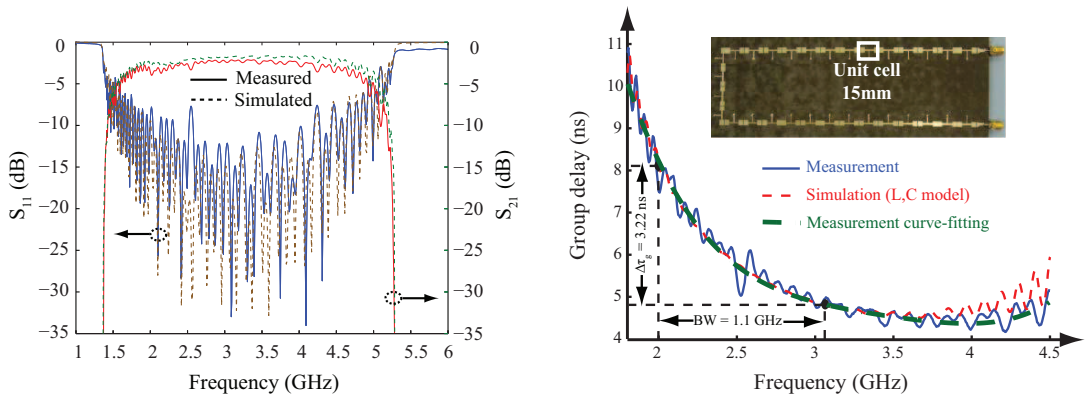

(a) (b)

Figure 5.3 Measured responses for the 30-unit cell CRLH TL. a) S_{11} and S_{21}. b) Comparison between theoretical, simulated, and measured delays at various carrier frequencies. The transition frequency $\omega_o = 2.55$ GHz.

to the more significant CRLH dispersion at lower left-handed frequencies when compared to the higher right-handed frequencies within the CRLH TL passband. Thus, a dispersive medium will cause signal distortion, which is proportional to delay times here, i.e., longer delay times experience more distortion. However, distortion can be plainly compensated by introducing a secondary dispersive medium with an equal but opposite delay slope demonstrated experimentally in [41]. Thus, due to distortion, the time delays of an impulse are measured as a mean value of rise, center, and fall times. The measured time delays at 2 GHz are 8.13 ns and 8.54 ns for impulse and CW, respectively, while at 3.25 GHz, the measured delays are 5.36 ns and 5.39 ns, respectively. As can be seen, the measured and simulated delays closely agree with each other for impulse and CW.

Figure 5.3 shows the measured and simulated time delays achieved for various carrier frequencies within the CRLH TL passband. The simulation results closely follow the theoretical results of (5.2). The tuning sensitivity $\partial\tau_g/\partial\omega$, as predicted by (5.3), is more pronounced at lower frequencies, due to the slow-wave compression occurring in the left-handed band of the CRLH transmission line. In addition, with increasing carrier frequency up to 3.5 GHz, both the simulated and experimental delays decrease similarly, as predicted by (5.2) and (5.3), with a small discrepancy between simulation and measurement. However, above 3.5 GHz, the delay increases due to the stop-band proximity, where at the cut-off $v_g = 0$ and $\tau_g = \infty$.

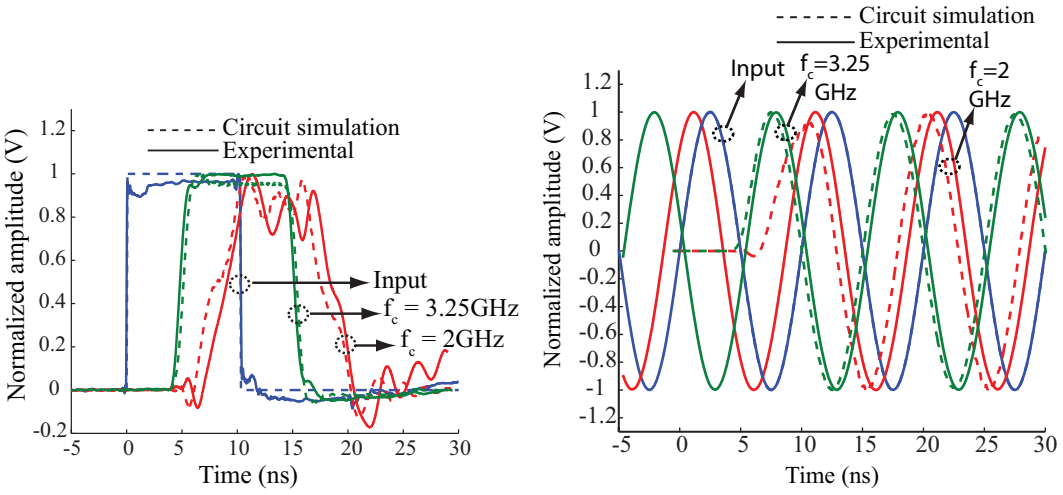

Figure 5.4 Time delayed waveforms for different carrier frequencies (experimental and circuit). (a) Impulse wave. (b) Continuous wave.

Two types of losses need to be considered in the present delay system. The first and main source of loss is the passive diode mixer(Mini-circuits MCA-50MH), with a conversion loss of $6 - 8$ dB, which can be eliminated with an active mixer. The second source of loss is due to the CRLH TL, contributing both conductor/dielectric loss from the structure's length and radiation loss from its leaky-wave effect. Using Momentum, the conductor/dielectric loss is estimated to be $\alpha_{cd} = 5.8$ dB/m, while the radiation loss is $\alpha_{rad} = 1$ dB/m at 2.55 GHz, for the CRLH TL in Fig. 5.2. Thus, an impulse and CW would incur an acceptable insertion loss of 3.4 dB, where an impulse would radiate energy based on its spectral content (backward and forward for left/right-handed frequencies, respectively), while a CW would radiate in only one direction. To eliminate radiation, it suffices to enclose the CRLH TL within a shielding box [82].

5.2 Real-Time Frequency Discriminators ($\beta_2 \neq 0$ Application)

Based on the frequency dependent group delay property of a dispersive delay structure, its classical analog signal processing application is the compressive receiver,

mostly used in radar applications [7]. For instance, frequency discriminators are of paramount importance in FM radio for the demodulation of frequency modulated signals. Moreover, in adaptive wireless networks, they may be used to identify free frequency bands and henceforth increase the channel spectral efficiency. A typical system schematic of this receiver is shown in Fig. 5.5(a).

5.2.1 System Principle

A typical frequency discriminator system based on DDSs operates as follows. It employs two dispersive structures – here, two non-commensurate all-pass networks – with identical group delay response (e.g. up-chirped $\tau_g(\omega)$ function). The RF incoming frequencies $f_1, f_2, ..., f_N$ to be discriminated at the receiving antenna are mixed with a down-chirped (negative frequency ramp) pulse $x_0(t)$ modulated at a fixed frequency f_0, retaining only the lower side side-band using a band-pass filter. This chirped pulse is obtained by injecting a pulse into dispersive network #1, which is followed by a mixer inversion block to generate a down chirp. The mixed signal is then injected into dispersive network #2 with an exact group-delay response as the first. As the down-chirped signal propagates through network #2, the signal is compressed in time as a result of chirp cancelation. This leads to distinct compressed pulses, corresponding to the respective frequencies $f \in (f_1, f_2, ..., f_N)$ occurring at times $t \in (t_1, t_2, ..., t_N)$. Thus, each frequency is mapped onto time according to the mapping function $\omega = t/C$, where C is the dispersion slope of the dispersive networks. As an example, Fig. 5.5(b) shows the response of the system using dispersive non-commensurate all-pass networks with a linear group delay using a threefold cascade repetition of the network of Fig. 4.6(d) with the two incoming test frequencies $f_1 =$ 1.0 GHz and $f_2 = 2.2$ GHz. The system outputs two impulses occurring at $t_1 =$ 32.81 ns and $t_2 = 34.36$ ns, which are used to deduce the two incoming frequencies via the mapping $\omega = t/C$. This system using a CRLH structure is experimentally demonstrated in [41].

The frequency resolution (distance between the two closest frequencies that may be discriminated) and the operation bandwidth of the system critically depend on the group-delay characteristics of the dispersive structures. Two necessary conditions required for optimal system performance are the complete cancelation of frequency chirp by the second dispersive structure in order to achieve compression of the pulse

$x_0(t)$ centered at f_m to its initial width, and the realization of compression by a second dispersive structure independent of the mixed frequency f_m in order to avoid distortion after frequency translation.

These two important conditions are considered in Figs. 5.5(c) and (d). Fig. 5.5(c) illustrates the pulse problem which occurs in the compressive receiver when the dispersive structures exhibit a non-linear group delay response, as in [41]. In this case, the slope of the group delay function, $\beta_2 = d\tau/d\omega$, is a function of frequency. Therefore, the pulse at the input of the second dispersive structure, after the frequency translation of the mixer connected to the antenna, *does not* exhibit chirp perfectly opposite to that of the dispersive structure #2, which leads to imperfect chirp cancelation and, therefore, imperfect pulse shape restoration, as shown in Fig. 5.5(c). In contrast, if a dispersive structure exhibiting a linear group delay response [e.g. the one employed in (Fig. 5.5(b)] is used, this problem is perfectly solved, since the chirp shape is independent of the frequency translation, as illustrated in Fig. 5.5(d). This example illustrate an application where the linearity of the group delay is of paramount importance in the analog signal processing system, and further demonstrates the usefulness of the proposed non-commensurate all-pass network system which allows the design of such responses. Other analog signal processing systems requiring a linear group delay are real-time Fourier transformers [83][31] and time lenses [84].

5.2.2 Loop-Architecture Implementation

Another alternative and more practical implementation of a frequency discriminator is using the loop architecture as demonstrated in [3]. In the loop architecture a baseband pulse $v_0(t)$ is modulated with incoming multi-tone signal consisting of frequencies that needs to be discriminated. The resulting signal $v_{in}(t)$ is then injected into a DDS, which provides different propagation delays to different frequencies leading to their discrimination in the time domain. To achieve high frequency resolution, the output signal of the DDS is re-injected back into the DDS. This process is repeated until the desired frequency resolution is achieved. A typical result is shown in Fig. 5.7 where the desired frequency discrimination is achieved after the 6th turn.

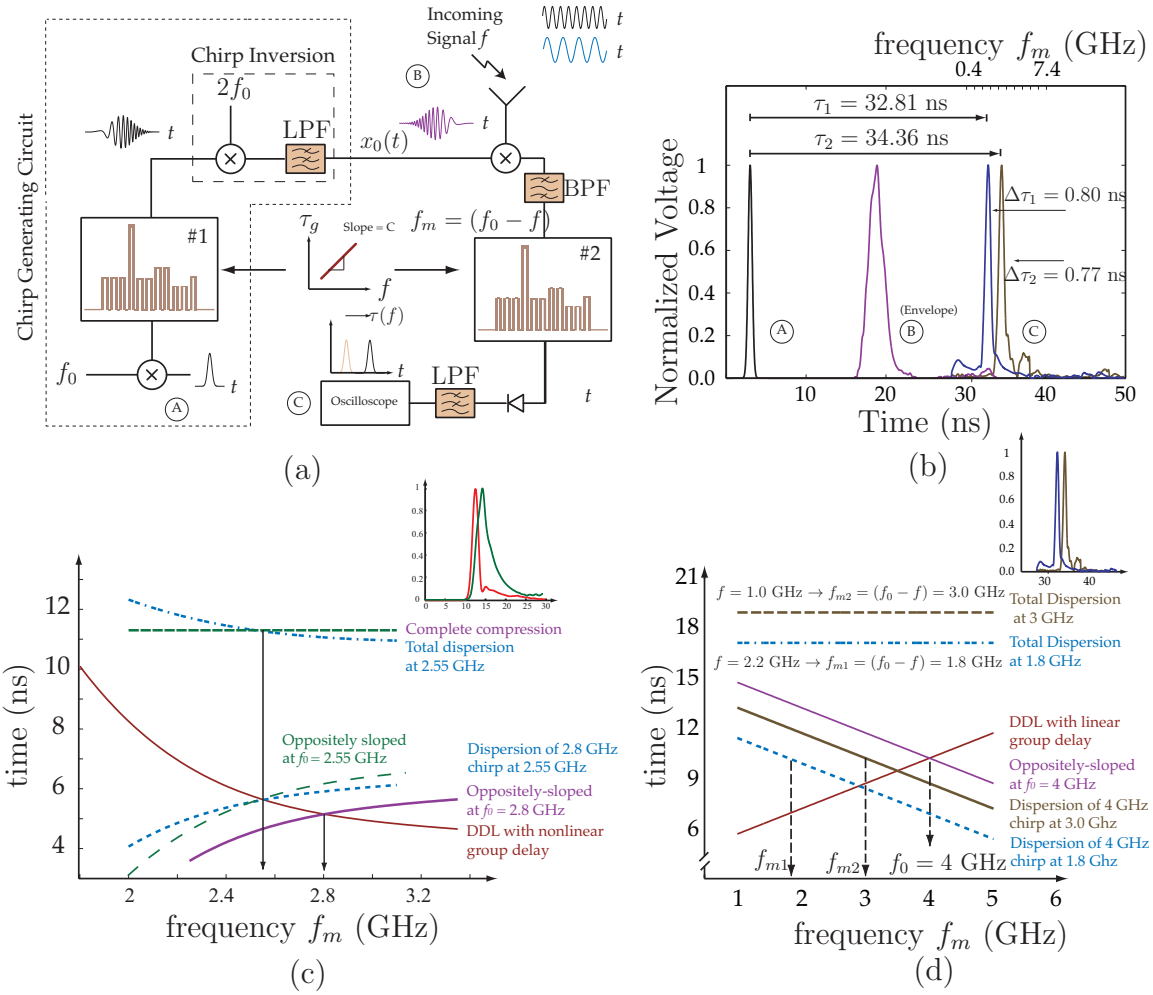

Figure 5.5 Real-time frequency discriminator. a) System. b) Circuit simulation results. c) Incomplete chirp cancellation in case of nonlinear dispersion. d) Complete chirp cancellation in case of linear dispersion.

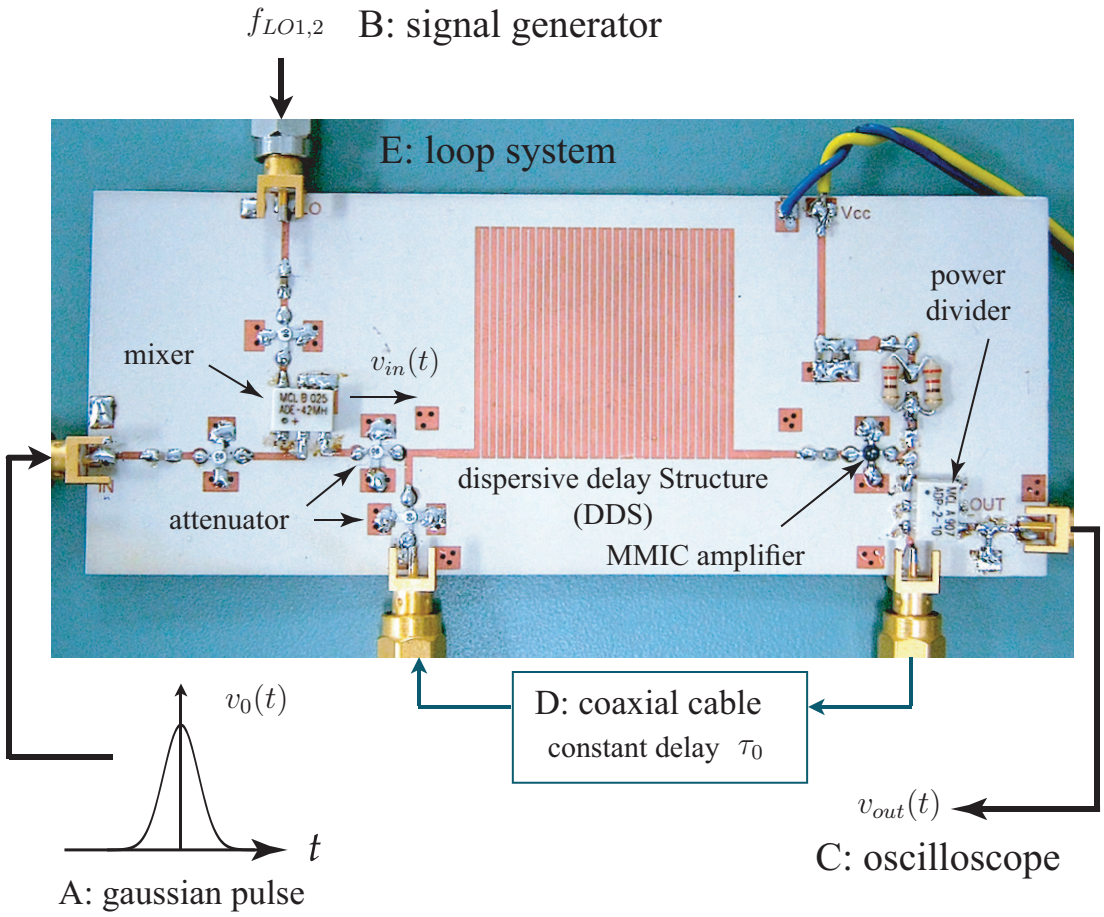

Figure 5.6 Experimental prototype of a frequency discriminator using a loop architecture [3].

5.3 Chipless RFID System ($\beta_n \neq 0$ Application)

Over the past few years, radio-frequency identification (RFID) systems have drawn considerable attention in the microwave community due to their applications in a diversity of applications, including communications, ticketing, transportation, logistics, tracking, inventory, human identification, and security, to name a few [85]. A typical RFID system comprises an interrogator (also called a reader) and many tags (also called labels). Compared to radar systems, RFID systems may operate not only over long distances (e.g. telemetry) but also over short distances (e.g. barcode replacement).

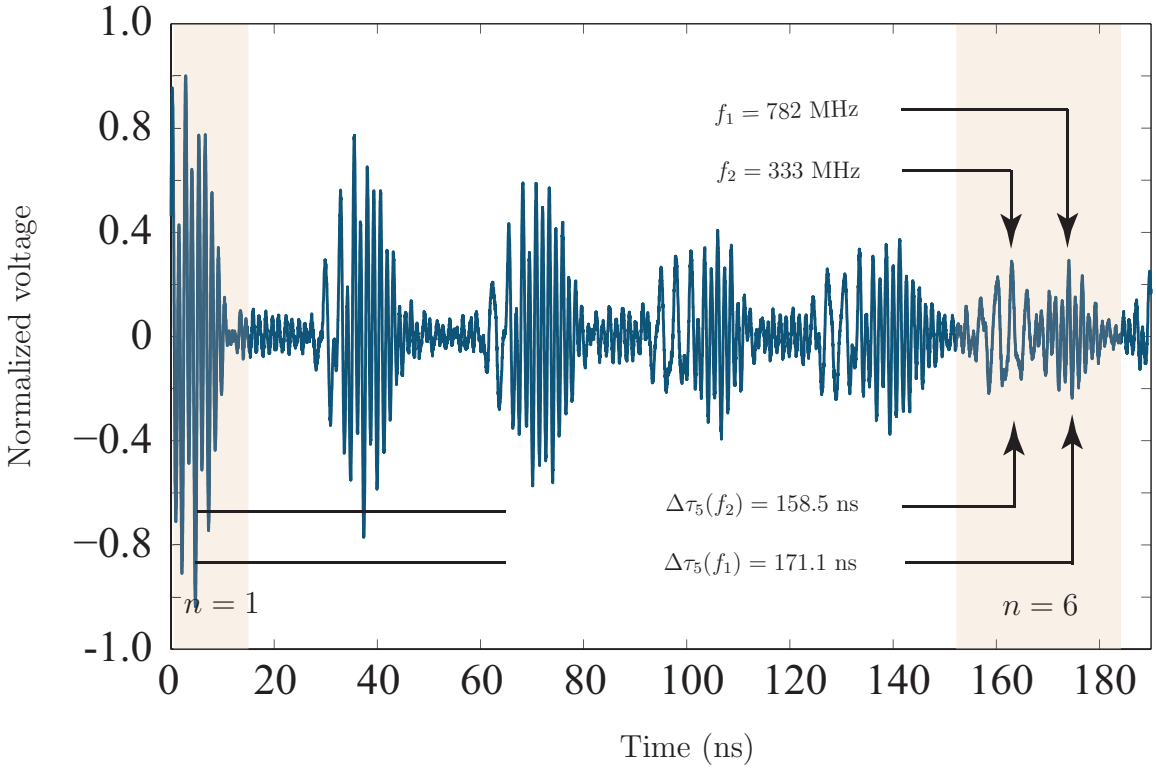

Figure 5.7 Measured time-domain output signal $[v_{out}(t)]$ for an input gaussian pulse, $v_0(t)$, modulated by a two tone signal in the system prototype of Fig. 5.6, demonstrating the concept of frequency discrimination. Here, τ_0 is 33.13 ns.

RFID systems may be classified as active or passive systems depending on whether the tags are powered up by their own power supply or by the RF energy provided by the interrogating signal. Passive tags can themselves be classified as chip and chipless tags and are restricted to relatively small distances to the reader. The latter are attractive because of their low-cost due to the absence of an integrated circuit. In addition, RFID systems may also be classified as either time-domain or frequency domain systems. Compared to frequency domain RFIDs, time-domain RFIDs have a fast response and, even though they require wideband circuits, they are particularly attractive due to their capability for fast signal processing in the time-domain.

Conventional time-domain RFIDs are primarily reflection-type devices and are generally based on impedance-stepped structures applying pulse-position modulation (PPM) coding onto the incoming pulsed signal [86][87][88][89][90]. Due to their re-

flective mode of operation, they may be contaminated by unwanted reflections, which may limit the number of encodable bits. Recently, a new proposal for a simple, passive and a frequency scalable time-domain chipless RFID system generating a PPM signature has been proposed in [91]. This system employs transmission-type all-pass dispersive delay structures (DDSs) to assign the PPM code onto the interrogating signal. This section provides an experimental validation of this system [19].

5.3.1 Principle

5.3.1.1 PPM based RFID System

The proposed RFID system is shown in Fig. 5.8. It consists of an RFID reader and a tag. The reader transmits a fixed interrogating signal $v_{\mathrm{Tx}}(t)$ given by

$$v_{\mathrm{Tx}}(t) = \sum_{n=0}^{N-1} A_n(t) = \sum_{n=0}^{N-1} A(t-\tau_n)\sin(\omega_n t), \tag{5.4}$$

where $A(t)$ is a baseband pulse. The RFID tag receives this signal and assigns it a PPM code in the form of a sequence of time delayed pulses $A_n(t)$, as the signal propagates through the DDS, to produce the output coded signal

$$v_{\mathrm{Rx}}(t) = \sum_{n=0}^{N-1} A[t-\tau_n-\tau(\omega_n)]\sin\{\omega_n[(t-\tau(\omega_n)]\}. \tag{5.5}$$

Thus, the tags require a mechanism providing frequency dependent time delays $\tau = \tau(\omega_n)$, i.e. a DDS, for coding. For example, the pulses $A_n(t)$ can positioned in the first half or the second half of a bit period to encode a bit 0 or a bit 1, respectively. After the signal has been encoded by the tag, it is sent back to the reader, where the assigned code is extracted.

In a binary system, the number of available codes depends on the number of pulses $A_n(t)$ in the interrogating signal $v_{\mathrm{Tx}}(t)$. An interrogating signal with N pulses can generate 2^N distinct codes. In the general case of an $M-$ary coding scheme, a larger number of codes can be generated for a given value of N.

The required DDS must have an engineerable group delay to achieve the required dispersive characteristics, i.e. $\tau = \tau(\omega_n)$. For this purpose, non-commensurate coupled-line DDSs are particularly suitable due to their transmission-type (as op-

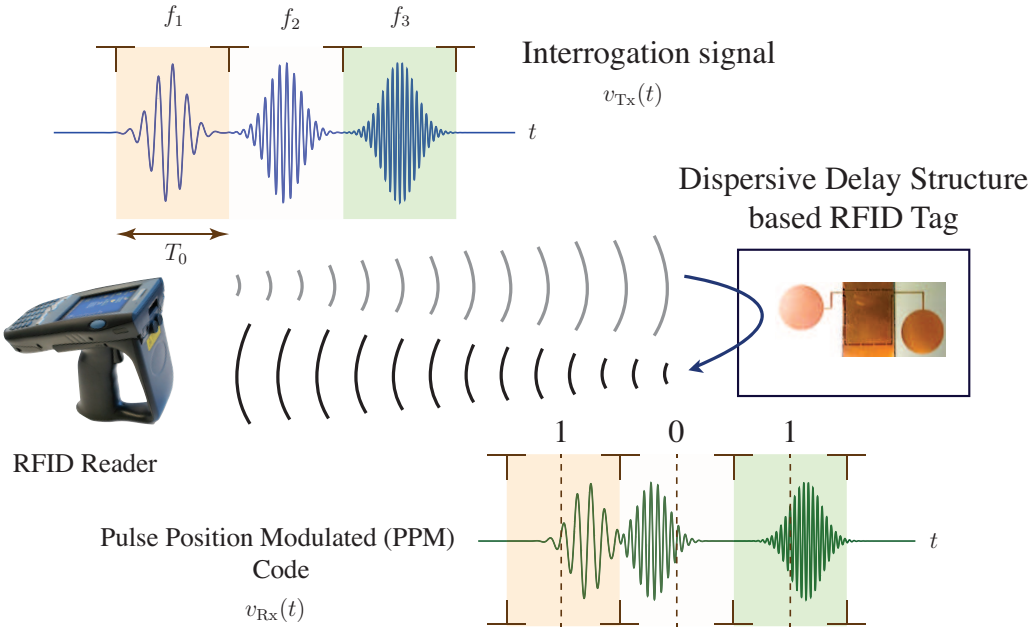

Figure 5.8 Proposed chipless RFID system based on a dispersive delay structures (DDSs).

posed to reflective-type) characteristics and planar configuration [92].

Non-commensurate coupled-line DDSs are typically based on microwave all-pass C-sections. A C-section, shown in Fig. 5.9(a), is composed of two coupled lines which are end-connected so as to form a 2−port network with an all-pass response, $|S_{21}(\omega)| = 1$. Its group delay exhibits a periodic variation in frequency with delay peaks occurring at odd multiples of the fundamental frequency where the coupled lines are quarter wavelength long. The non-commensurate DDS is realized by cascading a number of C-sections with different lengths and coupling levels, as shown in Fig. 5.9(b). By varying the lengths of individual C-sections, which are then typically inter-coupled, a quasi-arbitrary group delay response can be achieved as the superposition of the group delays provided by the individual C-sections with their peak τ_n centered at ω_n [92], as illustrated in Fig. 5.9(c).

5.3.2 System Features and Benefits

The proposed system offers several benefits as compared to other time-domain RFID systems. Firstly, it is a completely passive chipless RFID system and it may

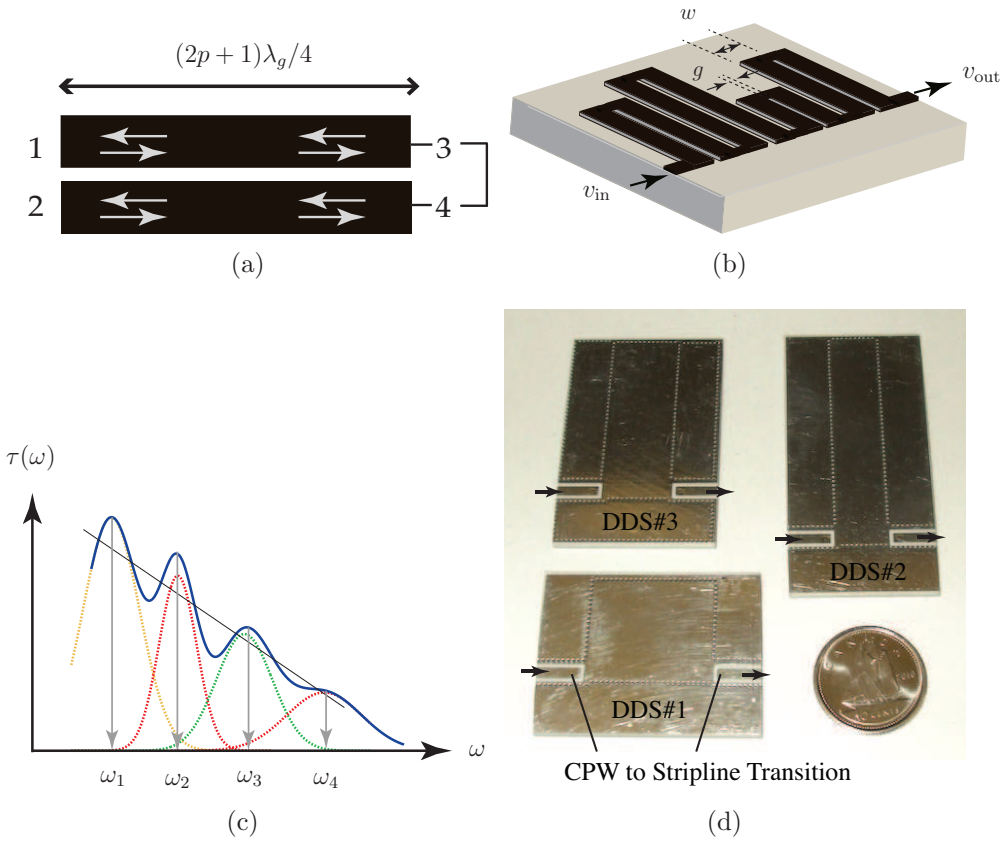

Figure 5.9 Group delay engineered microwave C-section based coupled-line DDSs. (a) C-section unit. (b) Overall non-commensurate DDS. (c) Principle of group delay realization. d) DDS prototypes in stripline technology with different group delay responses (internal C-section structure not shown). The line widths and line gaps are of $w = 21.75$ mil and $g = 8$ mil, respectively, in all cases.

therefore be easily scaled to high frequencies. Secondly, it can provide a large numbers of codes due to the flexibility of the DDSs. Thirdly, it is inherently broadband and may therefore handle ultrashort pulses, leading to fast responses. Finally, the proposed system may also be suitable for wired security systems, where the DDS would act as a hardware key.

5.3.3 System Demonstration and Results

The RFID system prototype consists of an RFID reader and several test tags. The RFID reader schematic is shown in Fig. 5.10. It generates the interrogating signal $v_{\mathrm{Tx}}(t)$ using a 1 ns long baseband square pulse $A(t)$, with a rise and fall times of 65 ps, also shown in the figure for the case of $N = 3$. This same signal is used for all the tags. The system can thus produce a total of $2^N = 8$ codes. The reader is connected to a broadband and a high gain transmitting horn antenna (S-band) to transmit $v_{\mathrm{Tx}}(t)$ towards the RFID tags. The subsequent coded signal is received using another identical horn antenna connected to a real-time oscilloscope, which represents the overall system output $v_{\mathrm{Rx,\,k}}(t)$ corresponding to the k^{th} tag. The horn antennas are further shielded using absorbers to minimize mutual coupling between them.

The RFID codes are generated using several C-section DDSs of the type shown in Fig. 5.9(b). The DDSs are fabricated in stripline technology using a 20 mil thick RO4003C substrate ($\epsilon_r = 3.55$) with a coplanar-waveguide to a stripline transition; they are shown in Fig. 5.9(d). The measured S-parameters and corresponding group delay responses are shown in Fig. 5.11(a). A good matching is obtained in the band of interest with $S_{11} < -12$ dB for all cases.

The two ports of the DDSs are then connected to two wideband monopole antennas in a cross-polarized configuration, as shown in Fig. 4(a), in order to isolate the incoming interrogating signal from the outgoing PPM coded signal. According to full-wave electromagnetic simulation (CST Microwave Studio), these antennas have a fidelity factor of 93%, which indicates negligible dispersion [93]. In addition, the DDSs in the tags are covered with an absorber to minimize scattering.

Figure 5.12 shows the measured time-domain signals for the three tags of Fig. 5.9(d). The interrogator is placed in the far-field of the tags. The tags are placed on an absorber. The output coded signal $v_{\mathrm{Rx}}(t)$ is seen to be significantly distorted. This is due to two main reasons. Firstly, the signals $A_n(t)$ with modulation frequencies ω_n

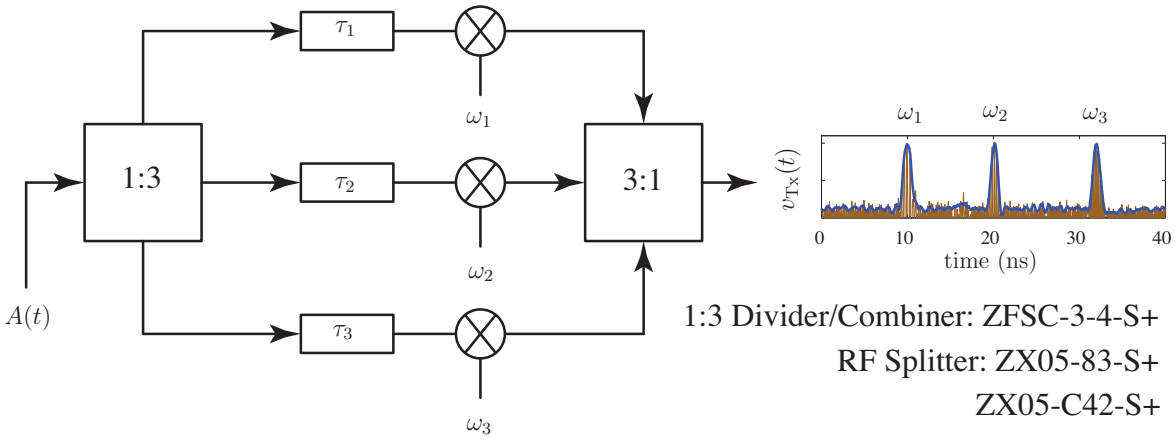

Figure 5.10 RFID reader schematic generating the interrogating signal $v_{\mathrm{Tx}}(t)$ composed of three pulses modulated with carrier frequencies $f_1 = 3$ GHz, $f_2 = 4$ GHz and $f_3 = 5$ GHz with $\tau_1 = 0$ ns, $\tau_2 = 10$ ns and $\tau_3 = 22$ ns, respectively. All the components are from Minicircuits. The baseband delay τ_n's were obtained using coaxial cables of different lengths.

experience different group delay shapes, as seen in Fig. 5.11(b), resulting in different dispersion broadenings. Secondly, all the antennas used in the experiments have a varying gain versus frequency response. Nonetheless, since the codes are related to the time delays and the bits are represented by the position of the pulse in the left half or right half of the bit period, the exact amount of time delay and the distortions suffered by the pulses are of minor importance. Despite these distortions, the individual pulses $A_n(t)$ are correctly delayed in the intended halves of the bit period following their group delay responses, and are properly encoded. For instance, the group delay response of tag#3 is so designed that $A_2(t)$, modulated with a 4 GHz carrier, is delayed less than the other two pulses $A_1(t)$ and $A_2(t)$. This is what is observed in $v_{\mathrm{Rx},3}(t)$ in Fig. 5.12(a), where the second pulse is delayed less than the others and is thus positioned in the left half of the corresponding bit period.

The PPM codes then can be recognized at the reader by extraction of the pulse delay information in a pre-defined bit period T_0 (10 ns, in this case), where each period contains one of the delayed pulses. A digital signal can be assigned to the peaks, as shown in Fig. 5.12(a), and the three PPM codes can thereby be determined as shown in Fig. 5.12(b).

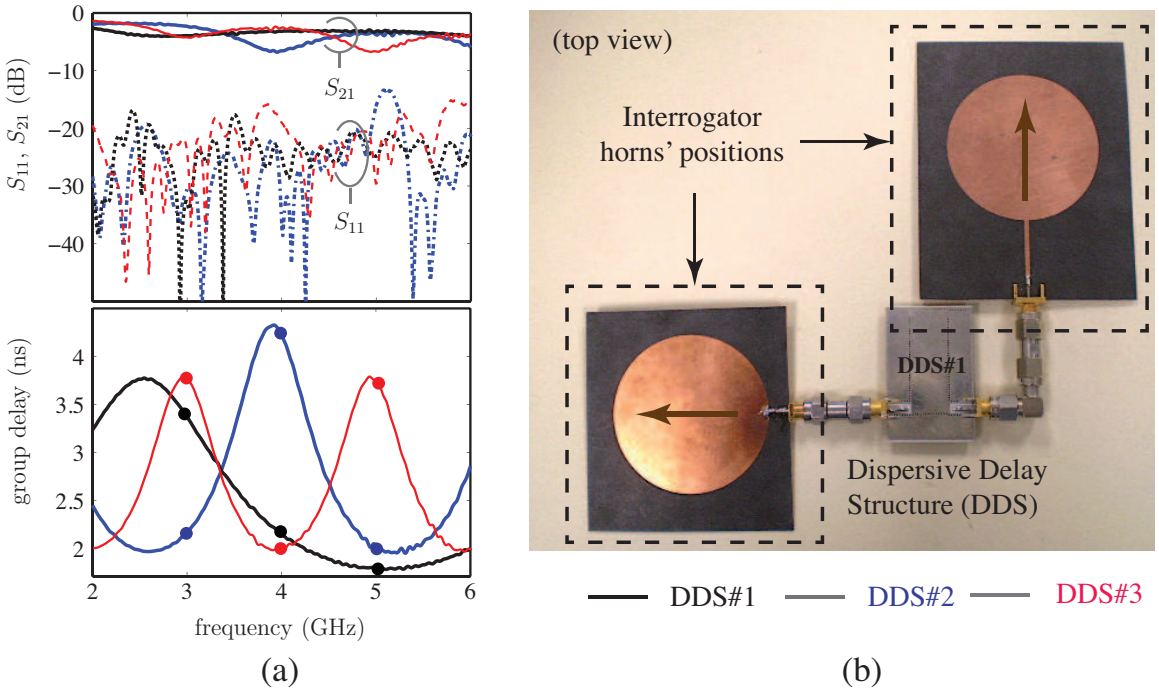

Figure 5.11 RFID Tags. a) Measured S-parameter and group delay responses of various DDSs of Fig. 5.9(d). b) Photographs of a tag consisting of a DDS connected to two cross-polarized monopole antennas.

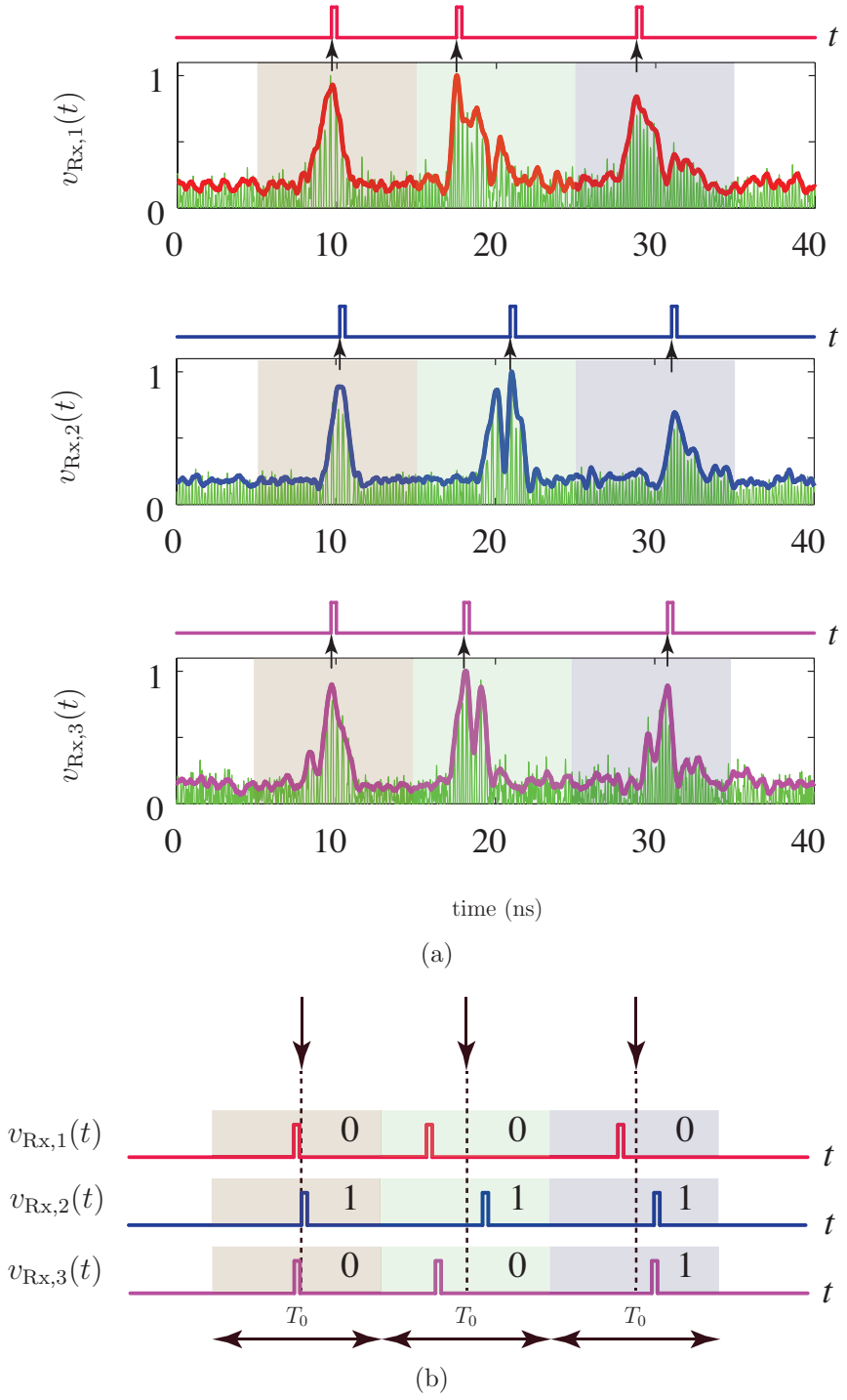

Figure 5.12 Measured time-domain signals. a) PPM coded signals $v_{\mathrm{Rx,k}}(t)$, $k = 1, 2, 3$, with their envelopes, along with numerically generated digital signals on top of each graph. b) Corresponding PPM extracted codes.

5.4 Dispersion Compensation of Log-periodic Dipole Arrays ($\beta_n \neq 0$ Application)

Log-periodic antennas are well-known for wide bandwidth operation and unidirectional narrow beam. They are based on the principle of scaling or similitude and exhibit adjacent element impedance and radiation characteristics repeating as a logarithmic function of the excitation frequency [94]. Despite their attractive wideband performance, these antennas are notorious for their highly dispersive characteristics leading to time spreading, frequency chirping and amplitude reducing of radiated pulses, all of which are highly undesirable in communication systems. Several attempts have been made to compensate the dispersion of such antennas. For example, in [95] the antenna is loaded with resonant lumped elements to dispersion-engineer the response of a log-periodic dipole array (LPDA). However, this technique affects the overall antenna behaviour and requires design corrections. Other techniques either require redesigning the antenna or altering the inherent properties of a log-periodic antenna [96].

In this section, a new technique, based on dispersive delay structures (DDSs), is proposed for dispersion compensation of log-periodic antennas and a demonstration is presented for the case of a LPDA [26]. The technique uses DDSs as a dispersion compensation component which is external to the antenna, and allows therefore a much simpler, more flexible and less invasive design.

5.4.1 Log-Periodic Dipole Arrays (LPDAs)

Fig. 5.13 shows a typical configuration of a printed LPDA. An LPDA antenna consists in a transmission line loaded by several radiating dipoles of different lengths and with different spacing radiating an end-fire beam in the plane of the antenna. The printed configuration consists of a line with an array of alternating dipole strips on both side of the substrate. The lengths of the successive dipoles are scaled by a constant factor Γ, and the spacing between the adjacent dipoles depends on a factor σ as

$$L_n = \Gamma L_{n-1}, \tag{5.6a}$$

$$D_n = \Gamma D_{n-1} + 2\sigma L_{n-1}, \tag{5.6b}$$

The LPDA design procedure is widely reported in literature, and is based on the choice of Γ and σ , which in turn determine the required antenna gain and frequency band of operation [97]. An LPDA can be matched in a wide frequency range. A typical matching response is shown in Fig. 5.14(a).

To assess the amount of distortion incurred to a wideband signal by an LPDA, a Gaussian pulse with full-width half maximum of 200 ps and modulated by wave of 3.5 GHz is fed to the antenna of Fig. 5.14(a). The corresponding radiation field in the time-domain is shown in Fig. 5.14(b). As can be clearly seen, the time domain pulse spreads in time with a frequency chirp (i.e. instantaneous frequency variation within the pulse envelope with higher frequencies appearing at earlier times). This frequency dependent phase distortion introduced by the LPDA has been extensively studied and is given by [96]:

$$\Phi(\omega) = \pi \frac{\ln(\omega/\omega_1)}{\ln \Gamma}. \tag{5.7}$$

where ω_1 is the frequency corresponding the smallest dipole of the LPDA. The group delay variation versus frequency, $\tau_g(\omega) = -d\Phi/d\omega$, can be obtained from Eq. 5.7. It is plotted in Fig. 5.14(a), which ideally should be a constant as a function of frequency for a dispersion free pulse profile.

5.4.2 LPDA Dispersion Compensation Technique

We propose to compensate for phase distortion in log-periodic antennas by connecting an external dispersive structure (DDS) at the input of the antenna, as shown in Fig. 5.15. The DDS used here is the non-commensurate coupled all-pass dispersive C-section network of Chapter 4 [2]. In such a configuration the DDS acts as a signal pre-distorter which properly adjusts the temporal phase of the original input pulse $x(t)$ by producing a chirped signal $y(t)$ which is fed to the dipole array. By appropriately designing the group delay characteristic of the DDS (positive slope in this case) to be exactly opposite to that of the dipole array (negative slope as shown in Fig. 5.14(a)), the phase distortion induced by the LPDA in the radiated pulsed signal can be completely cancelled. Thus, the radiated signal $z(t)$ is dispersion-compensated, i.e. it is exactly identical to original transmitted pulse $x(t)$, as desired.

Compared to conventional techniques, the proposed technique of dispersion compensation for log-periodic antennas offers distinct benefits. Firstly, the DDS acts as

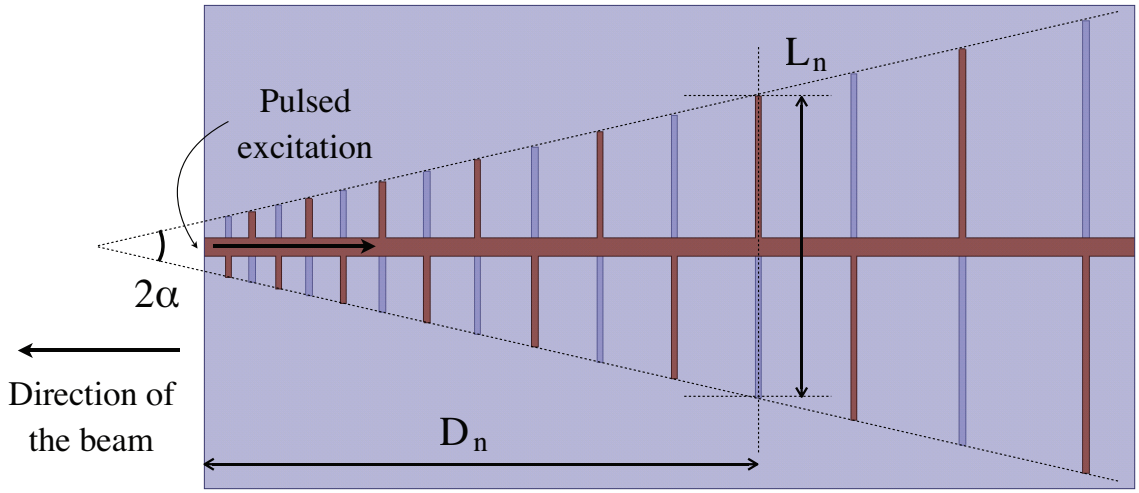

Figure 5.13 Typical planar configuration of log-periodic dipole array antennas.

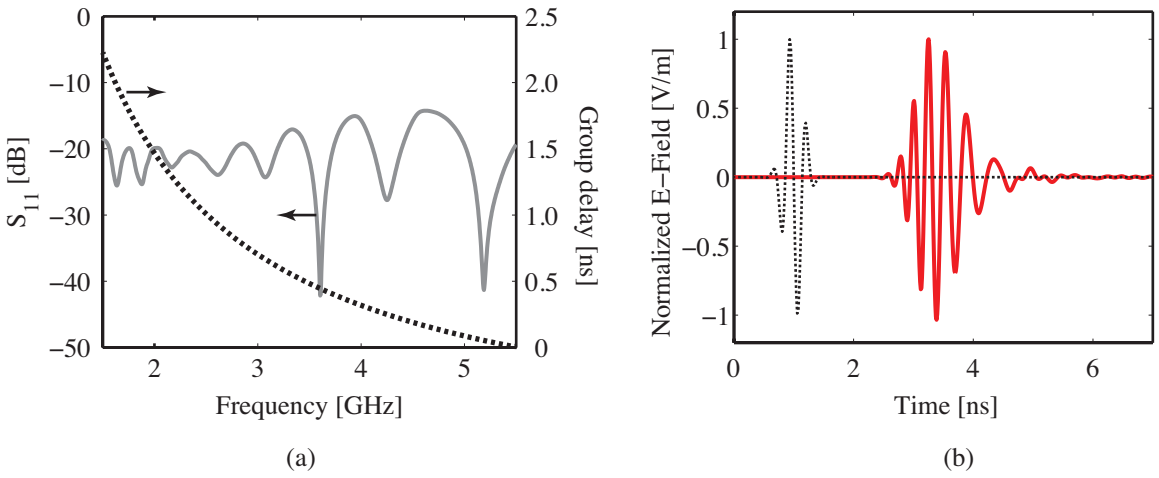

Figure 5.14 Computed reflection coefficient magnitude ($|S_{11}|$), group delay response and chirped radiated E-field (solid curve) in the far-field of the dipole array when excited with a broadband modulated pulse (dotted curve). The results are computed using FDTD based CST Microwave Studio.

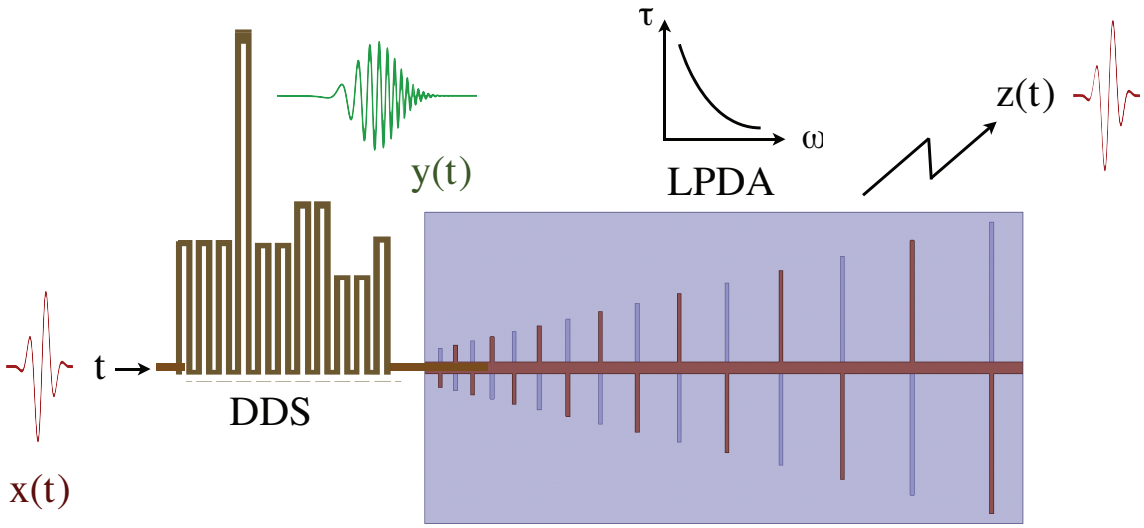

Figure 5.15 Proposed dispersion-compensation technique for LPDA where a dispersive delay Structure (DDS) is connected at the input of the LPDA as a pre-distorter.

an external and independent element to the antenna, and therefore is a plug-and-play component that may be easily connected to the antenna. As a result, the inherent properties of the antenna such as directivity and matching are unaffected. This makes the overall design of the system simple without requiring any modification of the antenna itself. Secondly, the C-section based DDS is inherently broadband, planar, flexible and frequency scalable, and can therefore be easily adapted to wide variety of log-periodic antenna designs, without requiring any lumped components.

5.4.3 Results

In order to compensate for the dispersion of the LPDA, the DDS should exhibit dispersion opposite to that of the antenna. This requires a group delay design target for the DDS: $\tau(\omega) = \tau_0 - \tau_g(\omega)$, where τ_0 is an arbitrary constant such that $\tau(\omega) > 0$ for the entire bandwidth of operation. To illustrate the dispersion compensation mechanism, consider the dispersion profile $\tau_g(\omega)$ of Fig. 5.14 corresponding to the LPDA of Fig. 1(a). For this case, the target group delay profile of the DDS is shown as a dotted curve in Fig. 3(a). To achieve this group delay design, a C-section based all-pass network of Fig. 5.15 is designed in a strip-line configuration and its

corresponding group delay is shown as a solid curve in Fig. 5.16(a). The DDS is reasonably matched ($|S11| < -20$ dB) over the entire bandwidth of operation (not shown here). The total dispersion $[\tau(\omega) + \tau_g(\omega)]$ is also shown. As can be seen, an overall desired flat group delay response is achieved.

Next, a modulated Gaussian pulse, identical to one in Fig. 5.14(b), is used as $x(t)$. The DDS output $y(t)$ is then computed using the Fourier transform relation, $Y(\omega) = X(\omega)S_{21}(\omega)$, where $X(\omega)$ and $Y(\omega)$ are the Fourier transforms of the $x(t)$ and $y(t)$, respectively, and $S_{21}(\omega)$ is the transfer function of the DDS. Next, the DDS output $y(t)$, is fed to the LPDA of Fig. 5.13. The radiated fields in time domain are then computed using commercial software CST Microwave Studio, as shown in Fig. 5.16(b). As can be seen, the dispersion of the LPDA has been cancelled and the original input $x(t)$ is faithfully radiated from the antenna, thereby validating the proposed dispersion compensation principle.

5.5 Summary

Four different guided-wave applications of DDSs has been presented. The first is a tuneable delay line system. This system offers several advantages over conventional systems where it is wideband with good matching, operational at high frequency, and is suitable for any planar circuit implementation technology. In addition, it offers variable tuning delay without changing the characteristics of the dispersive medium, preserving good matching throughout the tuning band. The second system is a frequency discriminator where the dispersive characteristics of DDSs can be used to differentiate multiple frequencies in the time-domain depending on the their respective group delays. The third system is an RFID system based on group delay engineered microwave C-section DDSs. In this system, the tags consist of various DDSs, implemented in stripline technology, whose group delay responses are engineered to provide different PPM codes. A 3-bit system has been successfully demonstrated with an RFID reader and various DDS based tags. The proposed concept offers system simplicity, frequency scalability and M-ary coding capability for large ID coding diversity. It may therefore be advantageously used in various RFIDs, encryption and decryption applications. Finally, a dispersion compensation technique has been proposed to compensate the time-domain distortions in a log-periodic dipole array, using a DDS as a pre-distorter. Although the concept has been demonstrated for dipole

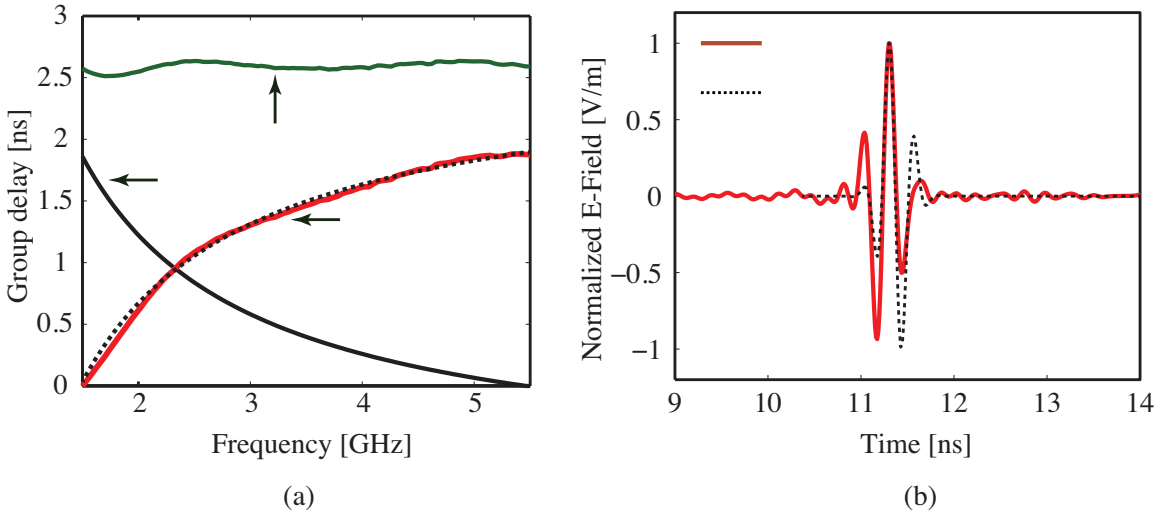

Figure 5.16 Dispersion compensation of a LPDA using a C-section based DDS. (a) Group delay response to compensate for the frequency dispersion of the LPDA of Fig. 1(b) computed using the MoM technique of [6]. (b) Radiated far-fields when the LPDA is excited with a broadband modulated pulse computed using FDTD based CST Microwave Studio, compared to the original input signal. A lossless DDS is designed in a strip-line configuration using a substrate of permittivity 6.15 with a total thickness of 50 mil, line- and gap-width of 16 mil and the structure configuration $(n_i, L_i) = [(18, 210), (6, 510), (4, 275), (4, 360), (2, 254), (20, 210)]$, where n_i is the number of line pairs of length L_i in mils.

arrays, it is applicable to wide ranges of dispersive components and devices wherever the dispersion needs to be compensated.

Chapter 6

Radiated-wave Applications

Unlike guided-wave analog signal processing components and systems presented in the preceding two chapters, where the applied electromagnetic energy is confined to the components and is prohibited from radiation, radiated-wave components and systems in this chapter harness the radiating properties of leaky-wave structures. This chapter presents two distinct applications of traveling-wave radiating structures, which in our case are based on composite right/left-handed (CRLH) transmission lines (TLs), to demonstrate two analog signal processing applications corresponding to narrowband and wideband signal processing application.

6.1 Full-Space Scanning Leaky-Wave Antennas

Traveling-wave antennas are antennas supporting wave propagation in a unique direction. When the wave has a phase velocity smaller than the speed of light (slow wave), the antenna structure guides the wave along its axis. In contrast, when the wave has a phase velocity larger than the speed of light (fast wave), and the structure is open for radiation, it can progressively radiate the wave as the signal propagates from its input to its end. Such a radiating structure is called a leaky-wave antenna (LWA) and its beam may be steered to different angles of space by tuning the frequency [94]. Planar periodic LWAs have been intensively investigated due to their low profile, low cost and ease of fabrication. A fundamental problem of these antennas has been the existence of an open stop-band in a narrow frequency region around broadside, which thereby prohibited a continuous beam-scanning from backfire to endfire including broadside with frequency. Recently, several novel structures have been proposed and demonstrated for microstrip type LWAs, such as CRLH LWAs [98, 4], phase reversal antenna [99], periodic microstrip antenna with double stubs [100] and periodic combline LWAs [101], where this open stop-band has been suppressed resulting in continuous beam-scanning in the entire radiation space. Another important

property of such LWAs is that they are inherently broadband in nature and thus are capable of processing wideband signals. Exploiting these two properties by using CRLH LWA as the radiating structure, two applications are described in this chapter, however the proposed systems can potentially employ any other traveling-wave structure as well. The first application is a *Frequency Division Diplexing Transceiver* for narrowband signal operation and the second application is a *Real-Time Spectrum Analyzer* for characterization of wideband signals.

The leaky-wave radiating principle of the CRLH TL structure is due to its dispersion curve penetrating into the fast-wave region bounded by two light-lines as shown in Fig. 6.1(a). Because the phase constant β changes continuously with frequency, the unique property of CRLH TL LWAs is the full-space frequency scanning of the main beam. Leaky-wave examples such as backfire-to-endfire frequency scanned LWAs, electronically scanned (operating at a fixed frequency) LWAs, and conical-beam LWAs have been reported. The typical dispersion curve of a CRLH transmission line is shown in Fig. 6.1(a). This curve always penetrates into the fast-wave region, $\omega \in [\omega_{BF}, \omega_{EF}]$, so that the transmission line, when open to free space, operates as a LWA within this frequency band. A CRLH LWA radiates from backfire ($\theta = -90°$) to endfire ($\theta = +90°$) including broadside ($\theta = 0°$) as frequency is scanned from ω_{BF} (where $\beta = -k_0$) to ω_{EF} (where $\beta = +k_0$) [98, 4], following the scanning law

$$\theta(\omega) = \sin^{-1}\left[\frac{\beta(\omega)}{k_0}\right], \tag{6.1}$$

shown in Fig. 6.1(b), where $\theta(\omega)$ is the radiation angle of the main beam, $\beta(\omega)$ is the dispersion relation, and k_0 is the free space wavenumber. According to this scanning law, the antenna maps each frequency within the fast-wave region to a specific angle in space, with the frequency sensitivity

$$\xi = \frac{d\theta}{d\beta}\frac{d\beta}{d\omega} = \frac{1}{\sqrt{k_0^2 - \beta^2}}\frac{d\beta}{d\omega}. \tag{6.2}$$

Finally, the beam width of the CRLH LWA is given by the general LWA relation [4, 102]

$$\Delta\theta \approx \frac{1}{(\ell/\lambda_0)\cos[\sin^{-1}(\beta/k)]} \tag{6.3}$$

where ℓ is the physical length of the structure and λ_0 is the free space wavelength. The beam width is minimum at broadside and increase progressively as the angle is moved towards either backfire or endfire.

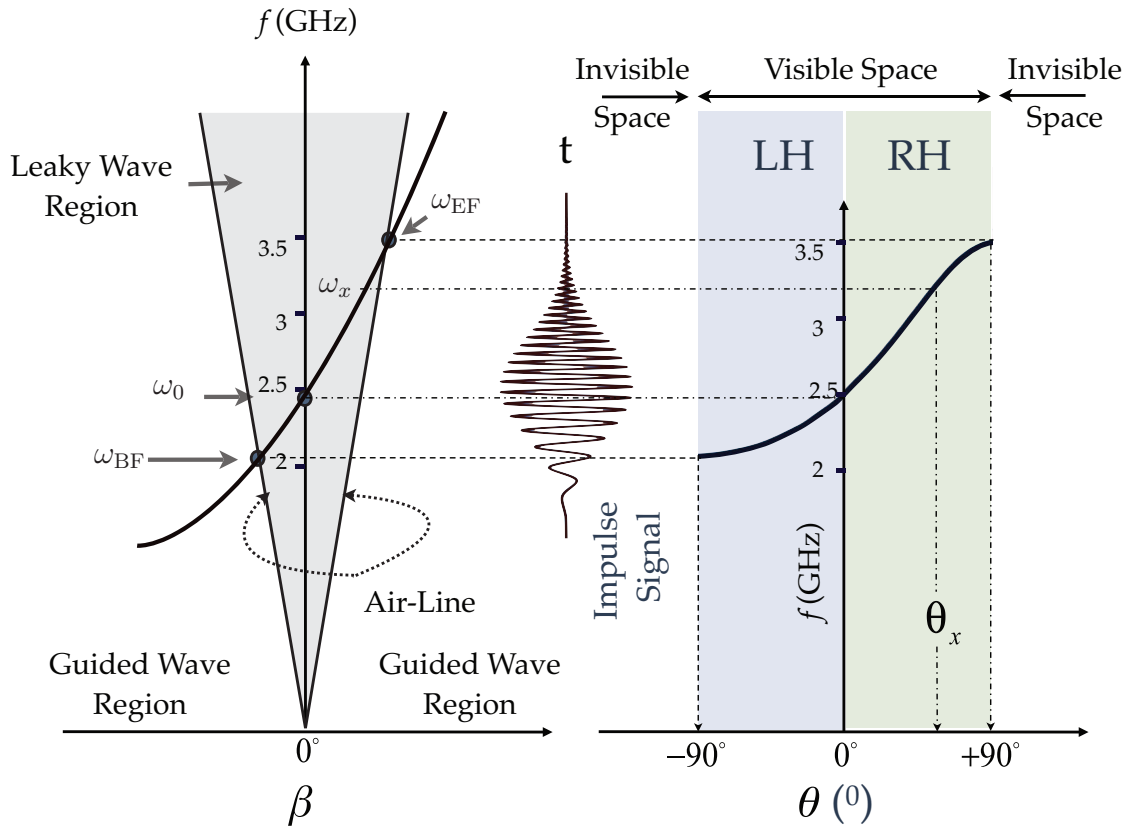

Figure 6.1 Frequency-space mapping for the CRLH LWA employed in the proposed RTSA. (a) Typical dispersion relation [4]. (b) Corresponding beam scanning relation from (6.1). These plots correspond to a 16-cell CRLH structure similar to [5].

The systems based on LWAs are classified in the GV (β_1) category because frequency scanning occurs mostly as a consequence of the term β_1, and even in the case $\beta_2 = 0$, although generally $\beta_2 \neq 0$. Therefore the two analog systems described next correspond to β_1 parameter class. The first system is a frequency division diplexing transceiver [27], which works in the continuous wave regime; and second is a real-time spectrum analyzer [29] which is suited for impulse regime operation.

6.2 Frequency Division Diplexing Transceiver

Frequency diplexer is an essential component in present satellite communication and radar systems [7]. Diplexing operation is achieved by either using two separate antennas as transmitter and receiver along with a switching device (active components) or using a single antenna used in conjunction with ferrite (magnetic) circulators [103][104]. Using a single antenna transceiver system is attractive from the point of view of lower system cost and simpler system implementation. Recently a novel frequency duplexer was introduced based on the composite right/left-handed (CRLH) [4] uniform ferrite loaded open waveguide operating at a single frequency utilizing the leaky-wave operation of the CRLH structure [105]. This section proposes a single antenna transceiver solution based on a passive CRLH LWA to realize a full-diplexing system, without requiring bulky magnets, and working simultaneously at two different Tx and Rx frequencies.

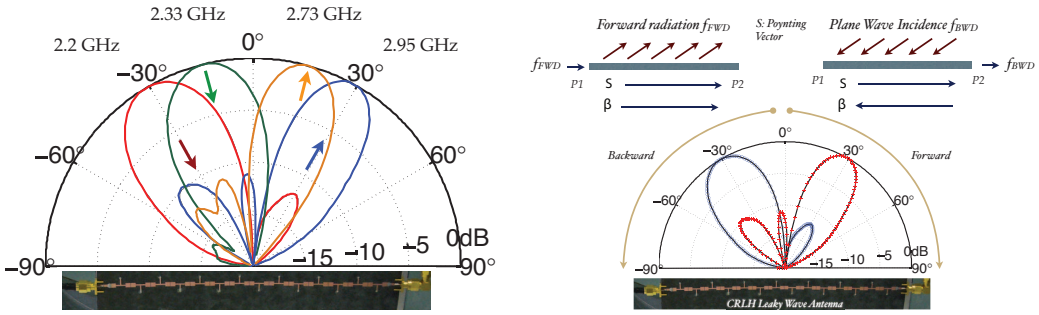

(a) (b)

Figure 6.2 Typical measured radiation properties of a CRLH LWA. a) Beam-scanning with frequency. b) Radiation patterns of a CRLH LWA in the transmitting (solid curve) and receiving modes for the cases of forward and backward radiating frequencies. The sketches on the top illustrate the LWA operation for the forward Tx and backward Rx cases. These patterns correspond to a 16-cell MIM CRLH structure similar to one in [5].

The system exploits the transmitting and receiving properties of a LWA i.e. the reciprocal radiation characteristics of CRLH LWA. Thus, the radiation pattern of a CRLH LWA in the transmitting and the receiving mode are identical as shown in Fig. 6.2(b) for the two cases of backward and forward radiation. The figure also illustrates the LWA operation for the forward radiation and backward receiving cases

as employed in the proposed frequency diplexing system. In the transmitting mode, the signal injected into port 1 at a frequency f_{FWD} is radiated in the positive quadrant ($90° > \theta > 0°$) following the beam scanning law of the LWA (Eq. 6.1). In the receiving mode, a plane wave incident on the LWA at a frequency f_{BWD} from the same positive quadrant, is received at port 2 due to anti-parallel phase and group velocities (f_{BWD} in the left-handed band of the LWA).

6.2.1 Proposed System

Based on the transmit and receive operations of the CRLH LWA described above, a full-diplexing transceiver system is proposed, as shown in Fig. 6.3(a). The system is a 4-port system consisting of a 2-port CRLH LWA (single antenna transceiver) and two Tx and Rx antennas. The systems emulates a simultaneous uplink and downlink transmission at frequencies f_{up} and f_{down}, respectively. The uplink transmission is achieved through port 1 of the LWA which is received by the Rx antenna. Similarly, the downlink transmission is obtained by the Tx antenna and using the second port 2 of the LWA as a downlink receiver.

The uplink transmission is done at a frequency f_{FWD} (f_{BWD}) corresponding to the forward (backward) radiation of the CRLH LWA along the angle $+\theta$ ($-\theta$). Similarly, the downlink transmission is done at a frequency f_{BWD} (f_{FWD}), designed to be in the left-handed (right-handed) band of the CRLH LWA, at an angle $-\theta$ ($+\theta$), which is then collected at the second port 2 of the LWA. Thus, by engineering the dispersion of CRLH LWA, so that the frequency f_{FWD} (f_{BWD}) is forward (backward) radiated along $+\theta$ ($-\theta$) and frequency f_{BWD} (f_{FWD}) is backward (forward) radiated along $-\theta$ ($+\theta$), a full-diplexing system can be realized.

If the radiation efficiency of the CRLH LWA is not 100%, the remaining signal power at the uplink frequency f_{up} from port 1 is present at port 2, which can be considered as an undesired signal leakage contaminating the downlinked power received at port 2 at f_{down}. Thus, to prevent any unwanted signal at port 2 except at f_{down}, a simple band-pass filter is required to suppress the unwanted frequency components.

6.2.2 System Demonstration

Fig. 6.3(b) shows the experimental setup to demonstrate the CRLH LWA based full-diplexing transceiver system proposed in Fig. 6.3(a). The setup consists of a

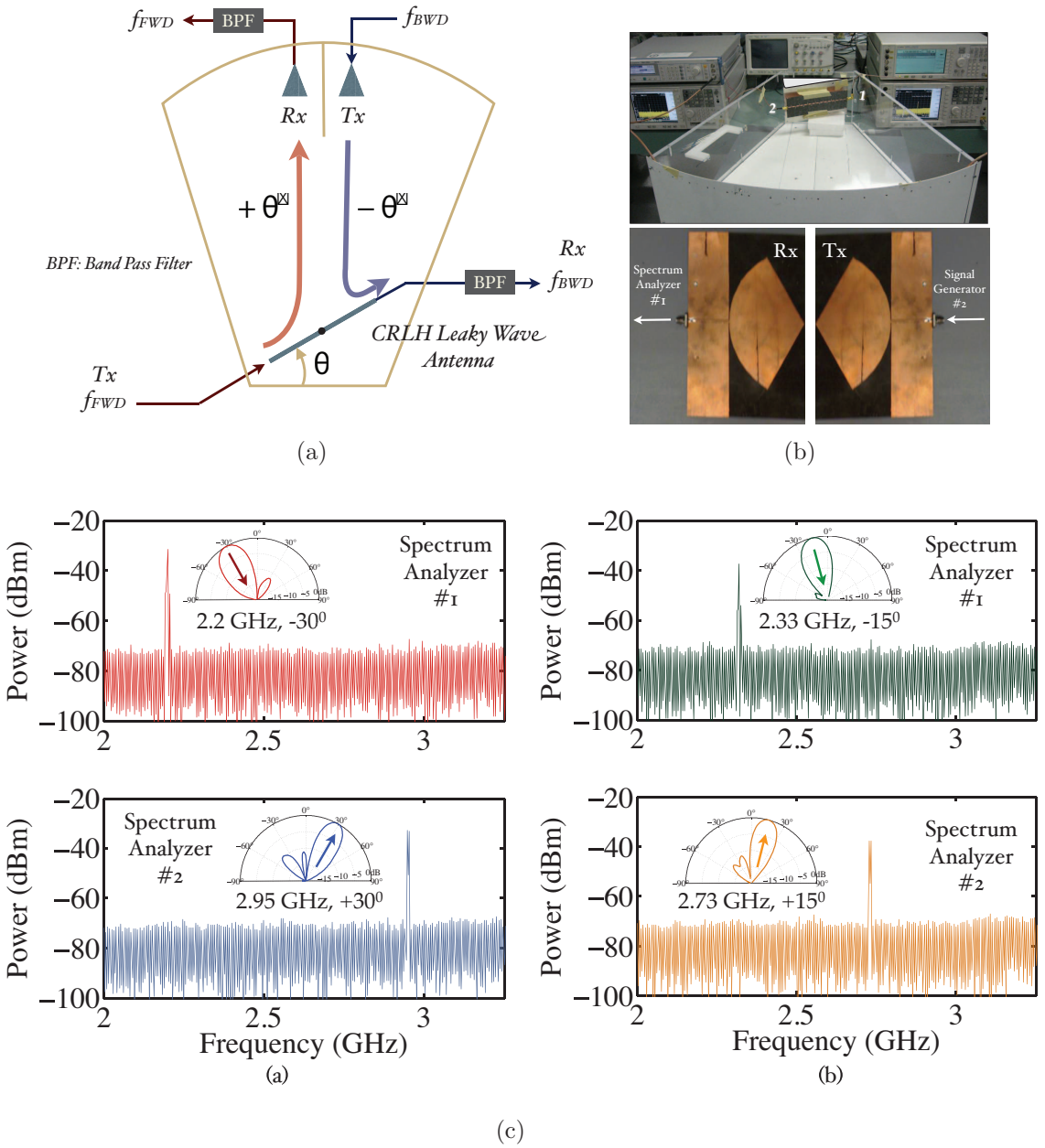

Figure 6.3 Proposed Frequency Division Diplexing Transceiver System. a) System principle. b) The experimental setup of a full-diplexing system employing CRLH LWA and two broadband antennas. c) Measurement power spectrum for the full-diplexing system for the two cases corresponding to $\theta = 30°$ ($f_{up} = 2.95$ GHz and $f_{down} = 2.2$ GHz) and $\theta = 15°$ ($f_{up} = 2.73$ GHz and $f_{down} = 2.33$ GHz).

CRLH LWA implemented in Metal-Insulator-Metal (MIM) technology [5] as the transceiver and two broadband bow-tie antennas as the Tx and Rx [97][20]. Port 1 of the CRLH LWA is connected to a RF generator 2 ($f_{up} = f_{FWD}$) and the forward radiation from the LWA at an angle θ is received by the Rx antenna which is connected to the spectrum analyzer 2. Thus, port 1 of the CRLH LWA and Rx constitutes the uplink channel. Similarly, the Tx antenna is connected to a RF generator 1 ($f_{down} = f_{BWD}$) and the transmitted signal is collected by the CRLH LWA at the port 2, since f_{BWD} belongs to the left handed band of the CRLH LWA. To provide isolation between the f_{up} and f_{down} signals at the Rx antenna and receiving port 2 of the CRLH LWA, two tuned narrow band-pass filters are employed (tuned at f_{up} and f_{down}) before the spectrum analyzers.

The system is tested for two cases of θ (30° and 15°) corresponding to two sets of f_{up} and f_{down} frequencies obtained from the scanning law of the antenna as shown in Fig. 6.1. The radiation pattern of the CRLH LWA at these various testing frequencies are shown in Fig. 6.2(a). The experimental setup is then tested for these two cases of θ, first with $f_{up} = 2.95$ GHz and $f_{down} = 2.2$ GHz corresponding to $\theta = 30°$ and second with $f_{up} = 2.73$ GHz and $f_{down} = 2.33$ GHz corresponding to $\theta = 15°$ respectively. The measured results are shown in Fig. 6.3(c) for the two cases where a successful full-diplexing operation of the system is achieved with simultaneous uplink and downlink transmission.

6.2.3 System Features and Benefits

The proposed system offers several benefits over conventional approaches. Firstly, the system consists of a *single CRLH LWA transceiver* for both uplink and downlink transmission resulting in a simpler system with reduced hardware and circuit requirements. Also for a given space, as opposed to a two-antenna transceiver system, a single antenna fully utilizes the available space leading to higher radiation efficiency and higher aperture efficiency in the receiving mode.

Secondly, the proposed system is a completely *passive* system which does not require any active devices such as switches or magnetic devices such as circulators as required in conventional transceiver systems.

Thirdly, the CRLH LWA is inherently *directive* in nature which is more suitable for long range point to point communication. Moreover, the directive nature of the

antenna also leads to a high isolation between the received signal and the transmitting port of the LWA.

Fourthly, the *isolation* between the leakage transmission signal through the LWA and the received signal at the receiver port of the LWA, depends on the selectivity of the bandpass filter used which can be made highly frequency selective resulting in a complete isolation between the two signals. This isolation can further be improved by increasing the radiation aperture of the LWA antenna (and thus making it more efficient [106]), so that maximum energy is radiated resulting in minimum energy being dumped at the second port. This furthermore also enhances the directivity of the CRLH LWA.

Finally, the proposed system can be *adapted* to any pair of uplink frequency f_{up} and downlink frequency f_{down} by either physically rotating the CRLH LWA transceiver or by engineering the dispersion curve of the CRLH structure using varactors [4] for a given angle θ.

It should be noted that, since the CRLH LWA beam scans with frequency following the beam scanning law (Eq. 6.1), the system is suitable for continuous wave operation only. This is the main limitation of the proposed system.

6.3 Real-Time Spectrum Analyzer (RTSA)

With the rapid emergence of ultra-wideband (UWB) systems, novel tools are required to reliably detect and characterize ultra-fast transient signals. In most of today's UWB systems, such as radar, security and instrumentation, and EMI/EMC, nonstationary signals, displaying rapid spectral variations in time, are inherently present [107]. In order to effectively observe such signals, both time information and spectral information are simultaneously needed. Thus, a real-time spectral analyzer is required to detect and monitor such transient signals with rapid time variations providing the evolution of instantaneous frequencies in real time.

The *joint time-frequency representation* is one manner to analyze such nonstationary signals. Joint time-frequency representations are two-dimensional plots of a signal where a 1D signal is represented as an image in a time-frequency plane, with the signal energy distribution coded in the color-scale levels of the image. The joint time-frequency representation of a given signal thus provides information on the temporal location of the signal's spectral components, which depends on the tempo-

ral/spectral structure of this signal [108]. Such analysis not only provides an intuitive insight into the transient behavior of the signals, but also completely characterizes their frequency, phase, and amplitude responses. Thus, the joint time-frequency representation is a highly informative tool for real-time spectrum analysis. Various numerical techniques exist to compute the joint time-frequency representations, with *spectrograms* and *Wigner-Ville distributions* being the most common [108].

Numerous *real-time spectrum analyzers* (RTSAs) are currently utilized for various applications. At microwaves, RTSAs are generally based on a digital short-time Fourier transform. For UWB signals with ultra-fast transients, small-gate duration is required in the short-time Fourier transform for high time resolution. Such small-gate durations inherently lead to a long acquisition time and large acquisition bandwidth. Thus, the short-time Fourier transform process requires heavy computational resources and large memory buffers [109]. These restrictions severely affect the system functionalities and limit its performance to only a few hundred megahertz of acquisition bandwidth, thereby preventing its application to UWB systems.

In optics, joint time-frequency analysis is often achieved by frequency resolved optical gating systems (FROG) , which are used to measure and characterize ultrashort optical pulses. This optical system is an analog implementation of the short-time Fourier transform employing a self-gating processes achieved by a nonlinear second harmonic generating crystal [110]. Another optical system capable of performing joint time-frequency analysis is the acoustic spectrum analyzer reported in [111], where Bragg cell plays the same role as the nonlinear crystal in the FROG (Frequency resolved electrical gating) systems. In acoustics, real-time spectrum monitoring is achieved using acoustic filters for speech signals analysis [112].

Whereas the optical and acoustic spectrum analyzers mentioned above are capable of handling and analyzing very broadband signals, the digital RTSAs available at microwaves are unfortunately restricted to bandwidths generally too narrow for practical broadband applications. To the best of the authors' knowledge, no microwave UWB RTSA is currently available. In this contribution, we propose a novel analog RTSA based on the spectral-spatial decomposition property of LWA for microwave UWB signal characterization [98, 4]. The principle of this system was introduced in [28] and validated in [29]. Compared to [28], this paper presents a full system characterization (including theory, architecture, detailed components, calibration, post-processing), experimental demonstration with a large diversity of testing

signals, and in-depth discussion of fundamental time-frequency resolution limitations with proposed solution. It should be noted that while other LWAs might be used in the proposed RTSA, the CRLH LWA imposes itself as the optimal choice because its unique seam-less full-space scanning capability allows the formation of gapless and maximal bandwidth spectrograms. Overall, the proposed RTSA system provides a flexible, fast, and frequency-scalable broadband real-time spectrum analysis solution.

6.3.1 State-of the Art RTSAs

The state-of-the-art real-time spectrum analyzers are based on computing the spectrogram of the test signal. Spectrograms can be obtained either using a digital or an analog approach as described in this section. The spectrograms obtained from either approach suffer from the well-known fundamental "uncertainty principle" limitation [108]

$$\Delta t \Delta f \geq \frac{1}{2}, \tag{6.4}$$

where Δt is the gate duration and Δf is the bandwidth of the gated signal. There is thus an inherent trade-off between time resolution and frequency resolution, where increasing time resolution decreases frequency resolution, and vice-versa.

6.3.1.1 Digital RTSAs

The short-time Fourier Transform is the most commonly utilized approach in the state-of-the-art microwave digital RTSAs [109]. The signal under test is periodically stored into memory buffers to which the short-time Fourier transform algorithm is digitally applied. Mathematically, the spectrogram of a signal $x(t)$ is calculated using

$$S(\tau, \omega) = \left| \int_{-\infty}^{\infty} x(t) g(t-\tau) e^{-j\omega t} dt \right|^2 \tag{6.5}$$

where $g(t)$ is a gate function. This approach, being purely digital, suffers from two drawbacks. Firstly, it requires fast processors to compute the spectrogram of the signal stored in the memory buffers to obtain the real-time response. Because of these computational resources and memory buffering requirements, short-time Fourier transform based RTSAs are limited to acquisition bandwidths of only a few hundred megahertz, restricted to spectrogram time resolution of only a few microseconds,

correlated with high acquisition time (computational delay) [109]. Currently available RTSAs cannot analyze signals with duration of less than around 50 μs. Consequently, short-time Fourier transform based RTSAs are not appropriate for ultra-wideband signal measurements and characterization.

6.3.1.2 Filter-Banks Approach

An alternative approach for microwave RTSAs is based on filter banks. In this approach, the test signal is split into N channels using a 1:N power divider and sent to N bandpass filters having contiguous central frequencies. Each filter monitors the corresponding frequency within a signal, which is then combined with the outputs of the other filters to generate the desired spectrogram of the signal [113] or to record the real-time variation of the various spectral components [112].

A disadvantage of this approach is the requirement of a large number of channels N in order to obtain a high frequency resolution. This leads to a complex and expensive system, and requires broadband dividers and high power ratios (1:N) difficult to implement at microwaves [114]. Moreover, this approach requires stringent requirements on the frequency selectivity of the narrow-band filters, which becomes particularly challenging at high frequencies, where increased losses decrease the Q of the filters.

Due to these prohibitive difficulties, this approach, although conceptually simple, has so far never been implemented or experimentally verified for RTSA to the best of our knowledge.

6.3.2 Proposed Analog RTSA

The proposed RTSA is shown in Fig. 6.4. It is based on the following three successive operations:

1. Spectral-spatial decomposition using a CRLH LWA to discriminate the frequency components of the testing signal.
2. Probing and monitoring of the time variation of each frequency component. Probing is achieved by antenna receivers, while monitoring is performed by envelope demodulation;
3. Post-processing, including analog/digital conversion, data processing, and display.

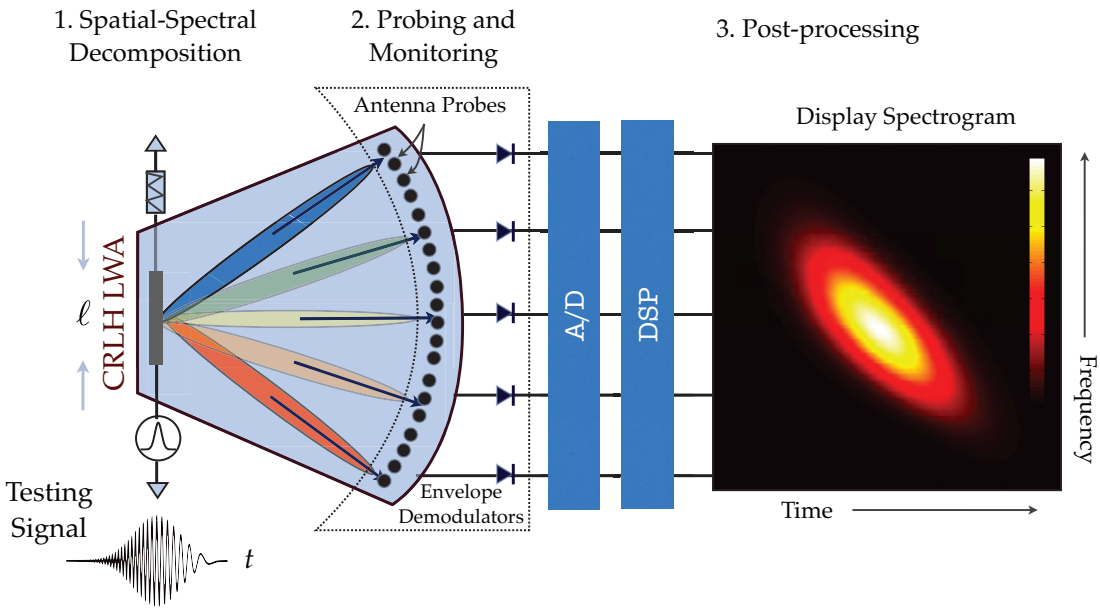

Figure 6.4 Proposed analog RTSA showing the CRLH LWA, the antenna probes, the envelope detectors, the A/D converters, the DSP block, and the display with the spectrogram.

The following three sections describe in details these three operations, while Sec. 6.3.2.4 deals with the calibration of the system.

6.3.2.1 CRLH LWA Spectral-Spatial Decomposition

As mentioned in Sec. III-A, the spectral-spatial decomposition decomposition used to discriminate the frequency components of the testing signal is obtained by employing a CRLH LWA. The CRLH LWA offers three benefits: 1) full-space radiation from backfire to endfire including broadside in the fundamental mode, offering a simple and real-time frequency-space separation mechanism; 2) frequency and bandwidth scalability, allowing to handle UWB signals; 3) simple and compact design and implementation.

According to (6.1), if the CRLH LWA is excited by a pulse signal, the various spectral components of the signal radiate in different directions at any particular instant. Thus, the CRLH LWA performs an *real-time spatial-to-spectral decomposition* of the signal following the beam-scanning law of the LWA, thereby discriminating the various spectral components present in the testing signal [28]. In this sense, the CRLH LWA may be seen as a microwave counterpart of an optical diffraction grating [115], with the advantage that the incoming signal is fed at the single point of the generator as opposed to requiring a spatial illumination.

6.3.2.2 Probing and Monitoring

Once the testing signal has been spectrally decomposed in space by the CRLH LWA, as described in Sec. 6.3.2.1, the various frequency components need to be probed and monitored in real-time. For this purpose, n antenna probes are arranged circularly in the far-field around the antenna at the positions $r(R, \theta_n = n\Delta\theta)$, where R is the observation distance from the center of the antenna and $\Delta\theta$ is the angular separation between two observation points (Figs. 6.4). For broadband applications, the far-field distance is given by $d_{ff} \approx 2\ell^2/\lambda_{min}$, where λ_{min} is the smallest wavelength in the operating frequency range. At each time instant, the different probes, based on their angular location in space θ_n, receive the different frequencies, thereby achieving real-time frequency-space mapping of the signal propagating across the LWA. The voltages induced along the antenna probes are subsequently envelope-demodulated and monitored as a function of time to track the temporal evolution of the different

spectral components of the input signal. The demodulated envelopes are then sent to the post-processing section for data processing.

6.3.2.3 Post-Processing

As shown in Fig. 6.4, the envelope demodulated induced voltages across the antenna probes, are next converted into digital format via A/D converters, combined, and then post-processed. After digitizing and combining the envelope demodulated voltage waveforms from the antenna probes, an energy distribution function $g(\theta, t)$ is obtained, where θ is the radiation angle. If the beam-scanning law were linear, the resulting spectrogram $S(\omega, t)$ would be directly proportional to this function $g(\theta, t)$ and would therefore be immediately available. Because the beam-scanning law of the CRLH LWA (6.1) is a *nonlinear* function of frequency, a post-processing operation is required to compensate for this effect. Instead of uniform angular spacing, the antenna probes can also be placed non-uniformly corresponding to uniform increment in frequency, thus avoiding an extra operation of spectrogram linearization. However, in order to avoid spatial crowding and overlapping in the forward region where the CRLH LWA exhibits a larger fast-wave bandwidth, uniformly spaced probes were employed which is also practically more convenient. The corresponding numerical algorithm is described next.

The measured angle distribution is chosen as uniform in the system (Figs. 6.4) while the corresponding frequency distribution is non-uniform due to the nonlinear CRLH scanning law. Since the final spectrogram $S(\omega, t)$ requires a uniform frequency distribution for display, the $\omega - \theta$ relation needs to be inverted. Since this relation is not available in closed form, because $\beta(\omega)$ is a complicated function which cannot be inverted, the following inversion procedure is used. A vector with uniformly spaced frequencies $\omega = [\omega_1 = \omega_{BF}, \omega_2, \ldots, \omega_n, \ldots \omega_N = \omega_{EF}]$ is defined across the leaky-wave frequency band and the corresponding vector of non-uniformly spaced angles $\theta = [\theta_1 = -90^\circ, \theta_2, \ldots, \theta_n, \ldots \theta_N = +90^\circ]$ is computed from (6.1). Next, a search routine locates for each (uniformly spaced) ω_n the corresponding time vector in the $g(\theta, t)$ distribution to obtain $S(\omega_n, t) = g(\theta_n, t)$. When this routine has been applied to all of the ω_n's, the sought spectrogram $S(\omega, t)$ is completed and sent to a display, as shown in Fig. 6.4.

6.3.2.4 System Calibration

Before various signals can be tested using the proposed RTSA system, a one-time power calibration procedure is required to account for the angular nonuniformity of the radiated signal, due to the directive radiation pattern of the CRLH LWA [4].

A constant amplitude linear frequency ramp signal $v(t) = \sin[\phi(t)] = \sin(\omega_0 t + ct^2)$ with frequency span $[\omega_1, \omega_2]$ and time span $[t_1, t_2]$ is fed into the CRLH LWA. In this signal, time and frequency are related by the instantaneous frequency $\omega(t) = \partial\phi/\partial t = \omega_0 + 2ct$. The power received at each probe location is then monitored and the power normalization vector $\xi(\theta)$ is constructed as $\xi(\theta) = P_t(t)/\max[P_r(\theta, t)]$, where $P_r(\theta, t)$ is the power received by the probe located at θ and assuming the transmitted power $P_t(t)$ is unity. This normalization vector compensates for the non-uniform gain profile of the transmitting and the receiving antennas, as well as for free space losses and possible impedance mismatch.

Once this calibration function has been determined with the calibration ramp, arbitrary testing signals $v(t)$ are obtained as the product of the measured signal and the power calibration function $\zeta(\theta)$.

6.3.3 Theoretical Demonstration

To verify the RTSA principle proposed in Fig. 6.4, CST's Microwave Studio full-wave simulator which is based on the finite integration time domain (FITD) technique is used. This setup is composed of two parts: the CRLH LWA, performing spectral-spatial decomposition decomposition, and the receiving probes, detecting the decomposed spectral components and monitoring their time variations. The CRLH LWA is constituted of 16 CRLH unit cells, with a unit-cell size of 1.48 cm, implemented in metal-insultator-metal (MIM) technology, similar to the structure in [5]. The receiving probes are ideal frequency-independent numerical probes co-polarized to the radiating CRLH LWA and arranged circularly in its far-field; the setup includes 37 of these probes with 5° of separation between them.

Various time-domain waveforms are injected into the LWA as testing signals, and the voltages induced at the numerical probes are recorded as a function of time. Subsequently, all of the recorded probe outputs are post-processed resulting in the spectrogram of the testing signals. Of note is that the received signal at the detectors incurs a constant delay τ_p with respect to the input signal, due to the circular con-

figuration of the probes around the LWA. This delay represents the propagation time in free space of the radiated wave from the CRLH LWA to the probes ($\tau_p \approx 3.33$ ns for a far-field distance of 1 m).

The first step is to calibrate the system with a constant amplitude frequency ramp to compensate for the non-uniform gain of the CRLH LWA, as described in Sec. 6.3.2.4. The response of the system to this ramp is shown in Fig. 6.5. The full-wave spectrogram closely follows the CRLH LWA's scanning law obtained from the extracted S-parameters from full-wave shown in right of Fig. 6.5. After this calibration step, the power normalization vector $\zeta(\theta)$ is recorded, and will be used in subsequent measurements of the testing signals. The extracted scanning law will be further employed for spectrogram linearization. The angle versus time plot in Fig. 6.5 displays few spurious power spots, which are due to the LWA side lobes received by the frequency-independent numerical probes. These spots may be removed by using frequency selective probes, as will be the case in the experiment. This completes the system calibration and the system can now be tested with arbitrary input signals.

In order to test the proposed RTSA, various time-domain functions are defined in CST Microwave Studio as the excitation signals of the CRLH LWA. First, a generalized modulated super-gaussian waveform with linear and quadratic chirps is defined by

$$v(t) = \exp\left[-\frac{1}{2}\left(\frac{t-t_0}{\sigma_0}\right)^{2m}\right]\sin(2\pi f_0 t + c_1 t^2 + c_2 t^3), \tag{6.6}$$

where c_1 and c_2 represent the linear and quadratic chirp parameters, respectively, and t_0 represents a time delay. By using different delays (t_0), signals with multiple pulse components can be also generated.

Second, a convenient function to model the nonlinear phase effect such as nonlinear self-phase modulation (SPM) is defined by [32]

$$v(t) = \mathrm{Re}[U(t)e^{j|U(t)|^2 z}], \tag{6.7}$$

where $U(t)$ is given by

$$U(t) = \exp\left[-\frac{1}{2}\left(\frac{t-t_0}{\sigma_0}\right)^{2}\right]\sin(2\pi f_0 t).$$

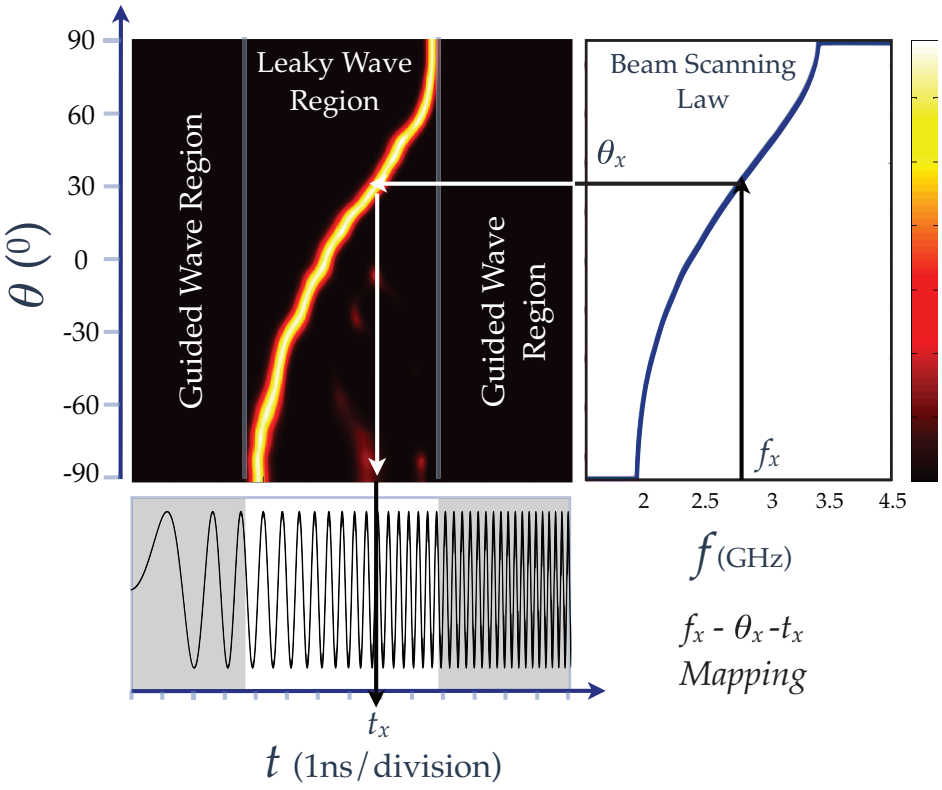

Figure 6.5 Full-wave response (top left) of the proposed RTSA system obtained for a linear frequency ramp (bottom left) compared to the beam scanning law (top right) of the antenna.

Finally, to model the pulse propagation in a dispersive medium such as a CRLH transmission line, the following Fourier transform approach is used [32]

$$v(t) = \Im^{-1}[\Im\{U(t)\}S_{21}(\omega)]. \tag{6.8}$$

Tab. 6.1 summarizes the various time-domain waveform parameters used in the testing signals. The corresponding post-processed (linearized) and power calibrated spectrograms, obtained by numerical envelope detection and interpolation of the received signals at the various probes, are shown in Fig. 6.13.

Fig. 6.13(a) shows the spectral distribution of a multi-component signal consisting of three gaussian pulses modulated at different frequencies and occurring at three different times, where the three time-frequency regions are well discriminated. A third order temporally chirped gaussian pulse (quadratic group delay) is shown in Fig. 6.13(b), where spectral beating, due to the coexistence of two different different times in the same frequency band, results in spectral oscillations in the signal spectrum. Fig. 6.13(c)-(d) show the spectrograms of two chirped gaussian pulses overlapping in time, which exhibit a typical spectral beating (same frequency components occurring at different times) pattern. Fig. 6.13(e) shows the spectral distribution of a gaussian pulse, generated from propagation in a purely nonlinear Kerr medium, where self-phase modulation is manifested by the monocycle-shaped pattern corresponding to the derivative of the gaussian phase of the input signal, as defined in (6.7) [32]. Finally, Fig. 6.13(f) show the spectral rearrangement of a gaussian pulse after propagation in a 60-cell CRLH (dispersive) transmission line with parameters $C_R = C_L = 1$pf, $L_R = L_L = 2.5$nH [4], where the asymmetric anomalous chirp, which is a characteristic of the dispersive CRLH transmission lines, can be clearly seen. These few examples demonstrate the capability of the proposed RTSA to analyze a wide variety of non-stationary signals.

To assess the accuracy of the spectrograms generated by the proposed system, the following test is done. A linearly chirped Gaussian pulse signal with the parameters defined in Tab. I is used and its simulated spectrogram is compared with the ideal mathematical spectrogram computed using the short-time Fourier integral of Eq.6.5. The gate function $g(t)$ used in the short-time Fourier integral was an equivalent square gate of $\Delta t = 2$ ns duration (where $\Delta t = \ell/v_g$, v_g being the group velocity along the antenna) corresponding to the physical length ℓ of the LWA in the RTSA system. The resulting spectrograms are shown in Fig.5 (a) and (b) and the error between the full-

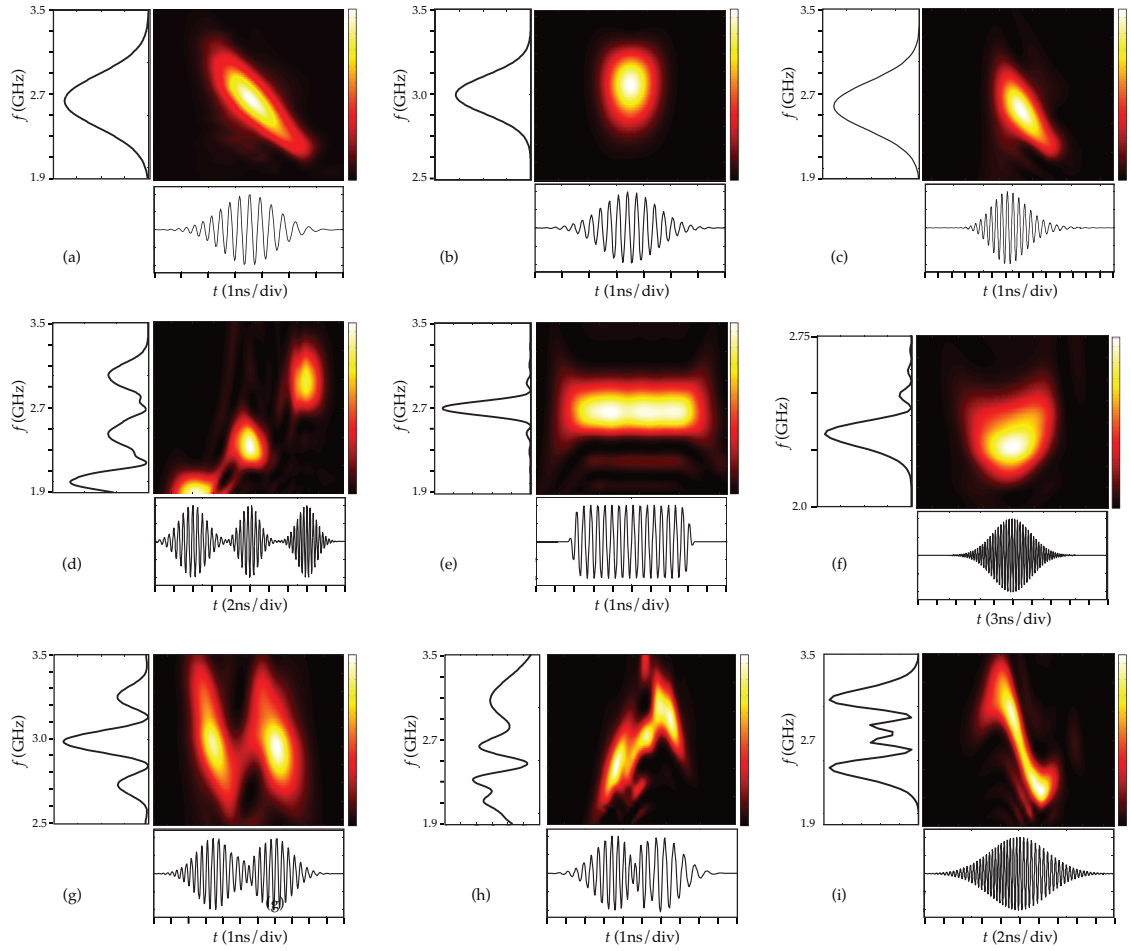

Figure 6.6 Full-wave (CST Microwave Studio) spectrograms. The input signals are generated by the time domain functions and parameters given in Tab. 6.1. a) Linear negatively chirped gaussian pulse. b) Modulated Gaussian Pulse. c) Dispersed pulse through a CRLH TL. d) Multiple modulated gaussian pulses. e) Modulated square pulse. f) Nonlinear cubicly chirped gaussian pulse. g) Doubly negative chirped gaussian pulses. h) Oppositely chirped gaussian pulses. i) Self-phase modulated pulses.

Table 6.1 Time-domain waveform parameters for the spectrograms of Fig. 6.13

Signal type	Signal parameters
a) Modulated Gaussians	$T = 1.41$ ns, $m = 1$, $f_0 = 2.0, 2.45, 3.0$ GHz, $c_2 = 0.25 \times 10^{26}$, $t_0 = 4, 10, 16$ ns
b) Nonlinear cubic chirp	$\sigma_0 = 5$ ns, $m = 1$ $f_0 = 2.27$ GHz, $c_2 = 0.25 \times 10^{26}$
c) Double chirp	$T = 1.8$ ns, $m = 1$, $t_0 = 0$ ns, 3 ns, $f_0 = 2.5$ GHz, $c_1 = -3.08 \times 10^{17}, -3.08 \times 10^{17}$
d) Double chirp	$T = 1$ ns, $m = 1$, $t_0 = 3.5$ ns, 6.0 ns, $f_0 = 4.11$ GHz, 1.9 GHz, $c_1 = -10^{18}, +10^{18}$
e) Self-Phase Modulated Pulse	$T = 5$ ns, $m = 1$, $f_0 = 2.75$ GHz, $z = 10$
f) Pulse propagation in a dispersive medium	$\sigma_0 = 1$ ns, $m = 1$, $f_0 = 2.6$ GHz
Linearly negatively chirped Gaussian pulse	$\exp\left[-\frac{1}{2}\left(\frac{t-3.5ns}{1ns}\right)^2\right]\sin(2\pi 4.2e9t - 1e18t^2)$

*(a-d) are parameters corresponding to (6.6), (e) corresponds to (6.7), and (f) corresponds to (6.8).

wave simulated and an ideal spectrogram is shown in Fig. 5(c). A close agreement is obtained between the two spectrograms with a mean error of 2.07%. The maximum observed error is 14.28%. The error is higher in regions of low power levels while the part of the spectrogram containing most of the signal's energy is faithfully generated. For example, the average error is doubled from 5 to 10% in the spectrogram regions where the mean power is reduced from 4.7 to 0.5% of the maximum power level. The errors are attributed to the following non-idealities in the system:

1. The beamwidth of the CRLH LWA is finite. Therefore, except at the exact pointing direction of the beam, an error is introduced due to the fact that some power is radiated towards unintended neighboring receivers. When the actual power that should reach these receivers is small, then the error is particularly significant. This is the reason why the error is larger in regions of low power as pointed above.
2. The CRLH LWA exhibits beam widths which vary with frequency.
3. The LWA exhibits a frequency nonlinear beam-scanning law requiring spectrogram linearization. This leads to a non-uniform sampling of frequency.
4. Due to the dispersive nature of the CRLH LWA [$v_g = v_g(\omega)$], the gate duration Δt corresponding to the space gate equal to the length of the CRLH structure also depends on frequency. Therefore, the result slightly departs from those which would be obtained with an ideal constant gate duration.

These errors may be minimized by using a beam-equalized LWA within the linear

range of it's beam scanning law.

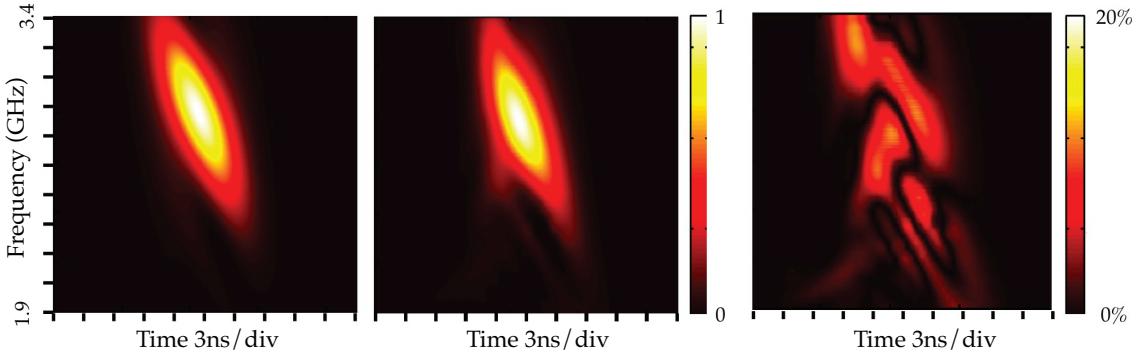

Figure 6.7 Spectrogram of a negative linearly chirped Gaussian pulse obtained using a) Short-Time Fourier Transform integral b) full-wave simulated proposed RTSA system c) Relative error between (a) and (b).

The generation of the full-wave results presented in the previous section are extremely time-consuming. Recently, an efficient time-domain Green's function approach for impulse regime electromagnetic systems with drastically reduced computational times was proposed in [116]. This approach constitutes an ideal numerical tool to model the proposed analog RTSA system. It provide not only a fast system modeling technique, but also a deep physical insight into the electromagnetic properties of the structure and a complete flexibility in terms of the possible testing pulses.

6.3.4 System Prototype and Measurements

This section demonstrates an experimental prototype of the proposed analog RTSA. It describes the various components of system and presents the measured spectrograms.

6.3.4.1 RTSA System Description

To experimentally demonstrate the analog RTSA system proposed in Fig. 6.4, a parallel plate architecture is devised to house the transmitting LWA and the array of patch antenna receivers. The system prototype is shown in Fig. 6.8(a), where the

system is designed for 60° radiation sector centered at the broadside direction. The output of the antenna receivers can be subsequently envelope detected and digitized to be sent to a computer for post-processing and spectrogram displaying. For simplicity, envelope detection and A/D conversion are achieved from the voltages induced at the antenna receivers using a digital oscilloscope (Agilent Infinium 81204B). Furthermore, in order to minimize reflections inside the housing, foam absorbers are placed on both sides of the prototype.

6.3.4.2 RTSA Components Description

As the transmitting CRLH LWA, a balanced 20.24 cm long (equal and mutually canceling CRLH series and shunt resonance frequencies) [4] MIM design (identical to the one used in the simulation analysis) was fabricated, as shown in Fig. 6.8(a). The measured beam-scanning law is shown in Fig. 6.9(a). Moreover, the normalized measured radiation patterns, including the $-30°$ to $+30°$ sector, are shown in Fig. 6.9(b). As expected, a smooth transition occurs from backward radiation to forward radiation through broadside as frequency is scanned through the transition frequency. According to (6.3), the beam width varies with the angle of radiation, with directivity maximum at broadside and decreasing toward grazing angles. This angular dependency of directivity may affect the frequency resolution of the RTSA since an excessively broad, while supposed to carry the information of one frequency component only, could be detected by undesired receivers in the neighborhood of the central receiver. Because of the inherently narrow bandwidth of the patch receivers, this effect is naturally suppressed.

The probing of spatially-spectrally decomposed signal is achieved by 16 far-field receiving patch antennas circularly arranged around the CRLH LWA within a 60° sector and 4° apart from each other, as shown in Fig. 6.8(b). These receiving antennas, fabricated on Rogers TMM11 substrate ($\epsilon_r = 9.2$, 15mils thickness), are all designed at different frequencies to match the CRLH scanning law according to their location, as shown in Fig. 6.8(b). It should be noted that the frequency resolution of the system is enhanced by the combined actions of the frequency-selective patch receivers and the directive CRLH LWA. Finally, the measurements were done using a 4-channel input oscilloscope, recording output voltages of 4 patch receivers at a time as shown in Fig. 6.8(c).

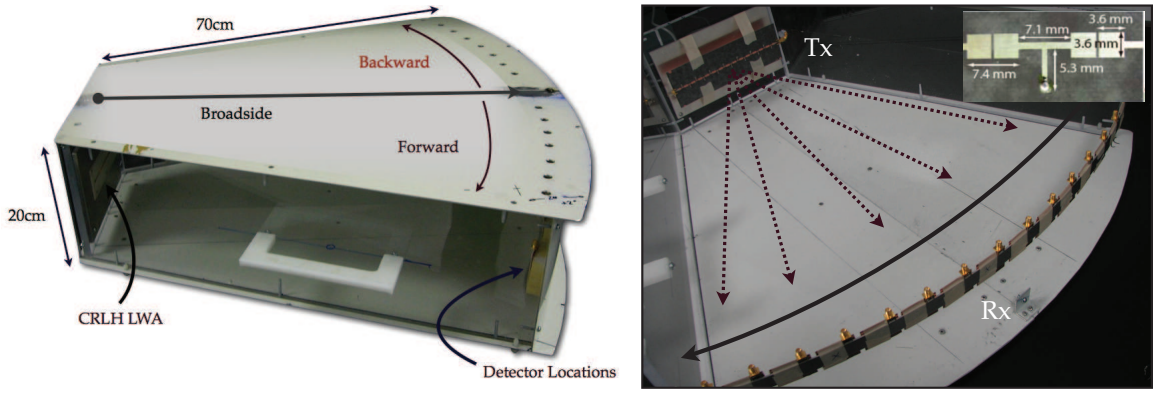

Figure 6.8 System prototype and measurement apparatus. a) Fabricated system prototype following the schematic in Fig. 6.4 covering a 60° radiation space including broadside. b) Prototype view showing the transmitting and receiving configurations showing an array of 16 patch antenna receivers (4° apart) designed at adjacent frequencies given in Tab. 6.2 to sample $\theta(\omega)$ response of the CRLH LWA. The dimensions of a unit cell of the CRLH leaky-wave antenna are shown in the inset.

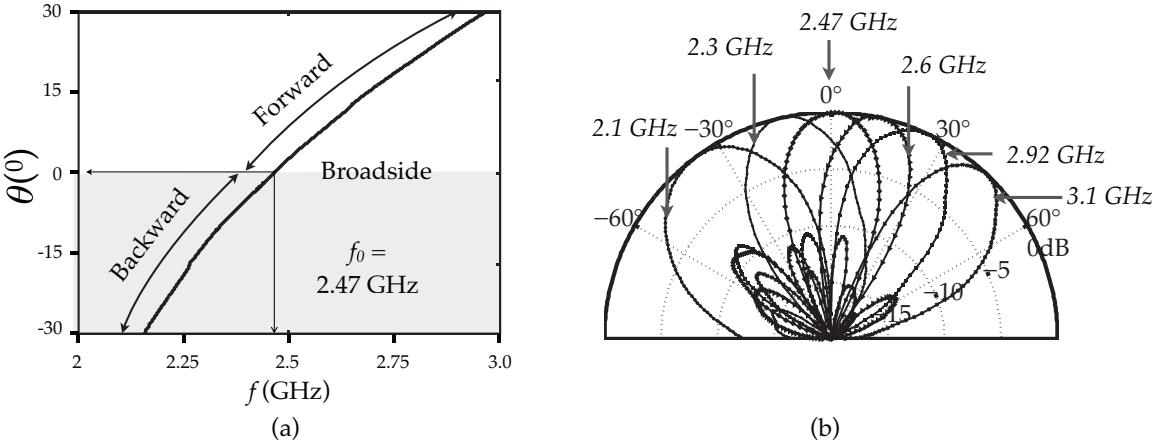

Figure 6.9 Experimental 14-cell CRLH LWA antenna characteristics a) Insertion and return losses. b) Fast-wave region with transition frequency at $f_0 = 2.47$ GHz. c) Beam-scanning law. d) Measured radiation patterns (azimuthal plane, E_ϕ component).

6.3.4.3 Measured Spectrograms

First a constant amplitude linear frequency ramp is fed into the CRLH LWA, as described in Sec. 6.3.2.4, to calibrate the system, as done in the full-wave simulation. The measured time-domain outputs at various detector locations are shown in Fig. 6.10. Due to the beam-scanning law shown in Fig. 6.9(a) of the CRLH LWA, the various detectors, with their operation frequencies as in Tab. 6.2, receive the corresponding frequencies present in the input frequency ramp occurring at different time instants ($\omega - t - \theta$ mapping). This fact is clearly observed from the gradual shift in the signal's voltage peak in the various time-domain waveforms probed by the different patch antenna receivers in Fig. 6.10. Furthermore, the normalized peak received power $P_{r,max}(\theta)$ versus angular location is given in Tab. 6.2, which is used to generated the power calibration vector, also shown in Tab. 6.2, to be used in subsequent measurements. It is of note that the power variation as a function of the radiation angle depends on the radiation angle (and thus frequency), the gain of the transmitting CRLH LWA, as well as the gain of the patch antenna receivers.

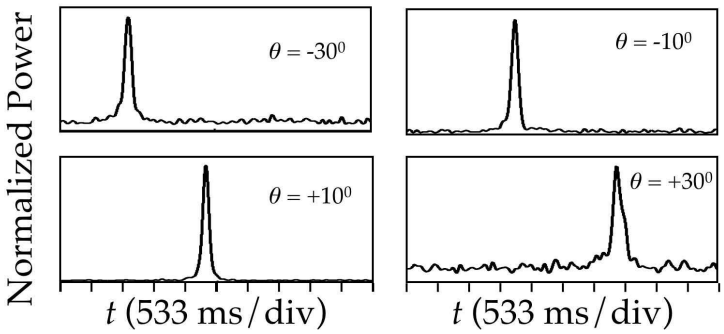

Figure 6.10 Experimental (normalized) time-domain output waveforms with delays corresponding to the $\omega-\theta-t$ sequence indicated in Fig. 6.5, at the four different patch receivers for a constant amplitude linear frequency ramp. The linear frequency ramp is generated using Rhode and Schwarz signal generator (SMIQ 06B). The received power as a function of radiation angle is given in Table 6.2 which is used for magnitude calibration.

After calibration and characterization, the system was tested with various input signals. The corresponding spectrograms are shown in Fig. 6.11. Fig. 6.11(a) shows the measured spectrogram of the modulated Gaussian pulse with a 20 ns time duration

Table 6.2 Experimental calibration data: power distribution (used for magnitude equalization)

Radiation Angle (deg)	Frequency (GHz)	Bandwidth (MHz)	$P_{r,max}(\theta)$ (dBm)	Normalization Vector $\zeta(\theta)$
$-30°$	2.177	40	-9.26	2.94
$-26°$	2.19	40	-5.07	1.79
$-22°$	2.23	60	-5.95	1.98
$-18°$	2.25	40	-10.75	3.44
$-14°$	2.28	50	-5.85	1.96
$-10°$	2.33	50	0	1.0
$-6°$	2.37	50	-4.87	1.76
$-2°$	2.41	60	-7.99	2.51
$2°$	2.46	50	-9.75	3.07
$6°$	2.51	60	-8.3	2.60
$10°$	2.56	70	-4.45	1.68
$14°$	2.61	80	-6.1	2.02
$18°$	2.67	80	-9.17	2.87
$22°$	2.72	80	-7.23	2.29
$26°$	2.8	100	-10.8	3.47
$30°$	2.88	80	-6.93	2.22

obtained using an arbitrary pulse generator. The transform limited nature of the broadband radiating Gaussian pulse is well recovered in the spectrogram. The same accuracy test is performed with the experimental prototype, using an equivalent time gate duration of 2.33 ns. A mean error of 7.46% was observed with the maximum error occurring in the low power regions of the spectrogram. For example, the average error is doubled from 5 to 10% in the spectrogram regions where the mean power is reduced from 9.95 to 5.3% of the maximum power level. Thus, the spectrogram regions containing most of the signal's energy were faithfully recovered.

Fig. 6.11(b) shows the spectrogram corresponding to a two-tone signal (2.25 GHz and 2.60 GHz), where two distinct spectral components are seen on the frequency axis. Fig. 6.11(c) shows the spectrogram of a modulated square pulse, where the main radiation lobe is well recovered with a few side-lobe levels. To test the system with a more complex input signal, a combination of a square pulse with a 10 ns time duration modulated at 2.75 GHz and a continuous wave at 2.25 GHz was fed into the CRLH LWA. This signal may emulate an ultra-fast transient interferer in the transmission channel at 2.25 GHz. The measured spectrogram is shown in Fig. 6.11(d). It is clearly seen that the frequency content of the transient square pulse is identified as soon as it occurs in the testing signal, which is different in this case from the CW transmission at 2.25 GHz. Also of note that the side lobes and nulls of the square pulse are also recovered verifying the square nature of the occurring transient. Fig. 6.11(e) shows the spectrogram of a gaussian pulse mixed with a two-tone signal, where the two modulation frequency bands are clearly seen. Finally, Fig. 6.11(f) shows the spectrogram of a negatively chirped pulse with a width of ≈ 17.5 ns. The negatively chirped pulse is obtained by feeding a 1 ns square pulse, modulated at 2.5 GHz, into 6 identical CRLH transmission lines having 14 unit cells in each line. The spectrum shown in Fig. 6.11(f) is measured at the output of the 6 identical CRLH transmission lines. The spectrum's amplitude level is low due to the propagation losses of the 6 identical CRLH lines, while the amplitude variations are due to the transmission characteristic of the CRLH lines (frequency-dependent Bloch impedance). The dispersion of the negatively chirped 17.5 ns pulse is observed in the spectrogram of Fig. 6.11(f), where higher frequencies are occurring early in time followed by lower frequencies occurring later in time. These few examples experimentally verify the proposed analog RTSA system.

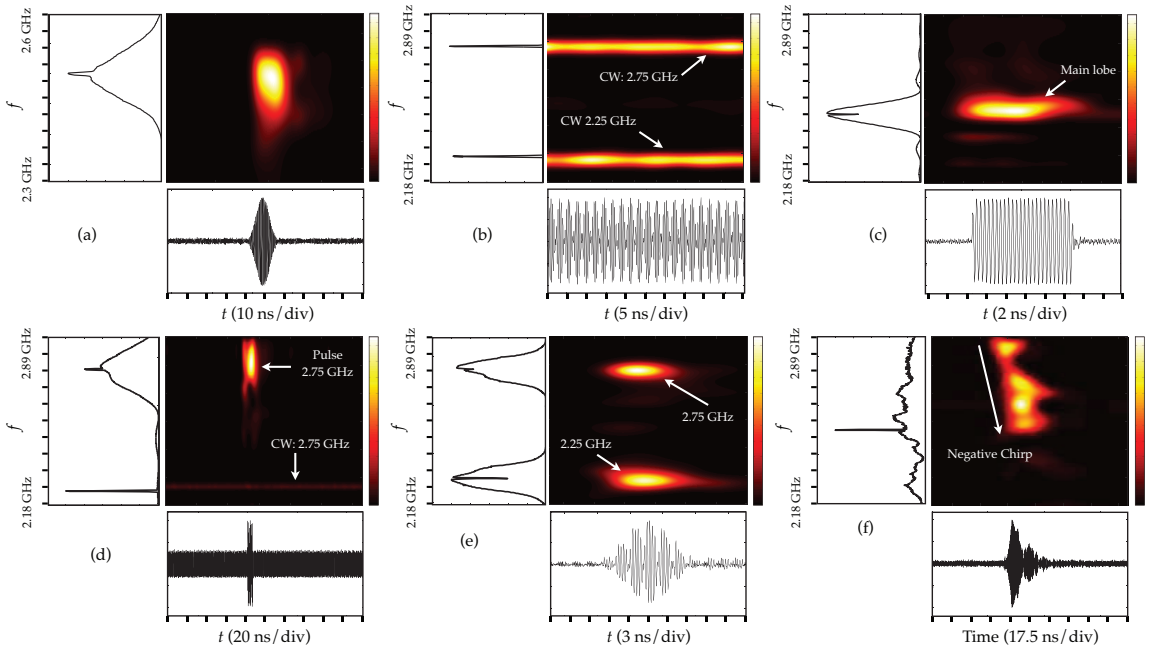

Figure 6.11 Measured spectrograms using the prototype shown in 6.8. All the plots are normalized with a maximum value of 1. a) Modulated gaussian pulse. b) Sum of two tones at $f = 2.25$ GHz and $f = 2.60$ GHz. c) Modulated square pulse at $f = 2.47$ GHz. d) Combination of a sinusoidal signal at $f = 2.25$ GHz and a modulated square pulse with a pulse width of 10 ns and a modulation frequency of $f = 2.75$ GHz. e) Gaussian Pulse mixed with a two-tone signal at $f = 2.3$ GHz and $f = 2.7$ GHz. f) Dispersed square pulse of 1 ns duration propagated along 6 CRLH transmission lines of 14 cells each. The time domain signals are measured in Agilent DSO and the corresponding spectrum (linear normalized scale) is measured on an Agilent spectrum Analyzer (E4446A-44GHZ).

6.3.4.4 System Characteristics

In the experimental prototype, the antenna patch receivers were directly connected to the 50 Ω input of the oscilloscope for measuring the waveforms of up to 4 simultaneous receivers. The oscilloscope used was Agilent's Infinium Digital Sampling Oscilloscope (DSO) 8120B with the following characteristics: noise floor = -55dBm, bandwidth = 12 GHz, rise/fall time (10-90%) = 35 ps, dynamic range = 40 dB for a power range between -55 dBm to -15 dBm, typical for signals used in this work. Therefore, the oscilloscope limits the dynamic range of the overall system to around 40 dB.

However a real system will employ chip envelope detectors. The received signal from each patch antenna, which is attenuated by ~ 30 dB due to free-space loss for a distance of 70 cm, is connected to an envelope detector. A high quality commercial diode detector (e.g. AD813 from Analog Devices) provides a broadband response ($1 - 8$ GHz), features a large dynamic range of $65 - 70$ dB and operates over a wide power range -60 to $+5$ dBm. Furthermore, such a detector can easily follow fast transient signals (similar to ones employed in full-wave simulations and experimental prototype) with a rise/fall time of 6 ns. Finally it is highly accurate with a ± 1 dB of error over the entire dynamic range, while also being resistant against temperature drift ($\pm$ 0.5 dB) and thereby is stable versus process and temperature variations.

Another important aspect of the detectors is the voltage slope (input voltage vs output voltage) as well as the intercept points. A detector calibration measurement can be performed to determine the slope and intercept points for each detector. Once each detector has been calibrated individually, the output voltage can be automatically calculated in the DSP. Alternatively, a calibration measurement can be performed sporadically to re-evaluate the slope and intercept points for each detector to make sure that no drift or offset has occurred. This will ensure the high accuracy of the RTSA proposed here.

Thus, by properly setting the available power at the receiver within the linear operating range of the envelope detector (using if required, a low noise broadband amplifier), the overall system can approach the maximum dynamic range allowed by the envelope detectors in the order of 50 dB. This means that a real RTSA system with diode detectors would provide a dynamic range superior to that provided by the oscilloscope.

6.3.5 System Features and Benefits

The proposed analog RTSA system offers several benefits and advantages compared to the conventional real-time analysis systems. Firstly, it is a completely *analog* system. Since no digital computation is required to generate the RTSA, the only digital processing is done at the post-processing stage, thus requiring neither fast processors nor large memory. Moreover, since the measurements are single-shot (no memory buffers), the systems operates therefore in a real-time mode.

Secondly, the proposed RTSA is a frequency-*scalable* system. The CRLH LWA may be designed at any arbitrary frequency to meet the requirements of the specific applications [4]. Moreover, the length of the CRLH lines (periodic in nature) can be tailored to obtain practically any lengths by cascading the required number of cells and engineering the footprint of the CRLH unit cell to obtained the desired directivity. Therefore, it is suitable for wide-variety of signals, from microwaves potentially up to milli-meter wave frequencies.

Thirdly, the proposed RTSA is inherently *broadband or UWB*, with bandwidth controllable by proper design of the CRLH transmission line. As experimentally demonstrated in [117], the CRLH line can easily attain a bandwidth of 100% using differential MIM structure. This exhibits a leaky-wave region of over 10 GHz. It can therefore handle ultrashort pulses and transient signals in the order of few nanoseconds to a few hundred picoseconds. This represents almost a 1000-fold improvement in time–frequency resolution compared to existing technologies [109].

Lastly, the proposed RTSA is based on far-field probe configurations. However, since the far-fields of the antenna may be deduced from its near-field measurements, by standard near-to-far-field transformations, the system maybe made more compact by using a near-field probing mechanism with additional post-processing.

6.3.6 Resolution Limitations

In contrast to a digital short-time Fourier transform, the proposed RTSA measures the spectrogram of the signal using an analog approach. Whereas a digital short-time Fourier transform time-gates and stores the signal to perform the digital Fourier transform operation, the analog RTSA works in a real-time mode by gating the spatial profile of the testing signal through the aperture of the LWA.

Thus, the physical length of the LWA represents a space gating mechanism which

controls the time resolution of the resulting spectrograms. The shorter the antenna is, the better the sampling of signal spatial profile is, and therefore the better the time resolution of the spectrogram is, and vice-versa. The space gate is thus effectively equivalent to a time gate of $\Delta t = \ell/v_g$, where v_g is the group velocity along the LWA. Moreover, the time resolution also depends on the detector's response time and on the sampling frequency. For the experimental prototype presented in Sec. 6.3.4, the shortest possible gate duration for a given aperture ℓ is thus $\Delta t \approx 2$ ns. This shortest gate imposes a lower limit on the signal duration which can be analyzed by the system prototype.

On the other hand, the physical length of the aperture controls the directivity of the LWA and therefore also controls the frequency resolution of the generated spectrogram. The longer the antenna is, the better the directivity is, and therefore the better the frequency resolution of the resulting spectrogram is, and vice-versa. Furthermore, the number of probes in far-field of the antenna controls frequency sampling of the spectrogram. In the demonstrated experimental prototype for example, the average frequency sampling is 45 MHz with the total acquisition bandwidth of 713 MHz.

Due to this fundamental tradeoff between the time and frequency resolution the antenna length is critical. A given analog RTSA will have a specified minimum time resolution directly related to this length. A commercial analog RTSA could offer CRLH LWA antennas of different lengths, which could be switched by the user to accommodate different signals.

6.4 Frequency Resolved Electrical Gating (FREG) System

Analog RTSAs as described in the previous section, generate the spectrograms of the signal in real-time using the spatial-spectral decomposition property of the CRLH LWA, with minimal requirement on computational resources. However, the time and frequency resolution of spectrograms generated using this technique unfortunately depends on the physical length of the CRLH LWA, which is fixed in a given system.

In this section, a complementary analog approach to obtain spectrograms where this hardware dependence is suppressed, at the cost of the requirement of periodicity of the input signals, is presented [30]. This approach is inspired from a similar system

known in optics as Frequency Resolved Optical Gating (FROG) [110], where a self-gating principle is applied to provide close to ideal spectrograms for arbitrary test signals. Here, we propose a microwave counterpart of the FROG system, which we term Frequency Resolved Electrical Gating (FREG).

6.4.1 Proposed System

In order to compute a spectrogram of a signal $A(t)$, a gating function $g(t)$ is required, as shown in Eq. (6.5). In the self-gating principle, instead of using a separate time signal as the gate function, the *envelope of the testing signal* itself is used as the gating function, i.e. $g(t) = |A(t)|$. The spectrogram of a signal $A(t)$ is thus modified as

$$S(\tau, \omega) = \left| \int_{-\infty}^{\infty} A(t)|A(t-\tau)|e^{-j\omega t}dt \right|^2 . \tag{6.9}$$

The proposed FREG system, based on this self-gating principle and on the spatial-spectral decomposition property of the CRLH LWA, is depicted in Fig. 6.12. The testing signal, whose spectrogram is to be generated, is split into two channels. One of the channels is envelope detected and passed through a tunable delay line. The two channels are then mixed together. The mixer thus performs the self-gating process at a given time delay instant τ. This self-gated signal is then injected into a CRLH LWA which spectrally resolves it in space. Once the frequency components are separated in space, antennas circularly placed in the far-field of the LWA receive the different frequency components corresponding their angular position. All the received signals are then digitized and summed, before being stored for spectrogram display. This process is repeated for different values of the time delay τ so that the entire test signal is scanned, according to Eq. (6.9), until the spectrogram is fully constructed. Since, the beam scanning law of Eq. 6.1 is nonlinear in nature, a final post-processing step is required to linearize the spectrogram.

6.4.2 System Features

The proposed system exhibits significant advantages over the analog RTSA system and purely digital systems. Due to the self-gating process, neither the time and nor the frequency resolutions of the generated spectrogram depend on the physical length

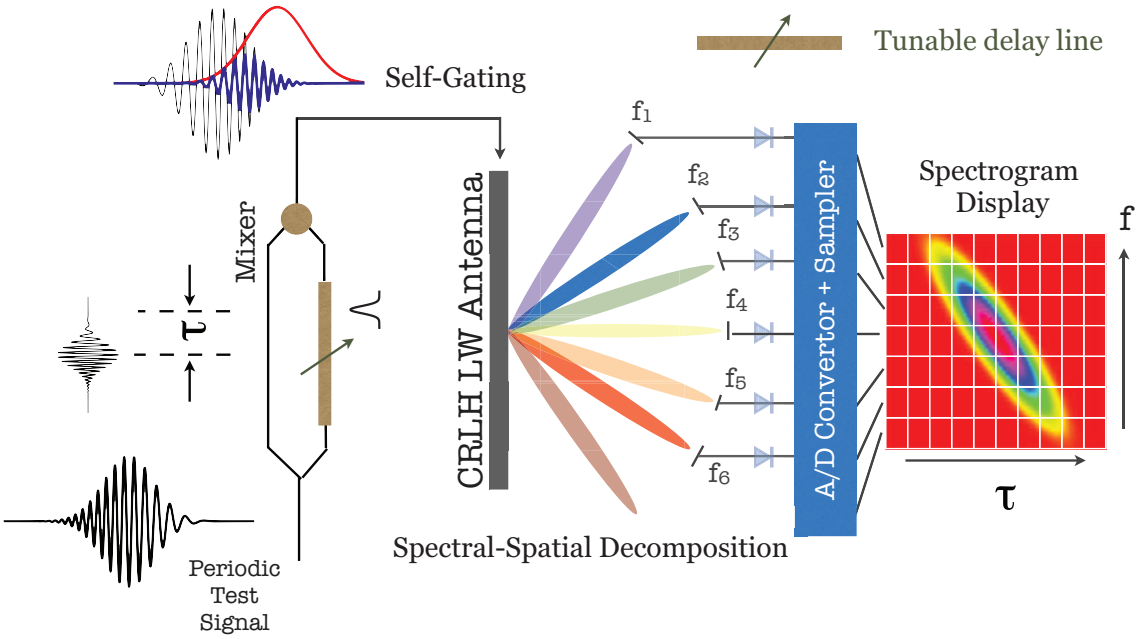

Figure 6.12 Proposed frequency resolved electrical gating (FREG) system.

of the antenna. The time and frequency resolutions are thus dependent only on the time signal itself and the hardware dependence spectrogram is suppressed. The LWA simply plays a role of spectral decomposer which, when longer (higher directivity), provides better separation of frequencies in space.

The choice of the gate duration is an important parameter to achieve an optimal time – frequency resolution in the spectrogram. An optimal gate duration for pulses with dominating phase variations is given by $T_g \approx 1/\sqrt{2|\phi''(t)|}$, where $\phi''(t)$ is the second time derivative of phase [118]. This duration permits the resolution of the fastest phase variations. For general pulse measurement, a gate duration as short as the testing signal itself or slightly shorter is thus desirable. Since the FREG system is based on self-gating, the gate duration is close to optimal and the corresponding spectrograms are ideal [110].

Moreover, the proposed system being analog in nature, does not require fast processors nor huge memory buffers, which avoids placing a heavy computational burden on the system. Furthermore, the system is frequency scalable and sufficiently broadband to handle a wide variety of UWB signals. As mentioned above, the length of the LWA controls the spectral decomposition of the gated signal, which is improved as the physical length of the antenna is increased.

Finally, since it uses a multi-shot measurement procedure, where the testing signal is gated several times with different time delays τ, the proposed FREG system requires a periodic signal. This is the main constraint of the FREG system.

6.4.3 Time-domain Green's function

In this section, the proposed FREG system is demonstrated numerically using an efficient time-domain Green's function approach [116]. This approach is used to compute the field radiated by a source constituted by an arbitrary (possibly dispersive, anisotropic and nonlinear) homogeneous leaky transmission line as a function of time. If the source is punctual, $J(\vec{r}_g, t') = \delta(\vec{r}_g)I(t')$, where $I(t') = A(t)|A(t-\tau)|$ is the gated signal in case of FREG, the voltage $V(\vec{r}, t)$ along a 1D line may be expressed as

$$V(\vec{r}, t) = -\frac{\mu_0}{2\pi} \int \tilde{G}_V(\vec{r}, \vec{r}_g; \omega)\, \tilde{I}(\omega)\, e^{j\omega t} d\omega, \tag{6.10}$$

where $\tilde{G}_V(\vec{r},\vec{r}_g;\omega) = \exp[-\gamma(\omega)R]$ denotes the Green's function in the frequency domain and $\tilde{I}(\omega)$ is the Fourier transform of the temporal waveform excited by the source. Once the current distribution on the structure has been computed from this expression for an arbitrary input pulse excitation, standard radiation integrals are used to determine the far-fields in the time domain [119]. This approach provides an ideal tool and a fast technique to model radiation from a CRLH LWA, which represents the spatial-spectral decomposition section of the FREG system.

6.4.4 Simulated Spectrograms

We will now compute the FREG spectrograms of various signals using the time-domain Green's function approach described in the previous section. Consider a 16-cell CRLH LWA with the parameters $C'_L = C'_R = 1$ pF, $L'_L = L'_R = 2.5$ nH and a unit cell size of 2 cms, easily implemented in metal-insulator-metal (MIM) technology [5]. In the FREG system, the envelope of the testing signals are numerically obtained and used as a gating function. The mixer performing the self-gating operation is modeled by a simple mathematical product taking into account the tunable time delay between the replica of the test signal and the gate signal, which is then fed into the CRLH LWA.

The various modulated testing pulses are gaussian-type signals which may be generally expressed as

$$A(t) = \exp\left[-\frac{1}{2}\frac{(1+jC_1)(t-t_0)}{T}^{2m} + jC_2(t-t_0)^3\right]\exp(j2\pi f_0 t)$$

where t_0 is the initial pulse offset, T is the full-width half maximum of the gaussian pulse, C_1 and C_2 are the chirp parameter, f_0 is the modulation frequency and m is an integer.

Fig. 6.13 shows FREG-generated spectrograms. Figs. 6.13(a) and (c) show the spectrograms of a down-chirped and up-chirped gaussian pulses, respectively. A faithful representation of a linear instantaneous frequency variation is obtained. The spectrogram of a modulated un-chirped super-gaussian pulse is shown in Fig 6.13(b), where the occurrence of all the frequency components of the signal at the same time instant are clearly seen. Finally, Fig. 6.13(d) shows the spectrogram of a cubically

chirped (down and up) gaussian pulse. The high frequency components occurring at two different times, characteristic of cubically chirped pulses, can be clearly identified. These few examples demonstrate the capability of the proposed FREG system to analyze a wide variety of non-stationary signals.

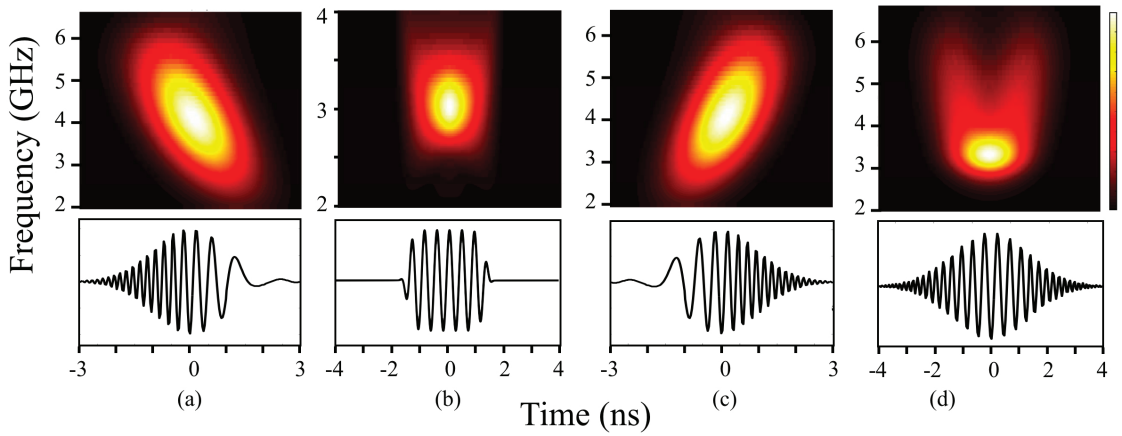

Figure 6.13 Simulated spectrograms a) Down-chirped gaussian pulse ($C_1 = -10$, $C_2 = 0$, $f_0 = 4$ GHz) b) Non-chirped super-gaussian pulse ($C_1 = C_2 = 0$, $f_0 = 3$ GHz) c) Up-chirped gaussian pulse ($C_1 = +10$, $C_2 = 0$, $f_0 = 4$ GHz) d) Cubically chirped gaussian pulse ($C_1 = 0$, $C_2 = 0.25 \times 10^{28}$). All pulse have a FWHM duration of 1 ns with a initial pulse offset of $t_0 = 6.5$ ns.

6.5 Summary

Two radiated-wave applications of full-space scanning leaky-wave structures has been presented. Firstly, a frequency division full-diplexing transceiver system based on the beam-scanning property of the CRLH LWA has been experimentally demonstrated. The full-diplexing operation of simultaneous uplink and downlink transmission was confirmed. The proposed system offers a passive transceiver solution with lesser hardware requirements and higher signal isolation due to the directive nature of the LWA and the band-pass filter employed in the system. Secondly, a novel analog real-time spectrum analyzer (RTSA) for the analysis of complex non-stationary signals has been presented, demonstrated, and fully characterized. This RTSA exploits

the space-frequency mapping (spectral-spatial decomposition) property of the composite right/left handed (CRLH) leaky-wave antenna (LWA) to generate the real-time spectrograms of arbitrary testing signals. Compared to digital RTSAs, it exhibits the advantages of real-time acquisition, low computational cost, frequency scalability, and broadband (UWB) operation. The system has been demonstrated both theoretically and experimentally. The theoretical demonstration has included both full-wave simulation by a commercial software and analysis by an efficient time-domain Green's function approach. The experimental demonstration has been based on parallel-waveguide prototype including an MIM CRLH LWA, 16 patch antenna probe detectors circularly arranged around the LWA, and a digital oscilloscope has been used to perform the A/D conversion and time-domain acquisition before the postprocessing and displaying of the spectrogram. In all cases, the RTSA has been able to generate the proper spectrograms in excellent agreement with theoretical predictions. The fundamental tradeoff between time and frequency resolutions inherent to all RTSA systems have been discussed and a inter-changeable multi CRLH LWA solution has been proposed to handle signals with different time durations. Due to its unique features and benefits compared to digital RTSAs, the proposed analog RTSA may represent an alternative solution of particular interest for high frequencies and UWB signals. Finally, an alternative configuration for real-time spectrum analysis, frequency resolved electrical gating, has been proposed where the time resolution of the resulting spectrum becomes independent of the length of the antenna at the cost of requirement of periodicity in the testing signals.

Chapter 7

Conclusions and Future Works

This thesis focuses on the recent advances of microwave dispersive networks for ASP in two regimes: guided-wave and radiated-wave. The C-section based all-pass networks have been exclusively employed in guiding applications, whereas CRLH leaky-wave structures has been used for radiating applications. The selected articles represent novel ASP concepts, components and systems all suited for impulse regime operation.

Chapter 2 introduced the concept of ASP and group delay engineering. Based on various dispersion parameters, the ASP applications have been classified and the concept of dispersive delay structures was introduced.

In Chapter 3 and 4, two types of non-commensurate all-pass dispersive delay structure have been presented - uncoupled cascaded C-sections and coupled cascaded C-sections. A complete closed-form group delay synthesis procedure has been provided for the case of uncoupled cascaded C-sections in Chapter 3, based on an efficient iterative procedure. It was found that this procedure required high coupling coefficients in the resulting C-sections. Among the various solutions that were proposed, the one utilizing the higher order harmonic response of the C-section was used to relax the high coupling coefficient requirement. In addition, another technique to boost the coupling coefficient in a C-section using ferrimagnetic substrates has also been proposed in Chapter 3. Chapter 4 continued the discussion on C-section all-pass networks and a coupled non-commensurate C-section network was introduced. The proposed structure provides a larger dispersion as compared to the uncoupled case for a given foot print size. However, it lacked a closed form synthesis procedure. Nonetheless, the proposed structure has been analyzed using a fast and an efficient full-wave analysis based on multiconductor transmission line theory utilizing coupled inductance and capacitance matrices. Finally using genetic algorithms to synthesize varied group delay responses, several prototypes have been presented.

Next two chapter were then dedicated to various instrumentation, communication

and security system applications. Whereas Chapter 5 focussed on guided-wave applications, radiative-wave applications were presented in Chapter 6. Among various guided-wave applications, four main applications were chosen: tuneable delay lines, frequency discriminators, group delay engineered RFIDs and dispersion compensation in log-periodic dipole array antennas, to cover several aspects of ASP applications of DDSs. In Chapter 6, radiative -wave application using CRLH leaky-wave antenna were introduced. Firstly, a frequency duplexing transceiver system was presented for narrowband application and next, a novel analog real-time spectrum analyzer was presented and demonstrated, which is useful for characterizing complex non-stationary signals.

Next three subsections presents some possible direct extensions of this work related to a) optimized and efficient DDS implementations, b) group delay synthesis procedures, and c) future ASP applications.

7.1 Waveguide Implementations of All-Pass Networks

Lets recall that the core of an ASP system is a dispersive delay structure (DDS), which is an frequency dependent group delay device, differentiating the various spectral components of a signal in the time domain from their different incurred propagation delays. The time resolution of an ASP system for a given set of frequencies within the frequency range $\Delta\omega = (\omega_{\max} - \omega_{\min})$ is proportional to the group delay swing of the DDS, $\Delta\tau = (\tau_{\max} - \tau_{\min})$. Therefore, DDSs with large $\Delta\tau$ are highly desirable in all ASP applications [3].

As has been seen, the group delay response of a DDS can be conveniently synthesized by a series cascade of non-commensurate all-pass C-sections contributing different group delays at different frequencies, as illustrated in Fig. 7.1 [6]. The C-sections are realized by coupled-line couplers shorted at one end. They are characterized by the voltage coupling coefficient k, which determines the group delay swing $\Delta\tau$: As k becomes larger, so does $\Delta\tau$, which results in higher resolution. Conventional all-pass C-sections, based on coupled transmission lines, suffer from two major issues: a) their k is restricted to relatively low values, typically less than 60%, due to fabrication limitations of edge-coupled and broadside-coupled coupled-line couplers [64],

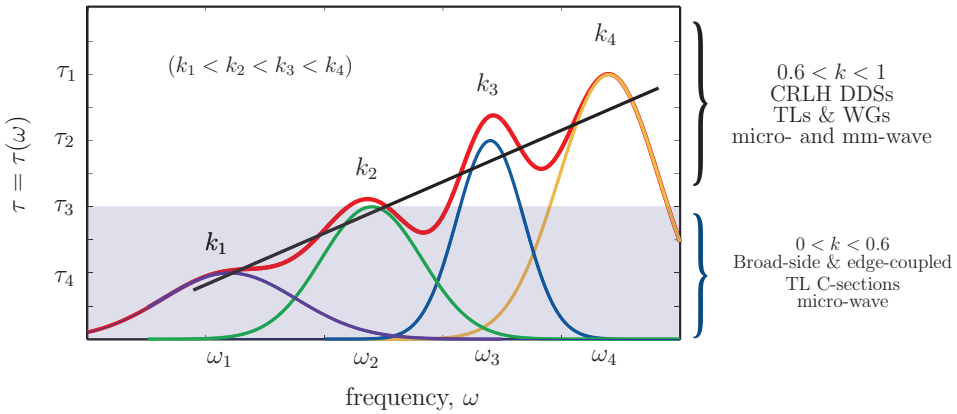

Figure 7.1 Principle of group delay engineering using cascaded non-commensurate all-pass C-sections consisting of shorted coupled transmission line structures [6]. The group delay swing $\Delta\tau_i$ is proportional to k_i, where k_i is the voltage coupling coefficient of the i^{th} section. Low k values may be realized using conventional C-sections while high k values require an alternative DDS, as the CRLH-CRLH coupler DDS proposed here.

and b) they cannot be implemented in waveguide technology, as waveguide couplers provide either forward-wave coupling or dispersionless backward coupling; therefore they cannot be scaled to very high frequencies due to prohibitive losses [66].

To address these issues, a new DDS based on coupled composite right/left-handed (CRLH) transmission lines is proposed. The proposed DDS uses a CRLH-CRLH coupler configuration, which is known to be capable of providing quasi-0 dB backward coupling (i.e. $k \approx 100\%$), as required for high ASP resolution, in convenient configuration which is uniplanar and does not require bonding wires [66]; this fact allows to solve issue a) above. Moreover, CRLH structures can be easily implemented in waveguide configuration [120], with smaller loss, compared to their transmission line counterparts, at high frequencies; which solves issue b) above.

Whereas, issue a) is solved as explained next, issue b) needs to be demonstrated. The waveguide implementation of such DDSs is critical for success of ASP concepts at high frequencies as it is expected to lead to compact and low-loss DDSs. This represents an important future effort required for successful and high impact ASP applications. CRLH based DDSs is an initial attempt to achieve this goal and some preliminary results will be presented next [16].

The 2-port transfer function of a coupled-line based DDS can be written in terms of the coupled (S_{21}) and through (S_{31}) S-parameters of the 4-port coupler (assuming perfect matching and infinite isolation) as [6]

$$S_{21} = S_{\text{coupled}} + \frac{S_{\text{through}}}{1 - S_{\text{coupled}}^2}, \tag{7.1}$$

from which the transmission group delay is obtained as $\tau(\omega) = -d \arg\{S_{21}(\omega)\}/d\omega$. So far in this work, only the conventional coupled-line couplers have been used, however, any kind of coupled-lines may be employed and on attractive possibility is a CRLH-CRLH coupler.

Fig. 7.2(a) shows a prototype of a typical metal-insulator-metal (MIM) implementation of a CRLH-CRLH coupler. It is composed of two CRLH transmission lines, which are designed to be balanced (i.e. exhibiting a seamless transition between the left-handed and right-handed frequency bands) in the absence of coupling. Its equivalent transmission line circuit model is shown in Fig. 7.2(b), where the two CRLH lines are coupled to each other through the capacitive and inductive coupling parameters C_m and L_m, respectively. The CRLH-CRLH coupler has the unique capability (while being uniplanar and not requiring bonding wires) of achieving arbitrary level of backward coupling (up to quasi-0 dB) with a high directivity [62]. Its typical coupling and return loss levels are shown in Fig. 7.2(c), where a high level of coupling is achieved between the input and the coupler port over a large bandwidth, with a maximum of -1.7 dB at 6 GHz.

The CRLH-CRLH coupler can be modelled using the quasi-TEM approach for planar microstrip couplers using the circuit model of Fig. 7.2(b), as described in [62]. Assuming perfect matching, $S_{11} = 0$, and infinite isolation, $S_{41} = 0$, the coupled and the through S-parameters are given by [62]

$$S_{\text{coupled}} = S_{21} = \frac{2\beta_r e^{-j(\beta_d - \beta_r)\ell}}{\beta_r(1 + e^{j2\beta_r\ell} - \beta_a(1 - e^{j2\beta_r\ell})}, \tag{7.2}$$

$$S_{\text{through}} = S_{31} = \frac{K_{BW}(1 - e^{-j2\beta_r)\ell}}{\beta_r(1 + e^{j2\beta_r\ell} - \beta_a(1 - e^{j2\beta_r\ell})}, \tag{7.3}$$

with $\beta_{d,r} = (\beta_I \pm \beta_{II})/2$, where $\beta_{I,II}$ are the two coupled-mode propagation constants of the coupler. This quasi-TEM model can be used to extract the circuit parameters of Fig. 7.2(b) either from full-wave simulated or measured S-parameters of the 4−port

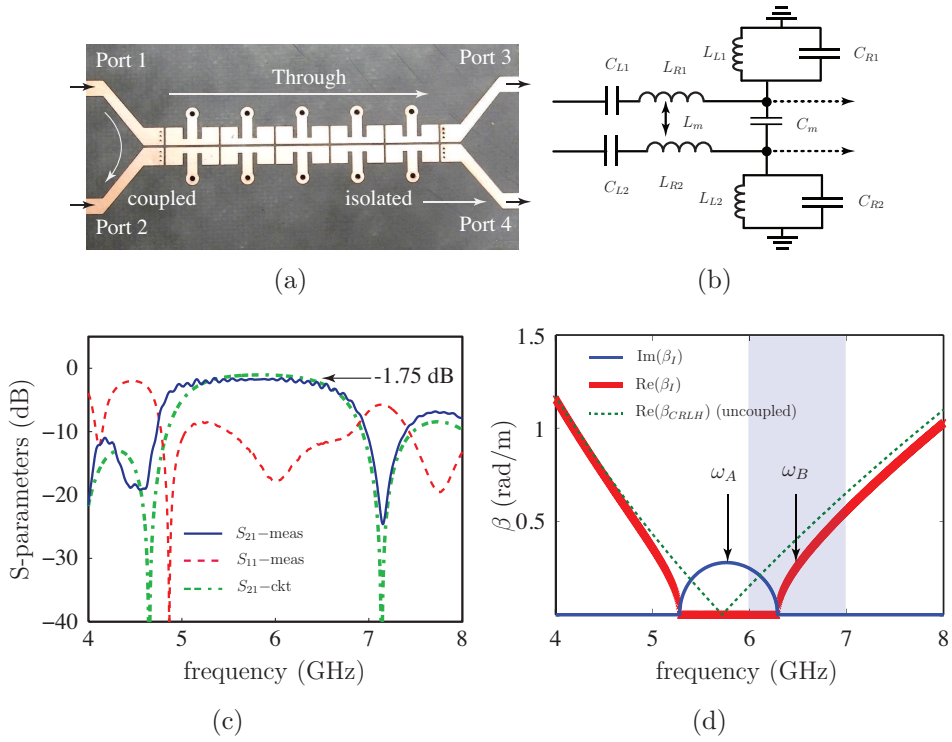

Figure 7.2 CRLH-CRLH coupler. a) Photograph of the fabricated prototype. b) Infinitesimal CRLH transmission line equivalent circuit model. c) Measured coupling and return loss levels, and circuit-model S_{21} curve with the curve-fitted parameters: $L_{R1} = L_{R2} = 2.4$ nH, $C_{R1} = C_{R2} = 0.863$ pF, $L_{L1} = LL2 = 0.748$ nH, $C_{L1} = C_{L2} = 0.412$ pF, $L_m = 0.4$ nH and $C_m = 0.15$ pF. d) Coupled-mode propagation constants β_I ($\beta_{II} = -\beta_I$, not shown), and uncoupled CRLH propagation constant.

coupler using curve fitting, as shown in Fig. 7.2(c). The corresponding coupled-mode propagation constants are shown in Fig. 7.2(d). Based on the coupling characteristics of a CRLh-CRLH couple, just like a C-section is formed by interconnecting two end ports of a conventional 4−port backward-coupling coupled-line coupler, a new DDS can be devised based on a CRLH-CRLH coupler, as shown in Fig. 7.3(a). The resulting structure acts as an all-pass C-section in a restricted frequency range with $|S_{21}| = 1$ where a frequency dependent group delay response is achieved. A typical response of the 2-port DDS is shown in Fig. 7.3(b), using to the circuit model of Fig. 7.2. As may be seen, the CRLH DDS exhibits a large group delay variation versus frequency along with unity amplitude transmittance, both being necessary

attributes for an efficient DDS. Fig. 7.3(b) also shows that this CRLH DDS achieves the same amount of dispersion ($\Delta\tau$) as would be achieved by a conventional C-section with a coupling factor of $k = 99.8\%$, a coupling level which would be extremely hard to achieve in practice.

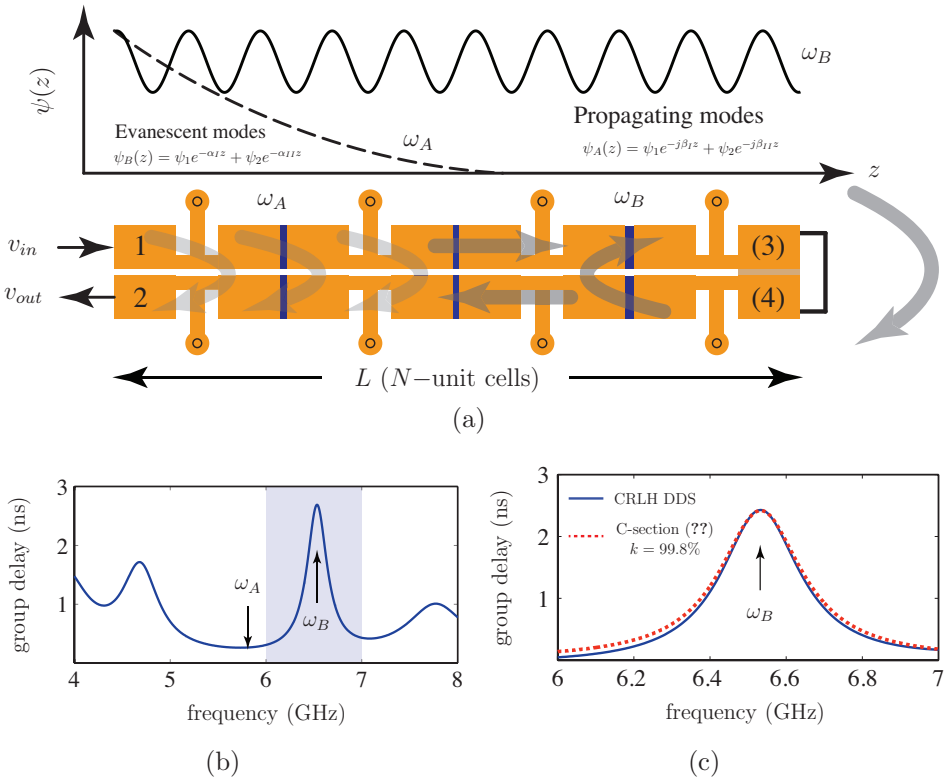

Figure 7.3 Proposed 2-port DDS formed by interconnecting the ports 3 and 4 of the 4-port CRLH-CRLH coupler. a) DDS layout. b) Circuit group delay response for the parameters of Fig. 7.2 computed using (7.1), (7.2) and (7.3). c) Zoom on the high group delay region of b).

The next future step is translate these ideas to high-frequencies and realize a completely shielded waveguide prototype realizing a prescribed group delay response as a cascade of several such coupled waveguide sections. A more general approach of waveguide-based DDS is based on cross-coupled techniques. This is described next.

7.2 Cross-Coupling Group Delay Synthesis Procedure

In this work, the employed DDSs were usually an all-pass network based on coupled transmission lines [57], [2]. An all-pass network requires that the magnitude be unity at all frequencies, which limits the implementation of DDSs to coupled transmission line sections or lattice circuits. Relaxing the all-pass networks requirement enable the DDS to be designed as cross-coupled networks using the coupling-matrix theory [52] and implemented in arbitrary coupled-resonator technology. This has three main advantages:

1. The DDSs based on cross-coupled networks naturally lead to waveguide-type implementations which are ideal, and much required, for high frequency ASP applications.
2. The cross-coupled synthesis provides rich tools for group delay synthesis and is expected to lead to novel research directions in future filter techniques.
3. The conventional C-sections based on transmission lines are restricted to low microwave frequencies and thus the coupled-resonator technology provides a seamless transition of the DDS concept from microwave to millimetre wave frequencies.

The future challenge is to synthesize the transfer function involving both magnitude and phase prescription. The general synthesis method for simultaneous magnitude and phase specifications was developed in [53] and later refined in [121]. A systematic synthesis method based on the coupling-matrix theory is much required for cross-coupled DDSs.

The objective here is to synthesize a transfer function for a lowpass response of the type shown in Fig. 7.4, where the group delay and magnitude are simultaneously prescribed over a specified frequency band ($0 \leq \Omega \leq 1$), while the response beyond the passband is of secondary importance, as shown in the shaded part of Fig. 7.4. Compared with conventional filter specifications [13], the DDS has no requirement for the magnitude selectivity and out-of-band performance.

A novel synthesis method is recently proposed in [122]. In this work, a sixth-order DDS with linear group delay response is designed to verify the proposed synthesis method. The synthesized coupling matrix and the corresponding folded-form topology

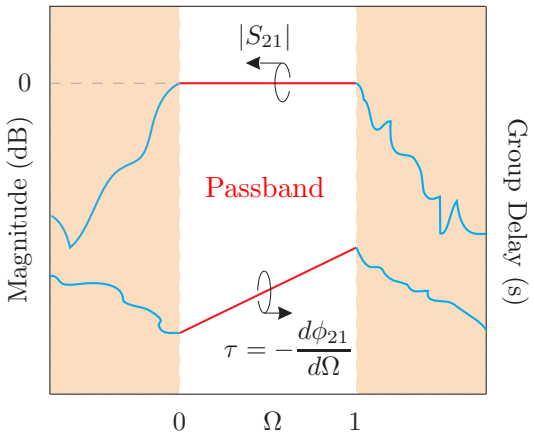

Figure 7.4 Ideal response of a cross-coupled DDS (Typical linear group delay example).

are shown in Fig. 7.5(a). The calculated scattering parameters and the group delay derived through the synthesized coupling matrix are shown in Fig. 7.5(b). It is noted that a linear group delay as well as low and flat insertion loss are achieved in the entire passband ($0 \leq \Omega \leq 1$). These initial results represents encouraging directions for group delay synthesis techniques and various new filter techniques are expected to come out of this effort.

7.3 Future ASP Applications

Apart from various ASP applications presented in Chapter 5 and 6, there are many related and advanced applications that needs to be explored and investigated based on system cost, performance and new concepts. Tab. 7.1 summarizes these ASP applications along with their fundamental characteristics. They can be categorized into four major categories:

1. The frequency discriminator presented in Chapter 5 is a building block of a frequency sniffer, using which various spectrum components can be detected in a given environment. These spectrum sniffers thus operate as passive (listening only) frequency sensors utilizing the DDS as a frequency discriminator [123]. Based on the delay versus frequency law of the DDS such sniffers can identify different signals in the environment of the wireless system in a very low-cost manner (compared to frequency-domain approaches), with applications

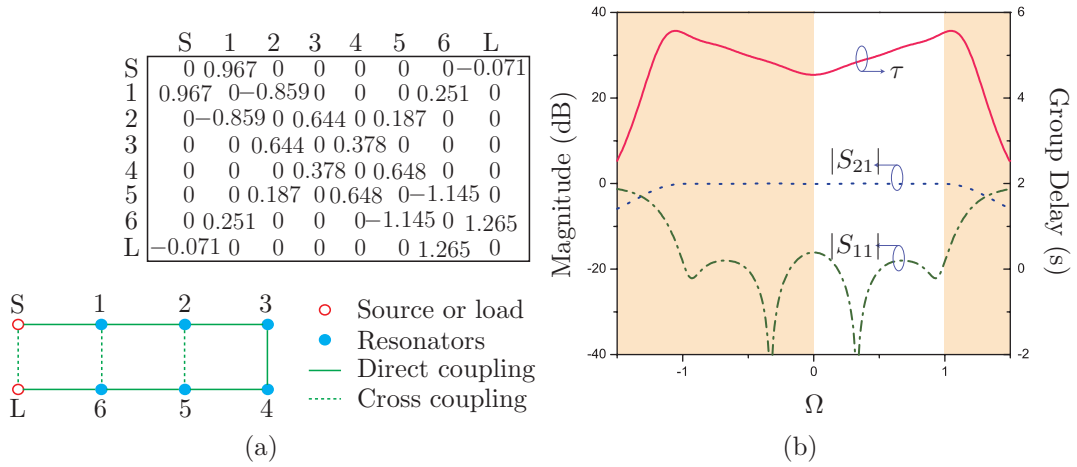

Figure 7.5 Group delay synthesis using cross-coupled techniques. a) Synthesized coupling matrix and folded topology for the cross-coupled DDS example. b) Scattering parameters of the sixth-order cross-coupled DDS.

including interference detection, white space determination and clear channel assessment for high-efficiency cognitive (adaptive) radio communication.

2. The real-time (RT) FMCW radars are the active counterparts of the spectrum sniffers, mostly utilizing the DDS as a frequency meter [3]. By allowing the location (possibly in conjunction with a direction of arrival estimator) and identification of users, it can enhance opportunistic communication systems using directive scanning antennas, leading to maximal data rates or low power consumption systems.

3. The PPM transceivers starting from the pulse position modulation (PPM) transmitter already reported [20], has a potential for applications in cost-effective short-range wireless transmission, as in the case of device-to-device file transfer or radio identifications (RFID) [19] of similar personal digital administrators (PDAs) for cooperative communications.

4. Finally, noting that an orthogonal frequency division multiplexing (OFDM) transmitter is essentially a digital inverse/Fourier transformer, an RT OFDM systems can be devised. Such systems may lead to some simplifications in the front-end (e.g. suppression of series-to-parallel converters) and have a potential to be competitive at millimeter-wave frequencies, where the AD/DA convert-

ers required in conventional OFDM systems may be prohibitively expensive or simply too slow.

Table 7.1 The Four ASP Application Categories

	Device	Operation	DDS Utilization	Applications
1.	Spectrum Sniffers	passive frequency sensing	frequency discriminator	interference detection, white space determination, clear channel assessment
2.	RT FMCW Radars	active frequency detection & ranging	frequency meter	users location & identification, for directive/adaptive opportunistic communication
3.	PPM Tranciev-ers	low-cost & short-range wireless transmission	pulse modulator	device-to-device file transfer, RFIDs of similar PDAs for cooperative communication
4.	RT OFDM Tranciev-ers	longer range & high data rate transmission	broadband RTFT	60 GHz communications

References

[1] V. Boucher, L. P. Carignan, T. Kodera, C. Caloz, A. Yelon, and D. Ménard, "Effective permeability tensor and double resonance of interacting bistable ferromagnetic nanowires," *Phys. Rev. B*, vol. 80, no. 8, pp. 1 – 11, Dec. 2009.

[2] S. Gupta, A. Parsa, E. Perret, R. Snyder, R. Wenzel, and C. Caloz, "Group-delay engineered noncommensurate transmission line all-pass network for analog signal processing," *IEEE Trans. Microw. Theory Tech.*, vol. 58, no. 9, pp. 2392 – 2407, 2010.

[3] B. Nikfal, S. Gupta, and C. Caloz, "Increased group delay slope loop system for enhanced-resolution analog signal processing," *IEEE Trans. Microw. Theory Tech.*, vol. 59, no. 6, pp. 1622 – 1628, Jun. 2011.

[4] C. Caloz and T. Itoh, "Electromagnetic metamaterials, transmission line theory and microwave applications," p. 352, Jan 2006.

[5] S. Abielmona, S. Gupta, and C. Caloz, "Experimental demonstration and characterization of a tunable CRLH delay line system for impulse/continuous wave," *IEEE Microw. Wireless Compon. Lett.*, vol. 17, no. 12, pp. 864 – 866, 2007.

[6] S. Gupta, A. Parsa, E. Perret, R. V. Snyder, R. J. Wenzel, and C. Caloz, "Group delay engineered non-commensurate transmission line all-pass network for analog signal processing," *IEEE Trans. Microwave Theory Tech.*, vol. 58, no. 8, pp. 2392–2407, Aug. 2010.

[7] M. Skolnik, "Introduction to radar systems," *3rd Ed, McGraw Hill*, 2011.

[8] M. Lewis, "SAW and optical signal processing," *in Proc. IEEE Ultrason. Symp., Rotterdam, The Netherlands*, pp. 800–809, Sept. 2005.

[9] C. Campbell, "Surface acoustic wave devices and their signal processing applications," *New York: Academic*, 1989.

[10] W. S. Ishak, "Magnetostatic wave technology: a review," *Proceedings of the IEEE*, vol. 76, no. 2, pp. 171 – 187, 1988.

[11] V. S. Dolat and R. C. Williamson, "A continuously variable delay-line system," *1976 Ultrasonics Symposium*, pp. 419 – 423, 1976.

[12] M. A. G. Laso, T. Lopetegi, M. J. Erro, D. Benito, M. J. Garde, M. A. Muriel, M. Sorolla, and M. Guglielmi, "Real-time spectrum analysis in microstrip technology," *IEEE Trans. Microw. Theory Tech.*, vol. 51, no. 3, pp. 705–717, Mar. 2003.

[13] G. Matthaei, L. Young, and E. M. T. Jones, *Microwave Filters, Impedance-Matching Networks, and Coupling Structures.* Artech House, 1980.

[14] S. Gupta, D. Sounas, Q. Zhang, and C. Caloz, "All-pass dispersion synthesis using microwave c-sections," *IEEE Trans. Microw. Theory Tech., submitted*, 2011.

[15] S. Gupta, L. P. Carignan, and C. Caloz, "Group delay swing enhancement in transmission-line all-pass networks using coupling and dispersion boosting ferrimagnetic substrate," *Microwave and Optical Technology Letters*, in press.

[16] S. Gupta and C. Caloz, "Highly dispersive delay structure exploiting the tight coupling property of the CRLH-CRLH coupler for enhanced resolution analog signal processing," *Microwave Symposium, 2011 IEEE MTT-S International, submitted*, Jun. 2011.

[17] S. Gupta, S. Abielmona, and C. Caloz, "Carrier frequency tunable impulse/continuous wave CRLH delay line system," *Proc. IEEE AP-S Int. Symp., Honolulu, HI.*, pp. 5523 – 5526, Jun. 2007.

[18] H. V. Nguyen, S. Abielmona, and C. Caloz, "Analog dispersive time delayer for beam-scanning phased array without beam-squinting," *in Proc. IEEE AP-S International Symp., San Diego, CA*, July 2008.

[19] S. Gupta, B. Nikfal, and C. Caloz, "Chipless RFID system based on group delay engineered dispersive delay structures," *IEEE Antennas Wirel. Propagat. Lett.*, vol. 10, pp. 1366–1368, Dec. 2011.

[20] H. Nguyen, S. Abielmona, and C. Caloz, "CRLH delay line pulse position modulation transmitter," *IEEE Microw. Wireless Compon. Lett.*, vol. 18, no. 8, pp. 527 – 529, 2008.

[21] S. Gupta and C. Caloz, "Temporal Talbot effect in left-handed metamaterial transmission lines," *in URSI Int. Symp. on Electromagnetic Theory (EMTS), Ottawa, ON*, Jul. 2007.

[22] J. S. Gómez-Díaz, A. Alvarez-Melcon, S. Gupta, and C. Caloz, "Spatio-temporal talbot phenomenon using metamaterial composite right/left-handed leaky-wave antennas," *J. Appl. Phys.*, vol. 104, pp. 1–7, Nov. 2008.

[23] ——, "Tunable talbot imaging distance using an array of beam-steered metamaterial leaky-wave antennas," *J. Appl. Phys.*, vol. 106, pp. 1–8, Oct. 2009.

[24] S. Gupta and C. Caloz, "Analog real-time Fourier transformer using a group delay engineered C-section all-pass network," in *IEEE Antennas and Propagation Society International Symposium*. IEEE, 2010, pp. 1–4.

[25] ——, "Analog inverse Fourier transformer using group delay engineered C-section all-pass network," in *European Microwave Conference (EuMC)*. IEEE, 2010, pp. 389–392.

[26] ——, "Dispersion-compensation technique for log-periodic antennas using c-section all-pass dispersive delay structures," *IEEE Int. Symp. Antennas Propagat. (ISAP), Jeju, South Korea*, Oct. 2011.

[27] S. Gupta, H. V. Nguyen, K. T, S. Abielmona, and C. Caloz, "CRLH leaky-wave antenna based frequency division diplexing transceiver," *Asia Pacific Microwave Conference (APMC) 2009, Singapore*, pp. 2014 – 2017, Dec. 2009.

[28] S. Gupta, C. Caloz, and S. Abielmona, "CRLH leaky-wave real-time spectrum analyzer (RTSA) with unrestricted time-frequency resolution," *in IEEE MTT-S Int. Microw. Symp. (IMS), Atlanta, USA*, pp. 807 – 810, 2008.

[29] S. Gupta, S. Abielmona, and C. Caloz, "Microwave analog real-time spectrum analyzer (RTSA) based on the spectral–spatial decomposition property of leaky-wave structures," *IEEE Trans. Microwave Theory Tech.*, vol. 57, no. 12, pp. 2989–2999, Oct. 2009.

[30] S. Gupta, J. S. Gómez-Díaz, and C. Caloz, "Frequency resolved electrical gating (FREG) system based on a crlh leaky-wave antenna for uwb signal characterization," *in Proc. 39th European Microwave Conf. (EuMC), Rome*, pp. 2014 – 2017, Sept. 2009.

[31] M. Muriel, J. Azaña, and A. Carballar, "Real-time Fourier transformer based on fiber gratings," *Optics Letters*, vol. 24, no. 1, pp. 1 – 3, Jan. 1999.

[32] G. P. Agrawal, "Nonlinear fiber optics," *New York: Academic Press*, 2005.

[33] M. J. Lancaster, "Passive microwave device applications of high-temperature superconductors," *Cambridge University Press, 1st ed.*, 2006.

[34] R. S. Withers, A. C. Anderson, P. V. Wright, and S. A. Reible, "Superconductive tapped delay lines for microwave analog signal processing," *IEEE Trans. on Magnetics*, vol. MAG-19, no. 3, pp. 480 – 484, March 1983.

[35] M. A. G. Laso, T. Lopetegi, M. J. Erro, D. Benito, M. J. Garde, M. A. Muriel, M. Sorolla, and M. Guglielmi, "Real-time spectrum analysis in microstrip technology," *IEEE Trans. Microw. Theory Tech.*, vol. 51, no. 3, pp. 705 – 717, 2003.

[36] M. Coulombe and C. Caloz, "Reflection-type artificial dielectric substrate microstrip dispersive delay line (DDL) for analog signal processing," *IEEE Trans. Microw. Theory Tech.*, vol. 57, no. 7, pp. 1714 – 1723, 2009.

[37] D. R. Smith, W. J. Padilla, D. C. Vier, S. C. Nemat-Nasser, and S. Schultz, "Composite medium with simultaneously negative permeability and permittivity," *Physics Review Letters*, vol. 84, no. 8, pp. 4148 – 4187, May 2000.

[38] C. Caloz and T. Itoh, "Application of the transmission line theory of left-handed (LH) materials to the realization of a microstrip LH transmission line," vol. 1, pp. 412– 415, June 2002.

[39] A. K. Iyer and G. V. Eleftheriades, "Negative refractive index metamaterials supporting 2-D waves," in *Proc. IEEE MTT-S International Microwave Symposium Digest, (IMS)*, vol. 2, Seattle, WA, USA, June 2002, pp. 412 – 415.

[40] A. A. Oliner, "A periodic-structure negative-refractive-index medium without resonant elements," in *Proc. IEEE AP-S International Symposium and USNC/URSI National Radio Science Meeting, URSI Digest*, San Antonio, TX, USA, June 2002, p. 41.

[41] S. Abielmona, S. Gupta, and C. Caloz, "Compressive receiver using a CRLH-based dispersive delay line for analog signal processing," *IEEE Trans. Microw. Theory Tech.*, vol. 57, no. 11, pp. 2617 – 2626, 2009.

[42] M. A. G. Laso, T. Lopetegi, M. J. Erro, D. Benito, M. J. Garde, M. A. Muriel, M. Sorolla, and M. Guglielmi, "Temporal self-imaging effects: theory and application for multiplying pulse repetition rates," *Selected Topics in Quantum Electronics, IEEE Journal of*, vol. 7, no. 4, pp. 728 – 744, 2001.

[43] G. L. Matthaei, L. Young, and E. M. T. Jones, "Microwave filters, impedance matching networks and coupling structures," *McGraw Hill,*, 1965.

[44] E. G. Cristal, "Analysis and exact design of cascaded commensurate transmission-line C-section all-pass networks," *IEEE Trans. Microw. Theory and Techniques*, vol. MTT-14, no. 6, pp. 285 – 291, 1966.

[45] V. P. Meschanov, I. V. Metelnikova, V. D. Tupikin, and G. G. Chumaevskaya, "A new structure of microwave ultrawide-band differential phase shifter," *IEEE Trans. Microw. Theory Tech.*, vol. 42, no. 5, pp. 762 – 765, May 1994.

[46] J. L. R. Quirarte and J. P. Starski, "Synthesis of schiffman phase shifters," *Microwave Theory and Techniques*, vol. 39, no. 11, pp. 1885 – 1889, Nov. 1991.

[47] T.-C. Mu, H. Ogawa, and T. Itoh, "Characteristics of multiconductor, asymmetric, slow-wave microstrip transmission lines," *IEEE Trans. Microw. Theory Tech.*, vol. 34, no. 12, pp. 1471 – 1477, 1986.

[48] J. S. Abel and J. O. Smith, "Robust design of very high-order all-pass dispersion filters," *Proc. of the 9th Int. Conference on Digital Audio Effects (DAFx-06), Montreal, Canada*, Sept. 2006.

[49] R. L. Crane, "All-pass network synthesis," *IEEE Transactions on Circuit Theory*, vol. 15, no. 14, pp. 474 – 477, Dec. 1968.

[50] R. Levy, "Theory of direct-coupled-cavity filters," *IEEE Trans. Microwave Theory Tech.*, vol. 15, no. 6, pp. 340–348, 1967.

[51] H.-T. Hsu, H.-W. Yao, K. A. Zaki, and A. E. Atia, "Synthesis of coupled-resonators group-delay equalizers," *IEEE Trans. Microwave Theory Tech.*, vol. 50, no. 8, pp. 1960–1968, Aug. 2002.

[52] R. J. Cameron, C. M. Kudsia, and R. R. Mansour, *Microwave filters for communication systems: fundamentals, design, and applications.* Wiley-Interscience, 2007.

[53] J. Rhodes, "Filters approximating ideal amplitude and arbitrary phase characteristics," *IEEE Trans. on Circuit Theory*, vol. 20, no. 2, pp. 120–124, Mar. 1973.

[54] V. P. Meschanov, I. V. Metelnikova, V. D. Tupikin, and G. G. Chumaevskaya, "A new structure of microwave ultrawide-band differential phase shifter," *IEEE Trans. Microwave Theory Tech.*, vol. 42, no. 5, pp. 762–765, May. 1994.

[55] H. S. Hewitt, "A computer designed, 720 to 1 microwave compression filter," *IEEE Trans. Microw. Theory and Techniques*, vol. MTT-15, no. 12, pp. 687–694, Dec. 1967.

[56] E. G. Cristal, "Analysis and exact design of cascaded commensurate transmission-line C-section all-pass networks," *IEEE Trans. Microwave Theory Tech.*, vol. MTT-14, no. 6, pp. 285–291, Jun. 1966.

[57] W. J. D. Steenaart, "The synthesis of coupled transmission line all-pass networks in cascades of 1 to n," *IEEE Trans. Microwave Theory Tech.*, vol. 11, no. 1, pp. 23–29, Jan. 1963.

[58] Q. Zhang, S. Gupta, and C. Caloz, "Synthesis of reflection-type phasor with arbitrary prescribed group delay," *IEEE Trans. Microw. Theory Tech., submitted*, 2011.

[59] M. Abramowitz and I. A. Stegun, *Handbook of Mathematical Functions with Formulas, Graphs, and Mathematical Tables*. New York: Dover Publications, 1972.

[60] T. Henk, "The generation of arbitrary-phase polynomials by recurrence formulae," *International Journal of Circuit Theory and Applications*, vol. 9, no. 4, pp. 461–478, Oct. 1981.

[61] Y. Horii, S. Gupta, B. Nikfal, and C. Caloz, "Compact multilayer C-section dispersive delay structures for analog signal processing," *IEEE Microw. Wireless Compon. Lett.*, in press.

[62] H. V. Nguyen and C. Caloz, "Generalized coupled-mode approach of metamaterial coupled-line couplers: complete theory, explanation of phenomena and experimental demonstration," *IEEE Trans. Microwave Theory Tech.*, vol. 55, no. 5, pp. 1029–1039, May. 2007.

[63] S. Gevorgian, *Ferroelectrics in Microwave Devices, Circuits and Systems: Physics, Modeling, Fabrication and Measurements*. Springer, 1st Ed, Jun. 2009.

[64] R. K. Mongia, I. J. Bahl, P. Bhartia, and J. Hong, *RF and Microwave Coupled-Line Circuit*. Artech House Publishers, 2nd Ed., May. 2007.

[65] S. Gupta, Y. Horii, B. Nikfal, and C. Caloz, "Amplitude equalized transmission line dispersive delay structure for analog signal processing," *in Int. Conference on Telecommunications in Modern Satellite, Cable and Broadcasting Services (TELSIKS), Niš, Serbia*, pp. 379–382, Oct. 2011.

[66] D. M. Pozar, "Microwave engineering," *Academic Press*, 2008.

[67] W. H. Louisell, "Coupled mode and parametric electronics," *New York Wiley*, 1960.

[68] L. P. Carignan, V. Boucher, T. Kodera, C. Caloz, A. Yelon, and D. Ménard, "Double ferromagnetic resonance in nanowire arrays," *App. Phys. Lett.*, vol. 52, pp. 062 504–1:3, Aug. 2009.

[69] S. Hellerstein, "Synthesis of all-pass delay equalizers," *Circuit Theory, IRE Transactions on*, vol. 8, no. 3, pp. 215 – 222, Sep. 1961.

[70] H. S. Hewitt, "A computer designed, 720 to 1 microwave compression filter," *IEEE Trans. Microw. Theory Tech.*, vol. MTT-15, no. 12, pp. 687–694, Dec. 1967.

[71] P. R. Clayton, "Analysis of multiconductor transmission lines," *John Wiley and Sons, 2nd Ed.*, 2008.

[72] J. O. Scanlan, "Theory of microwave coupled-line networks," *Proceedings of the IEEE*, vol. 68, no. 2, pp. 209 – 231, Feb. 1980.

[73] R. E. Collin, "Foundations for microwave engineering," *Wile, 2nd Ed.*, 1965.

[74] R. K. Mongia, I. J. Bahl, P. Bhartia, and J. Hong, "RF and microwave coupled-line circuits," *Artech House Publishers, 2nd Ed.*, May 2007.

[75] D. E. Goldberg, "Genetic algorithms in search, optimization, and machine learning," *Addison-Wisley publishing group*, 1989.

[76] *Genetic Algorithm and Direct Search Toolbox 2.4.2.*

[77] Y. Park and J. Azana, "Optical fiber system for real-time Fourier transformation of nanosecond-long broadband microwave waveforms," *Microwave Photonics (MWP)*, Jan 2010.

[78] M. Morgan, T. Newton, B. Hayward, and T. Boyd, "Non-reflective transmission-line filters for gain slope equalization," *Microwave Symposium, 2007 IEEE MTT-S International*, pp. 545 – 548, Jun. 2007.

[79] T. H. Lee, "Planar microwave engineering," *Cambridge*, 2004.

[80] W. M. Zhang, R. P. Hsia, C. Liang, G. Song, C. W. Domier, and N. C. J. Luhmann, "Novel low-loss delay line for broadband phased antenna array applications," *Microwave and Guided Wave Letters*, vol. 6, no. 11, pp. 395 – 397, Nov. 1996.

[81] H. V. Nguyen and C. Caloz, "Simple-design and compact MIM CRLH microstrip 3-dB coupled-line coupler," *Proc. IEEE MTT-S Int. Dig., San Fransisco, CA*, pp. 1733 – 1736, Jun. 2006.

[82] N. Yang, H. V. Nguyen, S. Abielmona, C. Caloz, and K. Wu, "Non-radiative CRLH boxed stripline structure with high Q performances," *Proc. International Symposium on Electromagnetic Theory (EMTS), Ottawa, ON*, pp. 1733 – 1736, Jul. 2007.

[83] T. Jannson, "Real-time Fourier transformation in dispersive optical fibers," *Optics Letters*, Jan 1983.

[84] J. Azaña and L. R. Chen, "General temporal self-imaging phenomena," *J. Opt. Soc. Am. B*, vol. 20, pp. 1447 – 1458, 2003.

[85] S. Preradovic and N. C. Karmakar, "Chipless RFID: Bar code of the future," *Microwave Magazine, IEEE*, vol. 11, no. 7, pp. 87–97, Dec. 2010.

[86] L. Z. Rodriguez, S. Tenhunen, and H. L.-R. Zheng, "An innovative fully printable RFID technology based on high speed time-domain reflections," *Conference on High Density Microsystem Design and Packaging and Component Failure Analysis HDP*, pp. 166–171, Jun. 2006.

[87] L. Z. Rodriguez, S. L. Z. B. Shao, and L.-R. Zheng, "Design and implementation of a fully reconfigurable chipless RFID tag using inkjet printing technology," *IEEE International Symposium on Circuits and Systems (ISCAS)*, pp. 1524–1528, May. 2008.

[88] J. Vemagiri, A. Chamarti, M. Agarwal, and K. Varahramyan, "Transmission line delay-based radio frequency identification (RFID) tag," *Microwave and Optical Technology Letters*, vol. 49, no. 8, pp. 1900–1904, Aug. 2007.

[89] C. Mandel, M. Schussler, M. Maasch, and R. Jakoby, "A novel passive phase modulator based on LH delay lines for chipless microwave RFID applications," *IEEE MTT-S International Microwave Workshop on Wireless Sensing, Local Positioning, and RFID*, pp. 1–4, Sept. 2009.

[90] H. S. Hartmann, "A global SAW ID tag with large data capacity," *Proceedings of IEEE Ultrasonics Symposium*, vol. 1, pp. 65–69, Oct. 2002.

[91] S. Gupta, B. Nikfal, and C. Caloz, "RFID system based on pulse-position modulation using group delay engineered microwave C-sections," *Proceedings*

of Asia-Pacific Microwave Conference Proceedings (APMC), pp. 203–206, Dec. 2010.

[92] S. Gupta, A. Parsa, E. Perret, R. V. Snyder, R. J. Wenzel, and C. Caloz, "Group delay engineered non-commensurate transmission line all-pass network for analog signal processing," *IEEE Trans. Microwave Theory Tech.*, vol. 58, no. 8, pp. 2392–2407, Aug. 2010.

[93] S. Joardar and A. B. Bhattacharya, "Two new ultrawideband dual polarized antenna-feeds using planar log periodic antenna and innovative frequency independent reflectors," *J. of Electromagn. Waves and Appl.*, vol. 20, no. 11, pp. 1465–1479, Nov. 2006.

[94] R. E. Collin and F. J. Zucker, "Antenna theory," vol. 2, 1969.

[95] R. W. Ziolkowski and P. Jin, "Metamaterial-based dispersion engineering to achieve high fidelity output pulses from a log-periodic dipole array," *IEEE Trans. Antennas Propag.*, vol. 56, no. 12, pp. 3619–3629, Dec. 2008.

[96] F. Merli, J.-F. Zürcher, A. Freni, and A. Skrivervik, "Analysis, design and realization of a novel directive ultrawideband antenna," *IEEE Trans. Antennas Propag.*, vol. 57, no. 11, pp. 3458–3466, Nov. 2009.

[97] W. L. Stutzman and G. A. Thiele, "Antenna theory and design," Jan 1998.

[98] L. Liu, C. Caloz, and T. Itoh, "Dominant mode leaky-wave antenna with backfire-to-endfire scanning capability," *Electronics Letters*, Jan 2002.

[99] N. Yang, C. Caloz, and K. Wu, "Full-space scanning periodic phase-reversal leaky-wave antenna," *IEEE Trans. Microw. Theory Tech.*, vol. 58, no. 10, pp. 2619 – 2632, 2010.

[100] S. Paulotto, P. Baccarelli, F. Frezza, and D. R. Jackson, "A novel technique for open-stopband suppression in 1-D periodic printed leaky-wave antennas," *IEEE Trans. Antennas Propagat.*, vol. 57, no. 7, pp. 1894 – 1906, 2009.

[101] M. Guglielmi and D. R. Jackson, "Broadside radiation from periodic leaky-wave antennas," *IEEE Trans. Antennas Propagat.*, vol. 41, no. 1, pp. 31 – 37, 1993.

[102] D. R. Jackson and A. Oliner, "Leaky-wave antennas," *Antenna Engineering Handbook, J. L. Volakis, Ed., 4th ed. New York: McGraw-Hill, Ch. 11*, Jan 2007.

[103] J. Grajal, A. Asensio, and L. Requejo, "From a high-resolution LFM-CW shipborne radar to an airport surface detection equipment," *Radar Conference, Proceedings of the IEEE*, pp. 157 – 160, 2004.

[104] P. D. L. Beasley, A. G. Stove, B. J. Reits, and B. As, "Solving the problems of a single antenna frequency modulated CW radar," *IEEE Int. Radar Conf. Rec.*, pp. 391 – 395, may 1990.

[105] T. Kodera, "Integrated leaky-wave antenna–duplexer/diplexer using CRLH uniform ferrite-loaded open waveguide," *IEEE Trans. Antennas Propagat.*, vol. 58, no. 8, pp. 2508 – 2514, 2010.

[106] H. Nguyen and S. Abielmona, "Highly efficient leaky-wave antenna array using a power-recycling series feeding network," *IEEE Antennas Wireless Propag. Lett.*, vol. 8, pp. 441– 444, March 2009.

[107] F. W. Thummler and T. Bednorz, "Measuring performance in pulsed single devices: a multi-faceted challenge," *Microwave J.*, vol. 50, no. 9, pp. 196 – 208, 2007.

[108] L. Cohen, "Time-frequency distributions-a review," *Proceedings of the IEEE*, vol. 77, no. 7, pp. 941 – 981, 1989.

[109] *http://www.tek.com/products/spectrum_analyzers*.

[110] R. Trebino, "Frequency-resolved optical gating: the measurement of ultrashort, volume 1," Jan 2000.

[111] J. P. Y. Lee and J. S. Wight, "Acoustooptic spectrum analyzer: detection of pulsed signals," *Applied optics*, vol. 25, no. 2, pp. 193 – 198, Jan 1986.

[112] D. E. Wood and T. L. Hewitt, "New instrumentation for making spectrographic pictures of speech," *The Journal of the Acoustical Society of America*, Jan.

[113] M. Amin and K. D. Feng;, "Short-time Fourier transforms using cascade filter structures," *IEEE Transactions on Circuits and Systems II: Analog and Digital Signal Processing*, vol. 42, no. 10, pp. 631 – 641, 1995.

[114] J.-J. Koo, S. Oh, M.-S. Hwang, C. Park, Y. Jeong, J. Lim, K.-S. Choi, and D. Ahn, "A new DGS unequal power divider," *Microwave Conference, 2007. European*, pp. 556 – 559, 2007.

[115] E. Hecht and A. Zajac, "Optics, 4th ed. new york: Barnes and noble," 2008.

[116] J. S. Gomez-Diaz, Alvarez-Melcon, and C. Caloz, "Characterization of pulse radiation by CRLH leaky-wave antennas using a time-domain green's function approach," *Antennas and Propagation Society International Symposium, 2008. AP-S 2008. IEEE*, pp. 1 – 4, 2008.

[117] H. Nguyen, N. Yang, and C. Caloz, "Differential bi-directional CRLH leaky-wave antenna in CPS technology," *Asia-Pacific Microwave Conference (APMC)*, pp. 1 – 4, 2007.

[118] L. Cohen, "Time-frequency analysis," *Englewood cliffs, NJ, Prentice-Hall*, 1995.

[119] C. A. Balanis, "Advanced engineering electromagnetics," *John Wiley and Sons*, 1989.

[120] Y. Dong and T. Itoh, "Composite right/left-handed substrate integrated waveguide and half mode substrate integrated waveguide leaky-wave structures," *IEEE Trans. Antennas Propagat.*, vol. 59, no. 3, pp. 767 –775, Dec. 2010.

[121] M. Abo-zahhad and T. Henk, "Design of selective lowpass sampled-data and digital filters exhibiting equiripple amplitude and phase error characteristics," *International journal of circuit theory and applications*, vol. 23, no. 1, pp. 59–74, Jan. 1995.

[122] Q. Zhang, D. Sounas, and C. Caloz, "Synthesis of cross-coupled dispersive delay structures," *in IEEE MTT-S Int. Microw. Symp. (IMS), Montreal, Canada*, submitted, 2011.

[123] S. Abielmona, S. Gupta, and C. Caloz, "Compressive receiver using a CRLH-based dispersive delay line for analog signal processing," *IEEE Trans. Microw. Theory Tech.*, vol. 57, no. 11, p. 2617?618, Nov. 2009.

[124] S. Ramo, J. R. Whinnery, and T. V. Duzer, "Fields and waves in communication electronics," *Wiley, 3rd ed.*, 2005.

Appendix A

Pulse Propagation in a Dispersive Media

An ideal LH TL consists of a series capacitance and a shunt inductance, and subsequently exhibits anti-parallel phase and group velocities [124]. However, such a line does not exist in nature because of the presence of parasitic series inductance and shunt capacitance which are responsible for right-handed (RH) contributions. To take into account these effects, Caloz et al. [4] developed the concept of a Composite Right/Left-Handed (CRLH) TL, which acts as a LH TL at low frequencies and RH TL at high frequencies. Depending on the relative values of the LH and RH contributions, this TL can be unbalanced or balanced, i.e. exhibiting with a gapless transition between the LH and RH bands. In the balanced case, which is the condition for intrinsic broadband matching, the propagation constant of the CRLH line splits into uncoupled LH and RH propagation constants, resulting into two uncoupled cascaded TLs, as illustrated in Fig. A.1. In this system, the RH TL, being non-dispersive, simply adds a delay term to the overall response, and only the LH TL is responsible for dispersion and subsequent distortion of the signal. Therefore, a balanced CRLH line is equivalent to an *ideal dispersive LH TL* with an extra constant group delay due to the RH contributions. This fact essentially reduces the analysis of a CRLH TL to the analysis of a purely LH TL.

Referring to the LH TL in Fig. A.1 (with $\Delta z/2 \to \Delta z$ for notational convenience), the current across the times-unit-length capacitance $C'_L = C_L \cdot \Delta z$ (F·m) and the voltage across the times-unit-length inductance $L'_L = L_L \cdot \Delta z$ (H·m) are $i(z) = \partial/\partial t\{C'_L[v(z) - v(z + \Delta z)]/\Delta z\}$ and $v(z + \Delta z) = \partial/\partial t\{L'_L[i(z) - i(z + \Delta z)]/\Delta z\}$, respectively. In the long wavelength (or metamaterial) regime ($\Delta z/\lambda \to 0$), these expressions reduce to $i(z) = -C'_L\partial^2 v/\partial z\partial t$ and $v(z) = -L'_L\partial^2 i/\partial z\partial t$, respectively. Inserting the first of these expressions into the second one yields the time-domain

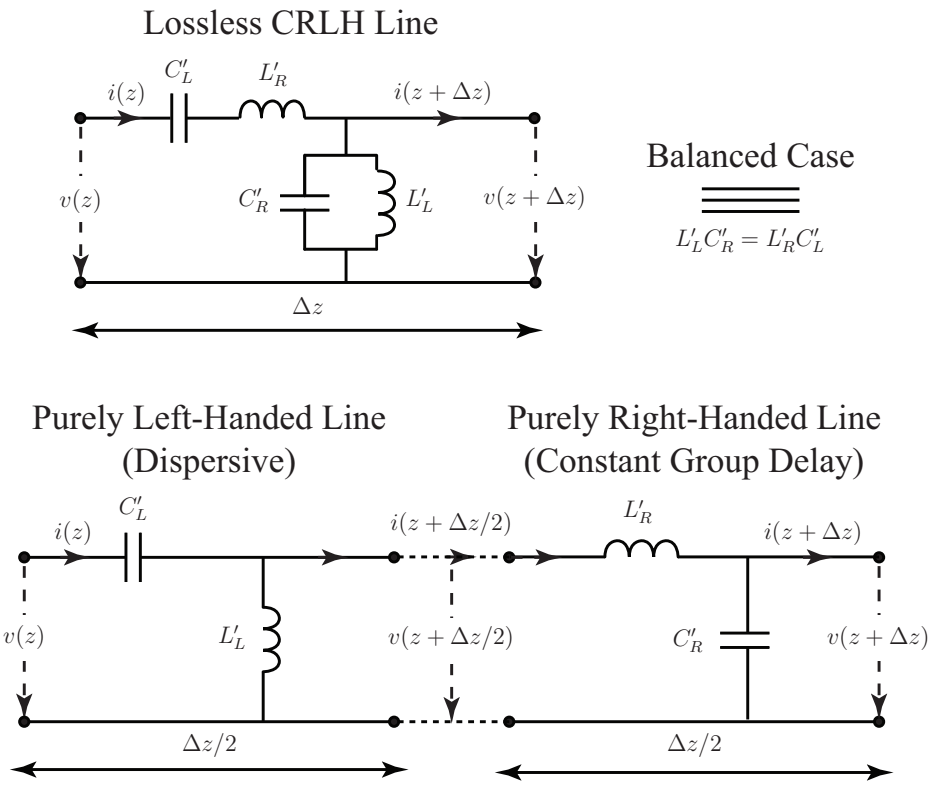

Figure A.1 A balanced CRLH transmission line is equivalent to the series connection of a purely LH (dispersive) line and a purely RH (constant group delay) line [4]. In dispersion analysis, the RH contributions can therefore be ignored and introduced in the end as a simple delay term. A physical CRLH TL is obtained by repeating a lumped CRLH unit cell of subwavelength size.

voltage wave equation

$$\frac{\partial^4 v(z,t)}{\partial z^2 \partial t^2} = \frac{v(z,t)}{L'_L C'_L}. \tag{A.1}$$

This equation may be simplified as follows. Firstly, taking the Fourier transform ($\mathcal{F}$) of both sides, multiplying by $d\tilde{v}/dz$, where $\tilde{v}(z,\omega) = \mathcal{F}[v(z,t)] = \int v(z,t)\exp(-j\omega t)dt$, integrating with respect to z, and taking the square root of appropriate sign to ensure causality, results into the spectral-domain version of the voltage wave equation

$$\frac{d\tilde{v}(z,\omega)}{dz} = j\frac{1}{\omega\sqrt{L'C'}}\tilde{v}(z,\omega) = -j\beta_L(\omega)\tilde{v}(z,\omega), \tag{A.2}$$

where $\beta_L(\omega) = -\omega_L/\omega$ is the propagation constant of a linear LH TL with $\omega_L = 1/\sqrt{(L'_L C'_L)}$ (rad/m·s) [4]. Accounting for the RH contribution $\beta_R(\omega) = \omega/\omega_R$ with

$\omega_R = 1/\sqrt{(L'_R C'_R)}$, the propagation constant of a balanced CRLH TL is given by $\beta(\omega) = \beta_R(\omega) + \beta_L(\omega)$. Upon dividing Eq. (A.2) by $\tilde{v}(z,\omega)$ and integrating the result over z, this equation takes the simpler form $\tilde{v}(z,\omega) = \exp[-j\beta(\omega)z]\tilde{v}(z=0,\omega)$, where $\tilde{v}(z=0,\omega)$ is the spectrum of the input pulse, which may be solved easily for a given input pulse. In order to gain deeper insight into the dispersive pulse propagation phenomenon, we will now simplify Eq. (A.2) by expanding $\beta(\omega)$ in Taylor series around a modulation frequency ω_0. This expansion reads

$$\beta(\omega) \approx \beta_0 + \beta_1(\omega - \omega_0) + \frac{1}{2}\beta_2(\omega - \omega_0)^2, \tag{A.3}$$

where $\beta_0 = (\omega_0/\omega_R - \omega_L/\omega_0)$ is the phase velocity, $\beta_1 = (1/\omega_R + \omega_L/\omega_0^2)$ is the inverse of the nondispersive part of the group velocity [32], and $\beta_2 = -\omega_L/\omega_0^3$ is the group velocity dispersion (GVD) parameter, and where the approximation holds for a narrow band signal ($\Delta\omega \ll \omega_0$), where $\Delta\omega$ is the bandwidth of the pulse. It is interesting to note here that the group velocity of the pulse in a LH TL given by $v_g = 1/\beta_1$ is proportional to the modulation (carrier) frequency. This implies that pulses modulated at different frequencies ω_0 will travel at different group velocities. Fig. A.2 shows the evolution of modulated Gaussian pulses along a (linear) LH line. Pulse width broadening accompanied by gradual amplitude decrease, which is an expected consequence of dispersion, is clearly observed in Fig. A.2(a). Figs. A.2(b) and 2(c) show the evolution of two identical co-propagating Gaussian pulses with different modulation frequencies. In the former case, the two pulses diverge (while broadening) because the earlier pulse has a higher group velocity; it is also apparent here that the pulse with higher modulation frequency experiences less dispersion, due to the fact that $\beta(\omega)$ becomes a more linear function of frequency when frequency increases. In the later case, the earlier pulse has a lower group velocity; consequently the two pulses first converge, then collide and finally diverge (while progressively broadening). Substituting Eq. (A.3) into Eq. (A.2) leads next to the wave equation $d\tilde{v}(z,\omega')/dz = -j(\beta_0 + \beta_1\omega' + 1/2\beta_2\omega'^2)\tilde{v}(z,\omega')$, where $\omega' = \omega - \omega_0$. At this point, we heuristically assume that the system admits a modulated pulse solution, i.e. $v(z,t) = A(z,t)\exp[j(\omega_0 t - \beta_0 z)]$, which corresponds to the spectral-domain expression $\tilde{v}(z,\omega') = \tilde{A}(z,\omega')\exp(-j\beta_0 z)$, where $A(z,t)$ is the slowly-varying envelope of the signal modulated at the frequency ω_0 and traveling with the phase velocity β_0. Finally, applying the operator $\partial/\partial t \leftarrow j\omega'$ with Eq. (A.3), we obtain the time-

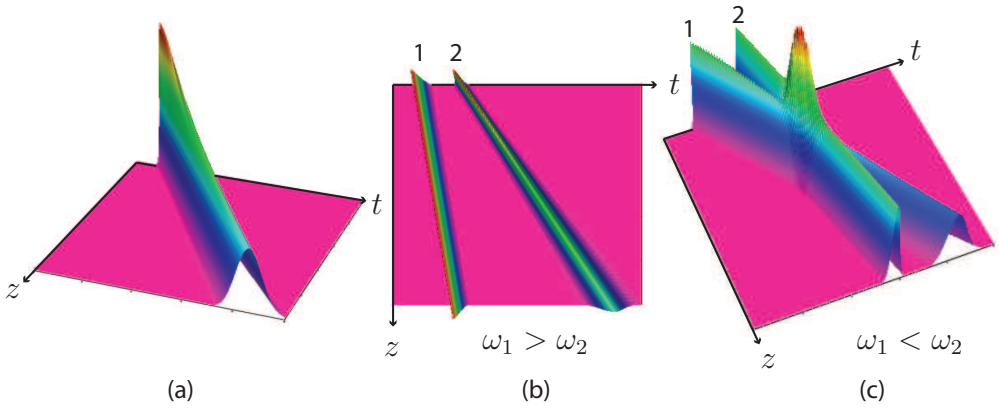

Figure A.2 Propagation of modulated Gaussian pulses (power) along a linear LH TL, i.e. $\mathcal{F}^{-1}[\tilde{v}(z,\omega)] = \mathcal{F}^{-1}\{\exp[-j\beta(\omega)z]\tilde{v}(z=0,\omega)\}$. a) Broadening due to dispersion. b) Dependence of group velocity and dispersion broadening on the modulation frequency, with earlier pulse having higher modulation frequency. (c) Idem, with earlier pulse having lower modulation frequency.

domain pulse propagation equation $dA/dz = -\beta_1 dA/dt + j\beta_2/2 d^2A/dt^2$ in terms of the envelope A. Using the retarded frame $T = t - \beta_1 z$ and taking into account that $\beta_2 < 0$, simplifies this equation to

$$j\frac{dA}{dz} - \frac{|\beta_2|}{2}\frac{d^2A}{dT^2} = 0, \tag{A.4}$$

which governs the broadening of the pulse envelope as it propagates along the line due to the GVD, β_2. It should be noted that this equation for a linear LH TL is identical to the one governing pulse propagation in a linear optical fiber in the anomalous dispersion regime [32].

Appendix B

Derivation of the C-Section Transfer Functions [Eq. (2.4)]

Consider an ideal lossless, perfectly matched and perfectly isolated TEM backward-wave coupled-line coupler, shown in Fig. 2.2(a). The 4-port scattering matrix is [74]

$$\begin{bmatrix} b_1 \\ b_2 \\ b_3 \\ b_4 \end{bmatrix} = \begin{bmatrix} 0 & s_1(\theta) & s_2(\theta) & 0 \\ s_1(\theta) & 0 & 0 & s_2(\theta) \\ s_2(\theta) & 0 & 0 & s_1(\theta) \\ 0 & s_2(\theta) & s_1(\theta) & 0 \end{bmatrix} \begin{bmatrix} a_1 \\ a_2 \\ a_3 \\ a_4 \end{bmatrix}, \quad \text{where} \tag{B.1}$$

$$s_1(\theta) = \frac{jk\sin\theta}{\sqrt{1-k^2}\cos\theta + j\sin\theta}, \tag{B.2a}$$

$$s_2(\theta) = \frac{\sqrt{1-k^2}}{\sqrt{1-k^2}\cos\theta + j\sin\theta}, \tag{B.2b}$$

and k is the voltage coupling coefficient. Prescribing $b_4 = a_3$ and $b_3 = a_4$ to model the shorting transmission line at the 3-4 port of the coupler in (B.1), transforms the 4-port coupled-line coupler into a 2-port C-section described by the following set of equations: $b_1 = s_1a_2 + s_2b_4$, $b_2 = s_1a_1 + s_2b_3$, $b_3 = s_2a_1/(1-s_1)$ and $b_4 = s_2a_2/(1-s_1)$. These equations lead to the 2-port transfer function

$$S_{21}(\theta) = \frac{b_1}{a_2} = \frac{b_2}{a_1} = \left(s_1 + \frac{s_2^2}{1-s_1}\right). \tag{B.3}$$

Finally, substituting (B.2) into (B.3), and rearranging the terms, we obtain the C-section transfer function

$$S_{21}(\theta) = \frac{\sqrt{1+k}\cos\theta - j\sqrt{1-k}\sin\theta}{\sqrt{1+k}\cos\theta + j\sqrt{1-k}\sin\theta}, \tag{B.4}$$

which can be written as

$$S_{21}(\theta) = \left(\frac{j\rho \cot(\theta) + 1}{j\rho \cot(\theta) + 1} \right), \tag{B.5}$$

where $\rho = \sqrt{(1+k)/(1-k)}$.

Appendix C

Demonstration that the Time-Bandwidth Product of a C-Section is Constant and Unitary

Consider the frequency ω_0 at which the length ℓ of the C-section represented in Fig. 2.2(a) is $\lambda_g/4$. The electrical length of a transmission line at ω_0 is $\theta(\omega_0) = \beta(\omega_0)\ell = (\omega_0/v_p)\ell = (2\pi/\lambda_g)(\lambda_g/4) = \pi/2$, so that $\ell = \pi v_p/2\omega_0$. Therefore, the electrical length of a transmission line versus frequency may be written as a function of ω_0 as $\theta(\omega) = \beta(\omega)\ell = (\omega/v_p)(\pi v_p/2\omega_0) = \pi\omega/2\omega_0$. Using (2.6) with this expression for θ, the area under the $(\tau - f)$ curve between the limits $f \in [0,\ 2f_0]$ is obtained as follows:

$$
\begin{aligned}
A &= \int_{f=0}^{f=2f_0} \tau(f)df = 2\int_{f=0}^{f=f_0} \frac{2a}{a^2 + (1-a^2)\cos^2\theta}\frac{d\theta}{d\omega}df \\
&= 4a\int_{\omega=0}^{\omega=\omega_0} \frac{1}{a^2 + (1-a^2)\cos^2\theta}\frac{d\theta}{d\omega}\frac{d\omega}{2\pi} \\
&= \frac{2a}{\pi}\int_{\theta=0}^{\theta=\pi/2} \frac{d\theta}{a^2 + (1-a^2)\cos^2\theta} \\
&= \frac{2a}{\pi}\frac{1}{a\sqrt{a^2+(1-a^2)}}\arctan\left(a\tan\theta\right)\Big|_0^{\pi/2} \\
&= \frac{2}{\pi}[\arctan\left(a\tan\theta\right)|_{\pi/2} - \arctan\left(a\tan\theta\right)|_0] \\
&= 1.
\end{aligned}
$$

Thus, the area under the $(\tau - f)$ curve of a C-section is independent of the coupling coefficient k (and thus a) and is always equal to *unity*.

Appendix D

Polynomial Generations Method

The references [53, 60] provide the formulas (3.31), but without any derivation [60] or with a rather complex derivation [53]. We present here a simple derivation.

Lets consider a specified phase response $\phi(\Omega)$ for $\Omega \in [\Omega_l, \Omega_h]$. The objective is to find an N^{th} order Hurwitz polynomial, i.e. a polynomial

$$H_N(s) = s^N + c_{N-1}s^{N-1} + \ldots + c_1 s + c_0 \tag{D.1}$$

with real coefficients c_i [59], such that $\arg\{H(j\Omega)\} \approx \phi(\Omega)$. The form of the polynomial imposes the restriction

$$\arg\{H_N(0)\} = 0. \tag{D.2}$$

Furthermore, the phase of $H_N(j\Omega)$ can be written as

$$j \tan[\arg\{H_N(j\Omega)\}] = \frac{H_N^{\text{o}}(j\Omega)}{H_N^{\text{e}}(j\Omega)}, \tag{D.3}$$

where $H_N^{\text{o}}(s)$ and $H_N^{\text{e}}(s)$ are the odd (odd-order terms) and the even (even-order terms) parts of $H_N(s)$, respectively.

To determine the N unknown coefficients $c_0,\ c_1,\ \ldots c_{N-1}$, N conditions are required. These conditions are provided by prescribing the phase $\phi(\Omega)$ at N different frequency points $\{\Omega; N\} = \{\Omega_1,\ \Omega_2,\ ...,\ \Omega_N\}$. The polynomial coefficients can then be determined numerically, by solving the linear system of equations

$$j \tan \phi_i = \frac{H_N^{\text{o}}(j\Omega_i)}{H_N^{\text{e}}(j\Omega_i)}, \tag{D.4}$$

but this approach does not provide an analytical solution. Therefore, we resort to an iterative procedure, where $H_N(s)$ is constructed from $H_{N-1}(s)$ and $H_{N-2}(s)$ under the condition

$$\{\Omega; N+1\} = \{\Omega; N\} \cup \{\Omega_{N+1}\}. \tag{D.5}$$

for any N. Equation (D.5) implies that the phases of $H_{N+1}(s)$ at $N+1$ frequency points consists of N phase points of the lower order polynomial $H_N(s)$ plus an additional phase point Ω_{N+1}. In other words, by adding an additional phase point to a lower order polynomial $H_N(s)$, the next order polynomial is constructed.

Applying (D.5) to the polynomials $H_N(s)$, $H_{N-1}(s)$ and $H_{N-2}(s)$, and using (D.3) yields

$$\frac{H_N^{\mathrm{o}}(j\Omega_i)}{H_N^{\mathrm{e}}(j\Omega_i)} = \frac{H_{N-1}^{\mathrm{o}}(j\Omega_i)}{H_{N-1}^{\mathrm{e}}(j\Omega_i)} = \frac{H_{N-2}^{\mathrm{o}}(j\Omega_i)}{H_{N-2}^{\mathrm{e}}(j\Omega_i)}, \tag{D.6}$$

for $\Omega_i \in \{\Omega; N-2\}$. Using the identity

$$\frac{a}{b} = \frac{c}{d} = \left(\frac{\alpha a + \beta c}{\alpha b + \beta d}\right), \tag{D.7}$$

which holds for arbitrary a, b, c, d, α and β, (D.6) transforms into

$$\frac{H_N^{\mathrm{o}}(j\Omega_i)}{H_N^{\mathrm{e}}(j\Omega_i)} = \frac{\alpha(j\Omega_i)H_{N-1}^{\mathrm{o}}(j\Omega_i) + \beta(j\Omega_i)H_{N-2}^{\mathrm{o}}(j\Omega_i)}{\alpha(j\Omega_i)H_{N-1}^{\mathrm{e}}(j\Omega_i) + \beta(j\Omega_i)H_{N-2}^{\mathrm{e}}(j\Omega_i)}. \tag{D.8}$$

If

$$H_N(s) = \alpha(s)H_{N-1}(s) + \beta(s)H_{N-2}(s), \tag{D.9}$$

with $\alpha(s)$ and $\beta(s)$ even polynomials, so that the odd/even part of $H_N(s)$ is a linear combination of the odd/even parts of $H_{N-1}(s)$ and $H_{N-2}(s)$, (D.8) is directly satisfied. Since $\alpha(s)$ is an even polynomial and multiplies a polynomial of order $N-1$, it should be constant, $\alpha(s) = \alpha_{N-1}$. Similarly, since $\beta(s)$ is an even polynomial and multiplies a polynomial of order $N-2$, it should have the form $\beta(s) = \beta_2 s^2 + \beta_0$. From the general form (D.1) the leading coefficients of $H_N(s)$ and $H_{N-2}(s)$ must be 1. Therefore, $\beta_2 = 1$ and

$$H_N(s) = \alpha_{N-1}H_{N-1}(s) + (s^2 + \beta_0)H_{N-2}(s). \tag{D.10}$$

The polynomial (D.10) has the same phase as $H_{N-1}(s)$ and $H_{N-2}(s)$ at $\{\Omega; N-2\}$. The last condition to satsufy is to esnure that $H_N(s)$ has the same phase as $H_{N-1}(s)$ at the frequency Ω_{N-1}. Selecting $\beta_0 = \Omega_{N-1}^2$, $H_N(j\Omega_{N-1}) = \alpha_{N-1}H_{N-1}(j\Omega_{N-1})$ and

$\arg\{H_N(j\Omega_N)\} = \arg\{H_N(j\Omega_{N-1})\}$. Therefore, the final recursive formula obeying condition (D.5) is

$$H_N(s) = \alpha_{N-1}H_{N-1}(s) + (s^2 + \Omega_{N-1}^2)H_{N-2}(s). \tag{D.11}$$

Since (D.11) computes $H_N(s)$ from $H_{N-1}(s)$ and $H_{N-2}(s)$, two initial conditions are required. The only choice which is consistent with (D.1) is $H_0(s) = 1$ and $H_1(s) = s + \alpha_0$, where α_0 is determined from the condition $\phi_1 = \arg\{H_1(j\Omega_1)\}$ as

$$\alpha_0 = \frac{\Omega_1}{\tan\phi_1}. \tag{D.12}$$

Similarly, α_1 is found from the condition $\phi_2 = \arg\{H_2(j\Omega_1)\}$. Specifically, substituting $s = j\Omega_2$ into (D.11) with $N = 2$ yields

$$H_2(j\omega_2) = \alpha_1(\alpha_0 + j\Omega_2) + (\Omega_1^2 - \Omega_2^2). \tag{D.13}$$

Therefore, $\phi_2 = \arg\{H_2(j\Omega_1)\}$ leads to

$$\alpha_1 = \left(\frac{\Omega_2^2 - \Omega_1^2}{\alpha_0 - \frac{\Omega_2}{\tan\phi_2}}\right). \tag{D.14}$$

Following a similar procedure using $\arg\{H_{i+1}(j\Omega_{i+1})\} = \phi_{i+1}$, it can be shown that

$$\alpha_i = \cfrac{\Omega_{i+1}^2 - \Omega_i^2}{\alpha_{i-1} - \cfrac{\Omega_{i+1}^2 - \Omega_{i-1}^2}{\alpha_{i-2} - \cfrac{\Omega_{i+1}^2 - \Omega_{i-2}^2}{\ddots \qquad \alpha_0 - (\Omega_{i+1}/\tan\phi_{i+1})}}}. \tag{D.15}$$

In summary, a N^{th} degree polynomial $H_N(s)$ exhibiting the prescribed phase samples $\{\phi; N\} = [\phi_1,\ ...,\ \phi_N]$ at the N frequency points $\{\Omega; N\} = \{\Omega_1,\ ...,\ \Omega_N\}$ can be generated by the recurrence relation (D.11) with the α_i's given by (D.15).

Appendix E

Determination of the Capacitance and Inductance Matrices

Consider the N coupled-line stripline structure shown in Fig. E.1(a), which may also be regarded as a multiconductor transmission line, embedded in a homogenous dielectric of thickness h of dielectric constant ε_r. The lines are assumed to have zero thickness, infinite conductivity, a width w and to be infinitely long in the longitudinal direction. To compute the capacitance matrix $\mathbf{C}$ for this structure, the Method of Moments (MoM) with the point-matching technique is applied, following [71]. This leads to a relationship between the total per-unit-length charge Q_i on the ith conductor due to all the line voltages, which may be expressed in matrix form as $\mathbf{Q} = \mathbf{CV}$.

For this computation, each line is divided into N_s segments, as shown in Fig. E.1(a) and the auxiliary matrix

$$\mathbf{B}_{NN_s} = \begin{bmatrix} \psi_{1,1} & \psi_{1,2} & \cdots & \psi_{1,NN_s} \\ \psi_{2,1} & \psi_{2,2} & \cdots & \psi_{2,NN_s} \\ \cdots & \cdots & \cdots & \cdots \\ \psi_{NN_s,1} & \psi_{2,2} & \cdots & \psi_{NN_s,NN_s} \end{bmatrix}^{-1} \tag{E.1}$$

is invoked, where $\psi_{i,j}$ is the potential at the center of the i^{th} segment due to a constant charge distribution of unit value (1 C/m^2) over the j^{th} segment, which may or may not be on the same conductor. The matrix $\mathbf{B}$ can be re-written in terms of block matrices $\mathbf{D}_{ij}$ as

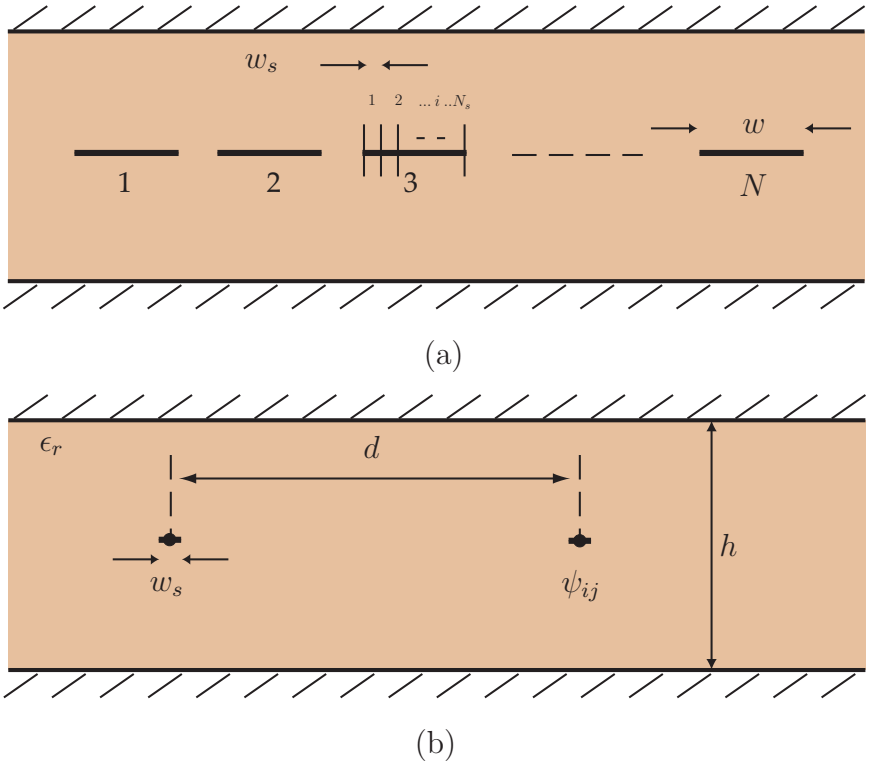

Figure E.1 Coupled-line transmission line network or, equivalently, multiconductor transmission line (cross-sectional view) in stripline technology.

$$\mathbf{B}_{NN_s} = (\mathbf{D}_{ij})_{Ns} = \begin{bmatrix} \mathbf{D}_{00} & ... & \mathbf{D}_{0j} & ... & \mathbf{D}_{0N} \\ ... & ... & ... & ... & ... \\ \mathbf{D}_{i0} & ... & \mathbf{D}_{ij} & ... & \mathbf{D}_{0N} \\ ... & ... & ... & ... & ... \\ \mathbf{D}_{N0} & ... & \mathbf{D}_{nj} & ... & \mathbf{D}_{NN} \end{bmatrix}, \tag{E.2}$$

where the block matrix entries in $\mathbf{B}$ are given by

$$(\mathbf{D}_{ij})_{N_s} = \begin{bmatrix} B_{i,j} & B_{i+1,j} & ... & B_{i+N_s,j} \\ B_{i,j+1} & B_{i+1,j+1} & ... & B_{i+N_s,j+1} \\ ... & ... & ... & ... \\ B_{i,j+N_s} & B_{i+1,j+N_s} & ... & B_{i+N_s,j+N_s} \end{bmatrix}. \tag{E.3}$$

Finally the elements of the per-unit-length capacitance matrix $\mathbf{C}$ are obtained as a function of the block matrices $\mathbf{D}_{ij}$ as

$$C_{ij} = w \sum \mathbf{D}_{ij} \tag{E.4}$$

and, for the considered case of an homogeneous dielectric medium surrounding the conductors, the inductance matrix $\mathbf{L}$ is given by [71][72]

$$\mathbf{L} = \mu_0 \epsilon_0 \mathbf{C}_0^{-1}, \tag{E.5}$$

where $\mathbf{C}_0$ is the capacitance matrix without dielectric, which shows that $\mathbf{L}$ may be computed directly from $\mathbf{C}$.

The problem is now to determine the $\psi_{i,j}$ in (E.1). For the stripline structures considered in this work, consider Fig. E.1(b), which represents two infinitely long and thin i^{th} and j^{th} filaments located midway between the ground planes separated by the distance d. The potential ψ_{ij} created by the j^{th} filament, carrying a per-unit-length

charge of 1 (C/m), on the i^{th} filament, is given by [71],[73]

$$\psi_{i,j}^{i\neq j} = \frac{t}{\pi^2\varepsilon}\left[\left(\sum_k^{\infty}\frac{E_m^{2k+1}}{(2k+1)^2}\right) - \left(\sum_k^{\infty}\frac{E_p^{2k+1}}{(2k+1)^2}\right)\right], \tag{E.6}$$

$$\text{where} \quad E_m = e^{-\frac{\pi}{t}\left(d-\frac{w_s}{2}\right)} \quad \text{and} \quad E_p = e^{-\frac{\pi}{t}\left(d+\frac{w_s}{2}\right)},$$

$$\text{and} \quad \psi_{ii} = \frac{2t}{\pi^2\varepsilon}\left[\frac{\pi^2}{8} + \sum_k^{\infty}\frac{E^{2k+1}}{(2k+1)^2}\right], \tag{E.7}$$

$$\text{where} \quad E = e^{-\frac{\pi w_s}{2}}.$$

Once all the potentials ψ_{ij}s have been computed for a given stripline configuration using (E.6) and (E.7), the final capacitance and inductance matrices are readily computed using (E.4) and (E.5).

Appendix F

Conversion between the $2N$-port Coupled-Line Structure and the 2-port All-Pass Network

Consider the $2N$-port network shown in Fig. 4.1(a) and 4.2(a) with the scattering matrix $\mathbf{S}^{(2N)}$ given by Eqs. (4.5) and (4.9), respectively. This matrix relates the reflected wave b_i and transmitted wave a_i of the i^{th} port as

$$\begin{array}{c} \\ \begin{bmatrix} b_1 \\ b_N \\ \hline b_2 \\ \dots \\ b_{2N} \end{bmatrix} \end{array} = \begin{array}{c} \begin{matrix} \quad\mathbf{S_1}\quad\quad & \quad\mathbf{S_2} \end{matrix} \\ \left[\begin{array}{cc|ccc} S_{1,1} & S_{1,N} & S_{1,2} & \dots & S_{1,N} \\ S_{N,1} & S_{N,N} & S_{N,2} & \dots & S_{N,N} \\ \hline S_{2,1} & S_{2,N} & S_{2,2} & \dots & S_{2N,2N} \\ \dots & \dots & \dots & \dots & \\ S_{2N,1} & S_{2N,N} & S_{2N,2} & \dots & S_{2N,2N} \end{array}\right] \\ \begin{matrix} \quad\mathbf{S_3}\quad\quad & \quad\mathbf{S_4} \end{matrix} \end{array} \begin{array}{c} \\ \begin{bmatrix} a_1 \\ a_N \\ \hline a_2 \\ \dots \\ a_{2N} \end{bmatrix} \end{array}, \tag{F.1}$$

where the matrix terms $S_{i,j}$ have been rearranged so as to isolate the first and last ports. This equation can be split up in two matrix equations as

$$\begin{bmatrix} b_1 \\ b_N \end{bmatrix} = \mathbf{S_1} \begin{bmatrix} a_1 \\ a_N \end{bmatrix} + \mathbf{S_2} \begin{bmatrix} a_2 \\ \dots \\ a_{2N} \end{bmatrix}, \tag{F.2a}$$

$$\begin{bmatrix} b_2 \\ \dots \\ b_{2N} \end{bmatrix} = \mathbf{S_3} \begin{bmatrix} a_1 \\ a_N \end{bmatrix} + \mathbf{S_4} \begin{bmatrix} a_2 \\ \dots \\ a_{2N} \end{bmatrix}, \tag{F.2b}$$

where $\mathbf{S_1}$, $\mathbf{S_2}$, $\mathbf{S_3}$ and $\mathbf{S_4}$ are the sub-matrices of $\mathbf{S}^{(2N)}$ indicated in (F.1).

The $2N$-port network can now be converted into a 2-port network by introducing

the end connections shown in Figs. 4.1(b) and 4.2(b). Specifically, the k^{th} port (except the 1^{st} and the N^{th} port) is connected to the $(k+1)^{\text{th}}$ port using a short transmission line section so that

$$\begin{bmatrix} b_k \\ b_{k+1} \end{bmatrix} = \mathbf{S_0}^{-1} \begin{bmatrix} a_k \\ a_{k+1} \end{bmatrix}, \tag{F.3}$$

where $\mathbf{S}_0$ is the 2×2 scattering matrix of a transmission line of length g (gap width) and width w'. The scattering matrix $\mathbf{S_0}$ may be obtained from the $ABCD$ transmission matrix given by

$$\begin{bmatrix} A & B \\ C & D \end{bmatrix} = \begin{bmatrix} \cos(\beta g) & jZ_0 \sin(\beta g) \\ j\sin(\beta g)/Z_0 & \cos(\beta g) \end{bmatrix},$$

where Z_0 is the impedance of the striplines of width w'. Next, substituting (F.3) in (F.2), we obtain,

$$\begin{bmatrix} \mathbf{S_0}^{-1} \\ ... \\ \mathbf{S_0}^{-1} \end{bmatrix}^t \begin{bmatrix} \begin{pmatrix} a_2 \\ a_3 \end{pmatrix} \\ ... \\ \begin{pmatrix} a_{2N-1} \\ a_{2N} \end{pmatrix} \end{bmatrix} = \mathbf{S_3} \begin{bmatrix} a_1 \\ a_N \end{bmatrix} + \mathbf{S_4} \begin{bmatrix} a_2 \\ a_3 \\ ... \\ a_{2N-1} \\ a_{2N} \end{bmatrix}. \tag{F.4a}$$

Finally,

$$\begin{bmatrix} b_1 \\ b_N \end{bmatrix} = \mathbf{S_1} + \mathbf{S_2}(\mathbf{S_5} - \mathbf{S_4})^{-1}\mathbf{S_3} \begin{bmatrix} a_1 \\ a_N \end{bmatrix} \tag{F.5}$$

where $\mathbf{S_5} = [\mathbf{S_0}^{-1}\ \mathbf{S_0}^{-1}\ ...\ \mathbf{S_0}^{-1}]^t_{(2N-2)\times 2}$. The final 2-port scattering matrix is thus

$$\mathbf{S}^{(2)} = \begin{bmatrix} S_{11} & S_{12} \\ S_{21} & S_{22} \end{bmatrix} = \mathbf{S_1} + \mathbf{S_2}(\mathbf{S_5} - \mathbf{S_4})^{-1}\mathbf{S_3}. \tag{F.6}$$

Appendix G

List of Publications and Awards

G.1 Peer-reviewed journal publications

1. S. Gupta, D. Sounas, Q. Zhang and C. Caloz, "All-Pass Dispersion Synthesis using Microwave C-sections," *IEEE Trans. Microwave Theory Tech.*, under review.
2. Q. Zhang, S. Gupta and C. Caloz, "Synthesis of Reflection-Type Phasor with Arbitrary Prescribed Group Delay," *IEEE Trans. Microwave Theory Tech.*, under review.
3. B. Nikfal, S. Gupta and C. Caloz, "Low-Cost and High-Efficiency Pulse Compressor based on Mixing with an Auxiliary Pulse," *IEEE Microwave Wireles Compon. Lett.*, accepted.
4. S. Gupta, B. Nikfal and C. Caloz, "Chipless RFID System based on Group Delay Engineered Dispersive Delay Structures," *IEEE Antenna and Wireless Propagat. Lett.*, vol. 10, no. 1, pp. – , Dec. 2011. .
5. S. Gupta, L.-P. Carignan and C. Caloz, "Group Delay Swing Enhancement in Transmission-Line All-Pass Networks using Coupling and Dispersion Boosting Ferrimagnetic Substrate," *Microwave Opt. Technol. Lett.*, accepted.
6. Y. Horii, S. Gupta, B. Nikfal and C. Caloz, "Compact Multilayer C-Section Dispersive Delay Structures for Analog Signal Processing," *IEEE Microwave Wireless Compon. Lett.*, accepted.
7. B. Nikfal, S. Gupta and C. Caloz, "Increased Group Delay Slope Loop System for Enhanced-Resolution Analog Signal Processing," *IEEE Trans. Microwave Theory Tech.*, vol. 59, no. 6, pp. 1622-1628, Jun. 2011.
8. J. S. Gómez-Díaz, S. Gupta, A. Álvarez-Melcón, and C. Caloz, "Efficient time-domain analysis of highly-dispersive linear and non-linear metamaterial waveguide and antenna structures operated in the impulse-regime," *IET Microwaves,*

Antennas and Propagation, vol. 4, no. 10, pp. 1617-1625, Oct. 2010.

9. S. Gupta, A. Parsa, E. Perret, R. V. Snyder, R. J. Wenzel and C. Caloz, "Group Delay Engineered Non-Commensurate Transmission Line All-Pass Networks for Analog Signal Processing," *IEEE Trans. Microwave Theory Tech.*, vol. 58, Issue 8, Aug. 2010.
10. S. Gupta, S. Abielmona, C. Caloz, "Microwave Analog Real-Time Spectrum Analyzer (RTSA) based on the Spatial-Spectral Decomposition Property of Leaky-Wave Structures," *IEEE Trans. Microwave Theory Tech.*, Vol. 57,no. 12, pp. 2989-2999, Dec. 2009.
11. S. Abielmona, S. Gupta and C. Caloz, "Real-time analog signal processors based on CRLH dispersive delay line," *Trans. Microwave Theory Tech.*, vol. 57, no. 11, pp. 2617-2618, Nov. 2009.
12. J. S. Gómez-Díaz, S. Gupta, A. Álvarez-Melcón, and C. Caloz, "Time-domain GreenÕs function analysis and phenomenology of impulse-regime metamaterial transmission lines," *IEEE Trans. Antennas Propagat.*, vol. 57, no. 12, pp. 4010-4014, Dec. 2009.
13. J. S. Gómez-Díaz, S. Gupta, C. Caloz and A. Álvarez-Melcón, "Tunable Talbot Imaging Distance using an Array of Beam-Steered Metamaterial Leaky-Wave Antennas," *J. App. Phys.*, vol. 106, pp. 084908:1-8, Oct. 2009.
14. J. S. Gómez-Díaz, S. Gupta, C. Caloz and A. Álvarez-Melcón, " Impulse-regime CRLH Resonator for Tunable Pulse Rate Multiplication," *Radio Science*, vol. 44, pp. 1-9, RS4001, July 2009.
15. S. Gupta, C. Caloz, "Analog Signal Processing in Transmission Line Metamaterial Structures," *Journal of Radioscience and engineering*, vol. 18, no. 2, pp. 155-167, June 2009.
16. A. Shahvarpour, S. Gupta, and C. Caloz, "Study of Schrodinger solitons in left-handed SiO_2-Ag-SiO_2 and Ag-SiO_2-Ag plasmonic waveguides using a nonlinear transmission line approach," *J. App. Phys.*, vol. 104, pp. 124510:1-5, Dec. 2008.
17. J. S. Gómez-Díaz, S. Gupta, C. Caloz and A. Álvarez-Melcón, "Spatio-Temporal Talbot Effect using CRLH metamaterial Antennas," *J. App. Phys.*, vol. 104, pp. 104901:1-7, Nov. 2008.

18. S. Abielmona, S. Gupta, C. Caloz, "Experimental demonstration and characterization of a tunable CRLH delay line system for impulse/continuous wave," *IEEE Microwave Wireless Compon. Lett.*, vol. 17, no. 12, pp. 864-866, Dec. 2007.
19. J. Azaña and S. Gupta, "Complete family of periodic Talbot filters for pulse repetition rate multiplication," *Optics Express*, vol. 14, pp. 4270-4279. 2006.

G.2 Conference publications

1. S. Gupta and C. Caloz, "Highly Dispersive Delay Structure Exploiting the Tight Coupling Property of the CRLH-CRLH Coupler for Enhanced Resolution Analog Signal Processing," *in Proc. International Microwave Symposium (IMS) 2012*, Montreal, Canada, submitted.
2. S. Gupta and C. Caloz, "Dispersion-Compensation Technique for Log-Periodic Antennas using C-section All-Pass Dispersive Delay Structures," *in Proc. International Symp. on Antennas and Propagation (ISAP) 2011*, Jeju, South Korea, to be published.
3. S. Gupta, Y. Horii, B. Nikfal and C. Caloz, "Amplitude Equalized Transmission Line Dispersive Delay Structure for Analog Signal Processing," *in Proc. of International Conference on Telecommunications in Modern Satellite, Cable and Broadcasting Services (TELSIKS)*, Nis, Serbia, pp. 379-382, Oct. 2011.
4. S. Gupta, M. Samardzija, Y. She, J. Hirokawa, M. Ando and C. Caloz, "Corrugations for Suppressing Undesired Wave Propagation in the Transverse Direction in a 45° Linearly Polarized 76 GHz Parallel-Plate Waveguide Two-dimensional Slot-Array," *2011 IEEE International Symposium on Antennas and Propagation*, Spokane, Washington, pp. 3025-3028, July 2011.
5. S. Gupta, B. Nikfal and C. Caloz, "RFID System based on Pulse-Position Modulation using Group Delay Engineered Microwave C-Sections," *Asia Pacific Microwave Conference 2010*, Yokohama, Japan, pp. 203-206, Dec. 2010.
6. S. Gupta and C. Caloz, "Analog Inverse Fourier Transformer using Group Delay Engineered C-Section All-Pass Network," *40th European Microwave Conference*, Paris, France, pp. 389-392, Sept. 2010.

7. S. Gupta and C. Caloz, "Analog Real-Time Fourier Transformer Using a Group Delay Engineered C-Section All-Pass Network," *IEEE International Symposium on Antennas and Propagation and CNC/USNC/URSI National Radio Science Meeting*, Toronto, Canada, July 2010.

8. S. Gupta, J. S. Gómez-Díaz and C. Caloz, "Frequency Resolved Electrical Gating (FREG) System based on a CRLH Leaky-Wave Antenna for UWB Signal Characterization," *in Proc. 39th European Microwave Conf. (EuMC)*, Rome, September 2009.

9. J. S. Gómez-Díaz, S. Gupta, A. Álvarez-Melcón and C. Caloz, "Numerical Analysis of Impulse Regime Phenomena in Linear and Non-Linear Metamaterial Transmission Lines," *8th International Conf. on Electromagnetics in Advanced Applications (ICEAA)*, Torino, Italy, Sept. 2009.

10. J. S. Gómez-Díaz, S. Gupta, C. Caloz, and A. Álvarez-Melcón, "GreenÕs function analysis of spatio-temporal Talbot Phenomenon," *Proc. European Conf. Antennas Propagat. (EuCAP)*, Berlin, pp. 870-874, April 2009.

11. S. Gupta and C. Caloz, "Spatial Demultiplexer based on the Spectral Decomposition Property of the Metamaterial Leaky-Wave Antenna," *in Proc. XXIXth Assembly of Union Radio Science International (URSI)*, Chicago, IL, CD-ROM, Aug. 2008.

12. S. Abielmona, S. Gupta, H. V. Nguyen and C. Caloz, "Dispersion Engineered Impulse Regime Metamaterial Devices," *in Proc. XXIXth Assembly of Union Radio Science International (URSI)*, Chicago, IL, Aug. 2008.

13. A. Shahvarpour, S. Gupta, and C. Caloz, "Study of Schrodinger solitons in a left-handed plasmonic waveguide using a nonlinear transmission line approach," *in Proc. XXIXth Assembly of Union Radio Science International (URSI)*, Chicago, IL, CD-ROM, Aug. 2008.

14. S. Gupta, C. Caloz and S. Abielmona, "Leaky-wave based spectrum analyzer with unrestricted time-frequency resolution," *Proc. IEEE MTT-S Int. Microwave Symp. Dig.*, Atlanta, GA, pp. 807-810, June 2008.

15. C. Caloz and S. Gupta, "Phase-engineered metamaterial structures and devices," *in Proc. Progress in Electromagnetics Research Symposium (PIERS), Special session Metamaterials: From Microwave to Optical Frequency*, Hangzhou, China, March 2008.

16. C. Caloz and S. Gupta, "Dispersion and Nonlinearity Engineered Metamaterial Devices," *Advanced First International Congress on Advanced Electromagnetic Materials in Microwaves Electromagnetic Materials in Microwaves and Optics*, Rome, Italy, 627-630, 2007.

17. A. Rennings, J. Mosig, S. Gupta, C. Caloz, R. Kashyap, D. Erni and P. Waldow, "Super-Compact Power Splitter Based on Coupled Surface Plasmons," *ISSSE*, Montreal (QC), Canada, 2007, July-Aug. 2007, 471-474, 2007.

18. S. Gupta, S. Abielmona and C. Caloz, "Carrier frequency tunable impulse/continuous wave CRLH delay line system," *Proc. IEEE AP-S*, Honolulu, HI, June 2007, 5523-5526, 2007.

19. S. Gupta and C. Caloz, "Dark and bright solitions in left-handed nonlinear transmission line Metamaterials," *Proc. IEEE-MTT International Symposium*, Honolulu, HI, June 2007, June 2007, 979-982, 2007.

20. S. Gupta and C. Caloz, "Temporal Talbot effect in Left-handed Metamaterials Transmission lines," *Proc. in International Symposium on Electromagnetic Theory*, Ottawa, ON, CD-ROM, July (2007).

21. S. Gupta and J. Azaña, " Joint Time-Frequency analysis of ultrashort soliton propagation in nonlinear optical fibers," *Photonics North Symposium, Proc. SPIE Int. Soc. Opt. Eng.* 6343, 63430V, Quebec City, 2006.

22. S. Gupta and J. Azaña, "Time-Frequency Analysis of Temporal Talbot Effect," *Proc in IEEE LEOS Summer Topicals*, San Diego, California, US, 163-164, 2005.

23. S. Gupta, J. Azaña, P. F. Ndione, and R. Morandotti, " A new insight into the problem of temporal Talbot phenomena in optical fibers," *Photonics North Symposium, Proceedings of the SPIE*, Volume 5971, pp. 168-179, 2005.

24. T. Kaneko, Y. Horii, S. Gupta, B. Nikfal, and C. Caloz, "Design of Multilayer Broadside-Coupled Dispersive Delay Structures (DDS) for Real-Time Analog Signal Processing," IEICE Society Conference, Sapporo, Japan, Sep. 2011, submitted.

G.3 Patents

1. CALOZ, Christophe; NGUYEN Van-Hoang, GUPTA Shulabh, and ABIELMONA Samer, "Tunable delay system and corresponding method," Pub. No.: WO/2008/116289, International Application No.: PCT/CA2008/000516, Publication Date: 02.10.2008, International Filing Date: 18.03.2008.

G.4 Awards

1. *Second Prize*, Student Poster Contest, 3^{rd} Symposium et Assemblée Générale du CREER, École de Technologie Supérieure, Québec, Canada, 14 September 2011.
2. *Young Scientist Award (YSA)*, "Dispersion-Compensation Technique for Log-Periodic Antennas using C-section All-Pass Dispersive Delay Structures," *International Symp. on Antennas and Propagation (ISAP) 2011*, Jeju, South Korea, 25-28 October 2011.
3. *Second Prize*, Student Poster Contest, 2^{nd} Symposium et Assemblée Générale du CREER, Ecole Polytechnique de Montréal, Québec, Canada, 11 June 2010.
4. *Student travel grant*, "Analog Inverse Fourier Transformer using Group Delay Engineered C-Section All-Pass Networks," 40th European Microwave Conference 2010, Paris, September 28 - 30, 2010.
5. *Student Travel grant*, "Frequency Resolved Electrical Gating (FREG) System based on a CRLH Leaky-Wave Antenna for UWB Signal Characterization," European Microwave Conference (EuMC) 2009, 28 September - 2nd October 2009, Rome, Italy.
6. *Postdoctoral Fellowships for Foreign Researchers (Short-term)* by JSPS (Japanese Society for the Promotion of Science), 2009 with Prof. Makoto Ando, Tokyo Institute of Technology, Japan.
7. *Second Finalist*, International Microwave Symposium IMS (2008), "Leaky-wave based spectrum analyzer with unrestricted time-frequency resolution," Most creative and original microwave measurement system, Atlanta, GA, June 2008.
8. *Young Scientist Award (YSA)*, "Spatial Demultiplexer based on the Spectral Decomposition Property of the Metamaterial Leaky-Wave Antenna," XXIXth

General Assembly of Union Radio Science International (URSI), Chicago, IL, Aug. 2008.

9. *Young Scientist Award (YSA)*, "Temporal Talbot effect in Left-handed Metamaterials Transmission lines," International Symposium on Electromagnetic Theory, Ottawa, Canada, July 2007.
10. *Honorable Mention*, Student Paper Competition (Finalist) with a Travel grant in IEEE Antenna and Propagation Symposium (AP-S), Honolulu, Hawaii, US, June 2007.
11. *Honorable Mention* in ACM-ICPC Computer Programming contest, IIT-Kanpur, 6th December 2001.